

BIOSAR 2008
Technical Assistance for the Development of
Airborne SAR and Geophysical Measurements during the
BioSAR 2008 Experiment

Final Report

Prepared for

European Space Agency



Prepared by

German Aerospace Center DLR

Microwaves and Radar Institute (HR)

Oberpfaffenhofen

and

Department of Radar Systems

Swedish Defence Research Agency FOI

Linköping, Sweden

and

Centre for Research and Education in Remote Sensing
of the Biosphere CESBIO

Toulouse, France

and

Politecnico di Milano POLIMI

Miland, Italy

Contract: ESA contract No.: 22052/08/NL/CT

ESA study manager:

Malcolm Davidson (Technical Officer)

ESA-ESTEC

Prepared by:

Irena Hajnsek, Rolf Scheiber, Martin Keller, Ralf Horn, Seungkuk Lee (Prime Contractor)

Microwaves and Radar Institute (DLR-HR),

German Aerospace Center (DLR),

PO BOX 1116, 82234 Wessling, Germany

Lars Ulander, Anders Gustavsson, (Subcontractor of DLR)

FOI, Division of Sensor Systems

P.O. Box 1165, SE-58111 Linköping, Sweden

Gustaf Sandberg (Subcontractor of FOI)

Radar Remote Sensing Group (RRS)

Department of Radio and Space Science

Chalmers University of Technology

SE-412 96 Göteborg Sweden

Thuy Le Toan (Subcontractor of DLR)

Centre for Research and Education in
Remote Sensing of the Biosphere CESBIO

18 avenue. Edouard Belin

PO BOX 2801, Toulouse cedex 9, France

Stefano Tebaldini, Andrea Monte Guarnieri, Fabio Rocca (Subcontractor of DLR)

Politecnica di Milano (Polimi)

Dipartimento di Elettronica e Informazione

Piazza Leonardo da Vinci 32, Milano, Italy

Version date changes:

1.0 26/10/2008 version 1 provided to ESA

The authorship of this report is listed in the table below:

Chapter	Authors
2. Introduction	DLR
3. Description of the Study Area	FOI
4. BIOSAR Campaign Schedule	DLR
5. Airborne Data Acquisition	DLR
6. SAR Data Processing	DLR
7. Data Quality	DLR
8. BIOSAR Data Base	DLR
9. BIOSAR Data Analysis	DLR / FOI / CESBIO / POLIMI
10. / 11. Summary & Recommendation	DLR / FOI / CESBIO/ POLIMI
12. / 13. Appendix	DLR / FOI / CESBIO/ POLIMI

1 CONTENTS

1	Contents	2
2	Introduction	2
3	Test Site Description and Ground measurements	2
3.1	Test site description	2
3.1.1	Digital Elevation Model of the Test Site	2
3.1.2	SWEPOS GPS Reference Data	2
3.1.3	Areas for Radar Reflector Deployment at the Test Site	2
3.1.4	References	2
3.2	Ground Measurements	2
3.2.1	Positioning of the Four Large Radar Reflectors in Krycklan	2
3.2.2	Selection of Forest Stands for Field Inventory	2
3.2.3	Field Inventory of Selected Forest Stand.....	2
3.2.4	Field Observations.....	2
3.2.5	Additional Observations Made Within the Whole Area Imaged by E-SAR.....	2
3.2.6	References	2
3.3	Lidar data acquisition and processing.....	2
3.3.1	Lidar data processing.....	2
3.3.2	Field data	2
3.3.3	Modelling of biomass using lidar data.....	2
3.3.4	References	2
4	Airborne Campaign Overview	2
4.1	Campaign Objectives	2
4.2	Participants.....	2
4.3	Campaign Schedule	2
5	Airborne SAR Data Acquisition.....	2
5.1	Airborne Campaign Preparation	2
5.1.1	Calibration Check of the E-SAR System.....	2
5.1.2	Mission Logistics.....	2
5.1.3	Corner Reflectors.....	2
5.1.4	GPS Measurements	2
5.2	Measurement Overview	2
5.3	Radar Data Acquisition	2
6	SAR Data Processing	2

6.1	Processing Strategy	2
6.2	Transcription	2
6.3	RGI Data Processing	2
6.4	Digital Elevation Model	2
6.5	Processed Data	2
6.6	Image Examples	2
6.7	Interferometric Phase to Height Sensitivity	2
6.8	BIOMASS Spaceborne Simulation	2
6.8.1	Simulation parameters	2
6.8.2	Simulation Strategy	2
7	Data Quality	2
7.1	DEM Quality	2
7.1.1	DEM interpolation	2
7.1.2	Comparison of DEM (ellipsoidal) heights at the corner reflector positions:	2
7.2	Geocoding Quality	2
7.3	Calibration Checks	2
7.4	Conclusion	2
7.4.1	E-SAR data performance summary	2
8	Biosar Data Base	2
9	Biosar Data Analysis	2
9.1	Assessment of forest biomass retrieval by FOI	2
9.1.1	Relation between Backscatter and Biomass	2
9.1.2	Impact of Topography on SAR Backscatter Intensity	2
9.1.3	Evaluation of the Saatchi inversion model	2
9.1.4	References	2
9.2	Assessment of forest biomass retrieval by CESBIO	2
9.2.1	Datasets used in the study:	2
9.2.2	Impact of topography on the biomass-intensity relationship	2
9.2.3	Inversion of HV backscatter in biomass	2
9.2.4	Inversion using HH, HV, and VV using Saatchi et al., 2007 algorithm:	2
9.2.5	Inversion using intensity and height	2
9.2.6	Summary and further works	2
9.3	Assessment of forest height retrieval by DLR	2
9.3.1	Data Selection	2
9.3.2	Data Processing for Pol-InSAR	2

9.3.3	Spaceborne simulation data at P-band.....	2
9.3.4	Summary and Recommendation.....	2
9.3.5	References	2
9.4	Assessment of tomography by POLIMI	2
9.4.1	Work objectives.....	2
9.4.2	Description of the Data.....	2
9.4.3	Preliminary Analysis	2
9.4.4	SAR Tomography.....	2
9.4.5	Disjoint Tomographic Imaging of Ground and Volume: Algebraic Synthesis.....	2
9.4.6	Tomographic Processing	2
9.4.7	Tomographic Profiles	2
9.4.8	Large Scale Tomographic Analysis.....	2
9.4.9	Phase Stability and Phase Calibration	2
9.4.10	Conclusions	2
9.4.11	References	2
10	Summary	2
11	Recommendation.....	2
12	Appendix: Data Table	2
12.1	Data Processing	2
12.2	Description of Table	2
12.3	Data Tables.....	2
12.4	References	2
13	APPENDIX: Ground Photos	2

2 INTRODUCTION

This document describes the radar data acquired during the BIOSAR campaign carried out in October 2008 in Northern Sweden. The main objective of the BIOSAR campaign is summarised and a description of the flight campaign and the acquired airborne and ground data are given.

In the frame of its Earth Observation Envelope Programme of the European Space Agency (ESA), BIOSAR supports geophysical algorithm development, their calibration and validation as well as the simulation of future space-borne Earth Observation missions.

The next generation of ESA Earth Observation satellites include a series of innovative satellites dedicated to a specific application. BIOSAR supports the current selected candidate Earth Explorer Mission BIOMASS. The main objective of BIOMASS is the estimation of forest biomass in order to support carbon modelling using longer wavelength.

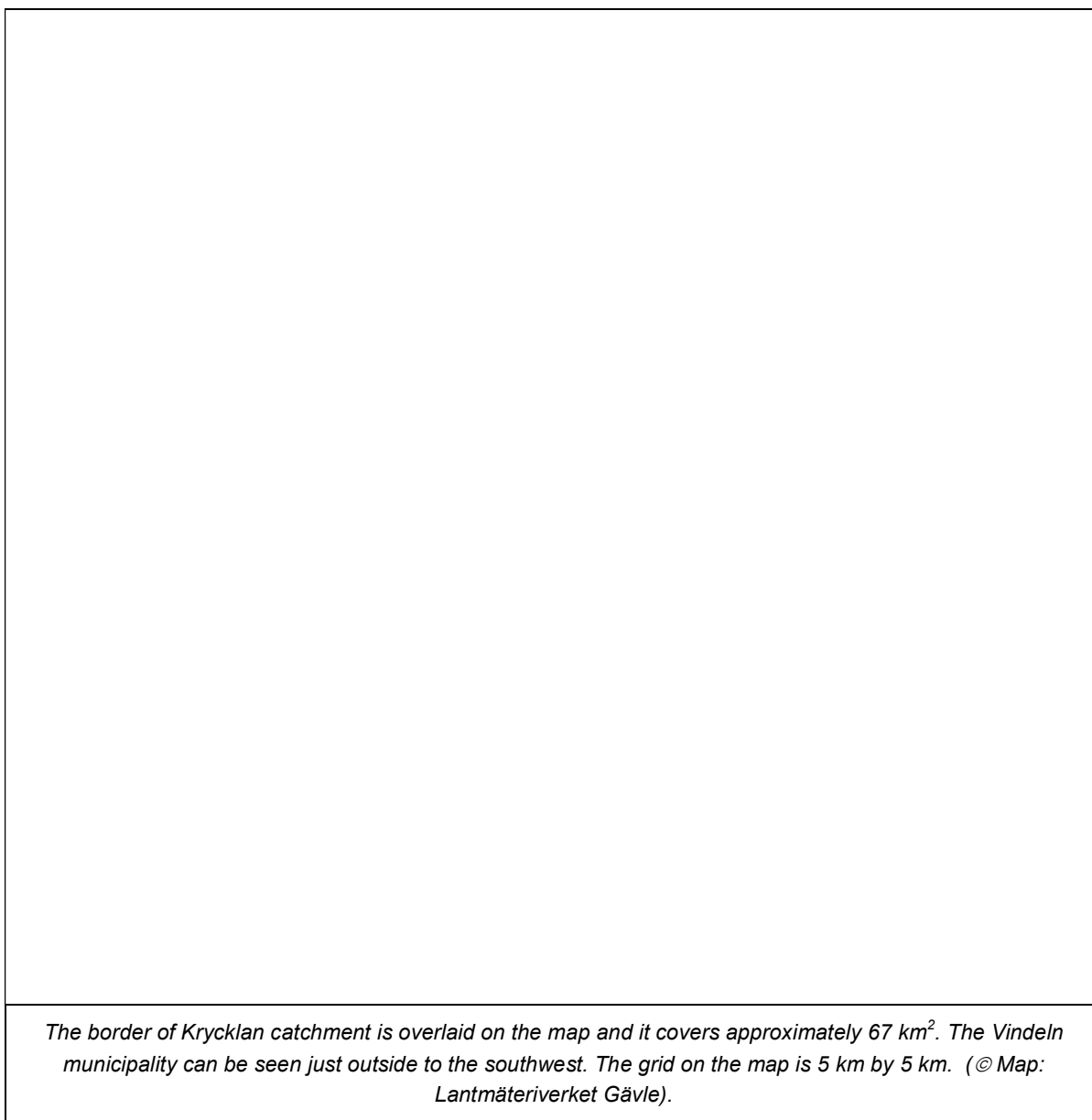
The BIOSAR 2008 campaign collects in-situ and airborne SAR in support of decisions being taken on satellite instrument configurations for the BIOMASS satellite mission. In addition it provides an important database for the study of longer term mission concepts. While the BIOSAR 2007 campaign collected data with the objective to investigate the effect of temporal decorrelation at P-band with 100MHz and 6MHz bandwidth in southern Sweden, BIOSAR 2008 recorded data at boreal forests with strong topographic effects in northern Sweden to investigate the effect on forest height estimation and radar backscatter signal variation.

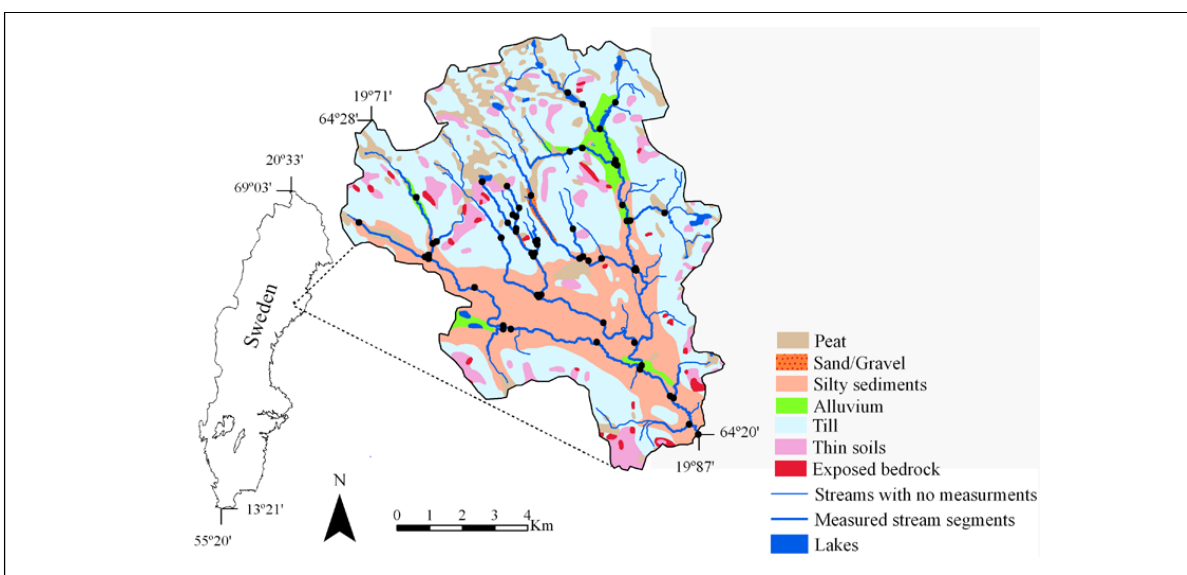
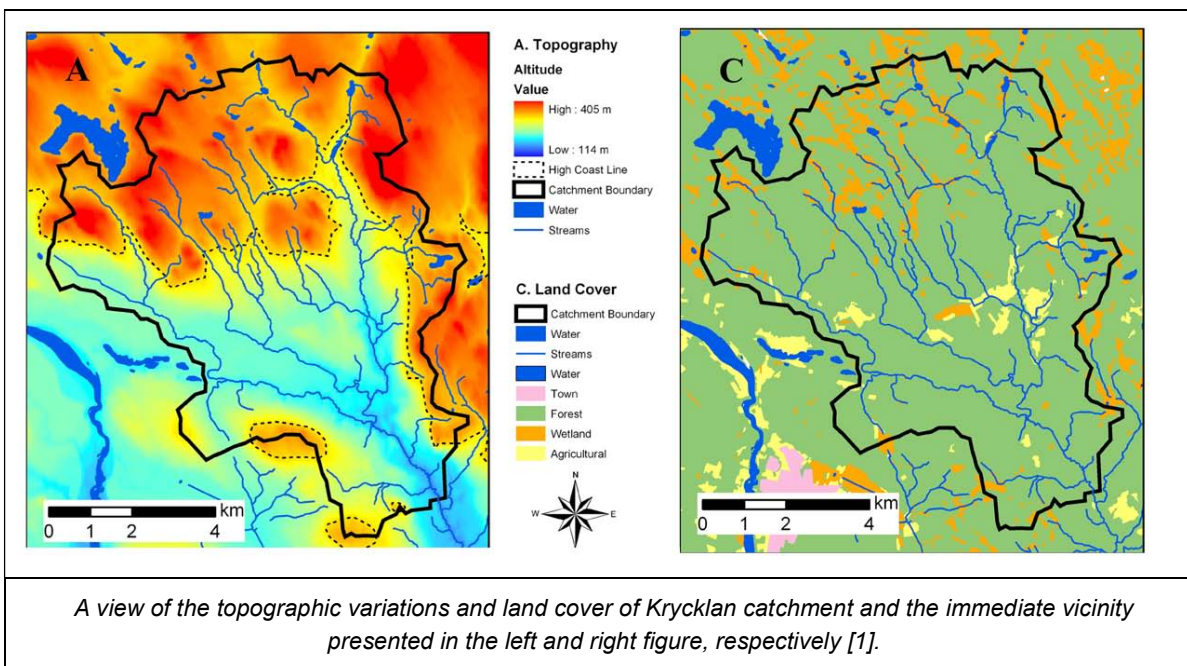
3 TEST SITE DESCRIPTION AND GROUND MEASUREMENTS

3.1 Test site description

The main objective with BIOSAR 2008 was to record SAR data over boreal forests with topographic effects to investigate the effect on biomass retrieval. In addition, the forest should exhibit characteristics typical for more northern latitudes in contrast to the BIOSAR 2007 campaign conducted in southern Sweden at the Remningstorp test site, found in a fairly flat landscape.

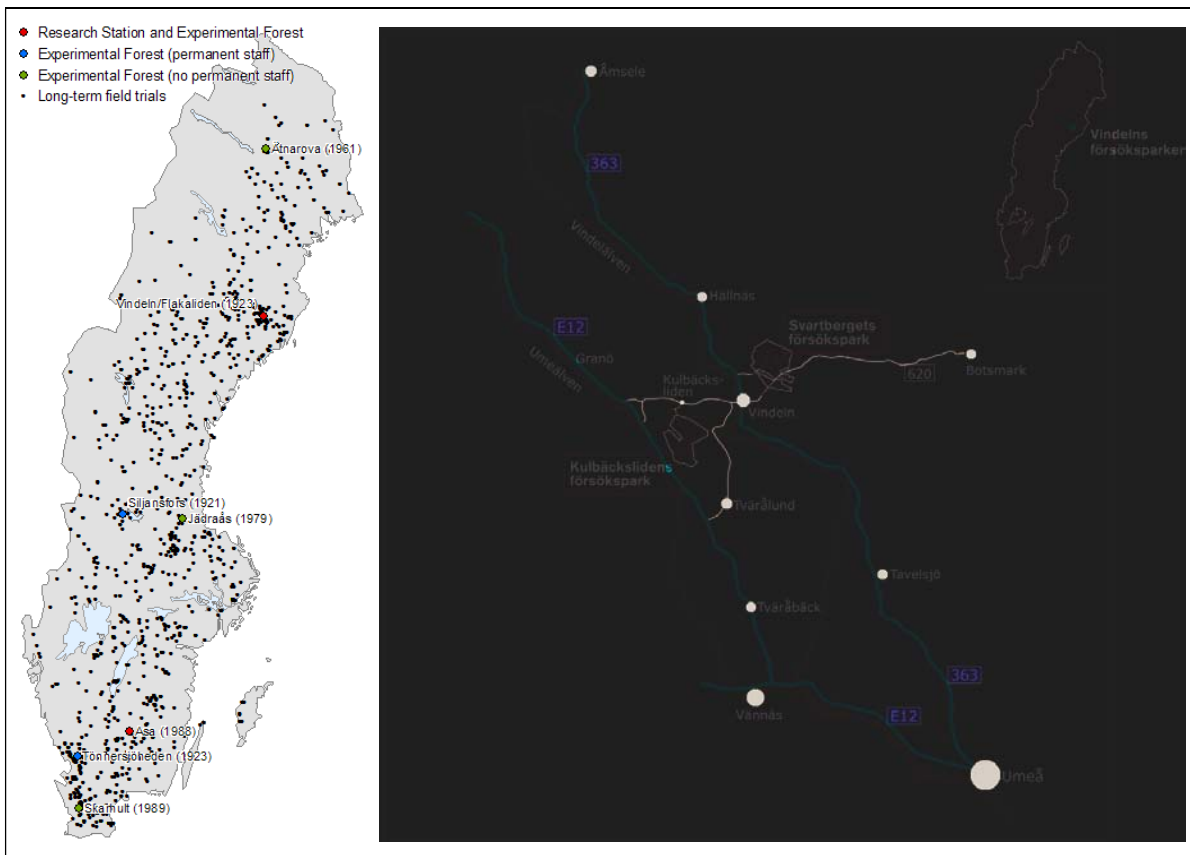
The test site selected for the BIOSAR 2008 campaign was a forested area in the Vindeln municipality, situated in the province of Västerbotten in northern Sweden about 50 km northwest of Umeå. Almost all part of the forests mapped by E-SAR is confined within Krycklan River catchment, which covers 6700 ha in total.





Krycklan catchment has been extensively used for research in various multidisciplinary programs. The focus since the early 1980's has been on forest hydrology, biogeochemical cycling, the role of acid deposition on stream water chemistry and more recently the influence of climate on aquatic ecology. To date almost 20 Ph.D. theses and more than 120 peer-reviewed papers in international scientific journals have resulted from these activities, e.g. [1], [2], [3], [4]. Information about the Krycklan Catchment Study (KCS) are also available from Internet [5], [6].

Krycklan catchment includes one part of Vindeln Experimental Forests, i.e. Svartberget Experimental Forest (64° 14' N, 19° 46'). It belongs to the unit for field-based forest research at the Faculty of Forest Sciences, Swedish University of Agricultural Sciences (SLU) [7]. The unit was established in 2004 and is responsible for all the experimental forests and field-based research stations, together with all long-term field trials, that are directly owned or under control by the faculty. Remningstorp used for BIOSAR 2007, on the other hand, is organized and operated as an independent foundation for research purposes with the forested land managed by the Forestry Society's Estate Management Company. Most of the forestry studies taking place at Remningstorp over the years have, however, in fact also been defined and conducted by SLU.

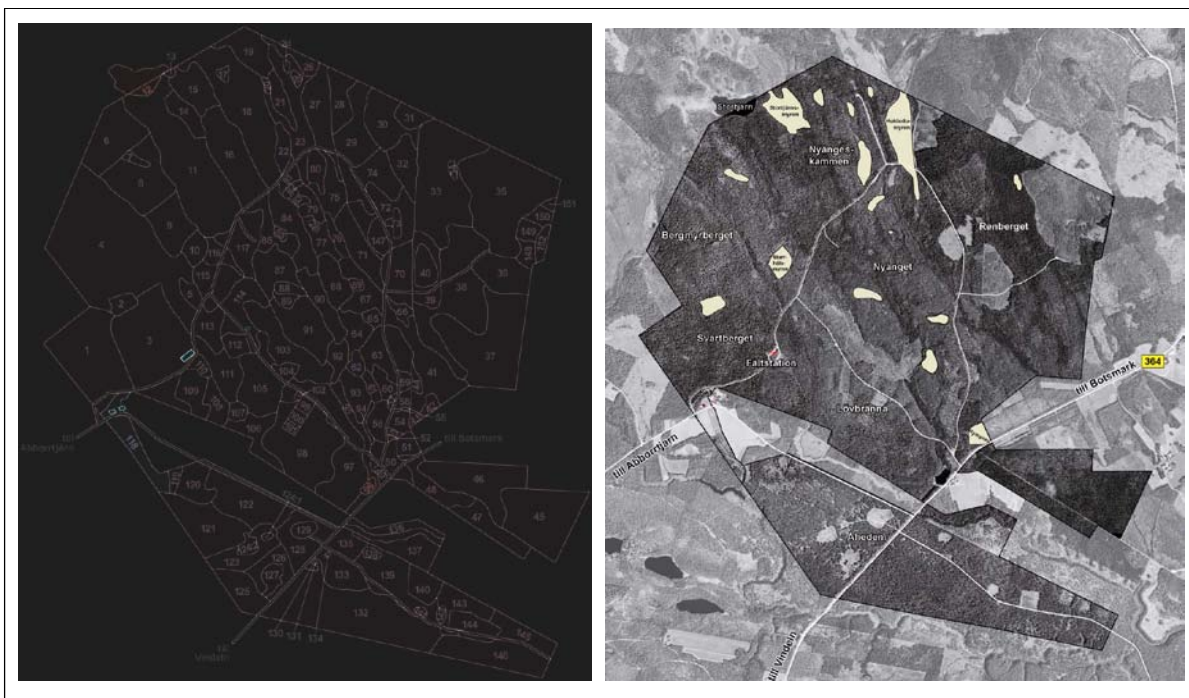


The unit for field-based forest research at SLU operates a few research stations and experimental forests in Sweden but also a large number of long-term field trials all over the country (left). Vindeln Experimental Forests is dominated by two large areas on the opposite side of the Vindel River ("Vindelälven"), i.e. Kulbäcksliden on the western and Svartberget on the eastern side. The size of the two areas are 1455 ha and 1076 ha, respectively, and both of them have been in operation since they were established in 1923 [8], [9]. The landowner for both sites is the state-owned forest company Sveaskog.

Mixed coniferous forest is the dominating forest type in the experimental forests in Vindeln. The bedrock consists almost entirely of gneiss. The dominating soil is moraine with variations in thickness. The climate conditions are an important limiting factor with respect to the northern location of the forests. The region is considered to be in between a coastal and an inland climate.

The ground mapping defined for the BIOSAR 2008 E-SAR missions over Krycklan catchment also resulted in that most of the experimental forest Svartberget was covered by those imaging swaths having a long extension in azimuth. The forest stand numbering for Svartberget is a part of all numbers used for stands

found within the whole catchment. This larger area (6700 ha) has a mix of forest companies and private landowners.



Map of the 1076 ha large experimental forest Svartberget (left). The shown forest stands 1 - 152 on the map originate from a standwise delineation made in 1990. It has been replaced and updated and is not valid for BIOSAR 2008. The same area is highlighted on the aerial photo by a slightly darker intensity for the greyscale modulation (right). The experimental forest is primarily found in the sector from west to south relative the middle point of Krycklan catchment. The main office building of the research station is depicted in red and found along a road just on the border to forest stand 3 on the map (440190 E, 7124830N in UTM Zone 34).

When the test site for BIOSAR 2008 was decided the process to get approvals to map and operate E-SAR in this area during the scheduled time period was initiated. One of the main paperwork issues was to get a permission to transmit at the three frequency bands planned for the campaign, i.e. P-, L- and X-band.

3.1.1 Digital Elevation Model of the Test Site

The existing Digital Elevation Model (DEM) covering the whole of Sweden is fairly coarse, i.e. having a grid size of 50 m by 50 m. The height accuracy of the DEM is claimed to be 2 m or better. The geo-coding of E-SAR slant range imagery results performed by DLR is based on this height data. Upon request and specification provided by DLR a coarse DEM was obtained from the National Land Survey of Sweden ("Lantmäteriverket", "Lantmäteriet" or "LMV") [10]. This product is commercial and subject to a license agreement. The data set purchased is therefore a single user license with DLR defined as the end-user. In case other research groups working with BIOSAR 2008 data are interested in this DEM product they have to order their own data set using the information and point of contacts found at the web site [10]. The area of interest to be included by the coarse DEM was defined by DLR in UTM Zone 34 coordinates according to:

- N 7130000 - E 436000 (Upper left corner, North-West)
- N 7118000 - E 448000 (Lower right corner, South-East)

The high resolution lidar based DEM acquired as part of the BIOSAR 2008 project is available without any commercial restrictions. It has a grid size of 0.5 m by 0.5 m. The airborne lidar acquisition had focus on mapping the whole of Krycklan to get full flexibility later on to position the E-SAR coverage arbitrary over the forest stands present within the watershed borders. This DEM has, however, not enough with data points outside Krycklan and can therefore not be used to geo-code the full E-SAR ground scenes which reach little beyond the border. Another lidar based DEM from 2006 covering the catchment is available at SLU. It has a coarser grid of 10 m by 10 m but the same limitation with lack of available height values close to but outside the area.

3.1.2 SWEPOS GPS Reference Data

In the post-processing to retrieve an accurate flight track of the E-SAR platform reference GPS data registered at a well-known fixed position on ground were provided by SWEPOS during BIOSAR 2008. The SWEPOS system is the Swedish national network of reference stations for GPS data and is operated by LMV [11]. The network consists presently of 26 complete and 125 simplified stations distributed over the the country. To achieve redundancy and reliable data access, the complete stations are equipped with two parallel GPS receiving systems and the power supply is also built to handle failures like power outages for a period of up to 48 hours. In addition, the GPS antenna is here mounted on pillars that are made of concrete and are placed on solid bedrock, often at high altitudes where the obstacles are in low elevations. The simplified stations have less redundancy and the antennas often mounted on available buildings with the supporting equipment indoors.



The complete SWEPOS GPS station Umeå is shown to the left whereas the antenna of the simplified station Vindeln can be seen in the photo to the right. (Photos from [11]).

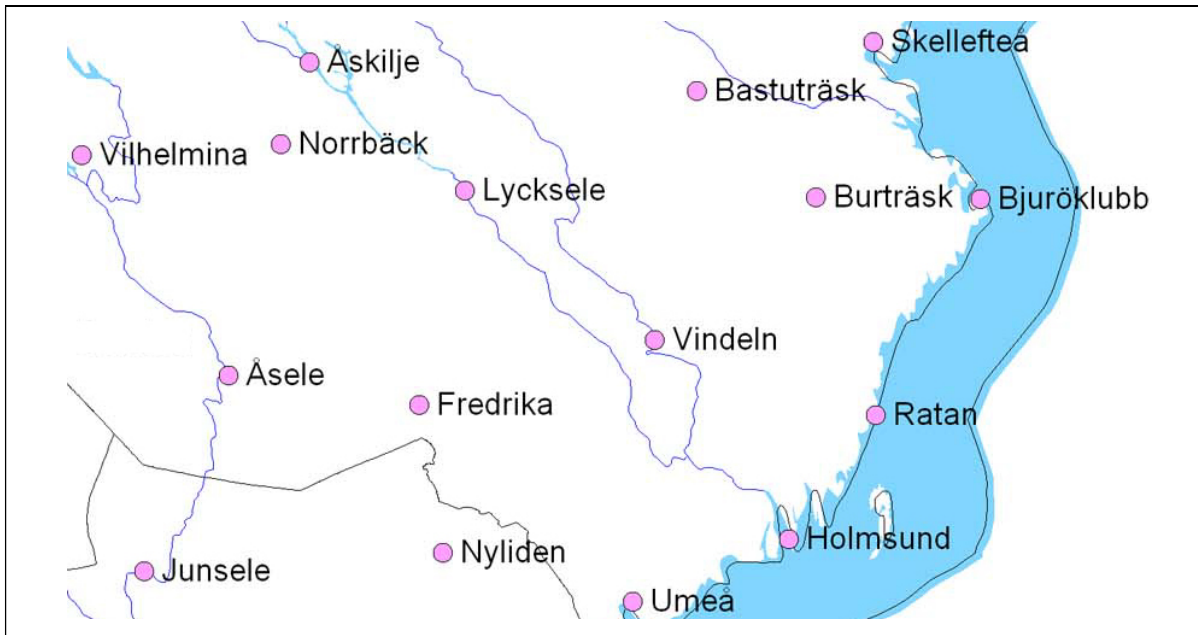
Data from five complete SWEPOS GPS stations and five simplified were requested for all time windows when detailed positioning was needed for the BIOSAR activities, i.e. all E-SAR flights and measurements of the deployed trihedral positions. The data were made available on a daily subscription basis and could be downloaded from an ftp-server at LMV. The main criterion to select the stations was to encompass the region of interest, i.e. Krycklan test site as well as Umeå airport used by the Dornier DO 228 aircraft with the E-SAR system installed onboard.

The position figures available for the different stations are given in the reference system SWEREF 99 which is the Swedish realisation of ETRS 89 (the European Terrestrial Reference System 1989).

Station	Latitude (SWEREF 99)	Longitude (SWEREF 99)	Height (ellipsoid, m)
Holmsund	63° 40' 22.239643"	20° 23' 19.116759"	32.4236
Ratan	63° 59' 8.117625"	20° 53' 44.037024"	31.3303
Skellefteå	64° 52' 45.101355"	21° 2' 53.825257"	81.1970
Umeå	63° 34' 41.291434"	19° 30' 34.531848"	54.4984
Vilhelmina	64° 41' 52.241600"	16° 33' 35.733914"	449.9356

Station	Latitude (SWEREF 99)	Longitude (SWEREF 99)	Height (ellipsoid, m)
Bastuträsk	64° 47' 33.692708"	20° 2' 11.93729"	274.8467
Bjuröklubb	64° 28' 50.106459"	21° 34' 29.691248"	69.2536
Burträsk	64° 31' 2.390528"	20° 39' 31.193565"	118.8323
Lycksele	64° 35' 9.256421"	18° 42' 10.968985"	253.9710
Vindeln	64° 12' 8.011756"	19° 42' 50.552947"	217.9642

In contrast to BIOSAR 2007 the density of SWEPOS stations was considered to be sufficient by DLR and therefore there was no need to deploy an extra GPS receiver on ground close to the airport or at the test site to register data during the E-SAR missions.



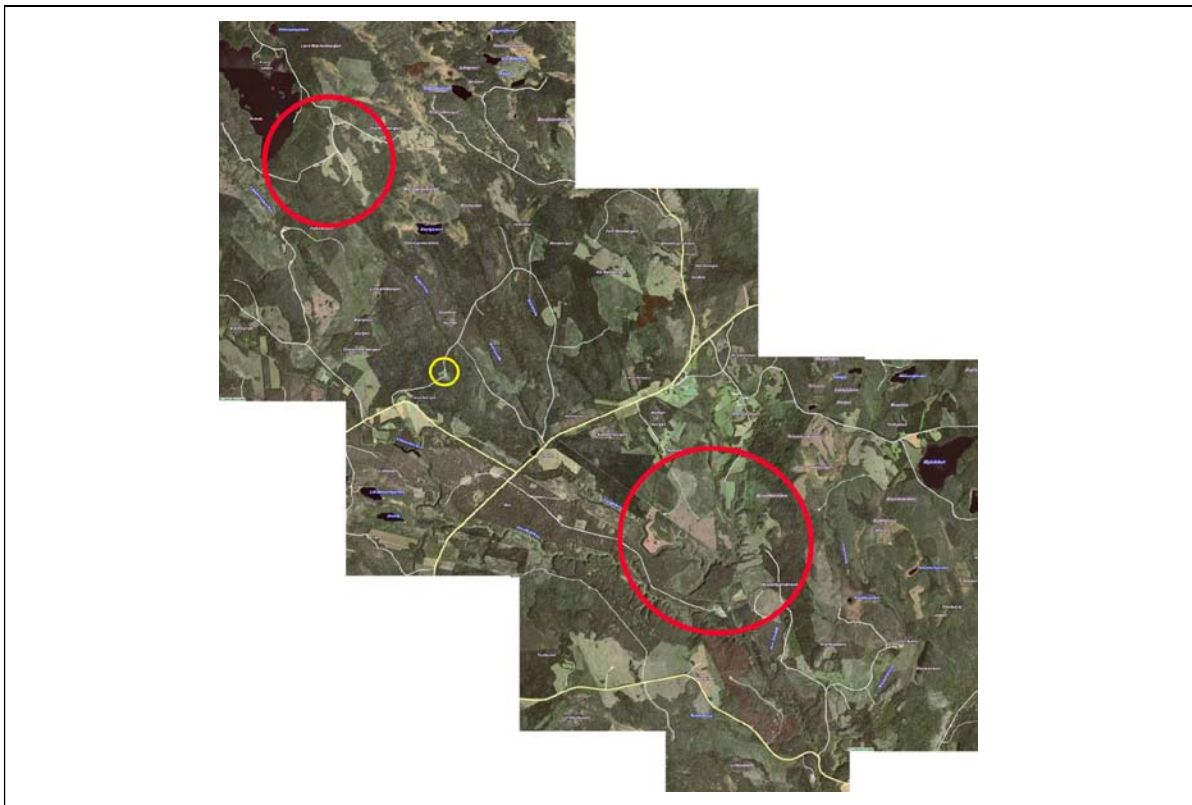
Locations of SWEPOS GPS stations in the region where the BIOSAR 2008 experiment were undertaken. The map shows the situation in November 2008 and the new facilities in Fredrika, Norrbäck, and Nyliden were not in full operation one month earlier. (Map from [11]).

The differential GPS post-processing was carried out by DLR for both the E-SAR flights and the position measurements of all targets deployed on ground. By using the same software any differences in parameter settings could be avoided and hence reduce the risk to introduce small unintentional errors in the output result.

3.1.3 Areas for Radar Reflector Deployment at the Test Site

When the E-SAR coverage of parts of Krycklan had been decided the work to find suitable open areas for deployment of radar reflectors was initiated. Based on an aerial photo covering all defined E-SAR swaths potential open areas were identified by FOI and DLR. People from the research station at Svartberget

went to check the present conditions and sent back captured photos. By this iterative procedure the preferred candidates for the reflector deployment were selected and the landowners could be contacted in advance of the experiment for areas located outside the experimental forest Svartberget. This was especially important for some of the locations where the vegetation close the reflector had to be cleared in preparation to or after the deployment, ranging from very small trees up to a few single large trees.

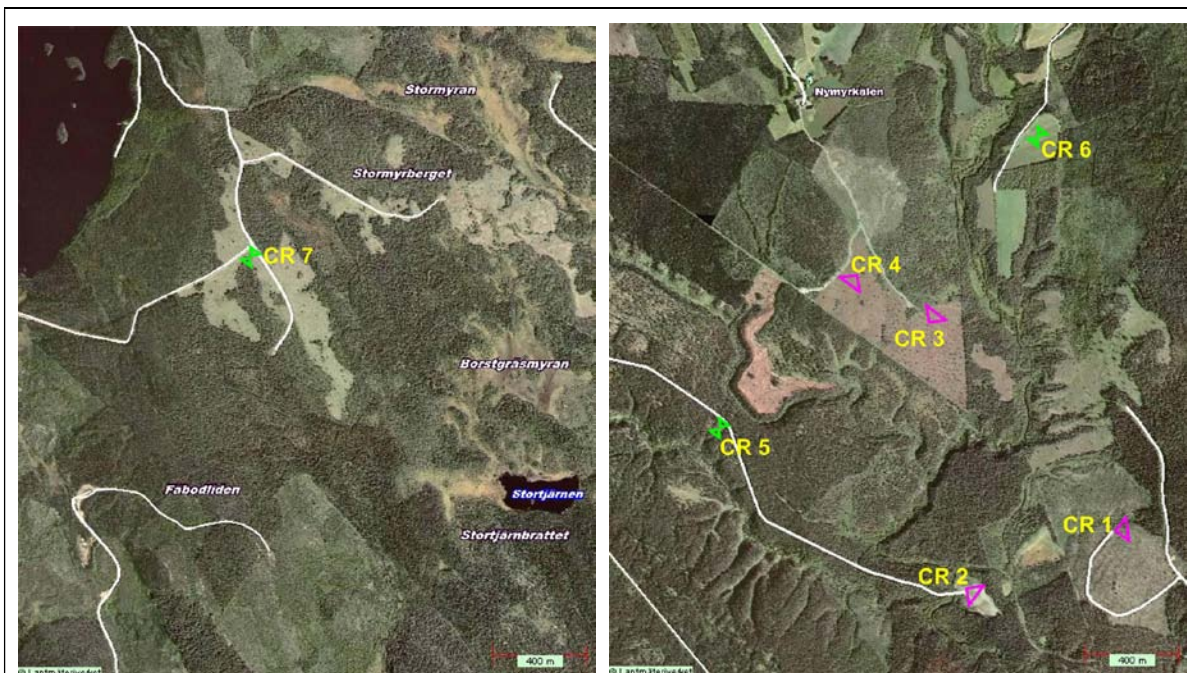


Based on the locations of the E-SAR swaths in the defined flight program for BIOSAR 2008 two main regions were identified where radar reflectors should be deployed in open areas, here marked by the red circles. The yellow circle points out the main building of the Svartberget Research Station. (Aerial photo from www.eniro.se, © Aerial photo: Lantmäteriverket Gävle).

FOI planned to provide four 5 m large trihedrals but this time without the smooth inner surfaces available in Remningstorp during BIOSAR 2007. The units available there were originally used in support to the calibration and validation phase of the Japanese ALOS radar satellite operating at L-band. The coarser mesh now planned for BIOSAR 2008 was recognized to be sufficient for reliable results on P-band but on the limit for L-band because of the larger mesh dimensions as well as the overall unevenness of each side, assembled using three individual squares and three triangles as well as aluminum L-profiles along the edges as reinforcement. Some indications that this trihedral type could work properly also at L-band were given by comparisons in the E-SAR data from Remningstorp 2007, where one trihedral not modified for ALOS was available (for the FOI CARABAS-II VHF SAR sensor) but not used in the BIOSAR 2007 SAR data analysis. To avoid any doubts of the results obtained at L-band in Krycklan DLR also provided two 1.5 radar reflectors. In addition, four 90 cm reflectors were also shipped from DLR to be used for the X-band interferometric SAR data acquisitions.

The 5 m and the 1.5 m reflectors should be placed in open areas as close as possible to the centre of the different swath widths. The idea was to place the two 1.5 m reflectors close to each other but with opposite pointing directions (180° off) corresponding to the two headings planned for the E-SAR mapping of the

larger area with focus on Pol-InSAR for interferometric and tomographic analysis. The two 5 m reflectors deployed and optimized for the same imaging geometry were on the other hand well separated from each other. The four 90 cm reflectors were also deployed in pairs with opposite pointing directions but now instead found in near range and far range, respectively, or vice versa when E-SAR illuminated the scene from the opposite side. The other 5 m reflectors were used for the two additional headings included in the imaging of the smaller but most topographic area in the southeast.



The approximate locations of the ten radar reflectors deployed in Krycklan during BIOSAR 2008. The area up in northwest is shown in the left aerial photo and the area in southeast in photo to the right. Corner reflectors (CR) 1 to 4 indicate the large 5 m FOI reflectors, CR 5 to 6 the 90 cm DLR reflectors (two at each site) and CR 7 the two 1.5 m reflectors. (Aerial photo from www.eniro.se, © Aerial photo: Lantmäteriverket Gävle).

The work with deployment of the radar reflectors started on Monday 6 October. The areas seen on photos only so far were visited together with staff members from Svartberget to decide on the more precise location of each reflector. It was obvious that some clearing of the vegetation was necessary at some of the reflector sites. The arrival of the DLR ground team on Wednesday 8 October increased the available manpower to mount the largest reflectors and took also lead on the deployment of the smaller ones. All preparations were completed in time before the first E-SAR flight mission scheduled for the afternoon on Monday 13 October.



Area for corner reflector CR1 (5m).



Area for corner reflector CR2 (5m).



Area for corner reflector CR3 (5m).



Area for corner reflector CR4 (5m).



Preparations for deployment of CR1



Preparations for deployment of CR1.



Deployment of CR1.



Deployment of CR1.



A four wheeler all-terrain vehicle (ATV) from Svartberget was in some cases needed to get the trihedral pieces to the final locations, here CR3.



The required elevation for the large reflectors was adjusted using two lift jacks in each corner and then the trihedral rested on wooden structures, here CR4.



One of the large reflectors, CR2, could rest on the two available lift jacks instead of a wooden structure.



All radar reflectors were prepared when the coordination meeting was held in Umeå on Monday 13 October.

3.1.4 References

- [1] I. Buffam, "Linking Landscape Characteristics, Streamwater Acidity and Brown Trout (*Salmo trutta*) Distribution in a Boreal Stream Network," *Acta Universitatis Agriculturae Sueciae*, 2007:33, Doctor's dissertation, ISSN 1652-6880, Umeå, Sweden, 2007.
- [2] I. Buffam, H. Laudon, J. Temnerud, C.-M. Mörth, and K. Bishop, "Landscape-scale variability of acidity and dissolved organic carbon during spring food in a boreal stream network," *Journal of Geophysical Research*, vol. 112, G01022, doi: 10.1029/2006JG000218, 11 pages, 2007.
- [3] H. Laudon, V. Sjöblom, I. Buffam, J. Seibert, and C.-M. Mörth, "The role of catchment scale and landscape characteristics for runoff generation of boreal streams," *Journal of Hydrology*, 344, pp. 198-209, 2007.
- [4] H. Laudon and I. Buffam, "Impact of changing DOC concentrations on the potential distribution of acid sensitive biota in a boreal stream network," *Journal of Hydrology and Earth System Science*, 12, pp. 425-435, 2008.
- [5] <http://ccrew.sek.slu.se>. Visited 2009-05-14.
- [6] <http://www.seksko.se/index.php?lang=en> > Research > Current Research > Krycklan Catchment Study. Visited 2009-05-14
- [7] <http://www.esf.slu.se/?eng=1>. Visited 2009-05-14.
- [8] G. Sirén and U. Barring (editors), "Kulbäckslidens och Svartbergets försöksparker," *Royal College of Forestry, Department of Reforestation, Research Notes, Nr 53*, Stockholm, 1974, (in Swedish).
- [9] H. Odin (editor), "The Forest Research Station at Vindeln," *SLU, Faculty of Forest Sciences*, Stencil nr 5, ISSN 0280-4328, Umeå, 1985.
- [10] <http://www.lantmateriet.se>. Visited 2009-05-14.
- [11] <http://swepos.lmv.lm.se>. Visited 2009-05-14.

3.2 Ground Measurements

3.2.1 Positioning of the Four Large Radar Reflectors in Krycklan

The four deployed 5 m trihedrals were planned to have the orientation and elevation angle figures found in the following table and retrieved based on the E-SAR imaging geometries defined for BIOSAR 2008:

CR	Baseplane elevation angle	Look direction angle*	Azimuth angle*
#1	10°	82°	352°
#2	10°	127°	37°
#3	10°	38°	308°
#4	10°	218°	128°

* = The compass declination in Krycklan is about 6° east, i.e. 352° magnetic corresponds to 358° true north.

The four large trihedrals were left elevated in the same fixed position during the whole period, i.e. about one week until the last E-SAR flight on Wednesday 15 October was brought to an end. It was more difficult to perform fine adjustments during the deployment in Krycklan compared to Remningstorp where the trihedral tilting mechanism was equipped with three different anchor points in the ground to which ropes were connected to tighten the outer corners of the reflector structure. The orientation and elevation angles (magnetic) were measured in more detail on Monday 13 and Tuesday 14 October to document the values obtained, including any subsidence effects occurring after the final mechanical adjustments. The results are summarized in the table below:

CR	Baseplane elevation angle	Look direction angle*	Horizontal
#1	12°	80.5°	1.2°
#2	10.7°	126.6°	1.4°
#3	10.2°	38°	0.4°
#4	11.2°	217.5°	0.6°

* = The compass declination in Krycklan is about 6° east, i.e. 308° magnetic corresponds to 314° true north.

Positioning of the apex for each 5 m trihedral was performed both before it was elevated and after the campaign when it had been dismantled. In the former case the measurements were carried out using an aluminium rod with a GPS antenna on top and raised to be well above the trihedral and thus have no obstacles from the reflector structure itself at low satellite elevations. The antenna was positioned at a height of 550 cm above the ground point on which the lower end of the rod rested. The trihedral structure gave support to the rod during the measurements with some ropes attached to keep it in a fixed position.

In the measurements conducted after the campaign a marker was put into the ground at the apex before the trihedral was lowered from its elevated position. When the trihedral had been dismantled a tripod with a GPS antenna was positioned above the marker and registration of the data required for differential post-processing was carried out. This method was recognized to be more reliable in terms of how accurate the true apex point could be identified and therefore it was this data set that was provided to DLR. It is estimated that the true apex position in elevated mode was correctly located and measured within an uncertainty less than 10 cm. The smaller reflectors (90 cm and 1.5 m) were only positioned after they had been removed with the GPS antenna mounted on a tripod. For all ten reflector sites positioned this way the antenna height above the apex point was noted and the each registration period was in the order of 30 minutes. The GPS receiver model used in all measurements was Ashtech Z-12.

CR	Date	Registration time (UTC)	GPS antenna height (cm)
#1	2008-10-17	10:14:32 - 10:35:49	137.0
#2	2008-10-17	13:13:40 - 13:29:45	137.0
#3	2008-10-17	09:16:31 - 09:36:07	137.0
#4	2008-10-17	08:21:13 - 08:41:57	136.0
#5A	2008-10-16	12:50:13 - 13:16:31	140.0
#5B	2008-10-16	12:16:49 - 12:44:44	132.8
#6A	2008-10-16	09:33:43 - 09:57:28	149.8
#6B	2008-10-16	10:02:25 - 10:24:31	149.8
#7A	2008-10-16	07:30:37 - 07:58:03	137.5
#7B	2008-10-16	08:10:59 - 08:33:30	132.8



Positioning of radar reflector CR3 using a 550 cm long aluminium rod with a GPS antenna mounted on the top. Measurements carried out before the trihedral was elevated according to the imaging geometry.



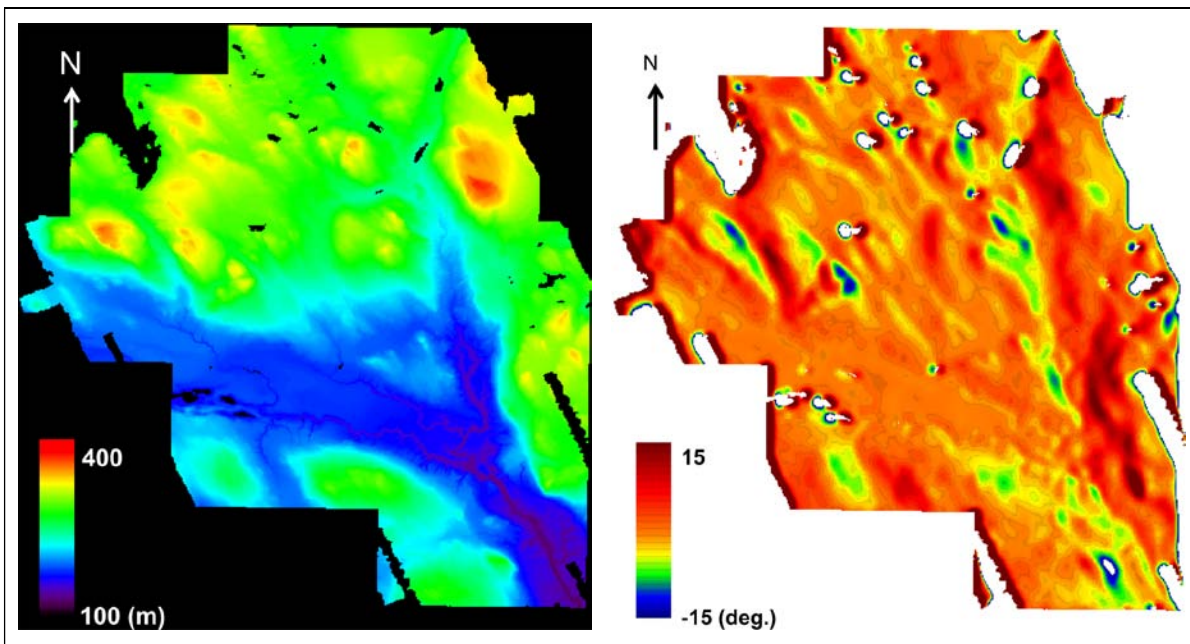
Positioning of radar reflector CR2 after it had been removed. A tripod with a GPS antenna mounted was used and adjusted above the marked footprint of the trihedral apex while elevated.

3.2.2 Selection of Forest Stands for Field Inventory

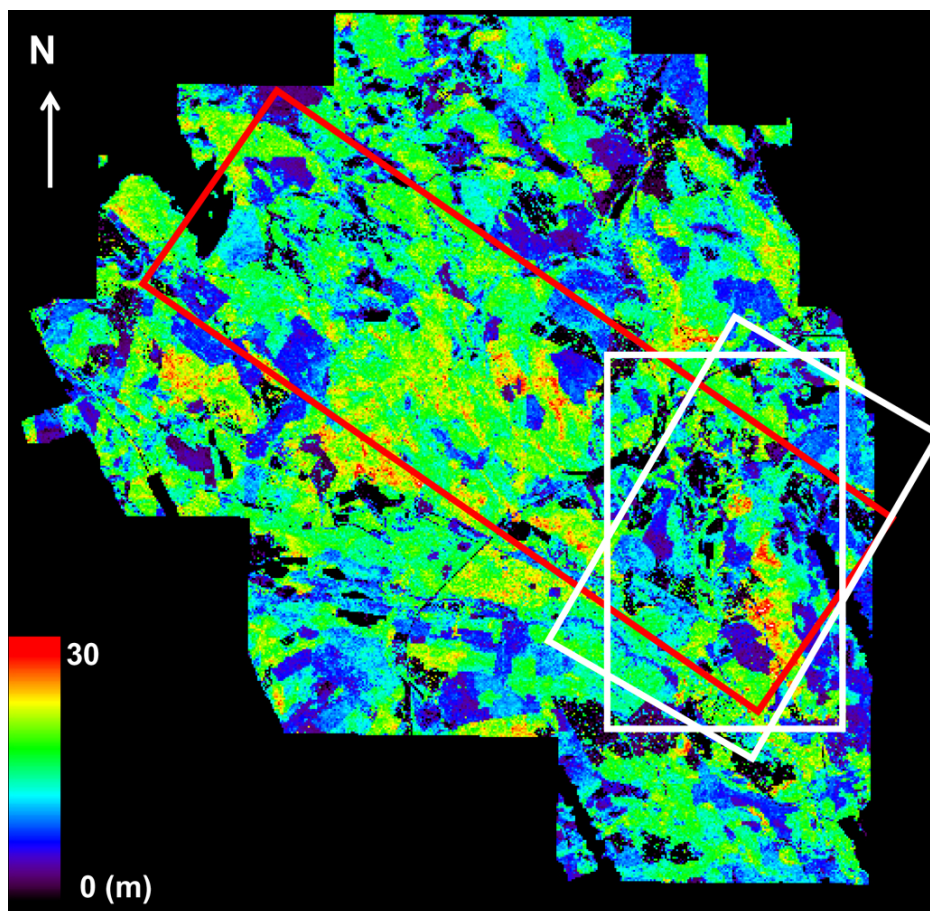
The whole Krycklan catchment could not be mapped by E-SAR with the total flight hours available during the week scheduled for the campaign, including the ferry flights from and back to Oberpfaffenhofen in southern Germany. A realistic core area for the E-SAR coverage in Krycklan was considered to be a ground swath of 3 km (range) by 10 km (azimuth), obtained with one imaging pass at P-band, L-band or X-band. Besides SAR acquisitions at three different frequency bands in separate imaging passes the main strip on ground should be mapped from two opposite look directions and for P- and L-band repeat this in 6 parallel tracks on each side with a given baseline spacing. The ground segment exhibiting most topographic variations should also be mapped from two additional look directions. With the maximum swath width for E-SAR this corresponds to a common circular area with a diameter of 3 km. The registration length in azimuth could thus be reduced significantly for those two extra headings and a figure of 4 km instead 10 km was prescribed to keep some margins.

Given all the constraints for the SAR mapping and available flight hours work was initiated to identify where to position the main radar strip within Krycklan in the best way to fulfill the different campaign objectives. In support to this work a 10 m by 10 m DEM was provided by SLU. This data set was retrieved from a laser mapping of the whole catchment carried out in 2006. With access to this DEM the ground slope distribution could be investigated. Using the same acquired laser data SLU also generated products more related to the vegetation cover and represented on the same raster grid size, e.g. density (vegetation

ratio) and forest heights maps. All such type of additional information describing the area was distributed to the BIOSAR 2008 team members. A first draft version for the E-SAR coverage was agreed on at a project meeting held at ESTEC on 27 March 2008 and primarily based on analyses of the ground slope and forest height values. The suggested location for the 10 km long main radar strip had an orientation from northwest toward southeast (or vice versa) in the azimuth (along-track) direction, with a centre line passing about 1 km north of the Svartberget Research Station. Within the proposed imaged area the major part of Svartberget experimental forest area was included. The most topographic variations for additional radar look directions were found in the southeastern region and were thus selected for the mapping using two additional flight headings with the E-SAR sensor, always looking to the left-hand side of the aircraft.



A DEM of the Krycklan area retrieved by SLU using data from a laser mapping conducted in 2006 (left). The generated DEM has a posting of 10 m by 10 m but is here resampled. Based on this data set DLR calculated the corresponding ground slope variations as a mean to facilitate the approximate positioning of the main 3 km (range) by 10 km (azimuth) E-SAR coverage planned for P-, L- and X-band (right).



Forest height estimates retrieved by SLU from the laser mapping of Krycklan conducted in 2006 and represented on the same original grid size as the DEM. The red rectangle shows the 3 km by 10 km main E-SAR imaging swath proposed for BIOSAR 2008. The central part within the two smaller white rectangles covers the ground area selected for studies of topographic effects on biomass estimation and planned to be mapped from totally four different look directions.

The next step was to make a more detailed analysis of the conditions within the main strip and check whether a sufficient number of forest stands for field inventory could be identified, with the variability in biomass ranging from low to high values as well as being found on ground surface from a few different slope classes. In the order of 30 forest stands were expected to be surveyed and defined based on the requirements from the BIOSAR 2008 project. In addition, about 100 more circular sample plots were planned to be undertaken during the same field inventory period by other SLU projects and thus not necessarily within the E-SAR mapped areas or with focus on stand levels. However, these extra *in-situ* samples will be used as additional training data for the biomass retrieval to be conducted for the new laser mapping planned for Krycklan catchment in 2008.

In the process to search for useful forest stands within the main strip the products generated from the laser data acquired in 2006 were the main information source. Consecutive compartments of 80 m by 80 m were investigated for the slope class with the stem volume calculated based on regression models provided by SLU and applied on the corresponding laser data. These results were then matched with the standwise delineation available to get a priority list among all stands to ensure a good stratification with respect to both slope and stem volume (biomass).

Within the forested area to be mapped there is a mix of landowners. The only standwise delineation covering the whole catchment and available at that time (June 2008) was generated from an automatic segmentation using the laser data from 2006 in combination with a SPOT-5 satellite image to retrieve the tree species composition. Work was, however, in progress at SLU to use recent aerial photos instead and compile a more accurate standwise delineation but this was not completed until the fall of 2008. Hence, there were some uncertainties to be taken care of by the field team when the inventory started in late June. Silvicultural activities could have changed the forest conditions significantly since the laser scanning and the delineation borders available could show large deviations when compared with reality. Visited stands that exhibited too much difference were therefore skipped by the field team and replaced with the next one on the list. In this manner there was an iterative process in which the stands finally were selected and measured *in-situ*. In fact, there was a possibility that the expected 30 representative forest stands could not be encompassed without some changes of the positioning for the main SAR swath, i.e. a shift and/or a rotation. In the end, however, it turned out that such an action was not necessary. Comparison later on with the new standwise delineation showed only minor differences and the new borders are now used for the geographical representation of the stands. There is, however, one exception where the new delineation is significantly larger compared to the area recognized as the stand during the survey. The revised extended part will thus lack circular sample plots. For this stand the original older delineation is therefore used to represent the forest stand.

In total, 31 forest stands were surveyed for *in-situ* measurements in Krycklan during the summer 2008. From the new standwise delineation carried out based on aerial photo interpretation those forest stands have been given the following numbers:

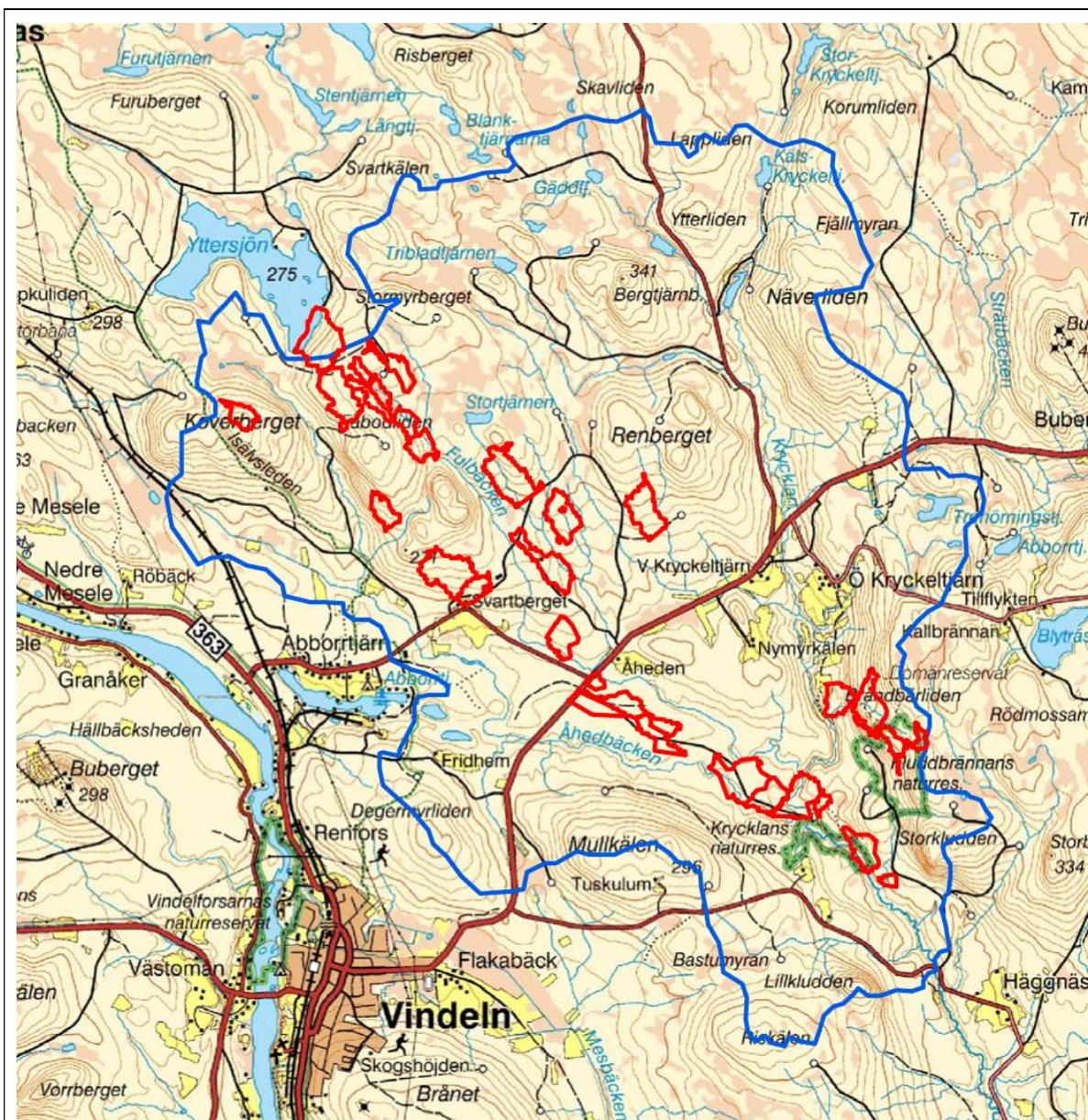
- 1474, 1493, 1517, 1812, 1892, 2228, 2269, 2625, 2626, 2629, 3245, 3611, 3614, 3628, 3689, 3715, 4035, 4038, 4115, 4451, 15096, 17637, 18147, 18278, 21577, 22838, 30097, 31818, 32398, 36169, 36979

The forest stand polygons have been produced using ArcGIS, i.e. a suite consisting of a group of geographic information system (GIS) software products developed and provided by the company ESRI. The output from this is a number of generated files which have been given the following file name syntax:

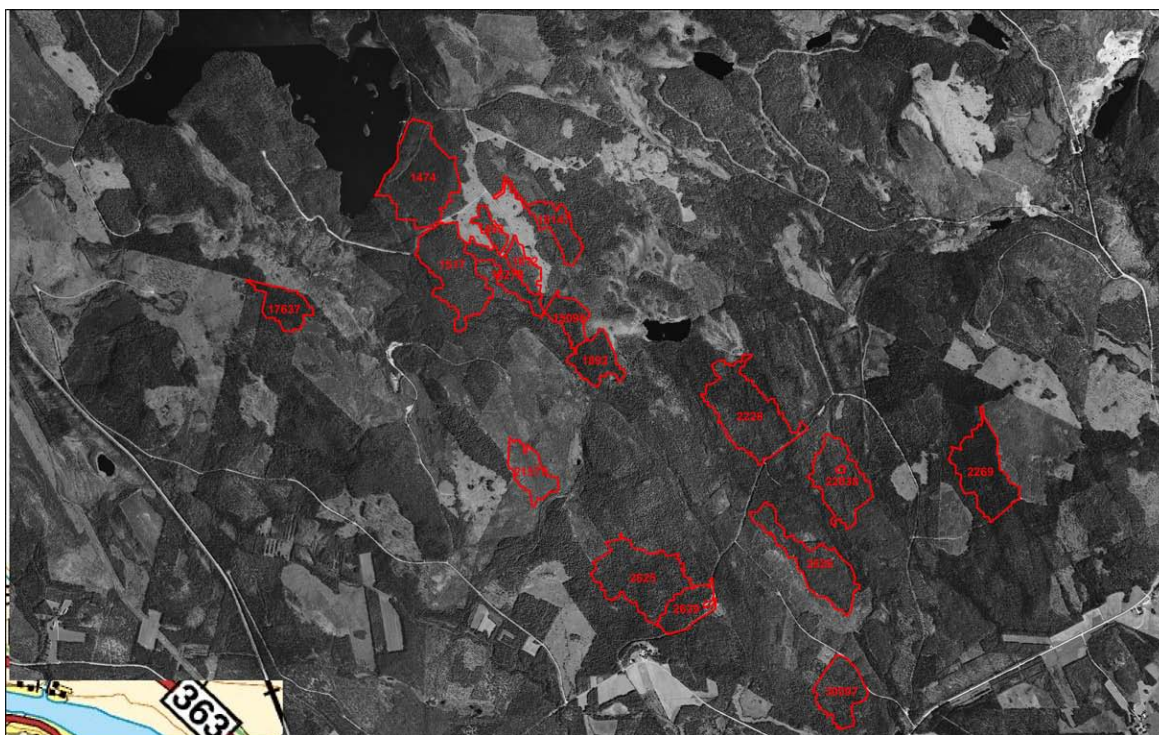
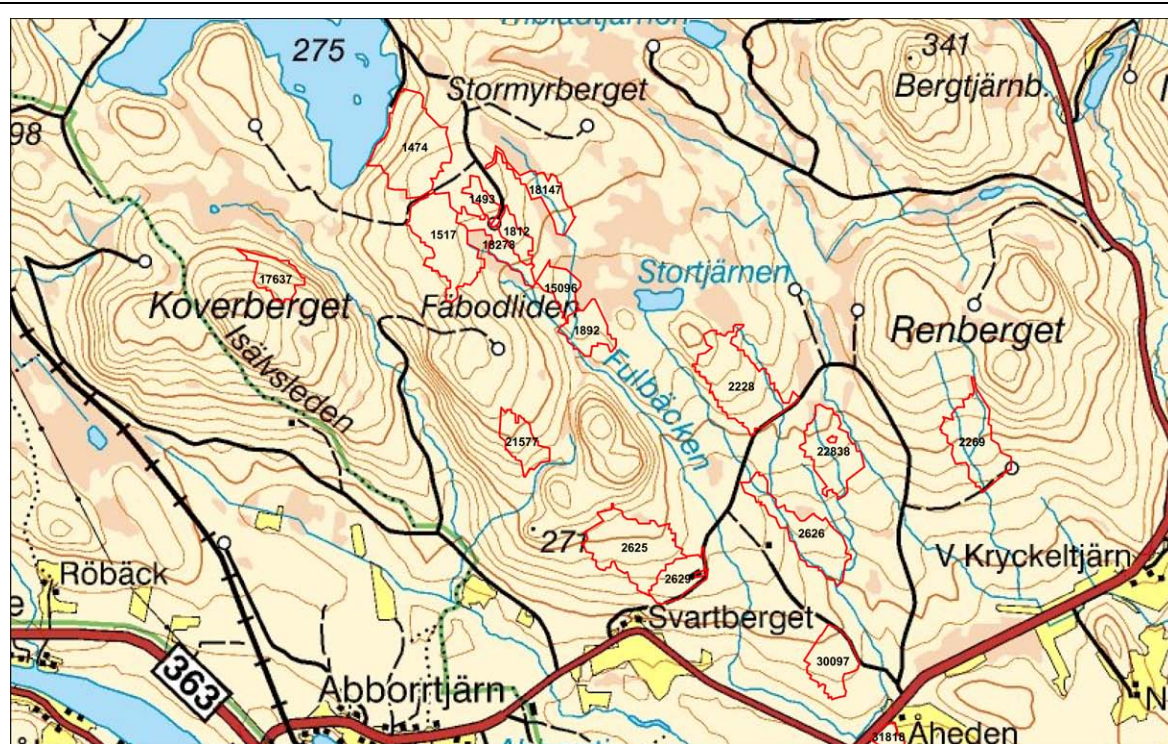
- "Avd_nyind_Utm34.*". Files generated by ArcGIS to describe the 30 forest stand polygons based on the new standwise delineation carried for Krycklan catchment

Forest stand 3715 is the one for which the older delineation has been kept to better represent the area within which the circular sample plots measured *in-situ* are found. The description of this single forest stand polygon is found in the files with the following name syntax:

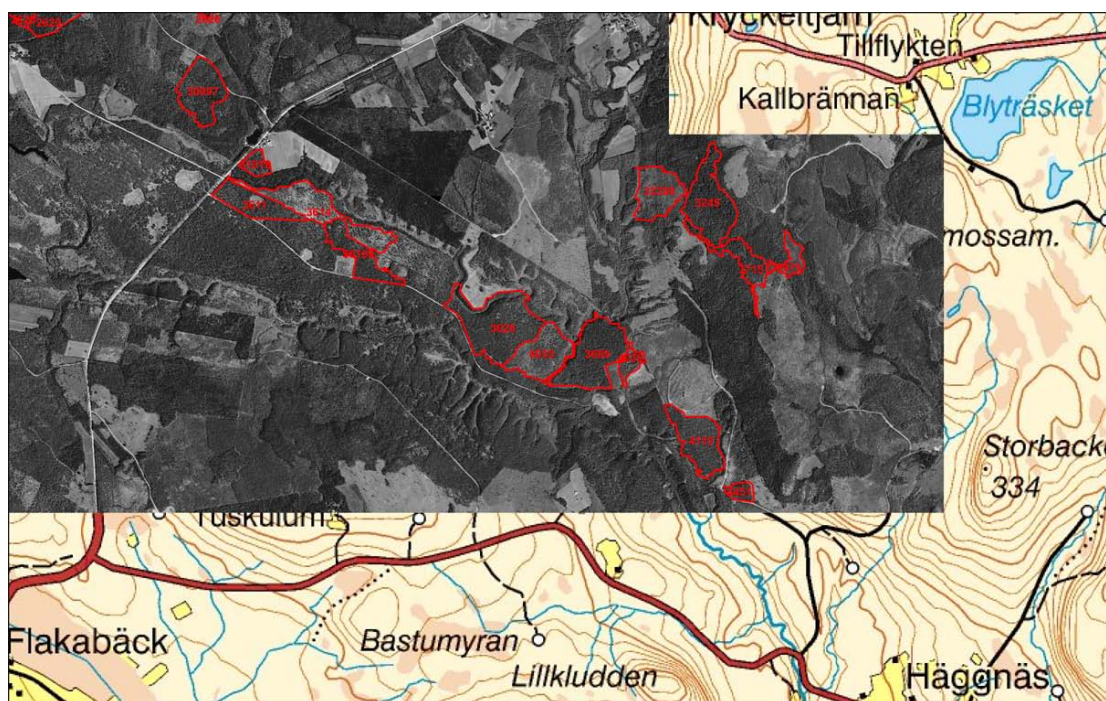
- "Avd_Utm34.*". Files generated by ArcGIS to describe the single forest stand polygon based on the older standwise delineation carried for Krycklan catchment



The 31 forest stand polygons are presented in red as an overlay on top of the map. The different forest stand numbers are not visible here. The border of Krycklan catchment is shown as the blue layer. (© Map: Lantmäteriverket Gävle).



Forest stands surveyed in the BIOSAR 2008 field inventory and located within the central and north-western part of the 3 km by 10 km large area mapped by E-SAR from opposite directions (look direction 44° and 224°, true north). (© Aerial photo and Map: Lantmäteriverket Gävle).



Forest stands surveyed in the BIOSAR 2008 field inventory and located within the central and south-eastern part of the 3 km by 10 km large area mapped by E-SAR from two opposite directions (look direction 44° and 224°, true north). Forest stand # 3245, 3628, 3689, 3715, 4035, 4038, 4115, 4451, 32398 and 36979 were also imaged from two more directions (look direction 268° and 313°, true north) to investigate the influence on topography and incidence angle on biomass estimation. (© Aerial photo and Map: Lantmäteriverket Gävle).

3.2.3 Field Inventory of Selected Forest Stand

In total, 31 stands were surveyed in field. The size of the selected stands varied between 2.4 and 26.3 ha. In selected stands, circular sample plots were laid out with a systematic spacing of 50 to 160 meters, depending on the size of the area. The spacing in each stand was determined with the aim of obtaining 10 plots. The resulting number of plots for all stands varied between 8 and 13, but with an average of 10 plots per stand. On the sample plots, having a radius of 10 meters, all trees with a dbh (diameter at breast height) > 4 cm were callipered and the species registered. On randomly selected sample trees (selected with probability proportional to their basal area) height and age were measured as well. On an average, 1.5 sample trees were selected per plot. On each plot additional site variables were collected such as site index, vegetation type, soil type, etc. and also previous treatments (such as thinning). Small parts of plots with non-productive land (i.e. with growth <1 m³/ha/yr) was not included, and in that case the proportion of non-productive land on the plot was registered. Plots that fell close to the boundary were mirrored into the stand. Field data was collected with the Heureka application module Ivent, developed for large-scale inventories at forest company level [1].

Estimates of different forest parameters were made at plot and stand level within the Heureka application module PlanWise, a system for long-term planning for larger forest holdings [1]. All trees on sample plots were measured for diameters and hence also for basal area. Height, volume (through form height) and biomass were predicted using static functions as described below.

3.2.3.1 Height and Volume

The height and form height of each caliper trees were predicted with Söderberg's larger height and form height functions [2], [3]. The volume of each tree is then obtained as the tree's basal area times the tree's form height. Söderberg's larger functions use (among other) tree age as an independent variable. Since tree age is not measured on all caliper trees, tree age is within the Heureka system at first imputed using Elfving's age functions for single trees [4].

Söderberg's functions are widely used in Swedish forest management applications and are known to result in accurate estimate over larger areas. However, at a stand scale it has been observed that the functions can result in systematic deviations, possibly because a misleading site index. To avoid such systematic deviations at stand scale, calibration factors for height and form height predictions can be calculated based on the sample trees [5]. On each sample trees, height was measured and then a more accurate prediction of volume was made by using volume functions with height and diameter as independent variables. Calibrations factors were then determined by the ratio of the measured height and the height prediction by Söderberg's function or the volume predicted by volume function and the volume derived from Söderberg's form height function, respectively. The volume was for sample trees determined by Brandel's smaller functions for Scots pine, Norway spruce and Birch [6] and by Erikssons's functions for Aspen [7] (no other broadleaved tree occurred among the sample trees).

3.2.3.2 Biomass

Biomass for tree fractions and whole trees (without root) was determined by Petersson's biomass functions [8]. Peterson's function uses, among others, the last five years' radial increment as an independent variable which was not measured in field. Petersson's functions are developed for long-term planning applications such as the Heureka system [1]. In such applications, the current forest state is forecasted for a 100 year period ahead, in e.g., five years periods. In that case, the last five years' radial increment is simply obtained from the basal area growth in the previous period. However, to estimate the current biomass, the last five years radial increment is approximated by the prediction of the coming five

years radial increment. Basal area growth of single trees is within the Heureka system predicated by Elfving's basal area growth functions for single trees [9].

3.2.3.3 Documentation of the Field Inventory

All *in-situ* data measured as well as the obtained estimates of different forest parameters are found in two different Excel-documents. In total, 311 circular sample plots were laid out within the 31 forest stands visited.

Each sample plot has a radius of 10 m and all centre coordinates for those, given in UTM Zone 34, are found the separate Excel-file:

- "Coordinates_Forest_Inventory_BioSAR_2008_Krycklan.xls". Excel-file containing the centre coordinates for all 311 circular sample plots in the field inventory conducted for the BIOSAR 2008 project.

The forest data are found in the following Excel-file:

- "Forest_Inventory_BioSAR_2008_Krycklan.xls". Excel-file containing all *in-situ* data measured as well as estimates of different forest parameters obtained from the field inventory conducted for the BIOSAR 2008 project.

This Excel-file is organized with seven separate worksheets covering the following items:

- Stand estimates
- Standard errors
- Stand estimates for tree species
- Biomass fractions
- Diameter and height percentiles
- Plot estimates
- Tree list

The only data from the field inventory included in this report are the results given in the worksheet of the Excel-document dealing with stand estimates:

Forest stand #	Mean diameter* (cm)	Mean age* (year)	Mean height* (dm)	Number of stems (no/ha)	Basal area (m ² /ha)	Volume (m ³ /ha)	Biomass (tons/ha)
1474	15.65	50.21	118.77	2473.27	25.63	150.21	85.67
1493	17.6	77.45	130.67	1451.49	19.07	120.72	72.39
1517	20.8	61.22	140.82	752.37	18.54	126.57	69.22
1812	17.11	57.05	131.22	1126.82	15.54	96.16	58.56
1892	23.76	107.46	169.37	873.58	23.88	187.43	103.68
2228	23.1	112.82	176.93	1330.54	32.2	271.4	134.51
2269	28.35	122.42	214.08	868.99	38.5	380.28	182.54
2625	26.54	131.92	180.57	840.34	25.81	219.86	119.13
2626	16.95	57.38	154.09	2151.77	31.7	242.16	106.24
2629	28.31	143.72	195.94	742.72	29.6	273.94	139.76
3245	28.84	140.52	201.48	1174.56	35.29	326.77	167.11
3611	26.37	157.15	173.6	1149.1	25.36	208.21	116.46
3614	16.38	56.52	103.76	596.11	7.39	39.74	23.07
3628	21.41	63.09	153.92	887.73	19.71	145.74	74.28
3689	22.67	127.8	171.33	633.44	19.01	152.75	86.03

3715	25.64	114.4	189.13	1229.47	35.86	316.46	158.23
4035	17.34	52.99	123.1	642.99	10.44	63.6	35.08
4038	18.28	83.72	132.3	1531.07	20.97	130.65	85.6
4115	21.32	124.83	157.56	925.45	22.82	175.77	89.31
4451	25.21	125.91	187.18	628.66	25.09	221.96	111.74
15096	21.36	124.87	157.25	1294.46	26.5	198.08	108.99
17637	20	117.7	139.34	1432.39	27.31	183.44	110.78
18147	18.76	90.67	142.64	1827.1	31.06	213	119.8
18278	19.17	86.88	138.74	1380.98	21.97	145.26	84.45
21577	12.02	34.85	95.6	1916.23	14.76	72.49	42.71
22838	21.01	76.19	165.8	1180.64	24.55	193.59	95.75
30097	27.53	144.12	173.65	1221.15	23.17	186.87	111.96
31818	23.6	93.27	159.92	1213.11	17.64	133.96	73.8
32398	8.65	30.62	75.1	2543.3	9.41	37.13	27.46
36169	22.01	101.06	157.72	1498.71	27.38	207.51	112.82
36979	12.58	60.49	86.99	1582	12.49	57.96	37.12

* = Basal area weighted numbers for mean diameter, mean age and mean height

3.2.4 Field Observations

Both the field inventory and the laser mapping were conducted a couple of month earlier than the BIOSAR 2008 campaign took place. During the campaign period most of the 31 surveyed stands were visited and some subjective observations were noted in a protocol. At least one photo was captured at the same point as an additional documentation of the current conditions. Soil samples were taken at some of the points for gravimetric determination of moisture. Another source of objective measurements available is the data registered by the weather station located close to the research station facility at Svartberget. Finally, additional photos with positions were registered within the whole area mapped by E-SAR and therefore not limited to the locations of surveyed stands only.

3.2.4.1 Field Observations at Surveyed Stands

Forest stands used in the field inventory were visited during four days of the campaign week in October 2008. Only 5 forest stands were not included and they are often found at a fairly large distance from the closest forest road. The 26 forest stands reached for taking some notes are summarized in the table.

Date	Forest stands visited (#)
2008-10-13	1474, 1493, 1517, 1812, 2625, 2629, 3611, 18278
2008-10-14	3245, 3614, 3628, 3689, 3715, 4035, 4115, 4451, 36169, 36979
2008-10-15	2228, 2269, 2626, 4038, 22838, 30097, 31818
2008-10-17	21577

The protocol used for the taken notes was the same one as during BIOSAR 2007. All gathered information from this activity have been compiled in a separate document together with photos captured at each point. The photos are also available as digital files in jpeg-format with the individual names according to what is found in the document:

- "Field_Observations_BioSAR_2008_Krycklan.pdf". Pdf-file containing subjective observations at surveyed forest stands and carried out during the BIOSAR 2008 campaign period.

One page from this document is given here as an example.



 <p><i>Kry_0072.jpg</i></p>	Site ID	2269
	Time	08-10-15 09:25
	Slope, %	5
	Growth stage	~200 years
	Ground	
	Herb layer	Moss, blue berry, lingon berry
	Litter type	
	Thickness	10 – 20 cm
	Wetness	Ditches w water See soil sample
	Weather	
Air temp.	4	
Precipitation	0	
Wind, m/s	1 – 3	
Wind direct.	-	
Notes	Fairly rough, Mainly spruce, some birch. Soil sam: x: 71 33 22 0 y: 16 94 20 4	
<p><i>Notes taken at one point within forest stand # 2269 from the field observations conducted during the BIOSAR 2008 campaign week, in this case on 15 October 2008.</i></p>		

3.2.4.2 Soil Moisture

Within Krycklan catchment a few sites with Time Domain Reflectometer (TDR) sensors deployed. During the BIOSAR 2008 campaign period the system located about 1 km northeast of the Svartberget Research Station was not in operation due maintenance and work on upgrading the network for automatic logging and storage of the sensor data to a remote computer.

The soil moisture measurements made are based on gravimetric measurements of soil samples taken at the points visited during the field observations of surveyed forest stands. Of the 26 stands documented soil samples were taken at 10 of those. The tool available for this activity was a conventional spade and the samples were put in a plastic bag with contributions from a few cm below the ground surface down to a maximum depth of about 1 dm. A GPS position was also registered using a handheld device, i.e. a Garmin model type 60CS. At one of the forested sites, however, it was difficult to acquire enough of GPS satellite signals at that moment and the position is therefore lacking.

The soil samples were first weighed before dried in an oven at the Svartberget Research Station. The oven had a constant temperature of 100 degrees Celsius (°C) and the different samples were exposed to this condition during four days (27-31 October 2008). The weights were then registered once again. As an extra check the samples were put back in the oven and dried for another couple of days but no significant change in weight could be noticed.

Forest stand #	Date	Sample coordinate UTM E	Sample coordinate UTM N	Mass of water (g)	Mass of dried bulk material (g)	Gravimetric water content (%)
2228	2008-10-15	440631	7125818	95	516	18
2269	2008-10-15	442399	7125419	304,5	93	327
2626	2008-10-15	440610	7125328	35	386	9
3245	2008-10-14	-	-	70.5	485	14
3715	2008-10-14	444896	7122708	82.5	554	15
4038	2008-10-15	444030	7121887	182.5	496	37
22838	2008-10-15	441092	7125558	90.5	562	16
30097	2008-10-15	441194	7124150	206	202	102
31818	2008-10-15	441431	7123562	58	491	12
36979	2008-10-14	445048	7122346	111.5	502	22

3.2.4.3 Weather Data

The weather data available from the BIOSAR 2008 campaign period are based on registrations made with the operational weather station found at the Svartberget Research Station (440190 E, 7124830N in UTM Zone 34). Data are continuously logged with some automatic data processing performed to generate representative values every 10 minutes as well as for each day, and both categories are archived digitally [10]. Date and time are tagged to the stored weather parameter samples. The time is always given as Swedish normal time and thus never changed over the seasons. Swedish normal time corresponds to UTC + 1h.

Archived data on a 10 minutes basis have been requested for the full period with experimental BIOSAR 2008 activities in the Krycklan area, i.e. 6-17 October 2008. The data have been provided by SLU in the following Excel-file:

- “Weather_Data_BioSAR_2008_Krycklan.xls”. Excel-file containing weather data registered at the Svartberget Research Station and covering the full BIOSAR 2008 period of two weeks. Weather parameters included are air temperature, soil temperature, relative humidity, global solar radiation and precipitation.



Main entrance to the Svartberget Research Station.



The backyard of the Svartberget Research Station. A mast belonging to the weather station can be seen in the forest to the left beyond the building complex.

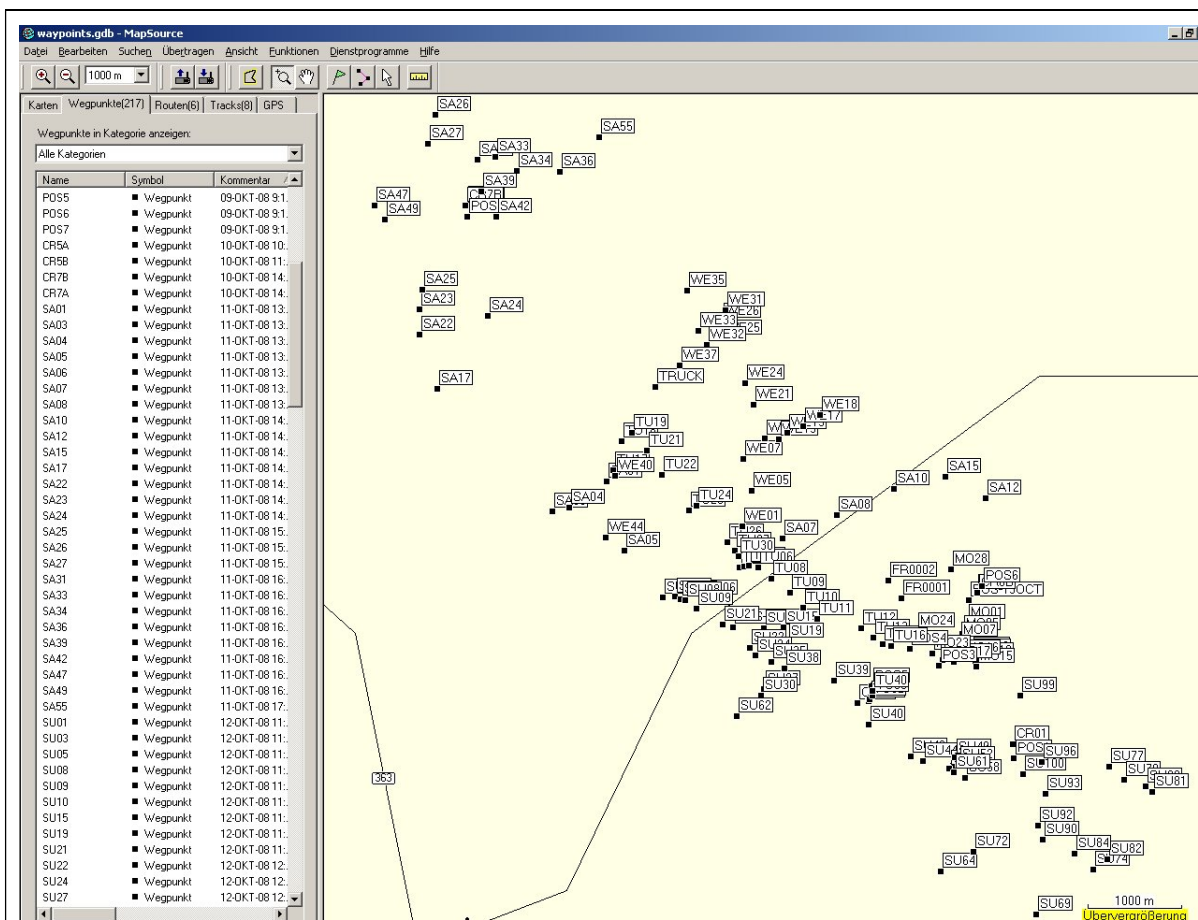
	
<p><i>Weather station equipment close to the backyard of the Svartberget Research Station.</i></p>	<p><i>Weather station equipment close to the backyard of the Svartberget Research Station.</i></p>

Climate data have been monitored at the Svartberget Research Station since 1980. Some general facts about the weather conditions for Krycklan catchment are found in [11] and summarized here. The annual mean air temperature is 1°C with 600 mm annual mean precipitation, of which one-third falls as snow. Covering of snow is present for 171 days on average (1980-1999), and spring snowmelt is the dominant hydrological event of the year, exposing up to 50% of the annual stream flow during a 3-6 week period in April-May.

During the measurement flights about 370 photos in the test site have been taken by DLR and the viewpoint has been measured with a handheld GPS as input for later analysis of the data. Nearly all accessible roads and paths have been visited and interesting features have been documented. The photos and a table including coordinates, view directions, and additional information are given in the attachment to this report. The original Garmin .gdb-file containing the waypoint coordinates is available on request at DLR.

3.2.5 Additional Observations Made Within the Whole Area Imaged by E-SAR

During the measurement flights about 370 photos in the test site have been taken by DLR and the viewpoint has been measured with a handheld GPS as input for later analysis of the data. Nearly all accessible roads and paths have been visited and interesting features have been documented. The photos and a table including coordinates, view directions, and additional information are given in the attachment to this report. The original Garmin .gdb-file containing the waypoint coordinates is available on request at DLR.



Marked GPS waypoints at the positions where photos have been taken in the test site.

3.2.6 References

- [1] <http://heureka.slu.se>. > In English. Visited 2009-05-14.
- [2] U. Söderberg, "Funktioner för skogliga produktionsprognoser. Tillväxt och formhöjd för enskilda träd av inhemska trädslag i Sverige," *SLU, Institutionen för skogstaxering, Rapport 14*, Umeå, 1986, (in Swedish).
- [3] U. Söderberg, "Funktioner för skogsindelning. Höjd, formhöjd och barktjocklek för enskilda träd," *SLU, Institutionen för skogstaxering, Rapport 52*, Umeå, 1992, (in Swedish).
- [4] B. Elfving, "Ålderstilldelning till enskilda träd i skogliga tillväxtprognoser," *SLU, Institutionen för skogsskötsel, Arbetsrapport 182*, Umeå, 2003, (in Swedish).
- [5] O. Lindgren, "A study on circular plot sampling of Swedish forest compartments," *SLU, Section for Mensuration and Management, Report 11*, Umeå, 1984.
- [6] G. Brandel, "Volymfunktioner för enskilda träd. Tall, gran och björk," *SLU, Institutionen för skogsproduktion, Rapport 26*, Umeå, 1990, (in Swedish).
- [7] H. Eriksson, "Volymfunktioner för stående träd av ask, asp, klibbal och contortatall," *Royal College of Forestry, Institutionen för skogsproduktion, Rapporter och Uppsatser 26*, Stockholm, 1973, (in Swedish).

-
- [8] H. Petersson, "Biomassafunktioner för trädfractioner av tall, gran och björk i Sverige," *SLU, Institutionen för skoglig resurshushållning och geomatik, Arbetsrapport 59*, Umeå, 1999, (in Swedish).
- [9] B. Elfving, "Grundytetillväxtfunktioner för enskilda träd, baserade på data från riksskogstaxeringens permanenta provtytor," *SLU, Institutionen för skogsskötsel, Arbetsrapport 190*, Umeå, 2004, (in Swedish).
- [10] http://www.esf.slu.se/ShowPage.cfm?OrgenhetSida_ID=4863. Visited 2009-05-14. (in Swedish).
- [11] H. Laudon and I. Buffam, "Impact of changing DOC concentrations on the potential distribution of acid sensitive biota in a boreal stream network," *Journal of Hydrology and Earth System Science*, 12, pp. 425-435, 2008.

3.3 Lidar data acquisition and processing

The laser scanning of Krycklan catchment as part of the BIOSAR 2008 campaign was performed on the 5:th and 6:th of August 2008 with the TopEye system S/N 425 mounted on a helicopter, at a flight altitude of 500 m above ground level for main strips and 250 m above ground level for cross strips. Approximately 70 km² was covered using an average point density of approximately 5 points per square meter in the main strips and 15 points per square meter in the cross strips

3.3.1 Lidar data processing

First, the lidar returns were classified as ground or vegetation returns using a progressive triangular irregular network densification method [1, 2] implemented in the TerraScan software [3]. A digital elevation model (DEM) was estimated using the lidar returns classified as vegetation hits. The height value of a lidar return was computed as the difference between the z-value of the lidar return and the z-value of the DEM at the lidar return x, y - position. Several variables were extracted from the lidar data for the field plots, based on the height distribution of lidar returns in the canopy. A height threshold of 10% of the maximum lidar height on the plot and a threshold of 1.0 m was applied in order to separate canopy returns from returns of ground, stones, and small vegetation, etc. The variables were the 10:th percentile (h10), 20:th percentile (h20), ..., 90:th percentile (h90), 95:th percentile (h95), and 100:th percentile (h100). A vegetation-ratio was calculated as the ratio between number of lidar returns above the height threshold and total number of returns on the plot. These variables were raster mapped at the entire study area using 10×10 m raster cell sizes, and also extracted at each field plot location (see below) to be used as independent variables in biomass modelling.

3.3.2 Field data

The field sample plots surveyed to assess stand biomass data (see Section 3.2.3) was utilized as ground truth data for lidar-based raster modelling of biomass. Furthermore, an additional 110 plots surveyed using the same methodology were also used. These additional plots were randomly positioned in the central part of the Krycklan area, using stratification in order to sample the full variation of tree species composition and tree height in the area. Positions of all plots were determined using post-processed differential GPS measurements of each plot centre. Tree height, diameter and biomass were estimated at all plots using the methodology described previously (see Section 3.2.3), and summarized to mean biomass per hectare (in metric tons/ha).

3.3.3 Modelling of biomass using lidar data

Models of biomass as a function of lidar measures were constructed using multiple regression and studies of the residuals. An attempt to capture differences in the relation of forest biomass and lidar measurements due to varying tree species proportions was made, using species information from an existing aerial stereo photo interpretation. Four strata were used; 1) Pine dominated forest (plots in stands with estimated stem volume proportion of pine higher than 70 %), 2) Spruce dominated forest (>50%), 3) Broad-leaf dominated forest (>50%), and 4) Mixed species forest (any other proportions).

Commonly, modelling forest stem volume using lidar crown canopy height measurements are made assuming log-linear relationships of the data sources [4]. Similar relations should be valid in biomass modelling, since biomass and stem volume show a linear relation. The current data do not show a strong log-linear relationship, rather a direct linear dependence to the height measurements. This is probably due

to lack of observations of young forests in the data. Here, in accordance with previous studies, a log-linear model was applied and fitted to each stratum separately:

$$\ln(B) = a + b \cdot P + c \cdot V + \varepsilon \tag{Eq. 3.1}$$

where B is biomass, P is the best performing height percentile of the lidar data and V is the proportion of lidar measurements classified as measurements of vegetation. To correct for bias introduced by non-linear back-transformation, a correction factor f was estimated by the ratio of the average biomass in the sample data and the average of the back-transformed fitted values [5]:

$$\hat{B}_{Corr} = \exp(\ln(B)) \cdot f \tag{Eq. 3.2}$$

Models were independently fitted to stratum 1 to 4 using the model in Eq. 3.1, using the vegetation ratio and the best performing percentile of the lidar data as independent variables. Evaluation of stand-level estimation accuracy was made using cross-validation of the 31 surveyed forest stands, and showed 15.6% RMSE, in per cent of the true mean biomass (87.0 tons/ha), and a bias of -3.49 tons/ha (underestimation).

Mean surveyed biomass (tons/ha)	RMSE (%)	Bias (tons/ha)	Mean error (%)
87.0	15.9	-3.49	15.6

3.3.4 References

[1] P. Axelsson, "Processing of laser scanner data - algorithms and applications," *ISPRS Journal of Photogrammetry and Remote Sensing*, vol. 54, no. 2-3, pp. 138-147, 1999.

[2] P. Axelsson, "DEM generation from laser scanner data using adaptive TIN models," *Proc. XIX ISPRS Congress*, held in Amsterdam, The Netherlands, 16-22 July 2000, International Archives of Photogrammetry and Remote Sensing, vol. XXXIII-B4, pp. 110-117, 2000.

[3] A. Soininen, "TerraScan for MicroStation, User's Guide," *Terrasolid Ltd.*, Jyväskylä, Finland, 2004.

[4] J. Holmgren, "Estimation of forest variables using airborne laser scanning," *Acta Universitatis Agriculturae Sueciae, Silvestria 278*, Doctor's dissertation, ISSN 1401-6230, Umeå, Sweden, 2003.

[5] S. Holm, "Transformationer av en eller flera beroende variabler i regressionsanalys," *Swedish University of Agricultural Sciences, Faculty of Forest Sciences, HUGIN, report 7*, Umeå, 1977, (in Swedish).

4 AIRBORNE CAMPAIGN OVERVIEW

4.1 Campaign Objectives

The BIOSAR 2008 campaign addresses important specific programmatic needs of ESA's Earth Explorer Mission BIOMASS. It will

- assess the potential of BIOMASS for biomass estimation in boreal forest,
- investigate temporal and spatial decorrelation at L- and P-band,
- explore the effects of topography and incidence angles at L- and P-band.

BIOSAR 2008 primarily investigates radar data of boreal forest in preparation of future spaceborne ESA missions.

4.2 Participants

The BIOSAR 2008 airborne campaign was carried out in cooperation with four different institutes:

German Aerospace Center (DLR), Microwaves and Radar Institute (HR)

P.O. Box 11 16, D-82230 Wessling, Germany
in the following referred to as **DLR-HR**

German Aerospace Center (DLR), Flight Operations (FB)

P.O. Box 11 16, D-82230 Wessling, Germany
in the following referred to as **DLR-FB**

Swedish Defence Research Agency

in the following referred to as **FOI**

Swedish University of Agricultural Sciences

in the following referred to as **SLU**

ORGANISATION Team:

ESA	Malcolm Davidson
DLR-HR	Irena Hajnsek, Ralf Horn
FOI	Lars Ulander, Anders Gustavsson
DLR-FB	Andrea Hausold

AIRBORNE Team:

DLR-FB	Michael Grossrubatscher Helmut Kirner Siegfried Judt
DLR-HR	Ralf Horn Peter Hackenberg

GROUND Team:

FOI	Anders Gustavsson Per-Olov Fröling Lars Ulander Olle Nyström Björn Flood
SLU	Johan Fransson Johan Holmgren Thomas Hörnlund Lena Jonsson Anna Ringvall Jörgen Wallerman
DLR-HR	Martin Keller

4.3 Campaign Schedule

Objectives for the BIOSAR 2008 campaign were to

collect fully polarimetric repeat pass interferometric L- and P-band data with different spatial baselines in a well known area with different boreal forest stands for interferometric and tomographic analysis,

collect single pass interferometric X-band data for DEM processing and

acquire fully polarimetric L- and P-band data of an area with strong topographic variations for an analysis of the influence of topography on the biomass estimation models.

These objectives lead to the following planned flight configuration:

E-SAR Mode	Frequency	Baseline Spacing	Objectives
SP-InSAR half baseline, 1 look-dir.	X-band vv	0m	DEM creation
RP-Pol-InSAR, 6 tracks, 2 look-dir.	L-band pol.	6m	Forest height inversion Forest height relation to biomass
RP-Pol-InSAR, 6 tracks, 2 look-dir.	P-band pol.	8m	Forest height inversion Forest height relation to biomass
PolSAR, 1 track, 1 look-dir	L-band pol.	-	Influence on topography and incidence angle on biomass estimation
PolSAR, 1 track, 1 look-dir	P-band pol.	-	Influence on topography and incidence angle on biomass estimation

The operation modes of the E-SAR system for the BIOSAR 2008 campaign

Flight directions are:

In-SAR, Pol-InSAR: 134°, 314° in flight level 130 / 140

Pol-SAR: 43°, 134°, 314°, 358° in flight level 100 / 110

5 AIRBORNE SAR DATA ACQUISITION

The planned data could be collected successfully. A critical event occurred during the first flight, when the tape recorder failed. A spare tape recorder had to be shipped to Umeå overnight and installed. All data could be collected then in two days of good weather, just before the arrival of rain and snow.

5.1 Airborne Campaign Preparation

5.1.1 Calibration Check of the E-SAR System

Before the start of the BIOSAR campaign the E-SAR system was tested in a flight over the calibration field in Kaufbeuren, Germany.

5.1.2 Mission Logistics

The ferry flight to the test site followed the Experiment Plan. The ferry flight from Oberpfaffenhofen to Umeå took approximately 7h flight time including two stops for refueling.

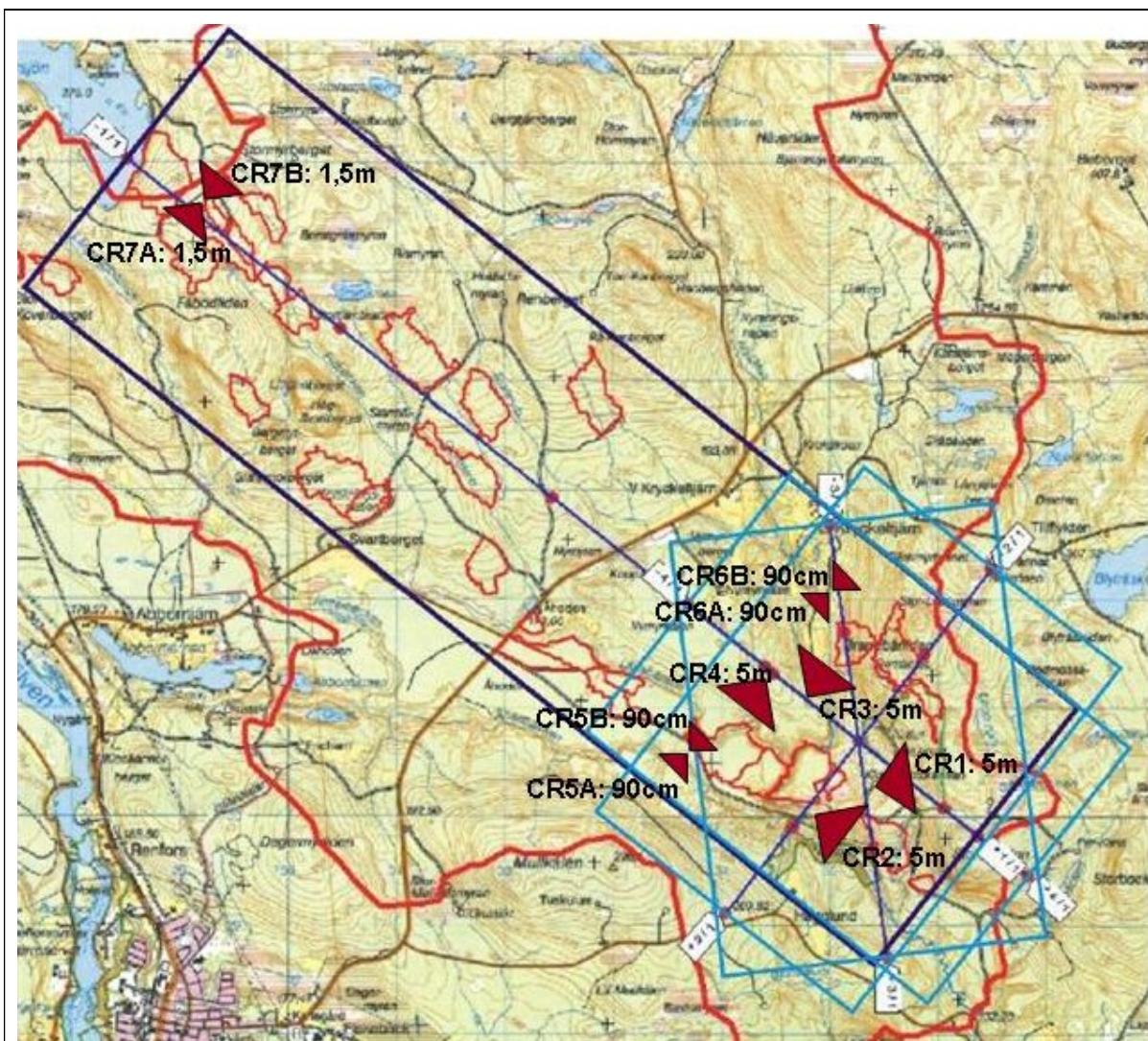
5.1.3 Corner Reflectors

Several sizes of corner reflectors were installed at the chosen test site. The corner reflectors are used for:

- radiometric and polarimetric calibration checks of the SAR data
- checking internal delays of the SAR system
- precise coregistration of repeat pass interferometric data
- checking the geocoding accuracy
- resolving an unknown for DEM creation

FOI mounted four reflectors of 4,98m edge length. Every reflector has a different look direction, so that in every data set one of these reflectors was visible. Additionally six smaller reflectors of 1,50m and 90cm edge length were placed by DLR for the X- and L-band Band calibration.

Some trees have been cut by SLU to make sure that the reflector signal is not overlaid by the backscatter of the tree.



Corner Reflectors in the Krycklan test area

All corner reflector positions have been measured by GPS from FOI. For a very high position accuracy of less than 5cm DGPS processing using SWEPOS reference stations data has been performed.

OUTPUT STATION COORDINATES (LAT/LONG/HT)

STA_ID	-- LATITUDE --	-- LONGITUDE --	-- ELLHGT --
CR_1	64 13 05.15946	19 51 16.50758	206.7846
CR_2	64 12 57.64282	19 50 29.15053	162.5432
CR_3	64 13 34.46891	19 50 20.88122	197.6070
CR_4	64 13 39.12274	19 49 50.54637	206.6753
CR5A	64 13 19.33153	19 49 13.10322	190.3322
CR5B	64 13 19.54048	19 49 13.17525	190.2810
CR6A	64 13 57.45942	19 50 48.01642	192.5000
CR6B	64 13 57.76720	19 50 48.50257	192.5854
CR7A	64 16 11.66671	19 44 02.31861	353.0352
CR7B	64 16 11.47011	19 44 01.74580	352.9189



Corner Reflector CR1 (5m)



Corner Reflector CR2 (5m)



Corner Reflector CR3 (5m)



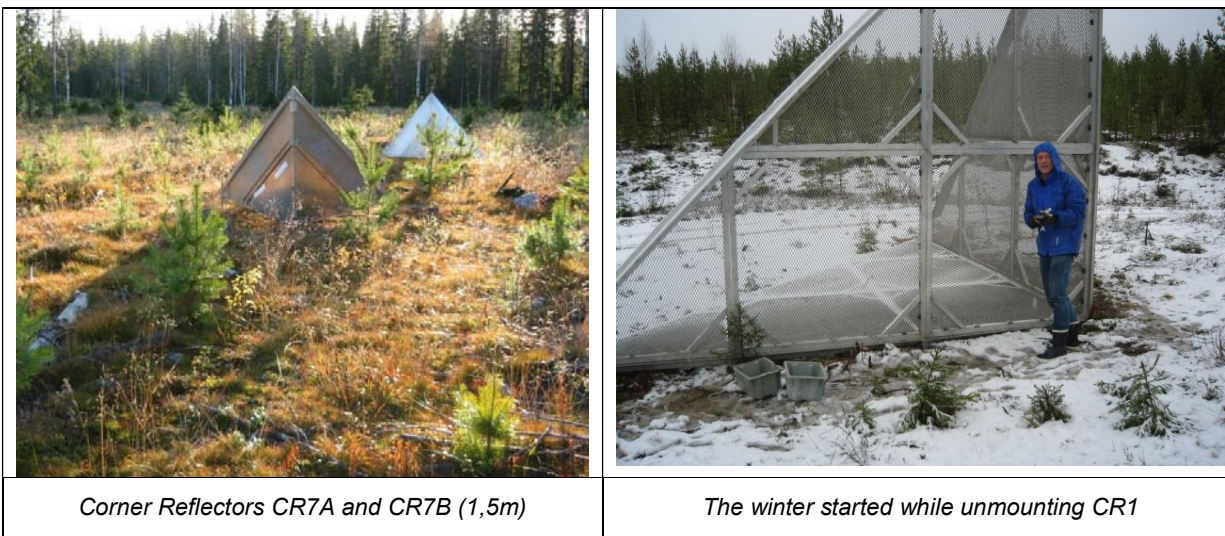
Corner Reflector CR4 (5m)



Corner Reflectors CR5A and CR5B (90cm)



Corner Reflectors CR6A and CR6B (90cm)



5.1.4 GPS Measurements

For high quality airborne SAR data it is necessary to know very precisely the position and altitude of the aircraft. For this purpose a DGPS/INS system is installed in the aircraft. The INS system has a very stable behaviour on short times. Its drift is compensated by GPS positions. During the flight an online DGPS system helps the pilot to stay on the track as precise as possible (some meters offset). After the flight, the real position of the aircraft is calculated by postprocessing DGPS for an accuracy of few centimetres. GPS data of the surrounding SWEPOS stations Vindeln, Umeå, Ratan, Lycksele and Holmsund have been used for postprocessing DGPS.

5.2 Measurement Overview

The airborne measurement campaign took place between 06.Oct.2008 and 17.Oct.2008 in the Krycklan test site near Vindeln in northern Sweden. In the first week, corner reflectors have been installed and their position has been measured by GPS. Photos of the area were taken to document the actual status.

On Sunday, 12.Oct. 2008, the aircraft arrived at Umeå airport. After briefing on Monday morning, the first flight was planned for Monday afternoon. During data recording in the air, the tape recorder failed without any possibility to be repaired during the campaign. A spare recorder was sent from DLR immediately by air to Stockholm and from there by truck overnight to Umeå where it arrived on Thursday morning. Already on Tuesday afternoon (14.Oct.2008) the first measurement flight could be resumed.

Due to incoming bad weather, the recordings were accelerated and all the other three flights were executed on Wednesday, 15.Oct.2008. Due to this very fast procedure, it was not possible to move the 5m reflectors before the X-band recording. A later data analysis confirmed that the X-band data are not disturbed by these reflectors. No extremely high signals from the 5m reflectors were found in the data.

The reflectors were dismantled on 16. and 17.Oct. and the aircraft flew back to Oberpfaffenhofen.

5.3 Radar Data Acquisition

Two overlapping sub-testsites have been mapped with SAR in the Krycklan test site. The first one covers a large area of about 10 x 3km and is recorded from both sides in L- and P-band for Pol-InSAR processing and in X-band in single pass interferometric mode. The second sub-testsite covers about 3 x 3km in the south-east of the larger area. It is mapped from four directions to analyse the influence of topography in L- and P-band PolSAR data. For easy recognition of the areas, they are coded in the name of the data set. The RGI file names of the large area contain the sequence of letters "t01", the file names of the small area contain "t02".

<p><i>Centre line of the area t01 and flight tracks for L- and P-band Pol-InSAR measurements</i></p>	<p><i>Centre lines of the area t02 and flight tracks for L- and P-band PolSAR measurements</i></p>
<p><i>Flight lines of flight 01 over the area t01. Red: data acquisition</i></p>	<p><i>Flight lines of flight 03 over the area t02. Red: data acquisition</i></p>

The following data have been acquired:

- Flight 1, 14.10.2008: P-band Pol-InSAR data of area t01 (6 passes looking to north-east, 6 passes looking to south-west).
- Flight 2, 15.10.2008: L-band Pol-InSAR data of area t01 (6 passes looking to north-east, 6 passes looking to south-west).
- Flight 3, 15.10.2008: P-band PolSAR data of area t02 (5 passes of different look directions).
- Flight 4, 15.10.2008: L-band PolSAR data of area t02 (4 passes of different look directions) and X-band SP-InSAR data of area t01 (1 pass looking to north-east).

6 SAR DATA PROCESSING

6.1 Processing Strategy

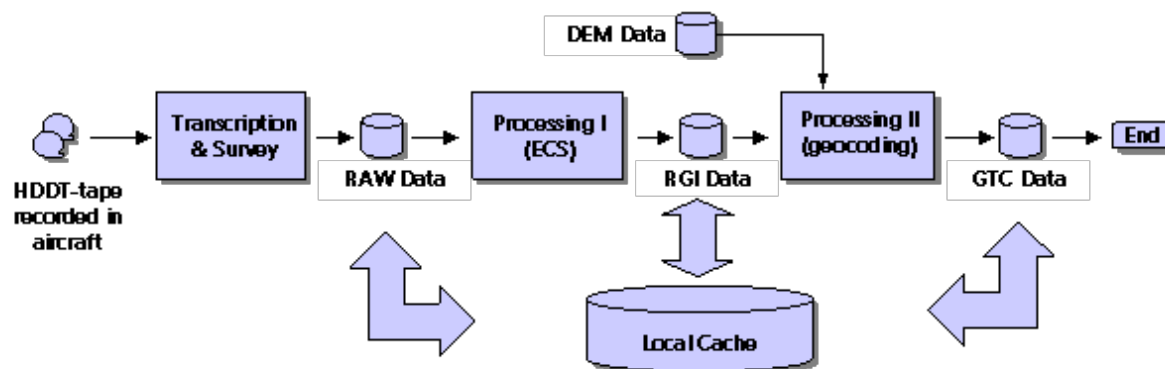
The data flow of standard E-SAR data processing consecutively reaches three product levels:

- RAW ... Raw product (after transcription from tape and survey processing)
- RGI ... Radar geometry image product (after high precision SAR processing)
- GTC ... Geocoded and terrain corrected product (after geocoding)

RAW products are not delivered by default. GTC product delivery is optional.

Processing for BIOSAR includes the generation of RAW, RGI and GTC products. The final delivery is done in form of RGI and GTC products.

The figure below illustrates the data flow for E-SAR processing:

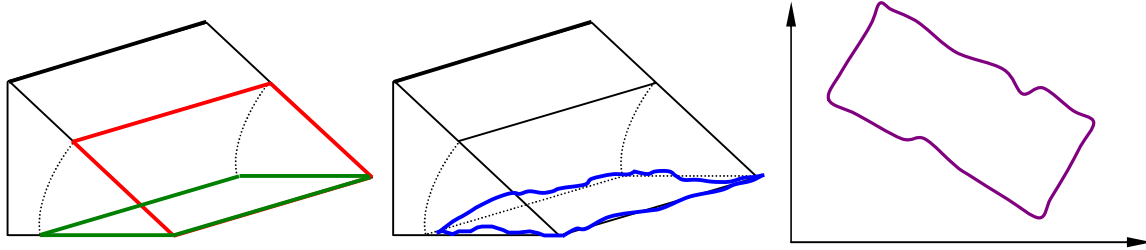


E-SAR processing workflow: (1) Transcription, (2) Precision SAR processing, (3) Geocoding

Step one includes data transcription and channel separation of recorded airborne SAR raw data from tape to hard disc, high precision navigation data processing and first data screening, i.e. survey processing (quicklook images) and flight track evaluations (squint variations and deviations from the nominal straight track).

Step two accomplishes high-precision SAR processing creating fully resolved SAR images in slant range geometry (non-varying resolution in azimuth and range). Additionally, the slant range image is projected to ground range geometry (assuming flat terrain). In that geometry, the image range resolution naturally degrades from far to near range according to steeper incidence angles.

Step three in the data processing chain is terrain-correction and geocoding which converts slant range data into the geometry of a three-dimensional geographic coordinate system (e.g. WGS84 or Bessel 1841 ellipsoid) and finally to its projection onto a projected geographic coordinate system (e.g. UTM or Gauss-Krueger).



SAR data geometries: SLANT range (red), GROUND range (green), GROUND range terrain corrected (blue), GEOCODED and terrain corrected (purple). The flight track is indicated as thick line.

For BIOSAR, all coordinates refer to the WGS84 earth ellipsoid. Coordinates are either given as lat/lon coordinates (latitude, longitude, ellipsoidal height) or in the UTM system, zone 34 (easting, northing, ellipsoidal height).

6.2 Transcription

The data transcription from tape to disc, channel separation and RAW product generation proceeded without problems.

6.3 RGI Data Processing

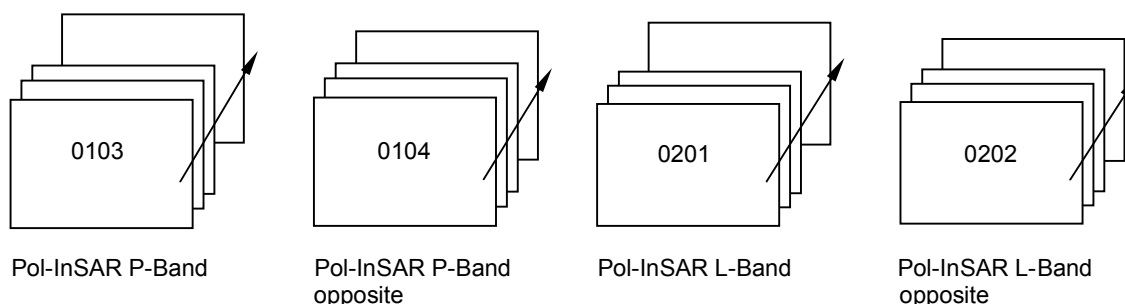
SAR processing for BIOSAR followed standard E-SAR processing in single pass PolSAR and repeat pass Pol-InSAR mode. In PolSAR mode, no DEM information, i.e. only the reference height in a data segment, is used for RGI product generation. The average terrain height used for RGI processing has been adapted to 200m while the topography in the area leads to real heights between 150m (river areas) and 400m (mountain tops). Processing in Pol-InSAR mode is always done with DEM information to allow topography dependent motion compensation and precise co-registration of data from different passes.

All data are processed to achieve the maximum slant range resolution of about 2m according to the E-SAR system bandwidth in L- and P-band. For the ground range detected multi-look data an azimuth resolution of 4.0m in P-band and 3.0m in L-band has been chosen. For speckle reduction, we usually form 4 azimuth looks with 50 percent overlap such that the single look resolution actually increases to $3\text{m} / (4+1)/2 = 1.2\text{ m}$ in L-band and $4\text{m} / (4+1)/2 = 1.6\text{ m}$ in P-band. This is also done for BIOSAR. For DEM creation X-band XTI data were processed with 16 looks for better speckle reduction and phase stability.

Especially P-band is very susceptible for radio frequency interferences (RFI). It is possible to increase the quality of RFI influenced data sets by using a RFI filter for the drawback of a reduced spatial resolution. In BIOSAR 2008 no RFI occurred, so no RFI filter has been used for processing.

In single pass processing, each scene is imaged in its individual image geometry (its individual flight track, velocity variations and aircraft roll, drift and pitch angles) due to varying wind conditions from scene to scene. In contrast to single pass processing, repeat pass processing allows to process scenes according to the image geometry of a reference scene (master) and to create interferograms (coherence and interferometric phase).

The data sets of flight 1 and 2 are therefore processed in repeat pass mode, i.e. all scenes within a data set are coregistered to a common master scene.



At BIOSAR 2008, the range delay has been adapted after the first two passes 08biosar0101 and 08biosar0102. Therefore, for P-band the next scenes with 8m horizontal offset were used as master.

The following scenes have been chosen as master scenes:

- 08biosar0103x1_t01 P-Band, Pol-InSAR, 8m offset, look-direction south-west
- 08biosar0104x1_t01 P-Band, Pol-InSAR, 8m offset, look-direction north-east
- 08biosar0201x1_t01 L-Band, Pol-InSAR, 0m offset, look-direction south-west
- 08biosar0202x1_t01 L-Band, Pol-InSAR, 0m offset, look-direction north-east

6.4 Digital Elevation Model

In scenes with varying terrain height (differences of more than 50 metres in a scene) it is important to include a precise digital elevation model for repeat pass SAR processing. Otherwise, platform motion errors cannot be estimated properly and corrected accordingly.

An external Digital Elevation Model (DEM) was ordered from Lantmäteriet, the National Land Survey of Sweden by FOI, and has been used in all BIOSAR repeat pass processing. The original DEM was delivered in text-format. It was already transformed from local coordinate system into UTM WGS 84 by Lantmäteriet.

These points were used as sampling points for a triangulation to create an interpolated 1m grid DEM. Due to the large size of this complete 1m grid DEM it was divided into three smaller parts: a south-eastern part, a central part, and a north-western part, each of 5100 x 5100 pixels size. All DEM coordinates are given in UTM, zone 34.

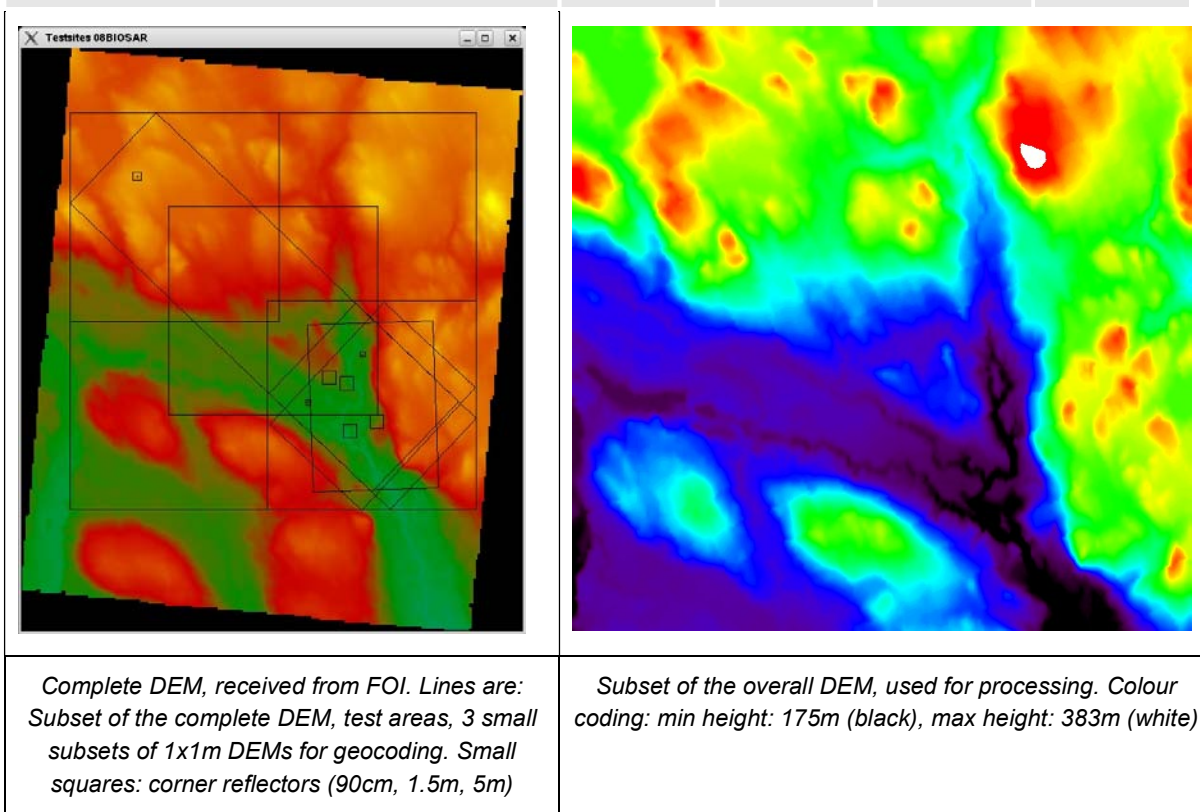
To be able to refer directly from the name of a data set which DEM was used for geocoding, the name of the data set is coded in the following way:

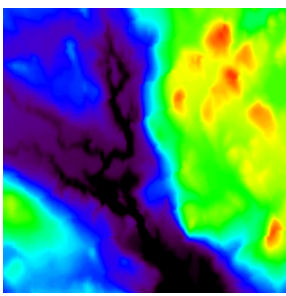
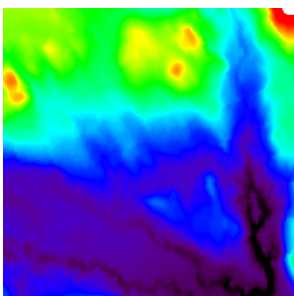
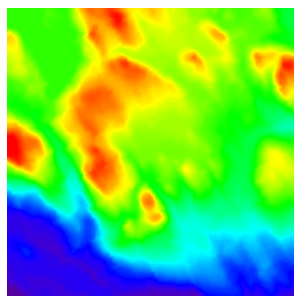
Each data set has a suffix of letters "tnm" where "n" describes the DEM used for geocoding and "m" the test area.

All Pol-SAR data of the small area t02 fit into DEM1. Geocoded data therefore have the suffix "t12". Since for RGI data no DEM was used for geocoding, the RGI suffix is "t02"

The Pol-InSAR data cover a much larger area. All three sub-DEMs have been used for geocoding. Therefore geocoded data exist as "t11", "t21", and "t31" while RGI data are labeled "t01".

DEM	min E	min N	max E	max N
dem_SVARTBERGET_WGS84utm34_1x1m.dat	437061	7119733	446881	7129293
dem1_SVARTBERGET_WGS84utm34_1x1m.dat	441782	7119733	446881	7124832
dem2_SVARTBERGET_WGS84utm34_1x1m.dat	439421	7121963	444520	7127062
dem3_SVARTBERGET_WGS84utm34_1x1m.dat	437061	7124194	442160	7129293



		
<i>Small subset 1 for geocoding: south-eastern part: DEM1</i>	<i>Small subset 2 for geocoding: central part: DEM2</i>	<i>Small subset 3 for geocoding: north-western part: DEM3</i>

6.5 Processed Data

This chapter gives an overview about the processed RGI and GTC data sets of the BIOSAR 2008 campaign.

Pol-InSAR Data Set – P-Band

The Pol-InSAR RGI data set in P-band encompasses 12 passes with respect to two master tracks (two look directions: track ID 11 and 21).

Scene ID	Test Site	Track	Band	Pol	Date	Purpose	Product
08biosar0103x1	t01	11	P	PM	14.Oct.2008	InSAR Master 8m left	RGI
08biosar0105x1	t01	12	P	PM	14.Oct.2008	InSAR Slave 16m left	RGI
08biosar0107x1	t01	13	P	PM	14.Oct.2008	InSAR Slave 24m left	RGI
08biosar0109x1	t01	14	P	PM	14.Oct.2008	InSAR Slave 32m left	RGI
08biosar0111x1	t01	15	P	PM	14.Oct.2008	InSAR Slave 40m left	RGI
08biosar0101x1	t01	10	P	PM	14.Oct.2008	InSAR Slave 0m	RGI
08biosar0104x1	t01	21	P	PM	14.Oct.2008	InSAR Master 8m left	RGI
08biosar0106x1	t01	22	P	PM	14.Oct.2008	InSAR Slave 16m left	RGI
08biosar0108x1	t01	23	P	PM	14.Oct.2008	InSAR Slave 24m left	RGI
08biosar0110x1	t01	24	P	PM	14.Oct.2008	InSAR Slave 32m left	RGI
08biosar0112x1	t01	25	P	PM	14.Oct.2008	InSAR Slave 40m left	RGI
08biosar0102x1	t01	20	P	PM	14.Oct.2008	InSAR Slave 0m	RGI

PM = Polarimetric Mode, i.e. fully polarimetric with channel sequence HH-HV-VV-VH

RGI = Radar Geometry Image product (includes calibrated radar reflectivity images in slant range and ground range image geometry), also co-registered version to master

The two master passes are geocoded and split up into three parts each. The slave scenes are not separately geocoded. The co-registered SLC-data can always be converted into geocoded geometry using conversion matrices. These matrices are included in the master GTC products.

Scene ID	Test Site	Track	Band	Pol	Date	Purpose	Product
08biosar0103x1	t11	11	P	PM	14.Oct.2008	InSAR Master 8m left	GTC
08biosar0103x1	t21	11	P	PM	14.Oct.2008	InSAR Master 8m left	GTC
08biosar0103x1	t31	11	P	PM	14.Oct.2008	InSAR Master 8m left	GTC
08biosar0104x1	t11	21	P	PM	14.Oct.2008	InSAR Master 8m left	GTC
08biosar0104x1	t21	21	P	PM	14.Oct.2008	InSAR Master 8m left	GTC
08biosar0104x1	t31	21	P	PM	14.Oct.2008	InSAR Master 8m left	GTC

PM = Polarimetric Mode, i.e. fully polarimetric with channel sequence HH-HV-VV-VH

GTC = Geocoded and Terrain Corrected product (includes geo-referenced terrain-corrected radar reflectivity images)

Pol-InSAR Data Set – L-Band

In L-band 12 passes have been processed in Pol-InSAR mode. Two master scenes 08biosar0201x1 (track 10) and 08biosar0202x1 (track 20) from opposite directions are available, each one together with five slave data sets with 6m to 30m baseline.

Scene ID	Test Site	Track	Band	Pol	Date	Purpose	Product
08biosar0201x1	t01	10	L	PM	15.Oct.2008	InSAR Master 0m	RGI
08biosar0203x1	t01	11	L	PM	15.Oct.2008	InSAR Slave 6m left	RGI
08biosar0205x1	t01	12	L	PM	15.Oct.2008	InSAR Slave 12m left	RGI
08biosar0207x1	t01	13	L	PM	15.Oct.2008	InSAR Slave 18m left	RGI
08biosar0209x1	t01	14	L	PM	15.Oct.2008	InSAR Slave 24m left	RGI
08biosar0211x1	t01	15	L	PM	15.Oct.2008	InSAR Slave 30m left	RGI
08biosar0202x1	t01	20	L	PM	15.Oct.2008	InSAR Master 0m	RGI
08biosar0206x1	t01	21	L	PM	15.Oct.2008	InSAR Slave 6m left	RGI
08biosar0208x1	t01	22	L	PM	15.Oct.2008	InSAR Slave 12m left	RGI
08biosar0210x1	t01	23	L	PM	15.Oct.2008	InSAR Slave 18m left	RGI
08biosar0212x1	t01	24	L	PM	15.Oct.2008	InSAR Slave 24m left	RGI
08biosar0214x1	t01	25	L	PM	15.Oct.2008	InSAR Slave 30m left	RGI

PM = Polarimetric Mode, i.e. fully polarimetric with channel sequence HH-HV-VV-VH

RGI = Radar Geometry Image product (includes calibrated radar reflectivity images in slant range and ground range image geometry), also co-registered version to master

The two master passes are geocoded and split up into three parts each. The slave scenes are not separately geocoded. The co-registered SLC-data can always be converted into geocoded geometry using conversion matrices. These matrices are included in the master GTC products.

Scene ID	Test Site	Track	Band	Pol	Date	Purpose	Product
08biosar0201x1	t11	10	L	PM	15.Oct.2008	InSAR Master 0m	GTC
08biosar0201x1	t21	10	L	PM	15.Oct.2008	InSAR Master 0m	GTC
08biosar0201x1	t31	10	L	PM	15.Oct.2008	InSAR Master 0m	GTC
08biosar0202x1	t11	20	L	PM	15.Oct.2008	InSAR Master 0m	GTC
08biosar0202x1	t21	20	L	PM	15.Oct.2008	InSAR Master 0m	GTC
08biosar0202x1	t31	20	L	PM	15.Oct.2008	InSAR Master 0m	GTC

PM = Polarimetric Mode, i.e. fully polarimetric with channel sequence HH-HV-VV-VH

GTC = Geocoded and Terrain Corrected product (includes geo-referenced terrain-corrected radar reflectivity images)

Single Pass InSAR Data Set – X-Band

One X-band single pass across-track interferometric (XTI) data set has been recorded in half baseline mode for X-band DEM creation. The recorded data was processed and a DEM was generated. The XTI-DEM is compared later on in this document to the external DEM obtained from the National Land Survey of Sweden.

The XTI-DEM was created directly from the RGI data. The X-band data set (radar reflectivity) has been geocoded to the same external DEMs 1-3 as it was used for geocoding of the L- and P-band data sets.

Scene ID	Test Site	Track	Band	Pol	Date	Purpose	Product
08biosar0405x1	t01	3	X	VV	15.Oct.2008	XTI half baseline	RGI

RGI = Radar Geometry Image product (includes calibrated radar reflectivity images in slant range and ground range image geometry)

Scene ID	Test Site	Track	Band	Pol	Date	Purpose	Product
08biosar0405x1	t11	3	X	VV	15.Oct.2008	XTI half baseline	GTC
08biosar0405x1	t21	3	X	VV	15.Oct.2008	XTI half baseline	GTC
08biosar0405x1	t31	3	X	VV	15.Oct.2008	XTI half baseline	GTC

GTC = Geocoded and Terrain Corrected product (includes geo-referenced terrain-corrected radar reflectivity images)

PoSAR Data Set

The PoSAR data set consists of 5 passes in P-band (one repetition) and 4 passes in L-band. The small area t02 was observed from four different look directions. All data sets have been geocoded to DEM1.

Scene ID	Test Site	Track	Heading	Band	Pol	Date	Purpose	Product
08biosar0301x1	t02	10	357°	P	PM	15.Oct.2008	PoSAR	RGI
08biosar0302x1	t02	20	313°	P	PM	15.Oct.2008	PoSAR	RGI
08biosar0303x1	t02	30	133°	P	PM	15.Oct.2008	PoSAR	RGI
08biosar0304x1	t02	40	42°	P	PM	15.Oct.2008	PoSAR	RGI
08biosar0305x1	t02	30	133°	P	PM	15.Oct.2008	PoSAR	RGI
08biosar0401x1	t02	10	357	L	PM	15.Oct.2008	PoSAR	RGI
08biosar0402x1	t02	20	313°	L	PM	15.Oct.2008	PoSAR	RGI
08biosar0403x1	t02	30	133°	L	PM	15.Oct.2008	PoSAR	RGI
08biosar0404x1	t02	40	42°	L	PM	15.Oct.2008	PoSAR	RGI

PM = Polarimetric Mode, i.e. fully polarimetric with channel sequence HH-HV-VV-VH

RGI = Radar Geometry Image product (includes calibrated radar reflectivity images in slant range and ground range image geometry)

Scene ID	Test Site	Track	Heading	Band	Pol	Date	Purpose	Product
08biosar0301x1	t12	10	357°	P	PM	15.Oct.2008	PolSAR	GTC
08biosar0302x1	t12	20	313°	P	PM	15.Oct.2008	PolSAR	GTC
08biosar0303x1	t12	30	133°	P	PM	15.Oct.2008	PolSAR	GTC
08biosar0304x1	t12	40	42°	P	PM	15.Oct.2008	PolSAR	GTC
08biosar0305x1	t12	30	133°	P	PM	15.Oct.2008	PolSAR	GTC
08biosar0401x1	t12	10	357	L	PM	15.Oct.2008	PolSAR	GTC
08biosar0402x1	t12	20	313°	L	PM	15.Oct.2008	PolSAR	GTC
08biosar0403x1	t12	30	133°	L	PM	15.Oct.2008	PolSAR	GTC
08biosar0404x1	t12	40	42°	L	PM	15.Oct.2008	PolSAR	GTC

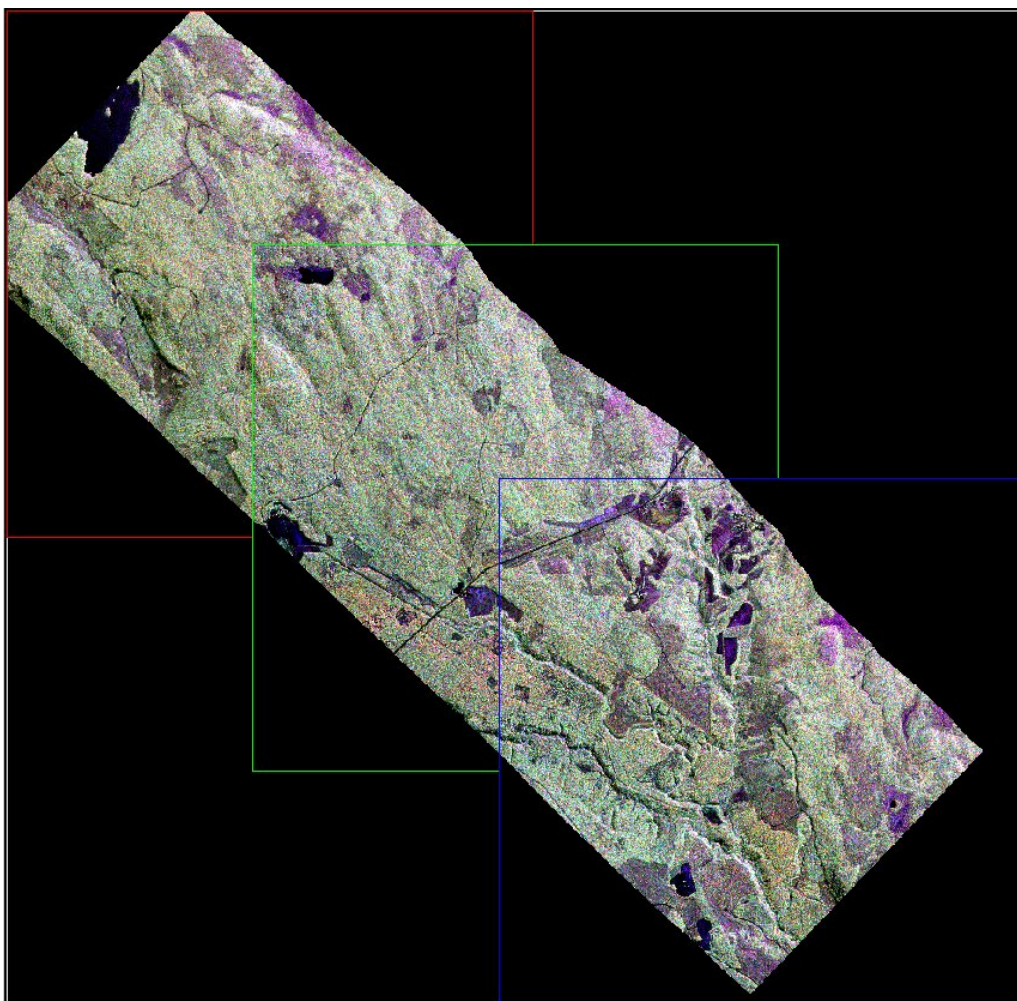
PM = Polarimetric Mode, i.e. fully polarimetric with channel sequence is HH-HV-VV-VH

GTC = Geocoded and Terrain Corrected product (includes geo-referenced terrain-corrected radar reflectivity images)

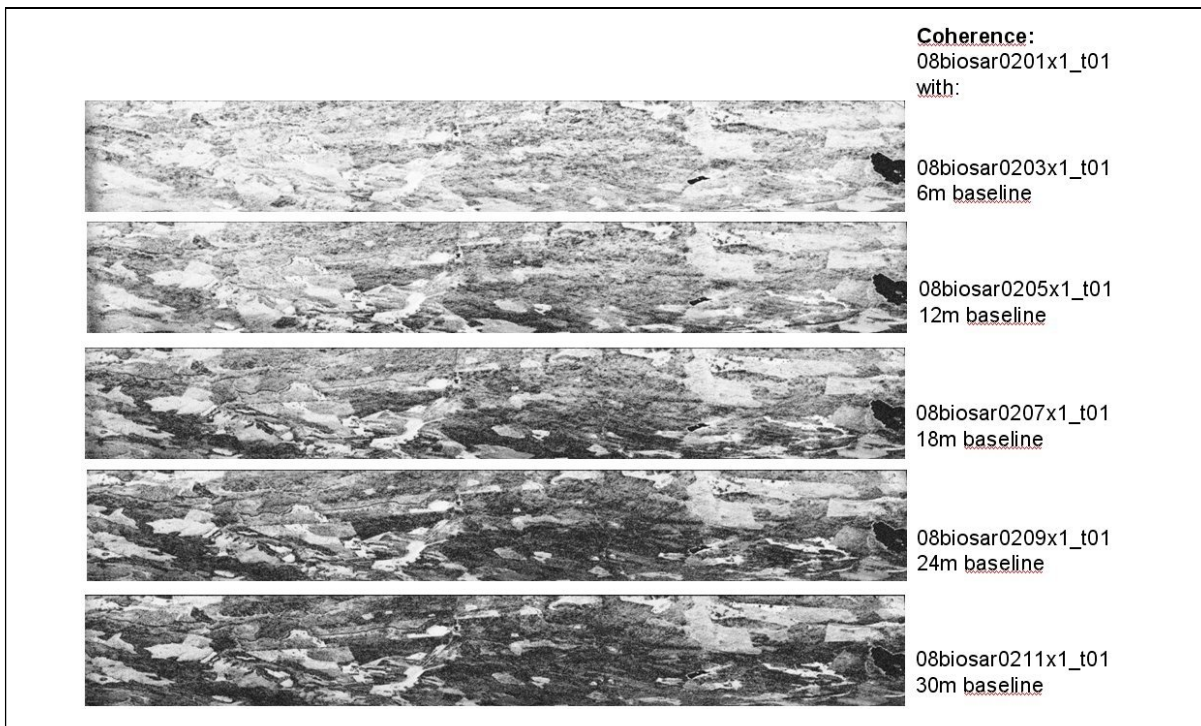
6.6 Image Examples



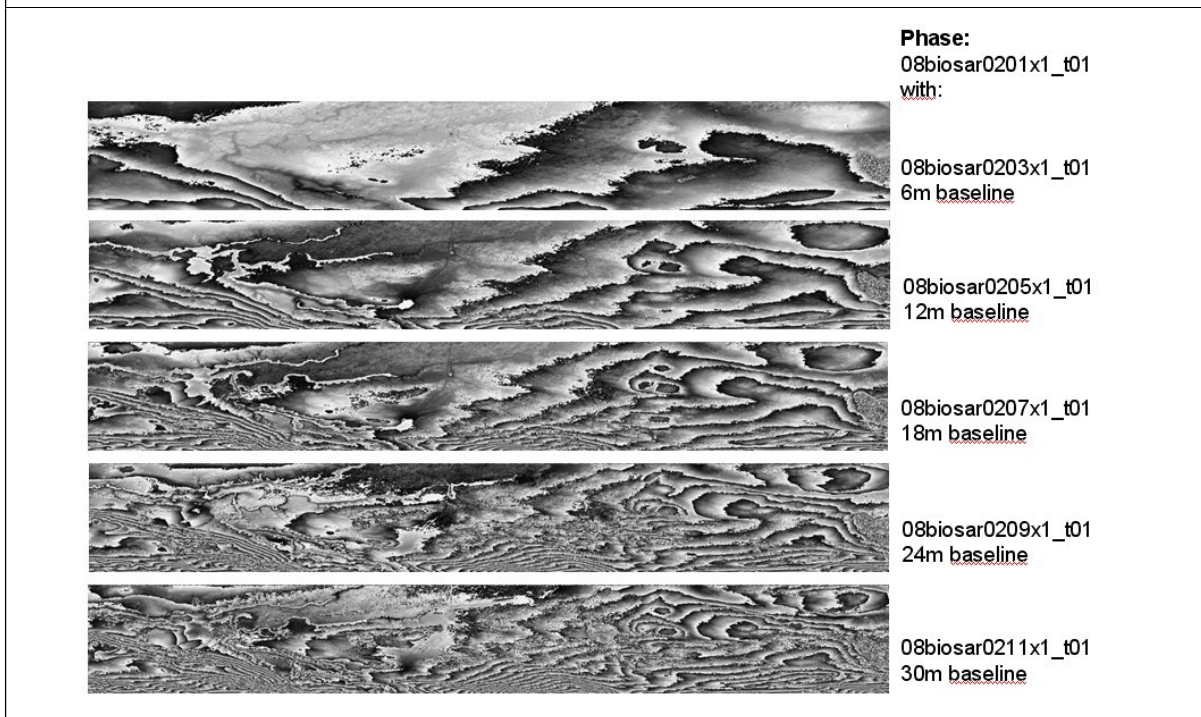
L-band RGI (t01) image of the large Krycklan test site (08biosar0201x1).



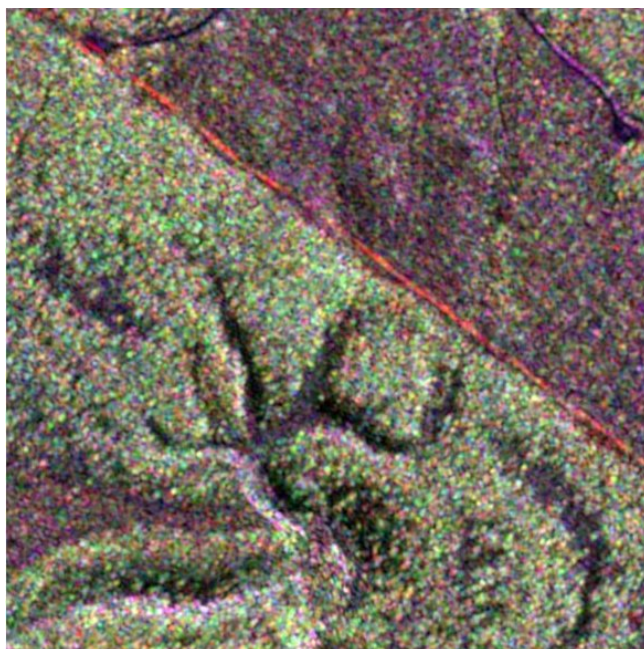
L-band GTC (t11:blue, t21:green, t31:red) images of the large Krycklan test site (08biosar0201x1). The complete data set has been divided into three geocoded parts for easier data handling.



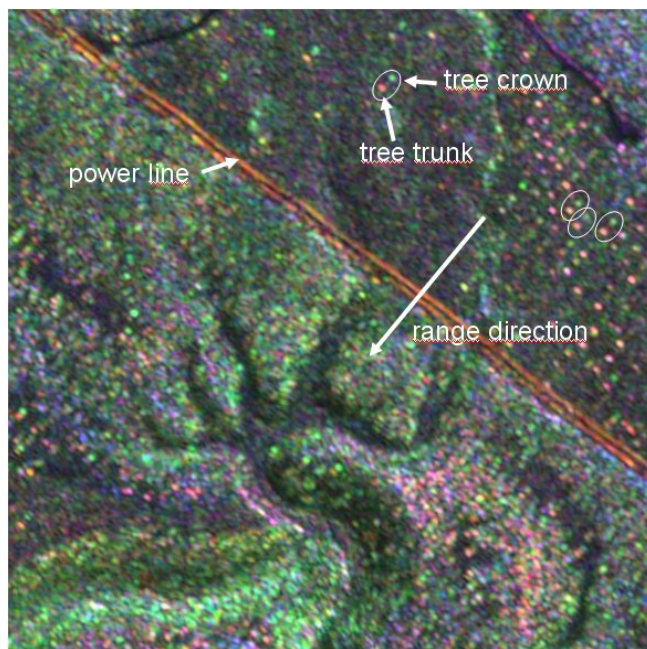
L-band RGI data: interferometric hh/hh coherence images of the large Krycklan testsite for different baselines. With increasing baseline the spatial decorrelation increases, especially the volume decorrelation in forested areas.



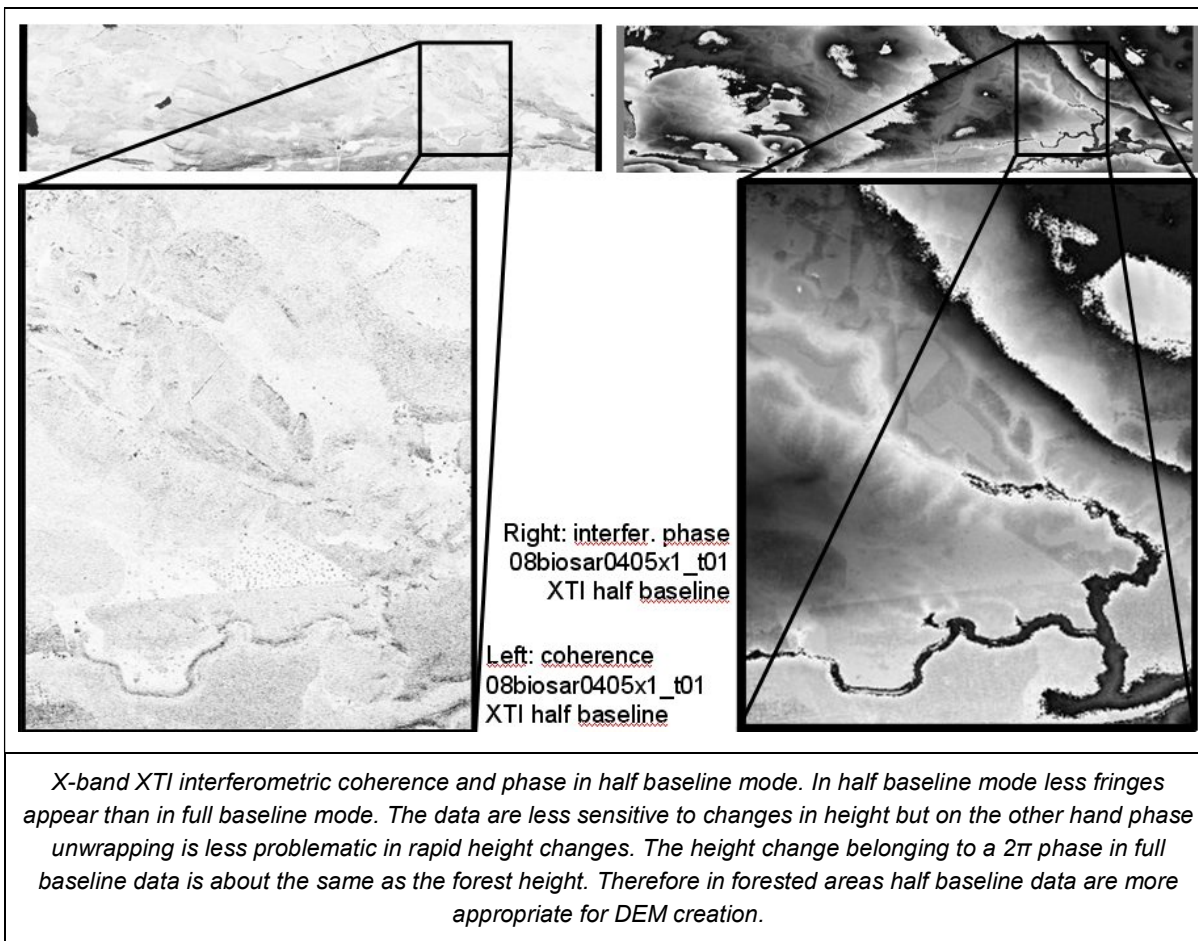
L-band RGI data: interferometric hh/hh phase images of the large Krycklan testsite for different baselines. With increasing baselines the density of fringes grows. Small height differences can be extracted more easily but the danger of phase unwrapping errors increases using large baselines.



L-band full resolution GTC subset of 08biosar0201x1_t11 (red: hh, green: hv, blue: vv). In the lower left part of the image a forested area with a valley can be seen. Parallel to the edge of the forest, a powerline is visible (red). The upper right part consists of a wide open area with single large seed trees and two unpaved roads with turning areas.



P-band full resolution GTC subset of 08biosar0302x1_t12 (red: hh, green: hv, blue: vv). Due to the larger wavelength, more energy penetrates through the canopy and is reflected by the trunks and the ground. Compared to the reflection of the tree crowns the propagation path of the double bounce reflection is longer. Therefore trees appear as two separated objects (trunk and crown) in the P-band data.



6.7 Interferometric Phase to Height Sensitivity

The kz factor is the interferometric sensitivity factor which relates changes in terrain elevation (vegetation height) to changes in interferometric phase. As such, it represents one of the essential parameters for Pol-InSAR forest height inversion. In the airborne geometry typical for E-SAR acquisitions strong variations of kz are found within one interferometric image pair because of the large variation of the look angle across the swath and because of the effective baseline variation along azimuth. To facilitate repeat-pass interferometric E-SAR data analysis the kz factor is precomputed for each slave acquisition (with respect to the master), archived and delivered as part of the RGI data product. The kz factor is computed as follows:

$$kz = \frac{4\pi B \sin(\theta + \xi)}{\lambda r \sin \theta}$$

where B is baseline length and ξ is baseline tilt from vertical, θ is look angle (incidence angle assuming zero slope), λ is wavelength and r is range. ξ and θ are given by

$$\xi = \tan^{-1} \frac{B_h}{B_v}; \quad \theta = \cos^{-1} \frac{h - h_{topo}}{r},$$

where B_h and B_v are horizontal and vertical baseline components (variable along azimuth), h antenna height above geoid and h_{topo} is local terrain elevation.

6.8 BIOMASS Spaceborne Simulation

The BIOMASS spaceborne simulation is performed for one set of interferometric P-band data (6 tracks) acquired within this project, illuminated from NE. The master is named 0103 (flight 1, pass 3), the slaves are 0101 (-8m horizontal baseline), 0105 (8m), 0107 (16m), 0109 (24m), and 0111 (32m).

6.8.1 Simulation parameters

Several parameters, typical for the BIOMASS mission had to be chosen for simulation results to demonstrate the example data sets. They are considered for the simulation processing as follows:

- The spatial resolution is set by the choice of range and azimuth bandwidth (chirp and Doppler bandwidth). The resolution setting is performed independently to single images.
- The peak and integrated sidelobe ratios PSLR, ISLR are set by the choice of the spectral apodization function (independently to single images).
- The noise equivalent sigma zero NESZ is chosen by coherent noise insertion (independently to single images).
- Ambiguities are inserted by attenuation, defocusing and shift of the original (low resolution) image. The interplay of the different polarisations is taken into account.

The following parameters (agreed with ESA) are used:

- Azimuth resolution (single look): 12.5 m (corresponding to 20 m antenna length)
- Slant range resolution (single look): 25 m (corresponding to 6 MHz bandwidth)
- Ground range resolution (single look) 60m – 30m @ 25°-55° incidence (airborne geometry)
- Peak to sidelobe ratio PSLR 20dB (by change of weighting factor)
- Distributed target ambig. ratio DTAR: 20dB (defocusing of ambiguities is considered.)
- Noise Equivalent Sigma Zero -28 dB
- Radiometric performance: as in high resolution data (airborne geometry)
- Ionosphere & temporal decorrelation: not altered

6.8.2 Simulation Strategy

The simulation strategy has been previously elaborated within the currently ongoing ESA project: Bio & Geo-Physical Retrieval Algorithms for Active Remote Sensing of Land Surfaces at P- and L-band: ESA-ESTEC contract number: 21131/07/NL/LvH), except for the temporal and ionospheric simulation.

The simulation steps performed for BIOSAR 2008 data can be summarized as follows:

1. The original SAR data is processed using the standard airborne SAR processor. The four polarisation channels are named `i<scene_id>.dat` for master data and `*.dat.final` for slave data, coregistered to the master data.

2. To reduce the spatial resolution the spectrum is filtered in range and azimuth according to the pre-defined resolution. The resulting data is named *.lowres.
3. By adding coherent noise, the NESZ is raised to the expected spaceborne level of -28dB. The resulting data is called *.nesz.
4. The last step is to insert ambiguities by attenuation, defocusing and shift of original low resolution data. The final extrapolated data is named *.saar. Azimuth and range ambiguities have been inserted.

The data flow is indicated in the Figure below and the details are described in the following subsections.

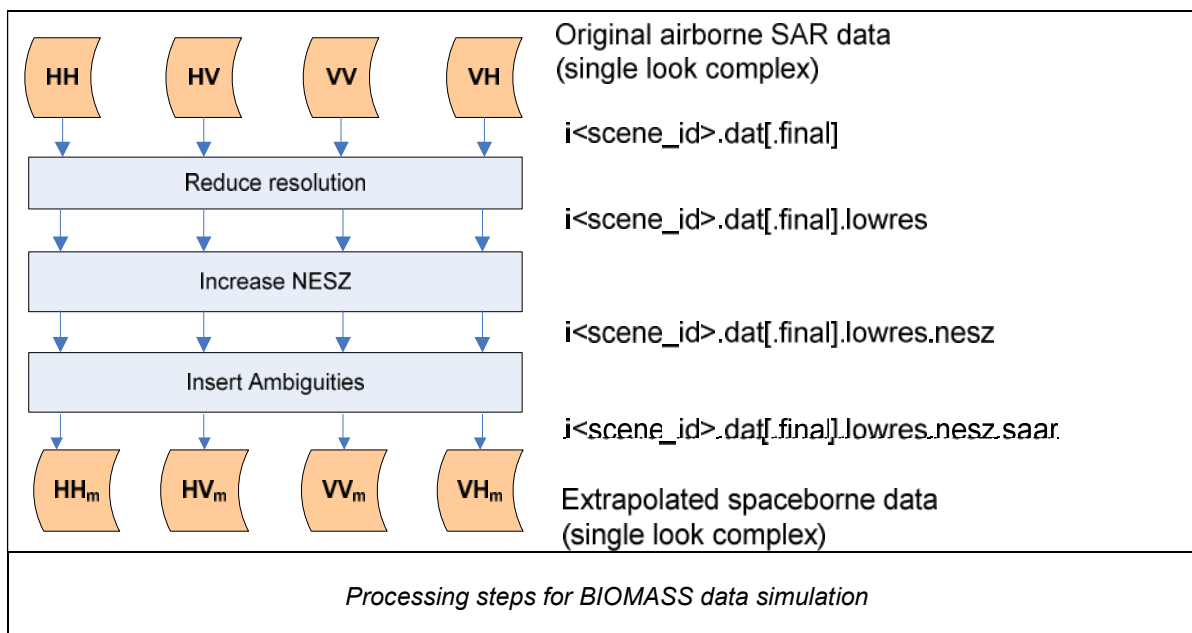
Step 1: Reduction of Spatial Resolution / PSLR, ISLR

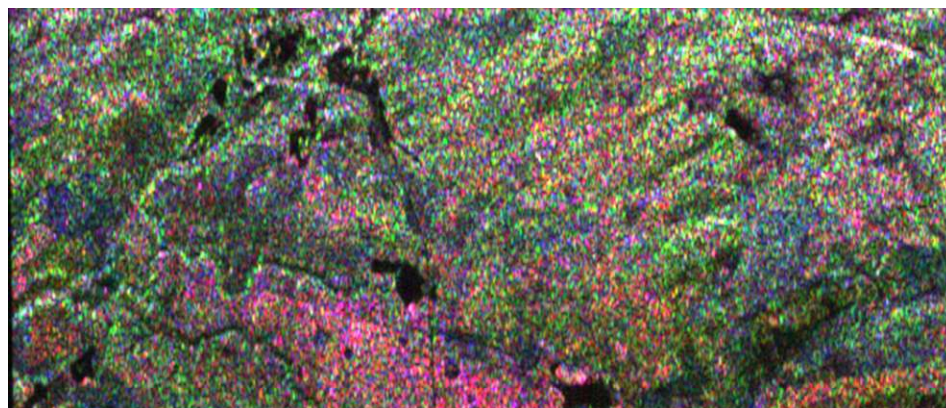
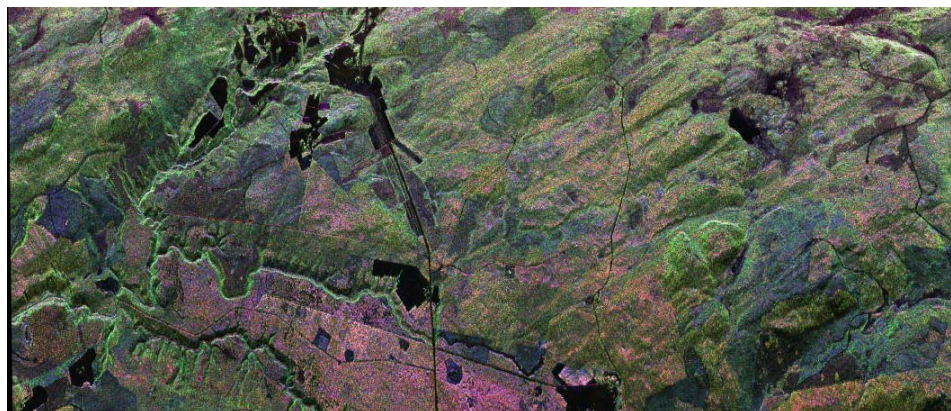
The spatial resolution depends on the on the spectral windowing by:

$$\rho_{rg} = k \frac{c_0}{2B_{rg}}; \quad \rho_{az} = k \frac{v}{B_{az}}$$

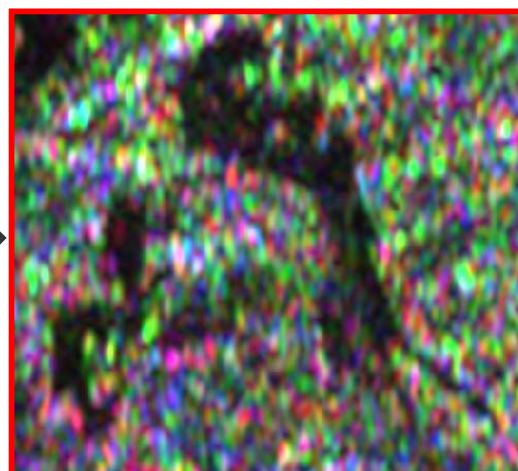
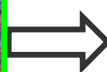
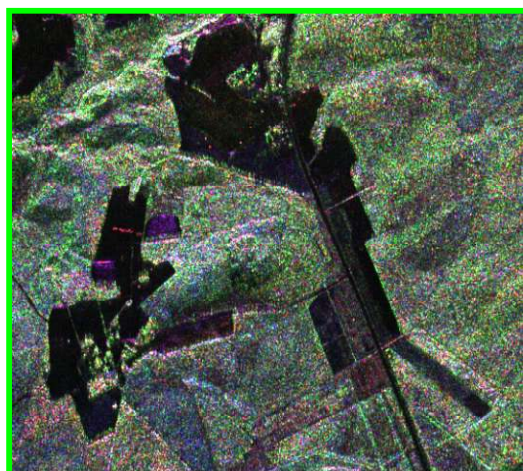
with k the resolution factor which depends on the used window type, c_0 the speed of light, v the platform velocity, B_{rg} the chirp bandwidth (in slant range) and B_{az} the Doppler bandwidth (in azimuth).

The PSLR and ISLR are determined by the shape of the window function. Special care has been taken on the removal of the spectral weighting of the full resolution data prior to bandpass filtering and on the normalisation to ensure unchanged absolute calibration of the data.





Comparison of full resolution E-SAR data and BIOMASS degraded resolution (look direction is from top)

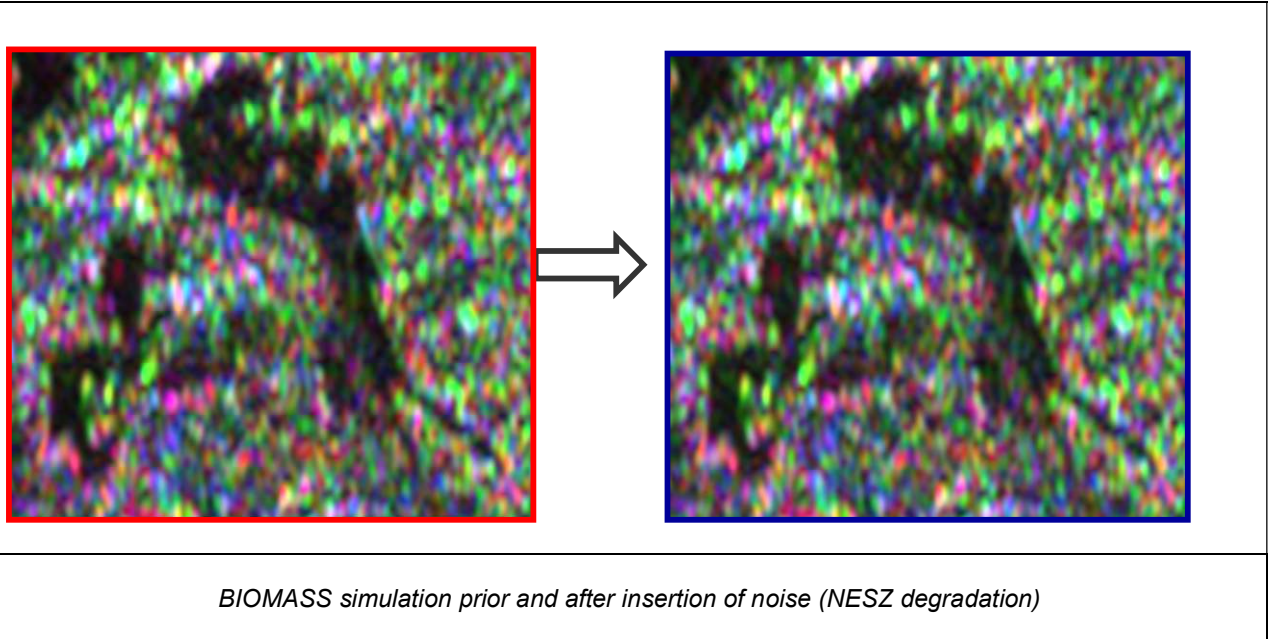


Comparison of full resolution E-SAR data and BIOMASS degraded resolution (full resolution zoom)

The image example above shows an image of the original airborne resolution (2m x 5m multilook, left), and of the degraded resolution (50m x 50m multilook, right).

Step 2: Increase of Noise Equivalent Sigma Zero - NESZ

Band limited Gaussian noise has been added coherently to the low resolution data. Spectral weighting and normalisation has been performed according to the settings used in the generation of the low resolution image.



Step 3: Insertion of Azimuth Ambiguities

The ambiguities were computed using the data itself (scene content dependent). The position of the ambiguities (the relative range and azimuth shift) was determined by the PRF time t_{PRF} and the Doppler rate k_a (see G.Cumming and F.H. Wong, "Digital Processing of Synthetic Aperture Radar Data", Artech House, Boston, 2005) .

$$t_{PRF} = PRF_{space} / k_a$$

$$k_a = \frac{2v_{rel}^2}{\lambda r_{space}}$$

$$\Delta az = \pm t_{PRF} \cdot v_{rel}$$

$$\Delta rg = \sqrt{r_{space}^2 + v_{rel}^2 \cdot t_{PRF}^2} - r_{space}$$

The attenuation and the additional azimuth defocusing were chosen due to the theoretical range displacement. The azimuth ambiguities for the spaceborne case in P-band occur at an azimuth position of 48km and a range position of 1.7km. The location of the added ambiguities in the simulation was decreased by a factor of 100 in azimuth and a factor of 10 in range.

Step 4: Insertion of Range Ambiguities

Range ambiguities arise from distances considerably different from those in the imaged area.

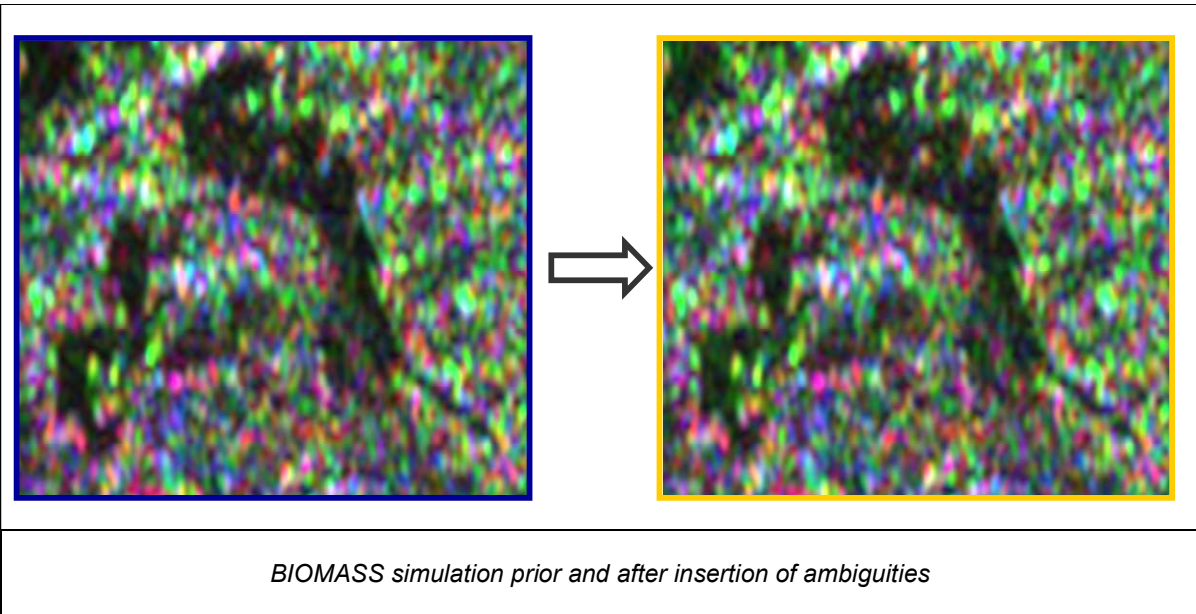
$$\Delta r_{PRF} = \pm n \cdot \frac{c_0}{2 \cdot PRF_{space}}$$

For polarimetric SAR there is a toggling between the different polarisations:

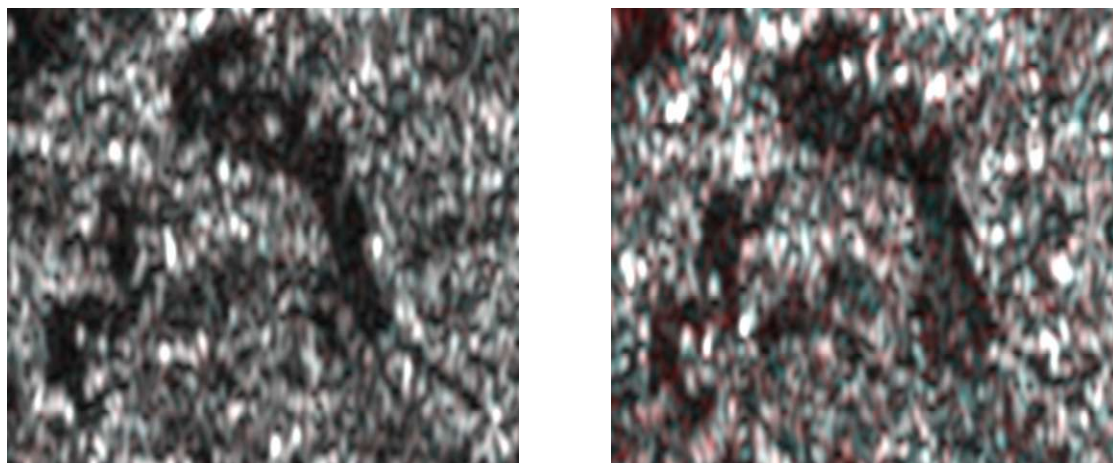
- Ambiguities from one channel correspond to a different polarisation
- Cross-polarised channels are affected by co-polarised range ambiguities (and vice versa)
- Range ambiguities are much more affecting HV and VH than the co-polarised channels.

For the simulation the same input data set (after the insertion of azimuth ambiguities) was used, but reversed in azimuth. The attenuation and defocusing was adapted according to the true range difference.

The effect of the inserted ambiguities is shown in the image below. On the left side the low resolution data including increased NESZ is presented, while on the right side the same data but with inserted ambiguities is shown.



Ambiguities appear much stronger in cross-polarised than in co-polarised data. This can be made visible in a different visualisation: Co-polarised (HH) data on the left and cross-polarised data (HV) on the right are shown as black-and-white images. The inserted ambiguities are shown in red. In the left image of the co-polarised data nearly no effect is visible while there is a clear evidence for ambiguities in the right image of the cross-polarised data.



Visualisation of BIOMASS ambiguities (in red) in co-polarised (HH, left) and cross-polarised (HV, right) polarimetric channels

The general impression is that the NESZ of BIOMASS as well as the ambiguity level does not deteriorate the quality to a considerable level. The main effect obviously comes from the decreased resolution, which is too coarse to resolve the detailed features, like roads and fences and even small settlements, visible in the original airborne images.

7 DATA QUALITY

The processed data have nominal quality without degradation by RFI. Minor problems occurred in repeat pass processing of P-band data. The originally foreseen masters could not be used as master by the processing software because they were recorded with a different range delay than all the other data sets. In repeat pass P-band it is difficult to estimate corrected navigation data directly from the radar data set itself. This was also the case in BIOSAR 2008. On the other hand, in P-band the coherency and phase of two repeat pass data sets is relatively stable concerning residual errors in the navigation data. Therefore this processing step has been skipped with no implication to data quality.

7.1 DEM Quality

For an analysis of the DEM quality, three types of input data can be used:

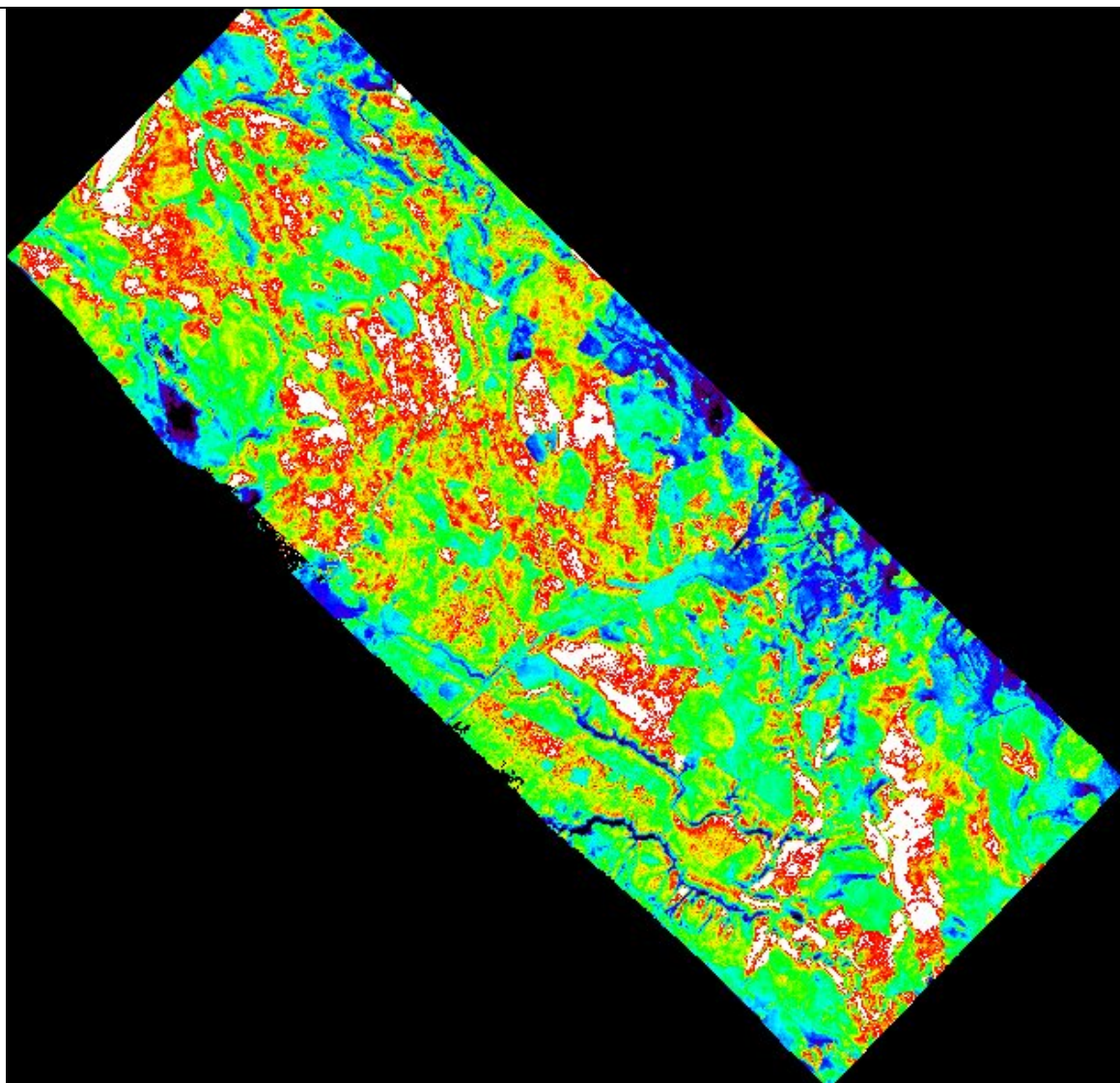
- the external DEM of the National Land Survey of Sweden, delivered by FOI
- the XTI-DEM created by X-band single pass interferometry
- the in-situ measured corner reflector positions (by differential GPS).

When comparing different types of DEMs, it is important to consider their origin to understand the differences that occur.

The DEM of the National Land Survey of Sweden is a model of the earth surface without vegetation cover. Usually, different types of measurements are used to create official maps and DEMs (triangulation and leveling, laser height measurements, GPS measurements).

The X-band DEM does not only show the topography but also vegetation cover. Over forested areas a large part of the signal is scattered back by the crowns of the trees while only a small part penetrates through the foliage and is reflected from the ground. This results in a measured DEM height which is near the height of the tree crowns. No height information can be retrieved in shadow and overlay areas.

The differences in between the two available DEMs have been computed. The image shows colour coded differences between -20m (black) to +20m (white).



Difference: X-band XTl half baseline DEM – external DEM. Near range: lower left. Colours: -20m (black) to +20m (white), blue-green colour is zero difference

The difference image of the available DEMs shows a stable behaviour over the whole test area with large differences mainly in overlay and shadow areas and in forests. No height ramp in azimuth is found. In far range (north-eastern parts) the XTl DEM tends to underestimate the height which leads to rather blue colour in the difference image.

Over forested areas the X-band DEM shows higher height values than the external DEM. This leads to a green/yellow/red/white colour in the difference image.

At the river areas with very narrow and steep gulches the external DEM is too coarse and overestimates the terrain height. In the difference image the rivers can therefore be seen in a blue colour.

7.1.1 DEM interpolation

The external DEM of the National Land Survey of Sweden was provided in the form of a text-file containing UTM coordinates and heights on a 50m non-regular UTM grid. Therefore an interpolation and resampling was necessary to create a regular sampled DEM of the test area.

In a first attempt, the external DEM has been read and resampled to a regular 50m grid directed to UTM North and East. This DEM has been further interpolated to a 5m grid, sufficient for standard RGI processing. A subset of the complete DEM has been cut out that covers all needed parts of the Krycklan test site.

For maintaining the spatial resolution in the geocoded data, it was decided to use a DEM with 1m grid size for GTC processing. Since the GTC products would be huge in a 1m version including large areas without data, the DEM was divided into three smaller parts before interpolating from 5m to 1m grid size: a division has been made into a south-eastern, a central and a north-western part.

Several different causes in combination with each other led to problems in the interpolated DEM:

- For the first time a very small GTC pixel size of only 1m was used to get an improved image quality in the GTC data.
- The original grid size of 50m is very large compared to 1m in the GTC data.
- The rows of the external DEM information were not parallel to UTM North and East direction which led to problems in our former conversion routine.
- The test area shows a strong topographic variation which enlarges the influence of DEM errors in the geo-location.

Two different problems occurred in the first attempt of the DEM conversion. The large difference in pixel size between the original 50m grid data and the interpolated 1m grid data, together with rounding errors of the sampling point coordinates led to steps in the interpolated DEM. In the DEM itself these steps were hardly visible but they showed up clearly in the incidence angle maps which are part of the GTC data set.

A second problem was the separate interpolation from 5m to 1m of the three parts of the test site. The separate interpolation did not lead to identical results in the interpolated DEMs and therefore to different geocoding results in the overlapping areas.

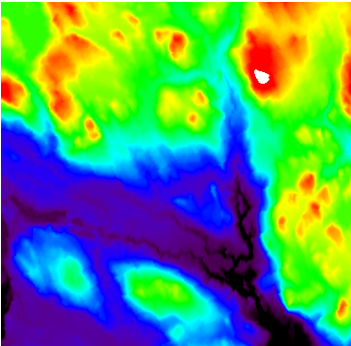
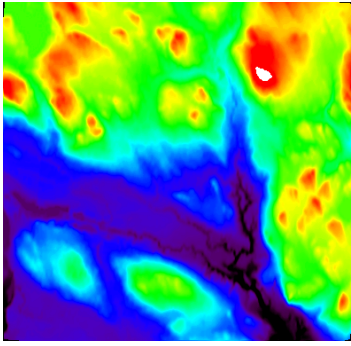
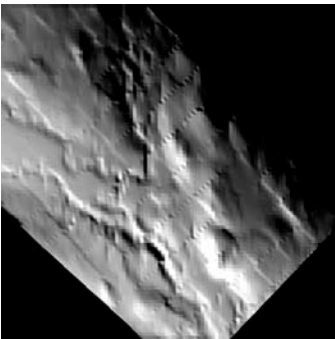
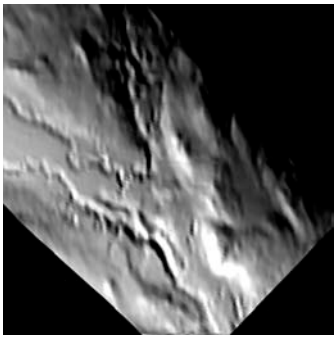
The strong requirements for the DEM interpolation in BIOSAR 2008 could not be achieved using our standard conversion routine. Therefore a completely new routine was developed using triangulation and cubic interpolation of the nodes which were imported from the external DEM without any rounding of their position values. A cubic interpolation method was used since linear interpolation leads to large triangles with the same inclination and sharp edges between the triangles. The cubic interpolation leads to smooth transitions of the inclinations for each point in the scene.

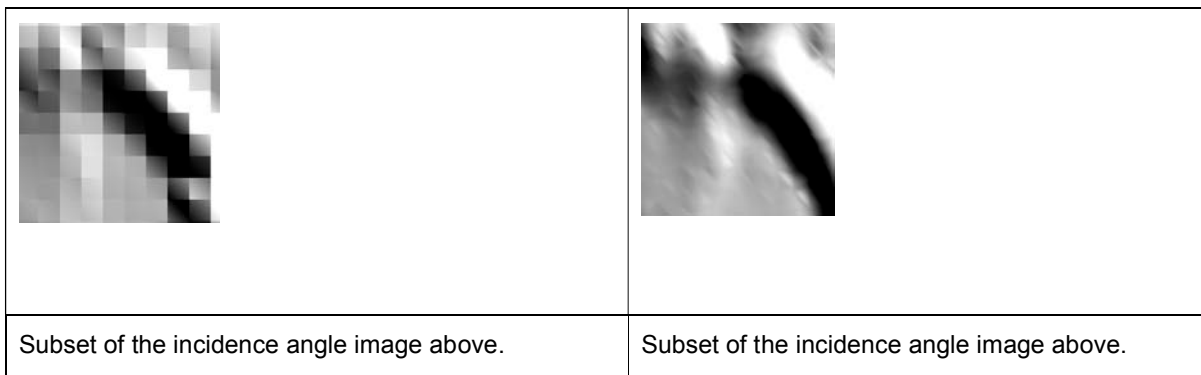
In this way the interpolation was done directly from the original 50m to the 1m grid. For a reduction of data size, this very large 1m DEM was divided into three parts (south-eastern, central part, and north-western part). Geocoding on the different DEM subsets was checked for consistency and no problems were found.

Note that the characteristics of the Krycklan testsite (topography variations of 100-300m and requirement of high spatial sampling of 1m together with the availability of the coarse resolution DEM) made the development of a new DEM interpolation procedure necessary. For test-sites mapped by E-SAR in the past, DEM generation/interpolation was performed differently as the DEM was either generated by means of single-pass E-SAR interferometry in X-band directly to the required grid spacing (AGRISAR, AQUIFEREX, INDREX-II) or an external DEM was linearly interpolated when the investigated test-site was nearly flat (BIOSAR-2007). The DEM of the BIOSAR 2007 campaign at Remningstorp was checked for

interpolation errors too. Only small errors were found which do not lead to problems during processing of the data. The area does not show large topographic variations and interpolation was only done to a 2m grid.

For comparison, the benefit of using the new interpolation method is shown in the figures below.

	
<p>Complete DEM, interpolated with former interpolation routine.</p>	<p>Complete DEM, interpolated with new triangulation interpolation method.</p>
	
<p>Incidence angles at the south-eastern sub-DEM using the former interpolation routine. Interpolation errors are clearly visible.</p>	<p>Incidence angles at the south-eastern sub-DEM using the new triangulation interpolation method. A much smoother representation of the ground could be created. Only the triangle borders remain visible as very fine lines.</p>



7.1.2 Comparison of DEM (ellipsoidal) heights at the corner reflector positions:

The heights of the different DEMs have been read at the corner reflector positions. By subtracting the measured differentially evaluated GPS height from the DEM height at the corner reflector position, the height difference has been calculated. Negative values indicate that the DEM height is below the true height.

CR name	UTM E	UTM N	GPS height	Diff to off. DEM	Diff to XDEM 0405 (half bl.)
CR01	444415	7121818	206.79	0.46	-0.12
CR02	443772	7121597	162.54	0.15	-1.40
CR03	443681	7122739	197.61	-0.11	-0.04
CR04	443275	7122891	206.68	2.02	-0.20
CR5A	442759	7122287	190.33	1.64	-0.53
CR5B	442760	7122293	190.28	1.69	-0.46
CR6A	444060	7123444	192.50	1.08	-0.56
CR6B	444067	7123453	192.59	1.18	-0.88
CR7A	438677	7127702	353.04	0.50	1.36
CR7B	438669	7127696	352.92	0.79	2.02

Reflector CR01
Measured GPS height: 206.79
Official DEM height: 207.25 Delta = 0.46
X_band DEM 0405: 206.67 Delta = -0.12

Reflector CR02
Measured GPS height: 162.54
Official DEM height: 162.69 Delta = 0.15
X_band DEM 0405: 161.14 Delta = -1.40

Reflector CR03
Measured GPS height: 197.61
Official DEM height: 197.50 Delta = -0.11
X_band DEM 0405: 197.57 Delta = -0.04

Reflector CR04
Measured GPS height: 206.68
Official DEM height: 208.70 Delta = 2.02
X_band DEM 0405: 206.48 Delta = -0.20

Reflector CR5A
Measured GPS height: 190.33
Official DEM height: 191.97 Delta = 1.64
X_band DEM 0405: 189.80 Delta = -0.53

Reflector CR5B
Measured GPS height: 190.28
Official DEM height: 191.97 Delta = 1.69
X_band DEM 0405: 189.82 Delta = -0.46

Reflector CR6A
Measured GPS height: 192.50
Official DEM height: 193.58 Delta = 1.08
X_band DEM 0405: 191.94 Delta = -0.56

Reflector CR6B
Measured GPS height: 192.59
Official DEM height: 193.77 Delta = 1.18
X_band DEM 0405: 191.71 Delta = -0.88

Reflector CR7A
Measured GPS height: 353.04
Official DEM height: 353.54 Delta = 0.50
X_band DEM 0405: 354.40 Delta = 1.36

Reflector CR7B
Measured GPS height: 352.92
Official DEM height: 353.71 Delta = 0.79
X_band DEM 0405: 354.94 Delta = 2.02

The comparison of the different types of DEMs and the corner reflector heights measured by GPS show a very good match. Mostly the differences are below 2m.

In summary both, the external DEM and the processed X-band DEM are of good quality. The heights are similar over the whole test area, no trend could be observed. In areas of strong topography and in forested areas the DEM heights differ due to their physical origin. In flat areas without vegetation like the surrounding of the corner reflectors the different DEMs are nearly similar and show differences in average < 2m.

7.2 Geocoding Quality

The corner reflectors in the test area can be used to check the geocoding data quality in terms of local position accuracy. It is clear that errors in the underlying DEM lead to distortions, i.e. local shifts in the corresponding geocoded data. The corner reflectors have been located in the geocoded geo-tif images and compared with their nominal positions. The corner reflector footprints are several meters wide, especially in the case of the large 5m-reflectors. Their positions can be located in the data with an accuracy of 1-2m.

Large test area t01, look direction to south-west, geocoded P-band data set: 08biosar0103x1_t11:

CR name	true position UTM E	true position UTM N	measured position UTM E	measured position UTM N	Difference in m E	Difference in m N
CR01	444415	7121818	444414	7121817	-1	-1
CR03	443681	7122739	443682	7122740	1	1
CR5B	442760	7122293	corner reflector signal too low, high background			
CR6B	444067	7123453	444065	7123452	0	0

Large test area t01, look direction to south-west, geocoded P-band data set: 08biosar0103x1_t21:

CR name	true position UTM E	true position UTM N	measured position UTM E	measured position UTM N	Difference in m E	Difference in m N
CR03	443681	7122739	443682	7122740	1	1
CR5B	442760	7122293	corner reflector signal too low, high background			
CR6B	444067	7123453	444066	7121452	-1	-1

Large test area t01, look direction to south-west, geocoded P-band data set: 08biosar0103x1_t31:

CR name	true position UTM E	true position UTM N	measured position UTM E	measured position UTM N	Difference in m E	Difference in m N
CR7B	438669	7127696	438669	7127695	0	-1

Large test area t01, look direction to north-east, geocoded P-band data set: 08biosar0104x1_t11:

CR name	true position UTM E	true position UTM N	measured position UTM E	measured position UTM N	Difference in m E	Difference in m N
CR04	443275	7122891	443276	7122892	1	1
CR5A	442759	7122287	corner reflector signal too low, high background			
CR6A	444060	7123444	444060	7123445	0	1

Large test area t01, look direction to north-east, geocoded P-band data set: 08biosar0104x1_t21:

CR name	true position UTM E	true position UTM N	measured position UTM E	measured position UTM N	Difference in m E	Difference in m N
CR04	443275	7122891	443276	7122892	1	1
CR5A	442759	7122287	corner reflector signal too low, high background			
CR6A	444060	7123444	444060	7123445	0	1

Large test area t01, look direction to north-east, geocoded P-band data set: 08biosar0104x1_t31:

CR name	true position UTM E	true position UTM N	measured position UTM E	measured position UTM N	Difference in m E	Difference in m N
CR7A	438677	7127702	438678	7127702	1	0

Large test area t01, look direction to south-west, geocoded P-band data set: 08biosar0201x1_t11:

CR name	true position UTM E	true position UTM N	measured position UTM E	measured position UTM N	Difference in m E	Difference in m N
CR01	444415	7121818	444416	7121817	1	-1
CR03	443681	7122739	443681	7122739	0	0
CR5B	442760	7122293	442759	7122293	-1	0
CR6B	444067	7123453	444067	7123452	0	-1

Large test area t01, look direction to south-west, geocoded L-band data set: 08biosar0201x1_t21:

CR name	true position UTM E	true position UTM N	measured position UTM E	measured position UTM N	Difference in m E	Difference in m N
CR03	443681	7122739	443682	7120739	1	0
CR5B	442760	7122293	442760	7122293	0	0
CR6B	444067	7123453	444067	7123452	0	-1

Large test area t01, look direction to south-west, geocoded L-band data set: 08biosar0201x1_t31:

CR name	true position UTM E	true position UTM N	measured position UTM E	measured position UTM N	Difference in m E	Difference in m N
CR7B	438669	7127696	438669	7127695	0	-1

Large test area t01, look direction to north-east, geocoded L-band data set: 08biosar0202x1_t11:

CR name	true position UTM E	true position UTM N	measured position UTM E	measured position UTM N	Difference in m E	Difference in m N
CR04	443275	7122891	443277	7122893	2	2
CR5A	442759	7122287	442761	7122289	2	2
CR6A	444060	7123444	444061	7123445	1	1

Large test area t01, look direction to north-east, geocoded L-band data set: 08biosar0202x1_t21:

CR name	true position UTM E	true position UTM N	measured position UTM E	measured position UTM N	Difference in m E	Difference in m N
CR04	443275	7122891	443277	7122892	2	1
CR5A	442759	7122287	442761	7122289	2	2
CR6A	444060	7123444	444061	7123445	1	1

Large test area t01, look direction to north-east, geocoded L-band data set: 08biosar0202x1_t31:

CR name	true position UTM E	true position UTM N	measured position UTM E	measured position UTM N	Difference in m E	Difference in m N
CR7A	438677	7127702	438677	7127701	0	-1

Large test area t01, look direction to north-east, geocoded X-band data set: 08biosar0405x1_t11:

CR name	true position UTM E	true position UTM N	measured position UTM E	measured position UTM N	Difference in m E	Difference in m N
CR04	443275	7122891	443276	7122891	1	0
CR5A	442759	7122287	442761	7122289	2	2
CR6A	444060	7123444	444060	7123444	0	0

Large test area t01, look direction to north-east, geocoded X-band data set: 08biosar0405x1_t21:

CR name	true position UTM E	true position UTM N	measured position UTM E	measured position UTM N	Difference in m E	Difference in m N
CR04	443275	7122891	443277	7122892	2	1
CR5A	442759	7122287	442761	7122289	2	2
CR6A	444060	7123444	444060	7123445	0	1

Large test area t01, look direction to north-east, geocoded X-band data set: 08biosar0405x1_t31:

CR name	true position UTM E	true position UTM N	measured position UTM E	measured position UTM N	Difference in m E	Difference in m N
CR7A	438677	7127702	438678	7127700	1	-2

Small test area t02, look direction to west, geocoded P-band data set: 08biosar0301x1_t12:

CR name	true position UTM E	true position UTM N	measured position UTM E	measured position UTM N	Difference in m E	Difference in m N
CR01	444415	7121818	444414	7121819	-1	1
CR02	443772	7121597	443773	7121596	1	-1
CR03	443681	7122739	443682	7122739	1	0
CR5B	442760	7122293	corner reflector signal too low, high background			
CR6B	444067	7123453	444066	7123454	-1	1

Small test area t02, look direction to west, geocoded L-band data set: 08biosar0401x1_t12:

CR name	true position UTM E	true position UTM N	measured position UTM E	measured position UTM N	Difference in m E	Difference in m N
CR01	444415	7121818	444415	7121818	0	0
CR02	443772	7121597	443770	7121596	-2	-1
CR03	443681	7122739	443682	7122739	1	0
CR5B	442760	7122293	442760	7122294	0	1
CR6B	444067	7123453	444066	7123453	-1	0

Small test area t02, look direction to south-west, geocoded P-band data set: 08biosar0302x1_t12:

CR name	true position UTM E	true position UTM N	measured position UTM E	measured position UTM N	Difference in m E	Difference in m N
CR01	444415	7121818	444415	7121817	0	-1
CR03	443681	7122739	443683	7122740	2	1
CR5B	442760	7122293	corner reflector signal too low, high background			
CR6B	444067	7123453	444066	7123452	-1	-1

Small test area t02, look direction to south-west, geocoded L-band data set: 08biosar0402x1_t12:

CR name	true position UTM E	true position UTM N	measured position UTM E	measured position UTM N	Difference in m E	Difference in m N
CR01	444415	7121818	444415	7121817	0	-1
CR03	443681	7122739	443683	7122741	2	2
CR5B	442760	7122293	442760	7122293	0	0
CR6B	444067	7123453	444066	7123452	-1	-1

Small test area t02, look direction to north-east, geocoded P-band data set: 08biosar0303x1_t12:

CR name	true position UTM E	true position UTM N	measured position UTM E	measured position UTM N	Difference in m E	Difference in m N
CR04	443275	7122891	443276	7122891	1	0
CR5A	442759	7122287	corner reflector signal too low, high background			
CR6A	444060	7123444	444061	7123445	1	1

Small test area t02, look direction to north-east, geocoded P-band data set: 08biosar0305x1_t12:

CR name	true position UTM E	true position UTM N	measured position UTM E	measured position UTM N	Difference in m E	Difference in m N
CR04	443275	7122891	443277	7122893	2	2
CR5A	442759	7122287	corner reflector signal too low, high background			
CR6A	444060	7123444	444061	7123444	1	0

Small test area t02, look direction to north-east, geocoded L-band data set: 08biosar0403x1_t12:

CR name	true position UTM E	true position UTM N	measured position UTM E	measured position UTM N	Difference in m E	Difference in m N
CR04	443275	7122891	443276	7122892	1	1
CR5A	442759	7122287	442761	7122288	2	1
CR6A	444060	7123444	444061	7123445	1	1

Small test area t02, look direction to north-west, geocoded P-band data set: 08biosar0304x1_t12:

CR name	true position UTM E	true position UTM N	measured position UTM E	measured position UTM N	Difference in m E	Difference in m N
CR01	444415	7121818	444415	7121819	0	1
CR02	443772	7121597	443773	7121596	1	-1

Small test area t02, look direction to north-west, geocoded L-band data set: 08biosar0404x1_t12:

CR name	true position UTM E	true position UTM N	measured position UTM E	measured position UTM N	Difference in m E	Difference in m N
CR01	444415	7121818	444414	7121819	-1	1
CR02	443772	7121597	443771	7121598	-1	1

In summary the corner reflectors appear in the data sets as bright areas of several meters diameter. In L-band, the 5m-reflector signals are about 10m wide, while in P-band the corner reflector footprint becomes as big as 15m x 10m. A measurement of the corner reflector coordinates is therefore only possible with an uncertainty of about 1-2m in each direction.

The corner reflector signals in the geocoded data show a deviation from their nominal positions of within 2m which includes the location uncertainty when detecting the reflector on the 1m grid.

7.3 Calibration Checks

The E-SAR system is not permanently mounted in its operating aircraft Do228 and hence must be calibrated after each mounting i.e. for every campaign.

The E-SAR system firmly uses a factor of 1.000.000 for amplifying the backscattered signal intensity to allow a 16 bit data representation with sufficient dynamics. This determines the E-SAR calibration constant which amounts to 60dB. Accordingly, 60dB is the RCS value difference expected after SAR processing for the corner reflectors.

In the following, the calibration constant (signal amplitude) is checked, amplitude imbalances between HH and VV polarisation and phase imbalances between HH and VV polarisation.

In BIOSAR 2007 it was found that the 5m corner reflectors deliver a stable signal for calibration in P- and L-band. For BIOSAR 2008 the X- and L-band sub-systems were calibrated over the calibration field near Kaufbeuren in Germany before the BIOSAR flight campaign. During processing of the BIOSAR data it was found that in L-band the signal level over the 5m reflectors was 2dB too low. At first, it was decided to process the L-band data with an increased signal level of 2dB to be comparable to the data of 2007 with respect to the 5m CR signature. After consultation with FOI and in agreement with ESA, a reprocessing of all L-band data was done to restore the original signal level without any manual adjustments.

In P-band, the 90cm corner reflectors (CR5A, CR5B, CR6A, CR6B) are not checked because they are too small to deliver a good signal. In X-band the 5m reflectors (CR01, CR02, CR03, CR04) are ignored. Their mesh surface does not appear as a smooth surface for X-band and therefore no specular reflection is assumed. The X-band signal of the 5m reflectors was found to be about 30dB below its theoretical value.

In the following table, information about the behaviour of the radar reflectors is given for the different passes. RCS values which differ by more than 1dB from the expected values are marked in red. Position errors of more than three pixels in range and five pixels in azimuth are also shown in red to be treated carefully during tiepointing as automatic detection might have failed.

P-Band Pol-InSAR																	
Filename	Filename-Extension	Band	Polarisation	Track	CR Info	Reflector Nr.	CR size [m]	CR azim [deg]	CR elev [deg]	Estimated RCS [dB]	Theory RCS - Estimated RCS [dB]	Calibration Factor [dB]	Signal to Background Ratio [dB]	Amplitude Imbalance [dB]	Phase Imbalance [deg]	Delta Range [pix]	Delta Azimuth [pix]
e08biosar0101x1	t01	P	PM	10	1 HH		5 308	10	34.6	0.7	59.3	27.7					
e08biosar0101x1	t01	P	PM	10	1 VV	3	5 308	10	34.5	0.8	59.2	25.8	0.1	9.1	0.0	-5.5	
e08biosar0101x1	t01	P	PM	10	4 HH		1.5 308	10	14.4	-0.1	60.1	10.4					
e08biosar0101x1	t01	P	PM	10	4 VV	10	1.5 308	10	13.7	0.7	59.3	7.9	0.7	34.2	-0.2	-5.4	
e08biosar0102x1	t01	P	PM	20	1 HH		5 128	10	34.6	0.7	59.3	26.1					
e08biosar0102x1	t01	P	PM	20	1 VV	4	5 128	10	34.0	1.3	58.7	25.5	0.6	9.2	0.2	-4.7	
e08biosar0102x1	t01	P	PM	20	4 HH		1.5 128	10	13.2	1.3	58.7	8.3					
e08biosar0102x1	t01	P	PM	20	4 VV	9	1.5 128	10	13.4	1.1	58.9	7.5	-0.2	24.7	-0.3	-3.8	
e08biosar0103x1	t01	P	PM	11	1 HH		5 308	10	34.6	0.7	59.3	27.4					
e08biosar0103x1	t01	P	PM	11	1 VV	3	5 308	10	34.4	0.9	59.1	25.8	0.2	9.7	0.1	-4.7	
e08biosar0103x1	t01	P	PM	11	4 HH		1.5 308	10	14.3	0.0	60.0	10.8					
e08biosar0103x1	t01	P	PM	11	4 VV	10	1.5 308	10	13.5	0.8	59.2	9.2	0.8	36.1	-0.3	-4.6	
e08biosar0104x1	t01	P	PM	21	1 HH		5 128	10	34.4	0.8	59.2	26.1					
e08biosar0104x1	t01	P	PM	21	1 VV	4	5 128	10	33.8	1.5	58.5	25.2	0.6	9.0	0.1	-4.8	
e08biosar0104x1	t01	P	PM	21	4 HH		1.5 128	10	13.0	1.4	58.6	7.9					
e08biosar0104x1	t01	P	PM	21	4 VV	9	1.5 128	10	13.7	0.7	59.3	8.2	-0.7	28.9	-0.3	-4.2	
e08biosar0105x1	t01	P	PM	12	1 HH		5 308	10	34.9	0.5	59.5	27.3					
e08biosar0105x1	t01	P	PM	12	1 VV	3	5 308	10	34.5	0.9	59.1	25.6	0.4	9.3	0.0	-4.7	
e08biosar0105x1	t01	P	PM	12	4 HH		1.5 308	10	14.3	0.0	60.0	11.0					
e08biosar0105x1	t01	P	PM	12	4 VV	10	1.5 308	10	13.6	0.7	59.3	8.7	0.7	38.0	-0.4	-4.6	
e08biosar0106x1	t01	P	PM	22	1 HH		5 128	10	34.6	0.7	59.3	26.6					
e08biosar0106x1	t01	P	PM	22	1 VV	4	5 128	10	34.0	1.3	58.7	25.1	0.6	8.6	-0.1	-4.9	
e08biosar0106x1	t01	P	PM	22	4 HH		1.5 128	10	13.0	1.4	58.6	8.5					
e08biosar0106x1	t01	P	PM	22	4 VV	9	1.5 128	10	13.8	0.6	59.4	8.1	-0.8	25.2	-0.3	-4.2	

P-Band Pol-InSAR																	
Filename	Filename-Extension	Band	Polarisation	Track	CR Info	Reflector Nr.	CR size [m]	CR azim [deg]	CR elev [deg]	Estimated RCS [dB]	Theory RCS - Estimated RCS [dB]	Calibration Factor [dB]	Signal to Background Ratio [dB]	Amplitude Imbalance [dB]	Phase Imbalance [deg]	Delta Range [pix]	Delta Azimuth [pix]
e08biosar0107x1	t01	P	PM	13	1 HH		5	308	10	34.8	0.6	59.4	27.9				
e08biosar0107x1	t01	P	PM	13	1 VV	3	5	308	10	34.5	0.9	59.1	26.1	0.3	8.6	0.0	-4.7
e08biosar0107x1	t01	P	PM	13	4 HH		1.5	308	10	14.2	0.1	59.9	10.5				
e08biosar0107x1	t01	P	PM	13	4 VV	10	1.5	308	10	13.5	0.8	59.2	8.5	0.7	36.1	-0.3	-4.7
e08biosar0108x1	t01	P	PM	23	1 HH		5	128	10	34.4	0.8	59.2	26.6				
e08biosar0108x1	t01	P	PM	23	1 VV	4	5	128	10	33.9	1.4	58.6	25.3	0.5	9.4	0.0	-4.8
e08biosar0108x1	t01	P	PM	23	4 HH		1.5	128	10	13.0	1.4	58.6	8.7				
e08biosar0108x1	t01	P	PM	23	4 VV	9	1.5	128	10	13.5	1.0	59.0	7.9	-0.5	27.7	-6.4	8.9
e08biosar0109x1	t01	P	PM	14	1 HH		5	308	10	34.7	0.6	59.4	27.5				
e08biosar0109x1	t01	P	PM	14	1 VV	3	5	308	10	34.4	0.9	59.1	26.1	0.3	8.7	0.0	-4.8
e08biosar0109x1	t01	P	PM	14	4 HH		1.5	308	10	13.7	0.7	59.3	9.8				
e08biosar0109x1	t01	P	PM	14	4 VV	10	1.5	308	10	13.4	0.9	59.1	8.1	0.3	37.7	-0.3	-4.8
e08biosar0110x1	t01	P	PM	24	1 HH		5	128	10	34.4	0.8	59.2	26.6				
e08biosar0110x1	t01	P	PM	24	1 VV	4	5	128	10	33.9	1.4	58.6	25.5	0.5	8.5	0.0	-4.7
e08biosar0110x1	t01	P	PM	24	4 HH		1.5	128	10	12.7	1.7	58.3	8.3				
e08biosar0110x1	t01	P	PM	24	4 VV	9	1.5	128	10	13.4	1.1	58.9	7.8	-0.6	25.5	-0.3	-4.6
e08biosar0111x1	t01	P	PM	15	1 HH		5	308	10	34.6	0.8	59.2	27.7				
e08biosar0111x1	t01	P	PM	15	1 VV	3	5	308	10	34.2	1.1	58.9	25.8	0.4	8.6	0.0	-4.9
e08biosar0111x1	t01	P	PM	15	4 HH		1.5	308	10	13.9	0.5	59.5	10.7				
e08biosar0111x1	t01	P	PM	15	4 VV	10	1.5	308	10	12.9	1.4	58.6	9.3	0.9	37.7	-0.3	-4.8
e08biosar0112x1	t01	P	PM	25	1 HH		5	128	10	34.4	0.9	59.1	26.7				
e08biosar0112x1	t01	P	PM	25	1 VV	4	5	128	10	34.0	1.3	58.7	25.4	0.4	8.7	0.0	-4.5
e08biosar0112x1	t01	P	PM	25	4 HH		1.5	128	10	12.3	2.1	57.9	7.6				
e08biosar0112x1	t01	P	PM	25	4 VV	9	1.5	128	10	13.5	0.9	59.1	8.0	-1.2	28.0	-6.5	8.5

L-band Pol-InSAR																	
Filename	Filename-Extension	Band	Polarisation	Track	CR Info	Reflector Nr.	CR size [m]	CR azim [deg]	CR elev [deg]	Estimated RCS [dB]	Theory RCS - Estimated RCS [dB]	Calibration Factor [dB]	Signal to Background Ratio [dB]	Amplitude Imbalance [dB]	Phase Imbalance [deg]	Delta Range [pix]	Delta Azimuth [pix]
e08biosar0201x1	t01	L	PM	10	1 HH		5	308	10	44.9	2.0	58.0	36.2				
e08biosar0201x1	t01	L	PM	10	1 VV	3	5	308	10	44.9	2.0	58.0	38.3	0.0	-13.5	-1.2	3.6
e08biosar0201x1	t01	L	PM	10	2 HH		0.9	308	0	17.1	-0.2	60.2	13.2				
e08biosar0201x1	t01	L	PM	10	2 VV	6	0.9	308	0	17.7	-0.8	60.8	13.6	-0.6	-3.1	-1.2	3.5
e08biosar0201x1	t01	L	PM	10	3 HH		0.9	308	20	18.5	-1.3	61.3	13.6				
e08biosar0201x1	t01	L	PM	10	3 VV	8	0.9	308	20	17.8	-0.7	60.7	10.8	0.6	1.6	-1.3	3.1
e08biosar0201x1	t01	L	PM	10	4 HH		1.5	308	10	26.0	-0.1	60.1	19.2				
e08biosar0201x1	t01	L	PM	10	4 VV	10	1.5	308	10	25.9	0.0	60.0	21.5	0.1	-4.7	-1.2	4.1
e08biosar0202x1	t01	L	PM	20	1 HH		5	128	10	44.9	1.7	58.3	34.8				
e08biosar0202x1	t01	L	PM	20	1 VV	4	5	128	10	45.2	1.4	58.6	36.8	-0.3	-13.2	-1.2	3.7
e08biosar0202x1	t01	L	PM	20	2 HH		0.9	128	20	18.0	-1.1	61.1	10.0				
e08biosar0202x1	t01	L	PM	20	2 VV	5	0.9	128	20	17.3	-0.4	60.4	8.5	0.7	4.3	-1.3	3.5
e08biosar0202x1	t01	L	PM	20	3 HH		0.9	128	0	17.0	-0.4	60.4	16.9				
e08biosar0202x1	t01	L	PM	20	3 VV	7	0.9	128	0	15.9	0.7	59.3	12.6	1.1	-2.4	-1.2	3.1
e08biosar0202x1	t01	L	PM	20	4 HH		1.5	128	10	25.9	-0.1	60.1	18.9				
e08biosar0202x1	t01	L	PM	20	4 VV	9	1.5	128	10	25.5	0.3	59.7	18.9	0.4	-0.3	-1.2	3.7
e08biosar0203x1	t01	L	PM	11	1 HH		5	308	10	44.7	2.2	57.8	36.4				
e08biosar0203x1	t01	L	PM	11	1 VV	3	5	308	10	44.7	2.2	57.8	38.0	0.0	-14.2	-1.3	3.1
e08biosar0203x1	t01	L	PM	11	2 HH		0.9	308	0	17.0	0.0	60.0	13.1				
e08biosar0203x1	t01	L	PM	11	2 VV	6	0.9	308	0	17.3	-0.4	60.4	13.5	-0.3	-2.8	-1.3	2.9
e08biosar0203x1	t01	L	PM	11	3 HH		0.9	308	20	18.2	-1.1	61.1	13.3				
e08biosar0203x1	t01	L	PM	11	3 VV	8	0.9	308	20	17.5	-0.4	60.4	10.9	0.7	1.4	-1.3	2.5
e08biosar0203x1	t01	L	PM	11	4 HH		1.5	308	10	25.8	0.0	60.0	19.2				
e08biosar0203x1	t01	L	PM	11	4 VV	10	1.5	308	10	25.6	0.2	59.8	21.4	0.2	-3.1	-1.2	3.2
e08biosar0205x1	t01	L	PM	12	1 HH		5	308	10	44.8	2.1	57.9	36.2				
e08biosar0205x1	t01	L	PM	12	1 VV	3	5	308	10	44.7	2.2	57.8	38.1	0.1	-14.3	-1.2	3.7
e08biosar0205x1	t01	L	PM	12	2 HH		0.9	308	0	17.1	-0.2	60.2	13.3				
e08biosar0205x1	t01	L	PM	12	2 VV	6	0.9	308	0	17.6	-0.6	60.6	13.7	-0.4	-4.2	-1.3	3.6
e08biosar0205x1	t01	L	PM	12	3 HH		0.9	308	20	18.3	-1.1	61.1	13.4				
e08biosar0205x1	t01	L	PM	12	3 VV	8	0.9	308	20	17.5	-0.3	60.3	11.0	0.8	1.7	-1.2	3.1
e08biosar0205x1	t01	L	PM	12	4 HH		1.5	308	10	26.0	-0.1	60.1	19.1				
e08biosar0205x1	t01	L	PM	12	4 VV	10	1.5	308	10	25.9	0.0	60.0	20.3	0.0	-3.1	-1.2	3.8

L-band Pol-InSAR																	
Filename	Filename-Extension	Band	Polarisation	Track	CR Info	Reflector Nr.	CR size [m]	CR azim [deg]	CR elev [deg]	Estimated RCS [dB]	Theory RCS - Estimated RCS [dB]	Calibration Factor [dB]	Signal to Background Ratio [dB]	Amplitude Imbalance [dB]	Phase Imbalance [deg]	Delta Range [pix]	Delta Azimuth [pix]
e08biosar0206x1	t01	L	PM	21	1 HH		5	128	10	44.8	1.8	58.2	34.1				
e08biosar0206x1	t01	L	PM	21	1 VV	4	5	128	10	45.2	1.4	58.6	36.2	-0.4	-11.8	-1.2	3.7
e08biosar0206x1	t01	L	PM	21	2 HH		0.9	128	20	17.9	-1.0	61.0	9.7				
e08biosar0206x1	t01	L	PM	21	2 VV	5	0.9	128	20	17.0	-0.1	60.1	8.7	0.9	4.9	-1.2	3.6
e08biosar0206x1	t01	L	PM	21	3 HH		0.9	128	0	16.9	-0.3	60.3	15.1				
e08biosar0206x1	t01	L	PM	21	3 VV	7	0.9	128	0	16.0	0.6	59.4	11.3	0.9	-1.4	-1.2	3.1
e08biosar0206x1	t01	L	PM	21	4 HH		1.5	128	10	25.7	0.0	60.0	19.2				
e08biosar0206x1	t01	L	PM	21	4 VV	9	1.5	128	10	25.6	0.1	59.9	19.2	0.1	-0.3	-1.3	3.7
e08biosar0207x1	t01	L	PM	13	1 HH		5	308	10	44.8	2.1	57.9	35.5				
e08biosar0207x1	t01	L	PM	13	1 VV	3	5	308	10	44.6	2.3	57.7	37.8	0.2	-10.8	-1.3	3.3
e08biosar0207x1	t01	L	PM	13	2 HH		0.9	308	0	17.0	-0.1	60.1	13.6				
e08biosar0207x1	t01	L	PM	13	2 VV	6	0.9	308	0	17.2	-0.2	60.2	13.6	-0.2	-2.4	-1.2	3.0
e08biosar0207x1	t01	L	PM	13	3 HH		0.9	308	20	18.2	-1.1	61.1	12.7				
e08biosar0207x1	t01	L	PM	13	3 VV	8	0.9	308	20	17.3	-0.1	60.1	10.6	0.9	6.5	-1.5	2.8
e08biosar0207x1	t01	L	PM	13	4 HH		1.5	308	10	25.9	-0.1	60.1	18.8				
e08biosar0207x1	t01	L	PM	13	4 VV	10	1.5	308	10	25.8	0.0	60.0	21.0	0.1	-3.3	-1.2	3.4
e08biosar0208x1	t01	L	PM	22	1 HH		5	128	10	44.8	1.8	58.2	34.8				
e08biosar0208x1	t01	L	PM	22	1 VV	4	5	128	10	45.2	1.4	58.6	36.8	-0.4	-11.4	-1.2	3.6
e08biosar0208x1	t01	L	PM	22	2 HH		0.9	128	20	18.1	-1.2	61.2	9.6				
e08biosar0208x1	t01	L	PM	22	2 VV	5	0.9	128	20	17.4	-0.5	60.5	9.5	0.7	8.4	-1.2	3.4
e08biosar0208x1	t01	L	PM	22	3 HH		0.9	128	0	16.9	-0.2	60.2	16.0				
e08biosar0208x1	t01	L	PM	22	3 VV	7	0.9	128	0	15.5	1.1	58.9	11.1	1.3	0.3	-1.2	3.0
e08biosar0208x1	t01	L	PM	22	4 HH		1.5	128	10	25.6	0.2	59.8	18.5				
e08biosar0208x1	t01	L	PM	22	4 VV	9	1.5	128	10	25.8	-0.1	60.1	19.6	-0.3	-1.5	-1.3	3.6
e08biosar0209x1	t01	L	PM	14	1 HH		5	308	10	44.8	2.1	57.9	35.6				
e08biosar0209x1	t01	L	PM	14	1 VV	3	5	308	10	44.7	2.2	57.8	37.6	0.1	-10.8	-1.3	3.5
e08biosar0209x1	t01	L	PM	14	2 HH		0.9	308	0	16.9	0.0	60.0	13.3				
e08biosar0209x1	t01	L	PM	14	2 VV	6	0.9	308	0	17.3	-0.4	60.4	13.0	-0.4	-1.3	-1.2	3.3
e08biosar0209x1	t01	L	PM	14	3 HH		0.9	308	20	18.4	-1.3	61.3	12.5				
e08biosar0209x1	t01	L	PM	14	3 VV	8	0.9	308	20	17.7	-0.5	60.5	10.0	0.7	5.6	-1.4	2.9
e08biosar0209x1	t01	L	PM	14	4 HH		1.5	308	10	25.9	-0.1	60.1	18.7				
e08biosar0209x1	t01	L	PM	14	4 VV	10	1.5	308	10	25.3	0.5	59.5	21.2	0.6	-1.0	-1.3	3.8

L-band Pol-InSAR																	
Filename	Filename-Extension	Band	Polarisation	Track	CR Info	Reflector Nr.	CR size [m]	CR azim [deg]	CR elev [deg]	Estimated RCS [dB]	Theory RCS - Estimated RCS [dB]	Calibration Factor [dB]	Signal to Background Ratio [dB]	Amplitude Imbalance [dB]	Phase Imbalance [deg]	Delta Range [pix]	Delta Azimuth [pix]
e08biosar0210x1	t01	L	PM	23	1 HH		5	128	10	45.0	1.6	58.4	34.9				
e08biosar0210x1	t01	L	PM	23	1 VV	4	5	128	10	45.5	1.1	58.9	36.6	-0.5	-11.6	-1.2	3.6
e08biosar0210x1	t01	L	PM	23	2 HH		0.9	128	20	18.4	-1.5	61.5	9.3				
e08biosar0210x1	t01	L	PM	23	2 VV	5	0.9	128	20	17.8	-0.8	60.8	9.8	0.6	6.6	-1.2	3.4
e08biosar0210x1	t01	L	PM	23	3 HH		0.9	128	0	16.8	-0.2	60.2	16.7				
e08biosar0210x1	t01	L	PM	23	3 VV	7	0.9	128	0	15.9	0.7	59.3	11.2	0.9	0.1	-1.2	2.9
e08biosar0210x1	t01	L	PM	23	4 HH		1.5	128	10	25.8	-0.1	60.1	18.5				
e08biosar0210x1	t01	L	PM	23	4 VV	9	1.5	128	10	25.6	0.2	59.8	19.4	0.2	1.4	-1.3	3.5
e08biosar0211x1	t01	L	PM	15	1 HH		5	308	10	44.7	2.2	57.8	35.8				
e08biosar0211x1	t01	L	PM	15	1 VV	3	5	308	10	44.8	2.1	57.9	37.1	-0.1	-13.4	-1.3	3.6
e08biosar0211x1	t01	L	PM	15	2 HH		0.9	308	0	16.7	0.3	59.7	13.4				
e08biosar0211x1	t01	L	PM	15	2 VV	6	0.9	308	0	17.6	-0.6	60.6	14.0	-0.9	-6.0	-1.1	3.4
e08biosar0211x1	t01	L	PM	15	3 HH		0.9	308	20	18.4	-1.3	61.3	12.0				
e08biosar0211x1	t01	L	PM	15	3 VV	8	0.9	308	20	18.4	-1.3	61.3	10.1	0.0	3.4	-1.5	3.2
e08biosar0211x1	t01	L	PM	15	4 HH		1.5	308	10	25.9	0.0	60.0	18.8				
e08biosar0211x1	t01	L	PM	15	4 VV	10	1.5	308	10	25.5	0.3	59.7	20.6	0.3	-2.4	-1.2	3.7
e08biosar0212x1	t01	L	PM	24	1 HH		5	128	10	44.7	1.9	58.1	35.4				
e08biosar0212x1	t01	L	PM	24	1 VV	4	5	128	10	45.6	1.0	59.0	37.0	-0.9	-13.2	-1.3	3.3
e08biosar0212x1	t01	L	PM	24	2 HH		0.9	128	20	17.8	-0.9	60.9	5.6				
e08biosar0212x1	t01	L	PM	24	2 VV	5	0.9	128	20	18.5	-1.6	61.6	7.7	-0.7	8.9	-1.3	3.1
e08biosar0212x1	t01	L	PM	24	3 HH		0.9	128	0	16.8	-0.1	60.1	17.6				
e08biosar0212x1	t01	L	PM	24	3 VV	7	0.9	128	0	15.9	0.7	59.3	12.4	0.8	-1.6	-1.2	2.6
e08biosar0212x1	t01	L	PM	24	4 HH		1.5	128	10	25.7	0.1	59.9	18.3				
e08biosar0212x1	t01	L	PM	24	4 VV	9	1.5	128	10	25.4	0.4	59.6	19.0	0.3	2.2	-1.2	3.3
e08biosar0214x1	t01	L	PM	25	1 HH		5	128	10	44.7	2.0	58.0	34.9				
e08biosar0214x1	t01	L	PM	25	1 VV	4	5	128	10	45.8	0.9	59.1	36.6	-1.1	-13.9	-1.2	3.7
e08biosar0214x1	t01	L	PM	25	2 HH		0.9	128	20	18.1	-1.2	61.2	9.4				
e08biosar0214x1	t01	L	PM	25	2 VV	5	0.9	128	20	18.8	-1.8	61.8	10.7	-0.6	5.5	-1.2	3.6
e08biosar0214x1	t01	L	PM	25	3 HH		0.9	128	0	16.6	0.0	60.0	14.9				
e08biosar0214x1	t01	L	PM	25	3 VV	7	0.9	128	0	16.1	0.5	59.5	10.7	0.5	-1.7	-1.2	3.0
e08biosar0214x1	t01	L	PM	25	4 HH		1.5	128	10	25.6	0.2	59.8	18.3				
e08biosar0214x1	t01	L	PM	25	4 VV	9	1.5	128	10	25.9	-0.2	60.2	19.2	-0.4	-0.8	-1.3	3.7

X-Band XTI																	
Filename	Filename-Extension	Band	Polarisation	Track	CR Info	Reflector Nr.	CR size [m]	CR azim [deg]	CR elev [deg]	Estimated RCS [dB]	Theory RCS - Estimated RCS [dB]	Calibration Factor [dB]	Signal to Background Ratio [dB]	Amplitude Imbalance [dB]	Phase Imbalance [deg]	Delta Range [pix]	Delta Azimuth [pix]
e08biosar0405x1	t01	X	VV	3	2 ch1		0.9	308	20	32.0	2.4	57.6	30.7				
e08biosar0405x1	t01	X	VV	3	2 ch2	5	0.9	308	20	32.4	2.1	57.9	31.3	-0.4	4.7	-0.8	1.5
e08biosar0405x1	t01	X	VV	3	3 ch1		0.9	308	0	35.1	-0.8	60.8	35.1				
e08biosar0405x1	t01	X	VV	3	3 ch2	7	0.9	308	0	35.3	-1.0	61.0	35.7	-0.2	84.3	-1.0	1.4
e08biosar0405x1	t01	X	VV	3	4 ch1		1.5	308	10	43.3	0.0	60.0	38.0				
e08biosar0405x1	t01	X	VV	3	4 ch2	9	1.5	308	10	43.1	0.2	59.8	38.4	0.3	28.5	-0.9	0.6

PoISAR																	
Filename	Filename-Extension	Band	Polarisation	Track	CR Info	Reflector Nr.	CR size [m]	CR azim [deg]	CR elev [deg]	Estimated RCS [dB]	Theory RCS - Estimated RCS [dB]	Calibration Factor [dB]	Signal to Background Ratio [dB]	Amplitude Imbalance [dB]	Phase Imbalance [deg]	Delta Range [pix]	Delta Azimuth [pix]
e08biosar0301x1	t02	P	PM	10	1 HH		5	352	10	34.8	0.6	59.4	33.2				
e08biosar0301x1	t02	P	PM	10	1 VV	1	5	352	10	34.4	1.0	59.0	29.1	0.4	7.1	0.1	-2.9
e08biosar0302x1	t02	P	PM	20	1 HH		5	308	10	33.4	2.0	58.0	27.9				
e08biosar0302x1	t02	P	PM	20	1 VV	3	5	308	10	34.2	1.1	58.9	27.0	-0.8	6.8	0.1	-3.1
e08biosar0303x1	t02	P	PM	30	1 HH		5	128	10	34.7	0.6	59.4	26.9				
e08biosar0303x1	t02	P	PM	30	1 VV	4	5	128	10	34.7	0.7	59.3	25.4	0.0	9.1	0.0	-3.3
e08biosar0304x1	t02	P	PM	40	1 HH		5	37	10	34.9	0.6	59.4	34.4				
e08biosar0304x1	t02	P	PM	40	1 VV	2	5	37	10	35.1	0.4	59.6	30.9	-0.2	16.9	0.1	-2.2
e08biosar0305x1	t02	P	PM	30	1 HH		5	128	10	34.7	0.7	59.3	26.5				
e08biosar0305x1	t02	P	PM	30	1 VV	4	5	128	10	34.6	0.8	59.2	25.4	0.1	8.2	0.0	-2.9
e08biosar0401x1	t02	L	PM	10	1 HH		5	352	10	43.8	3.0	57.0	42.4				
e08biosar0401x1	t02	L	PM	10	1 VV	1	5	352	10	44.1	2.8	57.2	41.7	-0.3	-16.2	-2.2	3.4
e08biosar0402x1	t02	L	PM	20	1 HH		5	308	10	44.1	2.7	57.3	36.2				
e08biosar0402x1	t02	L	PM	20	1 VV	3	5	308	10	44.3	2.6	57.4	36.7	-0.1	-18.4	-2.2	2.7
e08biosar0402x1	t02	L	PM	20	2 HH		0.9	308	0	17.4	-0.3	60.3	16.1				
e08biosar0402x1	t02	L	PM	20	2 VV	6	0.9	308	0	18.5	-1.5	61.5	15.2	-1.1	-14.7	-2.4	2.1
e08biosar0402x1	t02	L	PM	20	3 HH		0.9	308	20	16.8	0.2	59.8	18.1				
e08biosar0402x1	t02	L	PM	20	3 VV	8	0.9	308	20	17.2	-0.2	60.2	13.6	-0.4	-1.6	-2.4	2.5
e08biosar0403x1	t02	L	PM	30	1 HH		5	128	10	43.5	3.3	56.7	35.9				
e08biosar0403x1	t02	L	PM	30	1 VV	4	5	128	10	44.6	2.1	57.9	36.8	-1.1	-22.2	-2.6	2.8
e08biosar0403x1	t02	L	PM	30	2 HH		0.9	128	20	15.1	1.9	58.1	7.4				
e08biosar0403x1	t02	L	PM	30	2 VV	5	0.9	128	20	15.9	1.1	58.9	9.0	-0.8	-4.2	-3.0	3.1
e08biosar0403x1	t02	L	PM	30	3 HH		0.9	128	0	16.1	0.7	59.3	21.0				
e08biosar0403x1	t02	L	PM	30	3 VV	7	0.9	128	0	16.1	0.8	59.2	16.5	0.0	-18.8	-2.5	2.7
e08biosar0404x1	t02	L	PM	40	1 HH		5	37	10	43.6	3.3	56.7	42.5				
e08biosar0404x1	t02	L	PM	40	1 VV	2	5	37	10	43.5	3.3	56.7	39.6	0.0	-2.4	-2.4	2.7

7.4 Conclusion

In the following the SAR data quality is summarised for different frequencies.

P-band: In P-band, both types of reflectors (5m mesh reflectors and 1.5m aluminium plate reflectors) deliver a relatively stable backscattered signal. The differences in the backscatter intensity, as well as the intensity differences between hh and vv polarisation and for the single passes lie in the range of about 1dB, which is within specification.

The data of the large test area t01 show a slight dependence of the look direction. The data with look direction North-East (0104, 0106, 1018, 1010, 0112) have a slightly lower backscatter of the reflectors (about 0.5dB). This could be due to incorrect mounting of the reflectors, different squint angles, or a slight deformation of the reflectors CR04 and CR7A.

The amplitude imbalance between hh and vv polarisations is nearly everywhere below 1dB. The phase imbalance is below 10° for the 5m reflectors and in the range of 30°-40° for the 1.5m reflectors. Since the 1.5m reflectors are small for P-band the large phase imbalance is not trusted and these reflectors should not be used for a polarimetric calibration. Imbalances of below 12° are within specification for E-SAR.

The difference of the corner reflector positions in the SLC data from their expected values is mostly below 1 pixel in range and 5 pixel in azimuth. The larger values encountered for the 1.5m corner reflectors in the data sets 0108 and 0112 should not be trusted. They are due to short raw data where alignment to the master was not possible at raw data level (no impact on interferometric co-registration). The reflector is at the margin of the data set and automatic tiepoint location failed.

Any minor pixel shift from measured to nominal positions in the RGI product has no effect in the GTC product as those shifts are corrected in the geocoding process.

L-band: The behaviour of the corner reflector signals in L-band is ambiguous at first impression. In BIOSAR 2007 it was shown that good calibration results can be obtained in both L- and P-band using the 5m reflectors. In BIOSAR 2008 the processing shows a loss of 2dB in the backscatter of the 5m reflectors, while the 1.5m and 90cm reflectors showed normal values.

An idea to explain the different behaviour in 2007 and 2008 was that in 2008 all reflectors had a pure mesh surface whereas in 2007 three of four reflectors were lined with aluminium plates. On the other hand, in 2007 no difference in between the lined corner reflectors and the mesh reflector could be found. The only explanation for the 2dB loss at the 5m reflectors in 2008 could be therefore the possibility of a deformation of the reflectors in 2008. During mounting and deinstallation one has to step inside the reflector and the mesh is partially not planar any more. For a better understanding, the next time when the 5m reflectors are used for L-band, it is suggested to mount two reflectors (one mesh and one lined with aluminium plate) with the same azimuth and elevation angles not far from each other, together with a well calibrated 1,5m aluminium plate reflector.

The amplitude imbalance is nearly everywhere below 1dB, while the phase imbalance is in the range of about 5° for the small 1,5m and 90cm reflectors and about 15° for the 5m reflectors. The difference of the corner reflector position in the SLC data is about 1-2 pixels in range and about 3-4 pixels in azimuth.

X-band: In X-band the signature of the 5m reflectors has not been used. The mesh of these reflectors is too wide for specular reflection of X-band and delivers a signal which is about 30dB too low. The backscatter of the 1.5m and 90cm reflectors increases in range direction. This increase from 57-58dB in near range to about 60dB at around 50° look angle has also been observed in the calibration campaigns.

At look angles of more than 50° a decrease in the backscatter is observed at the calibration campaigns. At BIOSAR 2008 this decrease could not be found.

The amplitude imbalance between the two interferometric channels is near to 0dB while the phase difference between the two XTI channels can be 0°-360°. The difference of the corner reflector positions in the SLC data from their expected values is about 1 pixel in range and 1 pixel in azimuth.

E-SAR XTI data uses antennas with narrow aperture angle, compared to L- and P-band. Therefore the radiometric accuracy is reduced in this mode.

7.4.1 E-SAR data performance summary

The data quality analysis performed with the BIOSAR 2008 campaign data confirmed the expected performance of the E-SAR data products in terms of absolute and relative radiometric accuracy, polarimetric calibration performance, interferometric phase as well as location accuracy. Analysis of the radar-cross-section (RCS) of the deployed trihedrals confirms that the absolute radiometric accuracy of BIOSAR 2008 data is comparable to the BIOSAR data acquired in 2007 over Remningstorp.

The performance parameters are summarized in the table below:

Parameter	Accuracy	Remark
Absolute radiometric accuracy	+/- 1.0 dB	except X-band
Relative radiometric accuracy	+/- 0.5 dB	within flight period over the swath(*)
Co-polar amplitude imbalance	+/- 1.0 dB	Absolute within one scene
Co-polar phase	+/- 15 deg (+/- 5 deg)	absolute (within one scene)
Relative interferometric phase	< 10 deg	along azimuth (**)
Absolute horizontal location accuracy of geocoded data	+/- 2 m	assuming similar DEM accuracy; confirmed on CR locations

(*) The good performance benefits also from the INDREX-II campaign data (acquired by E-SAR in 2004), where homogeneous rain forest data was used to evaluate uncertainties in the radiometric calibration of the antenna elevation patterns (which originate mainly from the influence of the antenna fuselage). This analysis improved the relative radiometric accuracy over the swath.

(**) The accuracy of the relative interferometric phase along azimuth is achieved by the use of sophisticated residual motion error estimation and compensation approaches, which improve the solution of the integrated INS/GPS data in a relative sense between master and slaves. Absolute interferometric phase calibration has been attempted for the first time in BIOSAR 2008 using a newly developed approach based on detection of coherent scatterers and using the external DEM. For each repeat-pass interferometric data set, a phase correction matrix is provided. The approach and the use of the phase correction are described in the data analysis report of this project.

Note that absolute interferometric phase calibration is subject of present research and development and generally NOT performed for E-SAR repeat-pass interferometric data.

8 BIOSAR DATA BASE

The radar data in form of RGI and GTC products have been archived in DLRs DIMS (Data Information and Management System) and are available for the project partners via EOWEB, DLRs Internet portal for earth observation data. With a login and a password data can be downloaded by each participating institution.

The screenshot shows the EOWEB portal interface. On the left, there are navigation options like 'Catalogue', 'UserSet', and 'ShopCart'. Below that, 'Collections' are listed with checkboxes for 'Airborne Radar Sensor (AIRRS)', 'Experimental SAR (E-SAR)', and 'Geocoded and Terrain Corrected (GTC) Radar Geometry Images (RGI)'. A 'Query Mode' dropdown is set to 'Standard'. The 'Date' section has a date range from 2008-03-27 00:00:00 to 2009-03-27 23:59:59. The 'Area' section shows a 'Rectangle' search area with center coordinates (63.464, 18.524) and extension (21.540, 40.866). A 'Start Search' button is visible. The main area features a map with a grid and a red rectangle highlighting a search area. Below the map is a table with 11 columns: 'Id#', 'Abstract', 'Product Type', and 'Start Date'. The table contains 11 rows of search results for 'Radar Geometry Images BIOSAR SVARTBERGET' with various IDs and start dates. At the bottom, the status bar shows 'Latitude 64.306 Longitude 20.057' and 'Vertrauenswürdige Sites'.

The DLR's EOWEB portal for BIOSAR radar data downloads

9 BIOSAR DATA ANALYSIS

9.1 Assessment of forest biomass retrieval by FOI

9.1.1 Relation between Backscatter and Biomass

This section reports on standwise P- and L-band backscatter versus above-ground biomass from in-situ data. A total of 31 stands, varying in size from 2.4 to 26.3 ha, were defined to achieve geographic distribution across the imaged area and stratification with respect to biomass and surface slope classes. Approximately ten sampling plots (10 m radius) were laid out in each stand. For all trees (dbh > 4 cm) in each plot, diameter was measured and species determined. Tree height was measured on randomly selected sample trees and, on average, 1.5 sample trees were selected per plot. Additional variables were also collected, e.g. site index, vegetation type and soil type, and also previous treatments were noted (such as thinning). Height, volume and biomass for each tree as well as standwise estimates were computed using the Heureka system. See Section 3.2.3, for more details concerning the in-situ measurements and the Heureka system.

Standwise backscatter was determined based on SAR images, a high-resolution DEM, and the stand boundary polygons using the methodology described in Appendix 12. The results are also summarised in Appendix 12 in the form of one table for each flight track. All stands are included in all tables even if all stands are not covered. The backscatter is given for all linear polarization configurations (HH, VV, HV, VH) and in terms of the three parameters, i.e. β° , σ° and γ° . The latter represent different stages of processing, i.e. β° is the average radar-cross section per unit area in radar coordinates (azimuth x slant range), σ° is the average radar-cross section per unit ground-projected area (azimuth x ground range). γ° is obtained as σ° but with an additional normalisation to compensate for the increased path length through a constant-thickness layer as the incidence angle increases. γ° is often used in analysis of vegetation backscatter since it, to first order, compensates for incidence angle dependence.

The results for γ° versus in-situ biomass are given in Figures 9.1-9.3. Each point corresponds to the average backscattering coefficient for a single stand and one flight track. Results for both P- and L-band are given. Note that in total six different track headings were used in the flights and that the variability observed can be caused by temporal variations (e.g. soil moisture) or geometrical effects (e.g. local incidence angle).

Results for HV-polarisation are shown in Figure 9.1. In general, γ° increases with biomass for both PHV and LHV although there is a large spread in the data. It is noted that the total dynamic range of all backscatter values is largest for L-band (7 dB) compared to P-band (5 dB). The backscatter range is different for different biomass levels, particularly in P-band. The PHV backscatter range is 3-4 dB below 120 tons/ha, but only 1-2 dB above 120 tons/ha. A similar result seems to hold true at L-band, although less clear, with about 5 dB range below 120 tons/ha and about 3 dB above 120 tons/ha.

Results for HH-polarisation are shown in Figure 9.2. The results are here the opposite compared to HV-polarization, i.e. the total dynamic range for L-band (7 dB) is much less than for P-band (12 dB). The backscatter range is larger for both P- and L-band compared to HV-polarization. Just like HV-polarization, there is a general trend that the backscatter increases with biomass but with a large spread.

Results for VV-polarisation are finally shown in Figure 9.3. The dynamic range for L-band (7 dB) is about the same as for P-band (6 dB). It is noted that there is a general trend of increasing backscatter for higher biomass in L-band, but not in P-band.

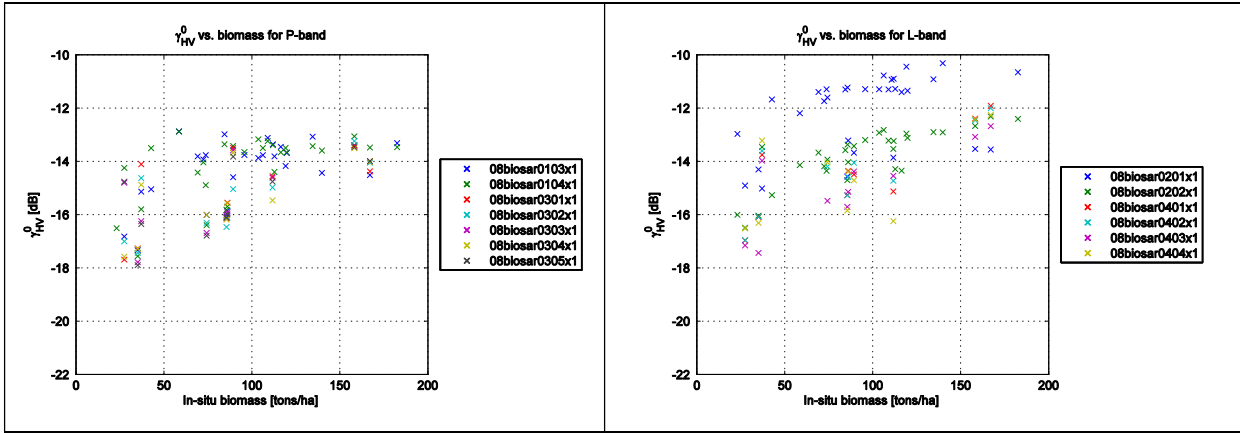


Figure 9.1. HV-polarized P-band (left) and L-band (right) data vs. in-situ biomass for all image scenes.

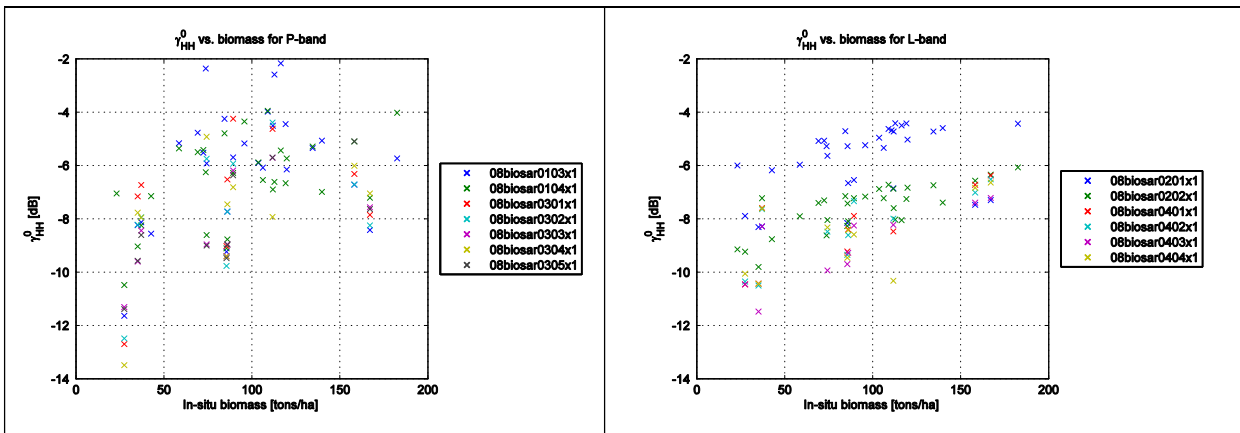


Figure 9.2. HH-polarized P-band (left) and L-band (right) data vs. in-situ biomass for all image scenes.

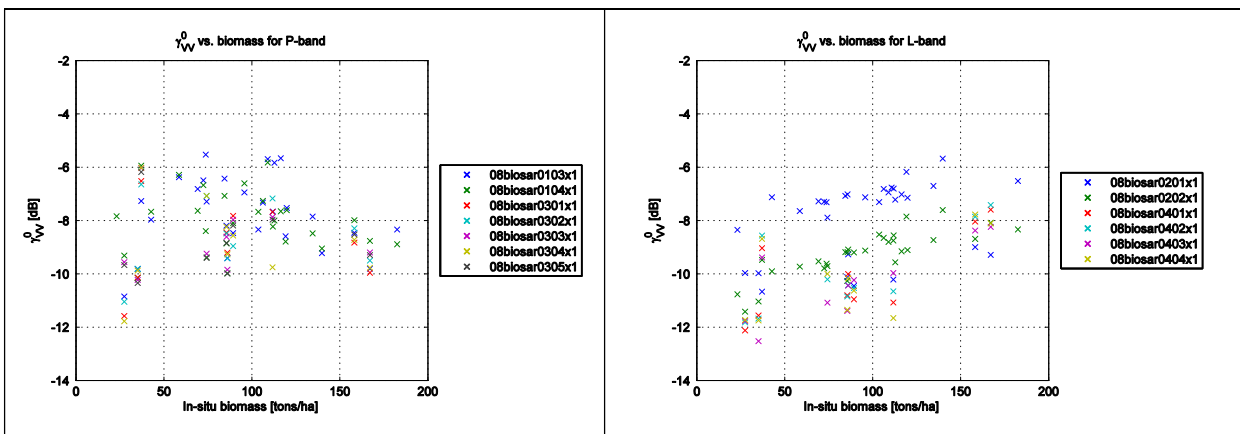


Figure 9.3. VV-polarized P-band (left) and L-band (right) data vs. in-situ biomass for all image scenes.

The results indicate that the variation of backscattering coefficient for a single stand imaged from different geometries can be rather large. The variability depends strongly on the frequency band and polarization, however, with the smallest variation observed for PHV and the largest for PHH.

The variability is attributed to mainly topographic effects but could also be due to temporal effects such as moisture variations. Stand structure characteristics could also contribute to the variability, e.g. aligned tree positions or preferred branch orientations, but this effect is considered less likely and the ground data does not support such an explanation.

Based on the results and conclusions from this section, we will further analyze the observed backscatter variability in the next section.

9.1.2 Impact of Topography on SAR Backscatter Intensity

In order to assess the impact of topography on the backscattering coefficient, between-scene variations in backscatter on stand level was investigated. For stands with sloping terrain, this provides a measure of the impact of topography since the different scenes have different viewing directions. As a measure of the backscatter variability between scenes the range of backscatter for a single stand was used. The range (R) of a quantity x is here defined as $R(x) = \max(x[dB]) - \min(x[dB])$, where the values for x are stand averages for the available image scenes.

In Figures 9.4-9.6, the range of stand-averaged backscatter (where the backscatter is defined as y^0) is plotted against the surface slope angle, i.e. stand-averaged surface slope based on least-squares fitting of planes over 50 m x 50 m pixel-centred DEM sliding blocks. We note that most of the stands have a stand-averaged surface slope angle of 5° with a few areas extending up to a maximum of 14°.

The results clearly show that PHV stands out compared to the other combinations of frequency band and polarization. That is, the observed range of backscatter for a single stand is, in general, less for PHV than any of the other combinations. Except for a few outliers, the backscatter range is observed to be less than 1.5 dB for PHV, compared to 3-4 dB for all other combinations.

The largest range of PHV backscatter is 3.5 dB but it corresponds to the stand with the absolute highest slope of 14°. As we will see below, this stand also has a very low biomass of about 30 tons/ha.

It is noteworthy that there is only weak dependency between the backscatter range and stand-averaged surface slope. This observation may seem to be in conflict with the statement that the backscatter variability is mainly attributed to topographic effects. However, it should be noted that the stand-averaged surface slope does not capture the small-scale topographic variations which is a major effect in modulating the double-bounce scattering terms as shown in [1].

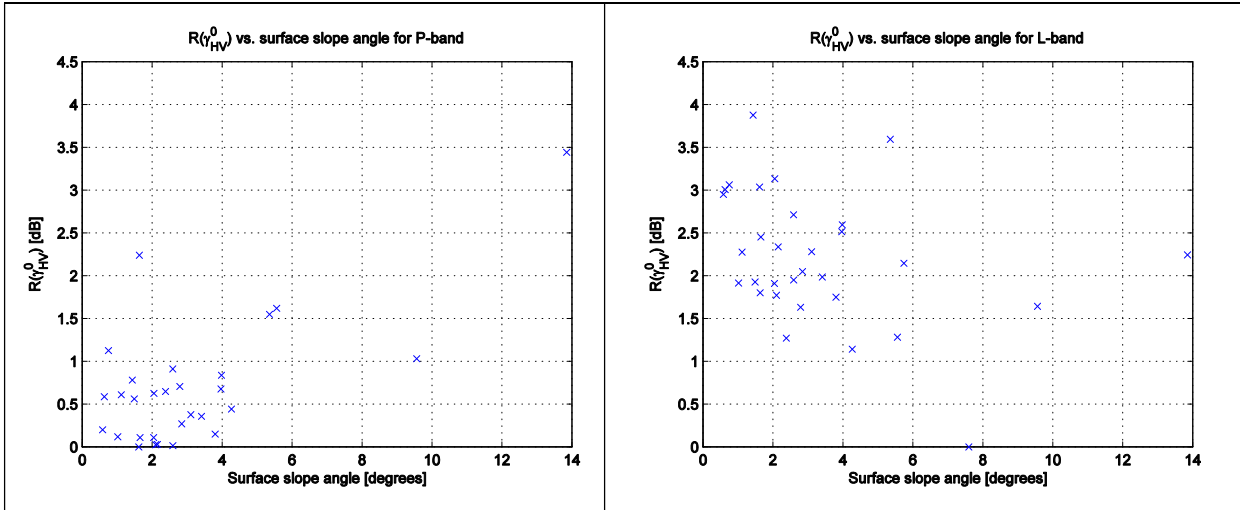


Figure 9.4. Range of backscatter vs. surface slope angle for HV-polarized P-band (left) and L-band (right) data. Each data point corresponds to a single stand and R is the observed range (max [dB] – min [dB]) of stand-averaged backscatter.

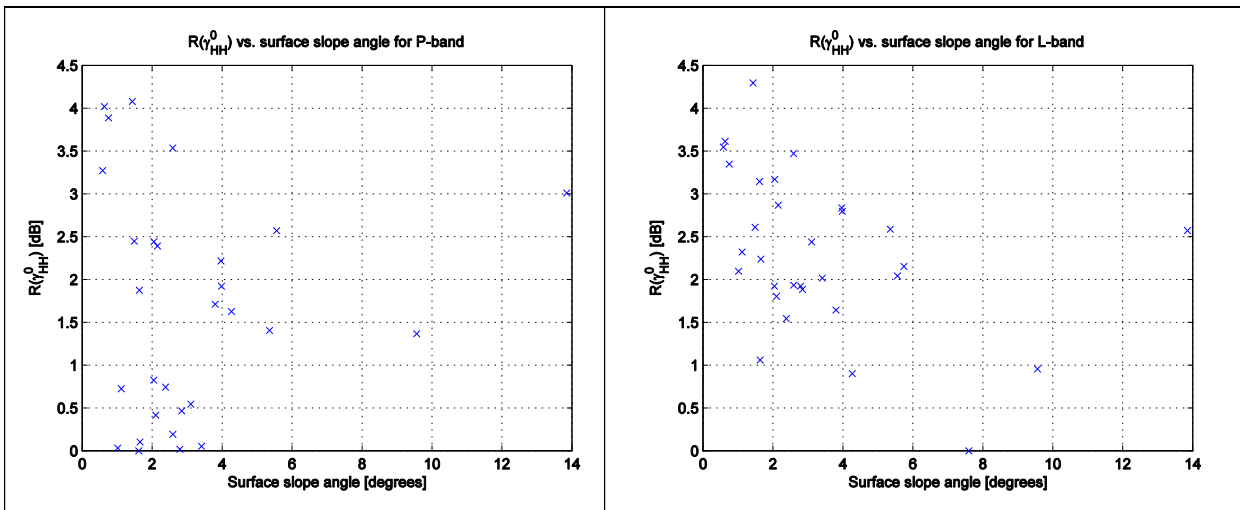


Figure 9.5. Range of backscatter vs. surface slope angle for HH-polarized P-band (left) and L-band (right) data. Each data point corresponds to a single stand and R is the observed range (max [dB] – min [dB]) of stand-averaged backscatter.

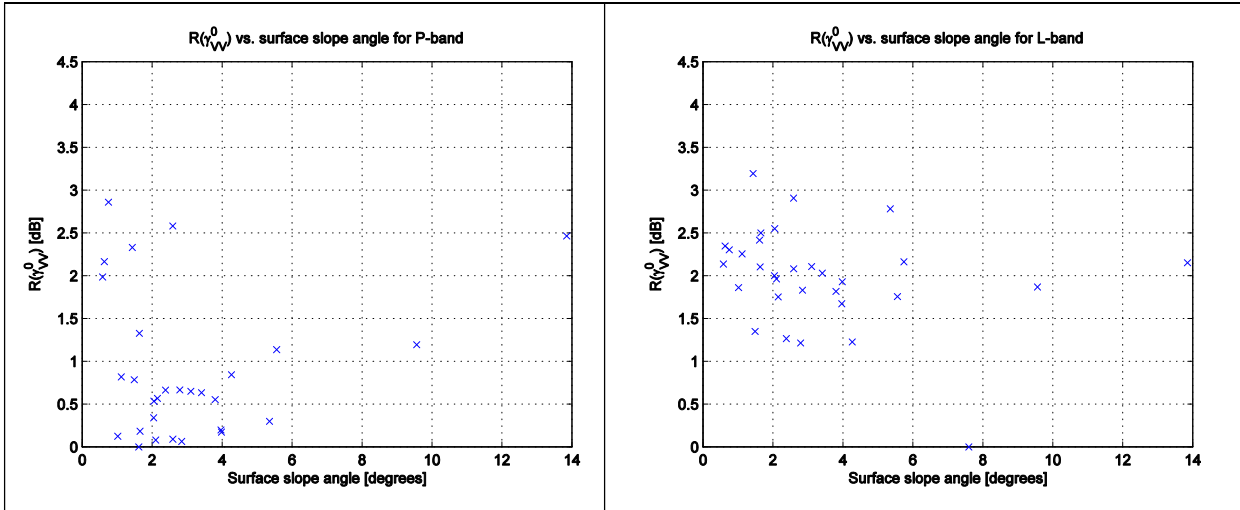


Figure 9.6. Range of backscatter vs. surface slope angle for VV-polarized P-band (left) and L-band (right) data. Each data point corresponds to a single stand and R is the observed range (max [dB] – min [dB]) of stand-averaged backscatter.

The next set of figures, Figures 9.7-9.10, show the backscatter range against *in-situ* biomass. Again, the results show that the observed range of backscatter for a single stand is, in general, less for PHV than any of the other combinations. Furthermore, they show that the two highest values of PHV backscatter range is observed for the stands which have a biomass less than 40 tons/ha, i.e., very low biomass. The other frequency and polarization combinations show a large variability.

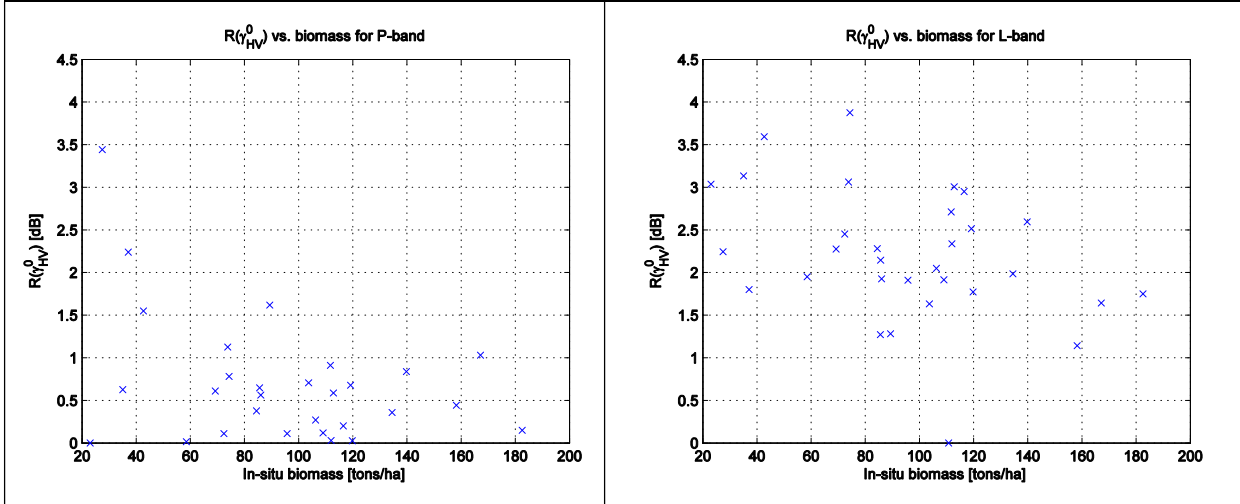


Figure 9.7. Range of backscatter vs. *in-situ* biomass for HV-polarized P-band (left) and L-band (right) data.

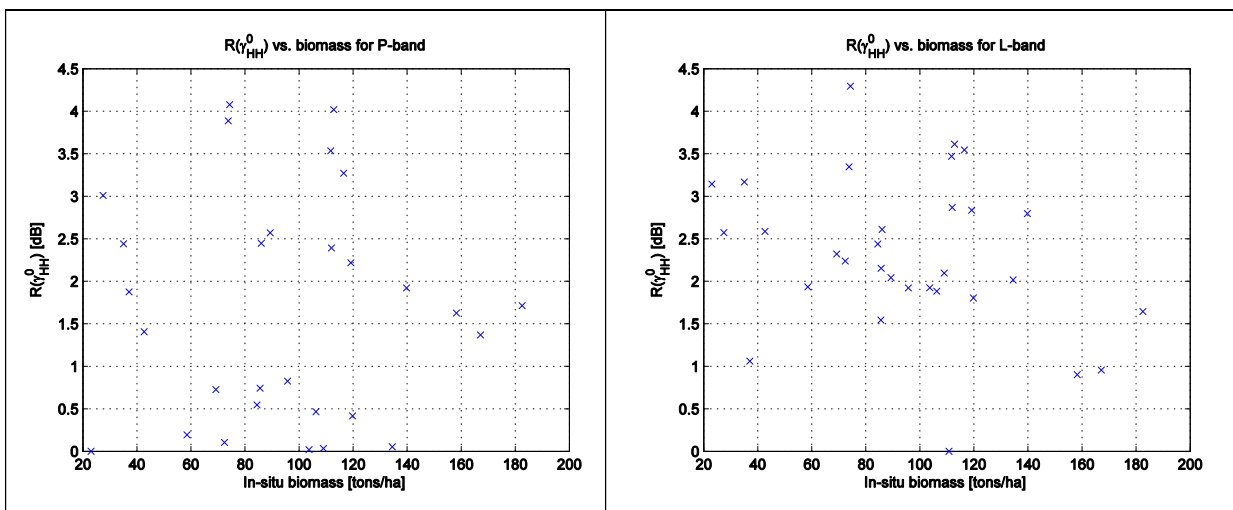


Figure 9.8. Range of backscatter vs. in-situ biomass for HH-polarized P-band (left) and L-band (right) data.

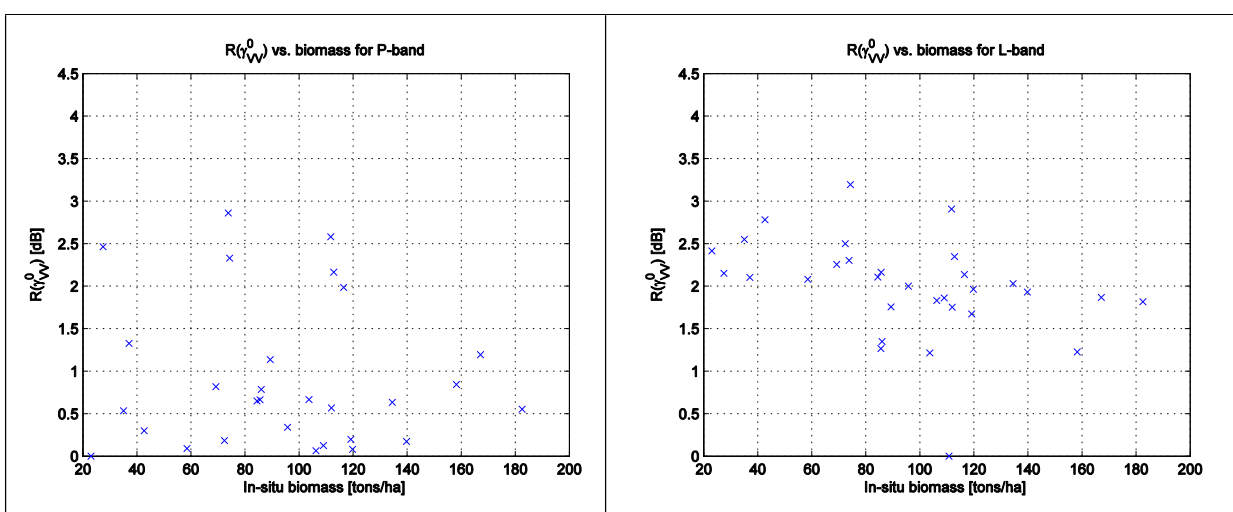


Figure 9.10. Range of backscatter vs. in-situ biomass for VV-polarized P-band (left) and L-band (right) data.

The final set of figures, Figures 9.11-9.13, show the backscatter range against range of local incidence angle. That is, range of local incidence angle for a single stand and for all imaging geometries. These plots show a clear dependence for all polarization combination at P-band and the range of local incidence angle. A large range of local incidence angle in general implies that the P-band backscatter range increases. PHV and PVV shows less than 1.5 dB backscatter range when the local incidence angle range is less than about 15°, whereas PHH shows a larger backscatter range up to 2.5 dB. Based on these results, we conclude that the local incidence angle has a major effect on the P-band backscatter. At L-band, however, there is no clear corresponding dependence on local incidence angle.

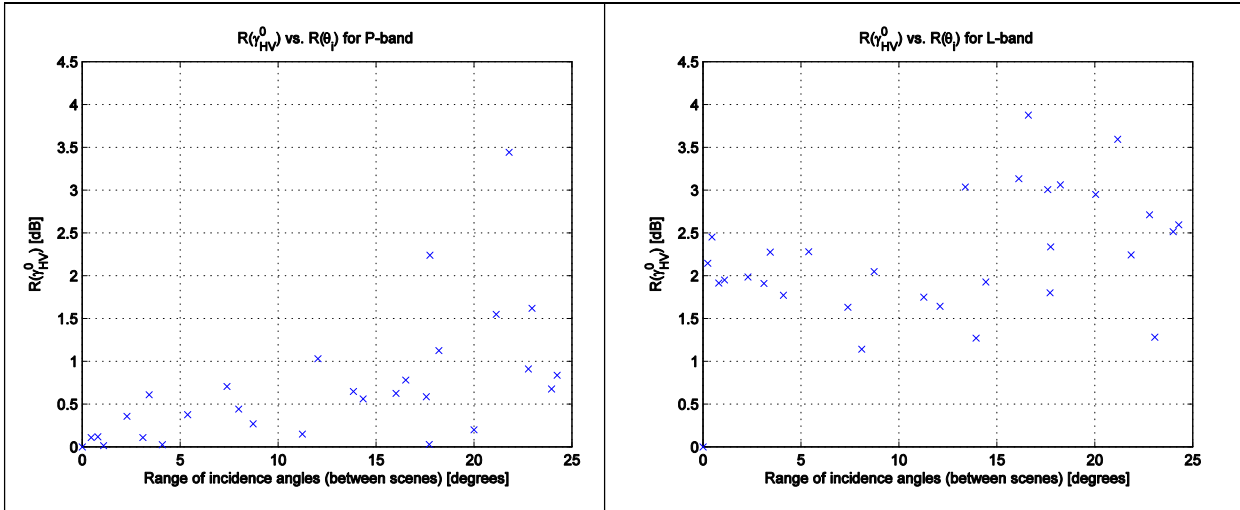


Figure 9.11. Range of backscatter vs. range of local incidence angles for HV-polarized P-band (left) and L-band (right) data.

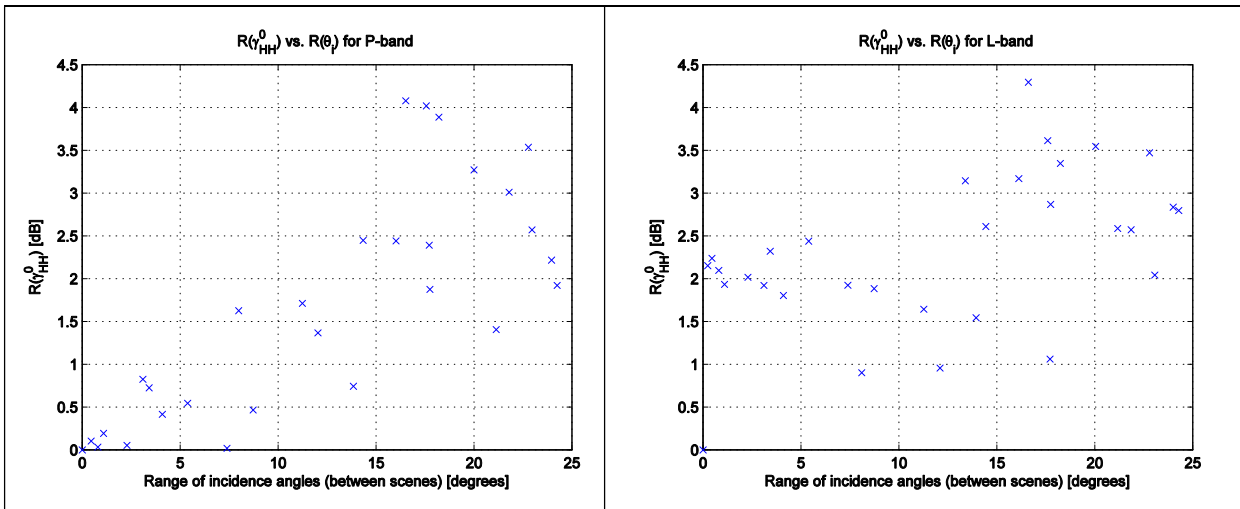


Figure 9.12. Range of backscatter vs. range of local incidence angles for HH-polarized P-band (left) and L-band (right) data.

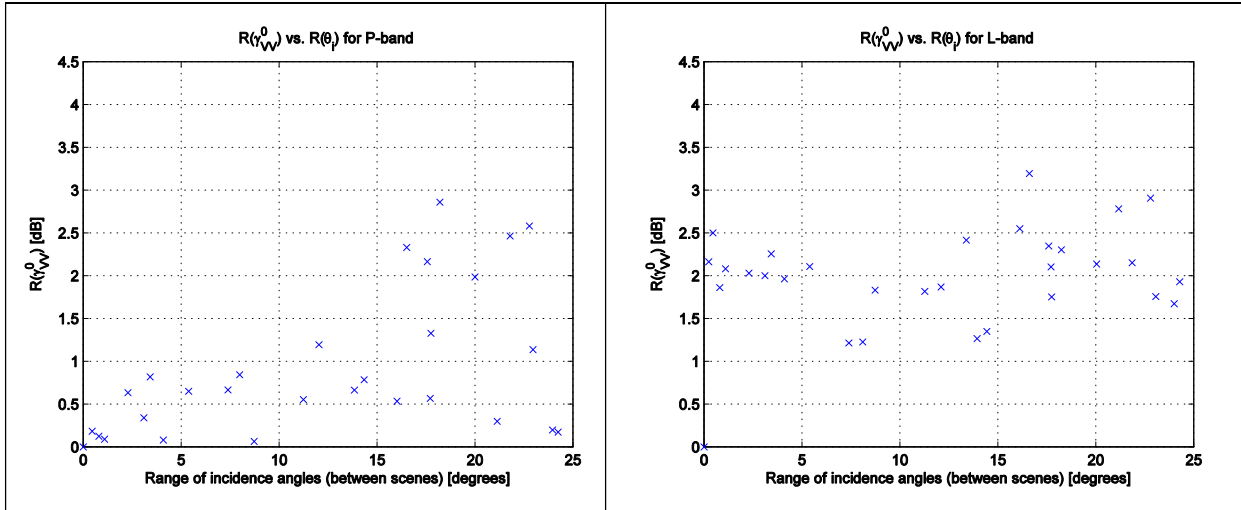


Figure 9.13. Range of backscatter vs. range of local incidence angles for VV-polarized P-band (left) and L-band (right) data.

9.1.3 Evaluation of the Saatchi inversion model

The methodology described in [2] has been used to estimate above-ground biomass. The methodology splits the inversion into two parts, i.e. estimation of the stem contribution (W_s) and estimation of the crown contribution (W_c) to the above-ground biomass. The regression functions presented in [2] are:

$$\begin{aligned} \log W_c = & a_0 + a_1 \sigma_{HV}^0 \cos(\theta_0 - \theta_i) + a_2 (\sigma_{HV}^0 \cos(\theta_0 - \theta_i))^2 \\ & + b_1 \sigma_{HH}^0 \sin(\theta_0 - \theta_i) + b_2 (\sigma_{HH}^0 \sin(\theta_0 - \theta_i))^2 \quad (\text{Eq. 9.1}) \\ & + c_1 \sigma_{HV}^0 \cos(\theta_0 - \theta_i) + c_2 (\sigma_{HV}^0 \cos(\theta_0 - \theta_i))^2 \end{aligned}$$

$$\begin{aligned} \log W_s = & a_0 + a_1 \sigma_{HV}^0 \sin(\theta_0 - \theta_i) + a_2 (\sigma_{HV}^0 \sin(\theta_0 - \theta_i))^2 \\ & + b_1 \sigma_{HH}^0 \cos(\theta_0 - \theta_i) + b_2 (\sigma_{HH}^0 \cos(\theta_0 - \theta_i))^2 \quad (\text{Eq. 9.2}) \\ & + c_1 \sigma_{HV}^0 \cos(\theta_0 - \theta_i) + c_2 (\sigma_{HV}^0 \cos(\theta_0 - \theta_i))^2 \end{aligned}$$

θ_0 and θ_i are incidence angles and local incidence angles, respectively. The regression coefficients for the equations above were estimated for both L- and P-band data using data from the 31 stands with *in-situ* measurements (available in tables in this report). Data from all available scenes were pooled into a single data set, i.e. multiple backscatter measurements (including correction for topography) were used for each stand. Only stands completely covered by radar data were used, giving about 100 measurement points for each frequency. Estimates of crown and stem biomass were then calculated using the estimated regression coefficients, including a correction factor to remove logarithmic bias. Total biomass estimates were then obtained by summing the stem and crown biomass. Results are presented in Figure 9.14 and Figure 9.15 for L- and P-band data, respectively. The estimated RMSE (including all scenes) was 35 tons/ha for L-band and 29 tons/ha for P-band, when using the same data for training as for validation.

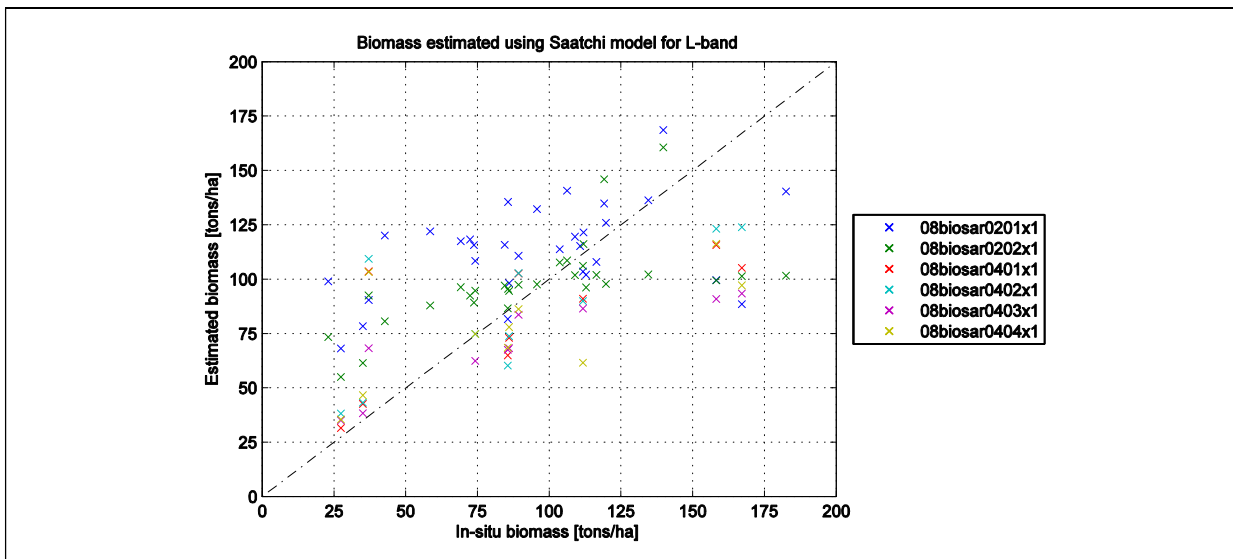


Figure 9.14. Results from estimating total (canopy + stem) biomass based on L-band data including all linear polarizations (HH, VV, HV) as well as ground surface slope from a DEM. Regression coefficients were estimated using all available (geocoded) L-band data.

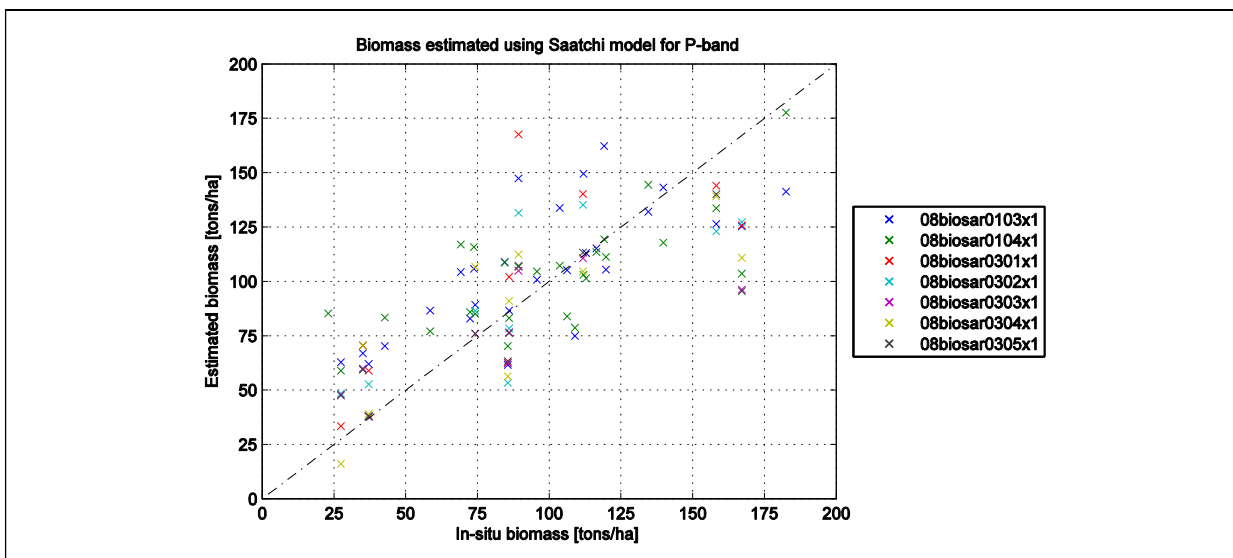


Figure 9.15. Results from estimating total (canopy + stem) biomass based on P-band data including all linear polarizations (HH, VV, HV) as well as ground surface slope from a DEM. Regression coefficients were estimated using all available (geocoded) P-band data.

9.1.4 References

[1] B. Hallberg, G. Smith-Jonforsen, L.M.H. Ulander, and G. Sandberg, "A physical-optics model for double-bounce scattering from stems standing on an undulating ground surface," *IEEE Transactions on Geoscience and Remote Sensing*, vol. 46, no. 9, pp. 2607-2621, 2008.

[2] S. Saatchi, K. Halligan, D. Despain, and R. Crabtree, "Estimation of forest fuel load from radar remote sensing," *IEEE Transactions on Geoscience and Remote Sensing*, vol. 45, no. 6, pp. 1726-1740, 2007.

9.2 Assessment of forest biomass retrieval by CESBIO

9.2.1 Datasets used in the study:

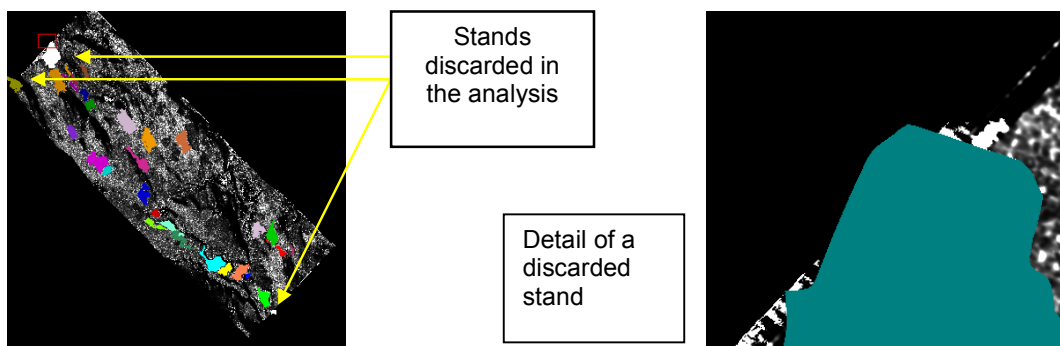
SAR data:

Table 1 lists the SAR data analysed by CESBIO

Scene ID	Test Site	Track	Heading	Band	Pol	Date	Product
08biosar0103x1	t11	11	-47°	P	PM	14.Oct.2008	GTC
08biosar0103x1	t21	11	-47°	P	PM	14.Oct.2008	GTC
08biosar0103x1	t31	11	-47°	P	PM	14.Oct.2008	GTC
08biosar0104x1	t11	21	132°	P	PM	14.Oct.2008	GTC
08biosar0104x1	t21	21	132°	P	PM	14.Oct.2008	GTC
08biosar0104x1	t31	21	132°	P	PM	14.Oct.2008	GTC
08biosar0301x1	t12	10	357°	P	PM	15.Oct.2008	GTC
08biosar0302x1	t12	20	313°	P	PM	15.Oct.2008	GTC
08biosar0303x1	t12	30	133°	P	PM	15.Oct.2008	GTC
08biosar0304x1	t12	40	42°	P	PM	15.Oct.2008	GTC

Forest data:

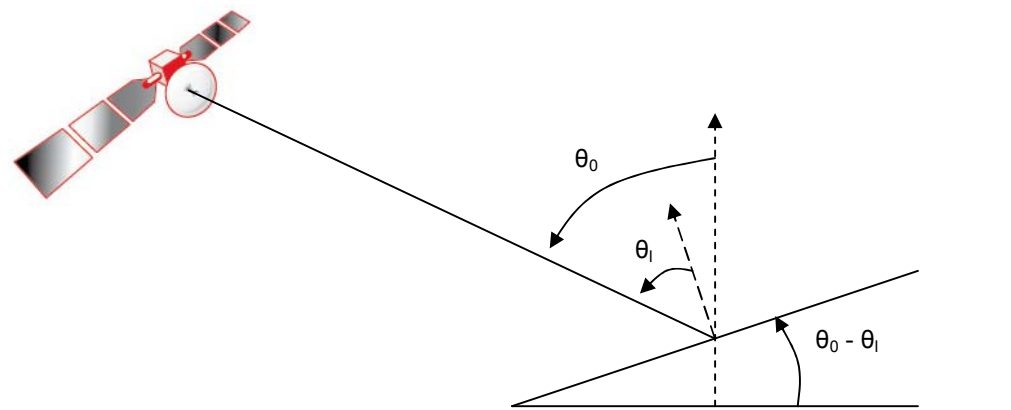
The forest stands listed in Section 3.2.3.3 are used in the analysis, except stands 17637, 1474 et 4451 because they are in the border of the images, as shown below.



9.2.2 Impact of topography on the biomass-intensity relationship

Image geometry

Figure 2 depicts the geometrical scheme of the radar observation.



Where θ_0 is the radar look angle (or radar incidence angle), θ_l is the local incidence angle, and $\theta_0 - \theta_l$ represents the local slope.

The value of θ_l for each pixel in each image is extracted from the corresponding « incmap08biosar* » file.

To calculate $\theta_0 - \theta_l$ for each pixel i, j which represents the local slope, the provided DEM is used, after converting in metre.

$$[\theta_0 - \theta_l]_{i,j} = \frac{DEM_{i+1,j-1} - DEM_{i-1,j+1}}{2\sqrt{2}.dx}$$

with dx the resolution in m. The radar incidence angle (look angle) θ_0 is recovered from :

$$\theta_0 = [\theta_0 - \theta_l] + \theta_l$$

Backscatter intensity normalisation

The radar backscatter intensity depends on the radar incidence angle. To reduce the effect of incidence angle, the radar backscattering coefficient is expressed in

$$\gamma^\circ = \frac{\sigma^\circ}{\cos \theta}$$

For flat terrain, $\theta = \theta_0$, the radar incidence angle, whereas for sloped terrain, $\theta = \theta_l$ in a first approximation.

The images at different headings have been transformed in images of γ° .

In order to assess the image angle-normalisation approach, Figure 3 overlays two gamma images from two headings, 132° and -47° acquired at the same date (tracks 11 and 21 on 14 October). The pixels of images in Figure 3 in greyish colour have the same gamma values, whereas red or blue colour denote higher values for one of the headings. It can be seen that the general effect of topography (forshortenning, layover) is still visible as well as effects due to differences in scattering phenomena (e.g. double bounce scattering on the river banks).

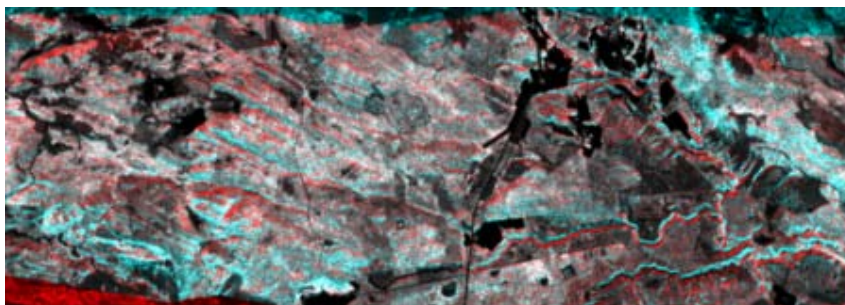


Figure 3: Overlay of γ° images from heading 132° (blue) and heading -47° (red).

Relationship γ° and forest biomass:

The mean backscatter γ° values are extracted from forest stands included in HH, HV and VV images of 2 headings 132° and -47° .

The γ° values are plotted as a function of forest above ground biomass in Figure 4.

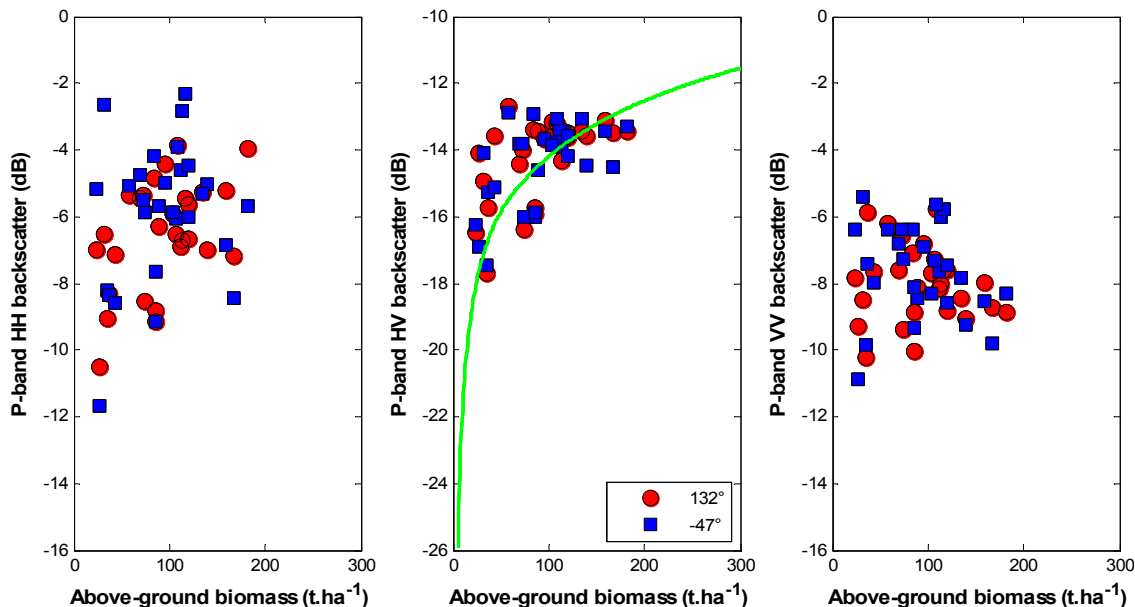


Figure 4: Backscatter coefficient expressed in γ° as a function of biomass at HH, HV, and VV extracted from images acquired with 2 different headings in BIOSAR-II (132° and -47°). The green curve is from past datasets (Le Toan et al., 2009) overlaid on HV BIOSAR-II data for comparison.

Figure 4 shows that the effect of topography is reduced when the intensity is normalised by the local incidence angle, especially for HV and VV, where the normalisation is well adapted to the volume scattering angular behaviour. The effect of topography remains high at HH, where the double bounce scattering needs to be accounted for. Figure 4 also shows that while HV can be used for biomass retrieval, the single use of HH is limited in terrain with topography (VV was already shown little sensitivity to biomass in past studies).

To compare the relationship between HV intensity with biomass in previous work, the set of equations derived from past data have been plotted on the HV images.

$$\gamma_{HV} = \begin{cases} -32 \cdot B^{-0.4343} - 10 & \text{for } B < 72 \text{ t/ha} \\ \frac{\log B - 4.5563}{0.18} & \text{for } B > 72 \text{ t/ha} \end{cases}$$

It can be noted in Figure 4 that the HV γ° values are in the same range of the expected γ° values from the above equations.

Effect of the local incidence angle on HV backscatter intensity:

In order to assess the effect of the local incidence angle on the relationship between the radar backscatter intensity and above ground biomass, γ° is averaged over pixels from forest stands analysed in Figure 4 located in local incidence angle range of 5° interval, from 0°-5°, 5°-10°, 10°-15° and >15° (Figure 5).

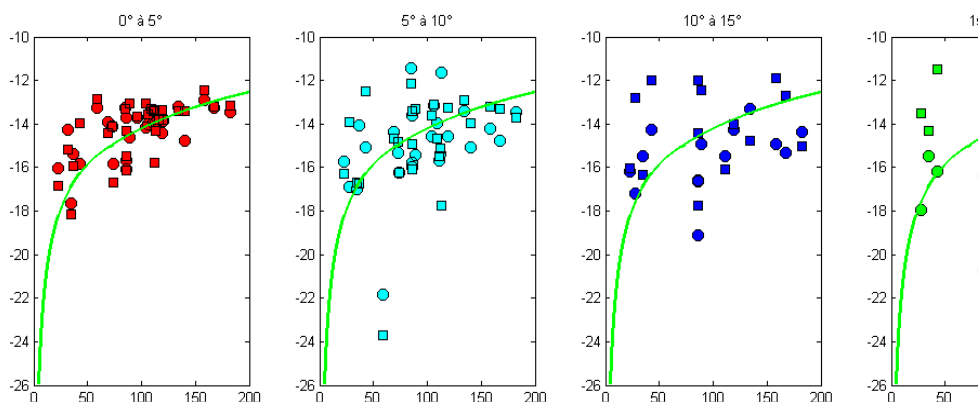


Figure 5: HV Backscatter intensity in γ° as a function of above ground biomass, averaged from pixels in the stands located in interval of local incidence angle, from 0 to 15° in 3 intervals, and for angle > 15°. The number of pixels from each data points in Figure 6 is sufficiently high to avoid dominant speckle effect. Squares are mean γ° extracted from 132° heading image, and circles from -47° heading image. The green curve is the HV- γ° versus biomass curve described above.

Figure 5 shows that, when the local incidence angle is < 5°, the relationship between the radar backscatter HV and biomass has less dispersion and can be described by the past HV curve. The data dispersion (e.g. around the curve) increases with the local incidence angle after 5°. Figure 4 shows that when the backscatter values are averaged over entire stands, no outlier points are found.

Further work should be done on the effect of topography on different radar resolutions.

Effect of the radar incidence (look) angle

For a given forest scene, the range of local incidence angle varies as a function of the radar look angle. Since the spaceborne P-band system may have a look angle from 20° to 30°, it should be interesting to selected data at radar incidence (look) angle from 20° to 30° from the data in Figure 5, and also from the other headings. However, there are insufficient stands located in the low range of incidence angle for the images of BIOSAR-II. Instead, data points corresponding to radar incidence angle < 40° are retained in Figure 6.

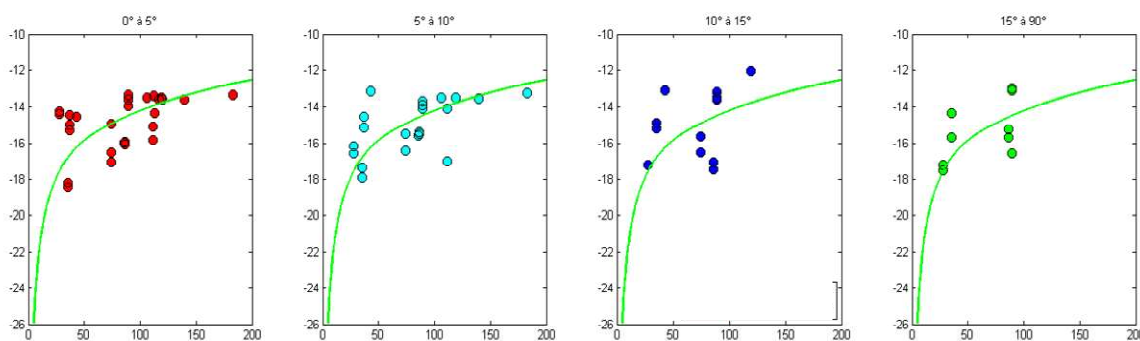


Figure 6: HV Backscatter intensity in γ° as a function of above ground biomass, averaged from stand pixels located in interval of local incidence angle, from 0 to 15° in 3 intervals, and for angle > 15°. Only the data corresponding to the radar look angle < 40° are retained. The data are from headings 132, -47, 42, 133, 313, 357 in Table 1.

The small number of data points does not permit conclusion, but when the incidence angle is restricted (< 40°), the outliers in Figure 5 are not included in Figure 6.

As a summary, the relation between HV radar backscatter intensity and above ground biomass is affected by topography. The effect is reduced when the backscatter coefficient is expressed in γ° (normalised by the local incidence angle). In particular, when the analysis is restricted to the range of incidence angle range prevailing in spaceborne systems, the topographic effect should be further reduced.

9.2.3 Inversion of HV backscatter in biomass

In a previous study (Le Toan et al., 2009), the HV backscatter intensity has been used for biomass inversion using the following equations:

$$\log B = \begin{cases} -\ln\left(\frac{-\gamma_{HV} - 10}{32}\right) & \text{for } \gamma_{HV} < -15\text{dB} \\ 4.5563 + 0.18 \cdot \gamma_{HV} & \text{for } \gamma_{HV} > -15\text{dB} \end{cases}$$

The data points at look angle of < 40° are inverted, and Figure 7 compares the estimated biomass to the inventory biomass. As expected, the RMSE is high (35 ton/ha, corresponding to 41, 8% of biomass).

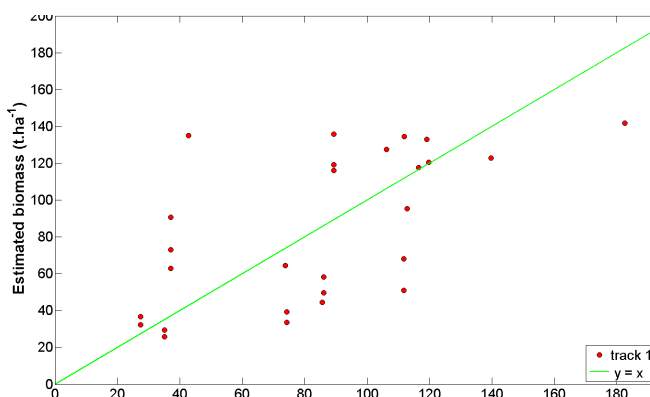


Figure 7: Inversion of HV backscatter intensity: comparison of estimated biomass with inventory biomass. RMSE is 35 ton/ha (41.8%).

9.2.4 Inversion using HH, HV, and VV using Saatchi et al., 2007 algorithm:

The method by Saatchi et al., 2007 provides an estimation of the crown biomass W_c and the stem biomass using σ_0 from HH HV and VV, and the local slope and 14 coefficients: :

$$\begin{aligned} \log(W_c) &= a_0 + a_1 \sigma_{HV}^0 \cos(\theta_0 - \theta_{loc}) \\ &\quad + b_1 \sigma_{HH}^0 \sin(\theta_0 - \theta_{loc}) \\ &\quad + c_1 \sigma_{VV}^0 \cos(\theta_0 - \theta_{loc}) \\ \log(W_s) &= a_0 + a_1 \sigma_{HV}^0 \sin(\theta_0 - \theta_{loc}) \\ &\quad + b_1 \sigma_{HH}^0 \cos(\theta_0 - \theta_{loc}) \\ &\quad + c_1 \sigma_{VV}^0 \cos(\theta_0 - \theta_{loc}) \end{aligned}$$

From analysis of the Yellow Stone dataset, Saatchi et al., 2007 derived the following set of coefficients.

Crown	Stem
$a_0 = 6.215$	$a_0 = 8.104$
$a_1 = 0.058$	$a_1 = 0.112$
$a_2 = -0.0017$	$a_2 = -0.0018$
$b_1 = 0.192$	$b_1 = 0.396$
$b_2 = 0.0098$	$b_2 = 0.0143$
$c_1 = 0.0962$	$c_1 = -0.131$
$c_2 = -0.0028$	$c_2 = -0.0081$

The algorithm requires as training datasets a minimum of 7 reference forest stands with crown and stem biomass and the local slopes from the DEM.

Since the forest data in BIOSAR-I consisted of a large number of stands, it is interesting to investigate the robustness of the algorithm using data from different headings, i.e. to investigate if a set of coefficients derived from other image headings can be used to invert a given image.

Inversion using training stands of the same image:

The 14 coefficients of the Saatchi equations are derived from images of heading 132° and -47°, using the forest data of the stands included in the images.

The following table compares the coefficients derived from each of the images.

track 132°		track -47°	
Crown	Crown	Stem	Stem
$a_0 = -11,9667$	$a_0 = -0,6554$	$a_0 = -2,5055$	$a_0 = -2,1542$
$a_1 = -2,8227$	$a_1 = -0,4741$	$a_1 = 0,685$	$a_1 = -0,5837$
$a_2 = -0,0923$	$a_2 = -0,0234$	$a_2 = -0,1953$	$a_2 = -0,2207$
$b_1 = -0,5704$	$b_1 = -0,1193$	$b_1 = 0,6998$	$b_1 = 0,1075$
$b_2 = -0,4262$	$b_2 = -0,0108$	$b_2 = 0,0198$	$b_2 = -0,0104$
$c_1 = 1,5216$	$c_1 = -0,2338$	$c_1 = -1,9122$	$c_1 = -1,3204$
$c_2 = 0,0865$	$c_2 = -0,0005$	$c_2 = -0,0798$	$c_2 = -0,0522$

Figure 8 shows the comparison between estimated biomass and inventory biomass. The results show good performance is obtained, when using the training set from the same image to be inverted. For two

headings, similar RMSE are obtained (about 24 ton/ha). It is noted that when the stand 3245 is discarded-one outlier in Figure 8, the RMSE are resp. 20.4 and 21.4 ton/ha for 132° and -47° images).

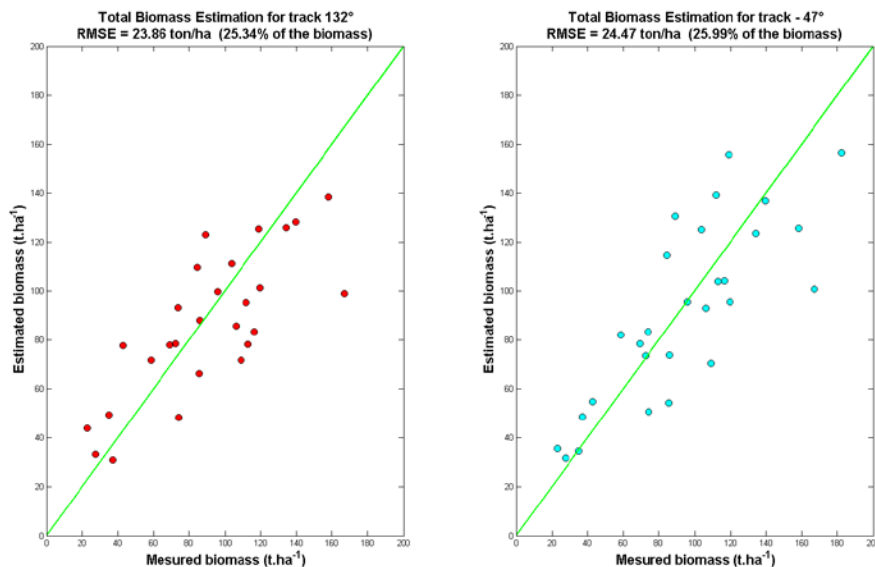


Figure 8: Comparison of estimated biomass and reference biomass using training stands from the same image. Left: image of heading 132°, and right: image of heading -47°.

Figure 9 shows the corresponding biomass map derived from heading 132° .

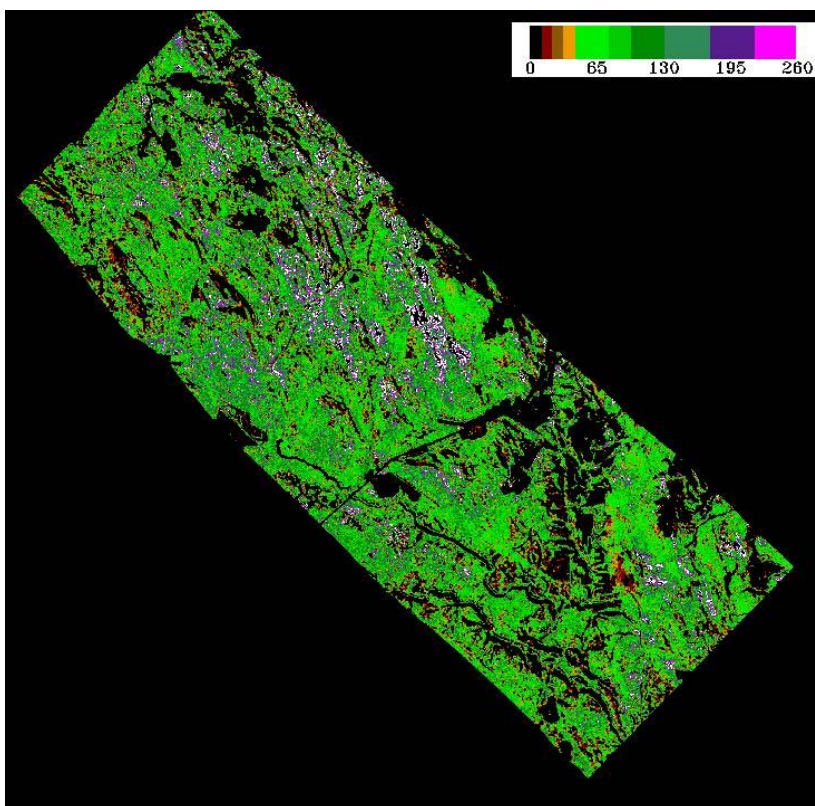


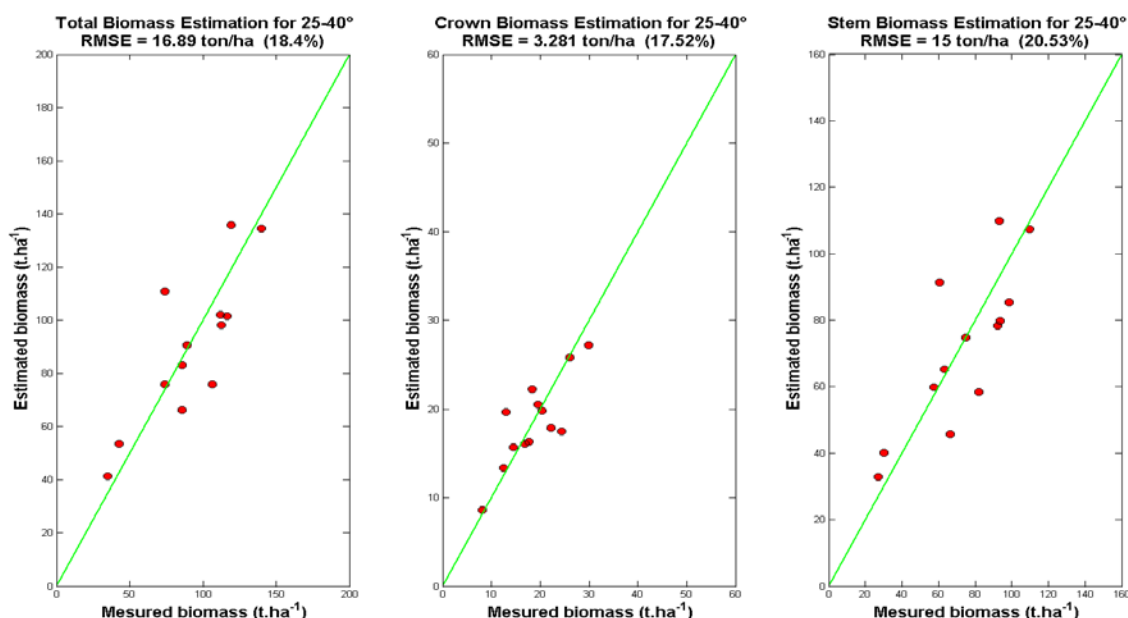
Figure 9: Biomass map using the Saatchi algorithm. Data are from image of heading 132° and the empirical regression uses the forest stands located in the images.

Assessing the generality of the algorithm:

To assess the generality of the algorithm, we first restrict the data points at radar incidence angle $< 40^\circ$, to better consider the spaceborne SAR condition, and we test the use of coefficients derived from one dataset to be applied to an other scene with similar forest conditions. For this purpose, we divide the datasets into two sets: the first is from heading 132° , where sufficient number of stands are found, and the second is a synthetic set including data from heading of 42° , 133° , 313° et 357° . The second set accounts for more various slope, orientation and biomass values. The test is to derive coefficients from one set and to apply the coefficients to the other set.

Results with radar look angle $< 40^\circ$

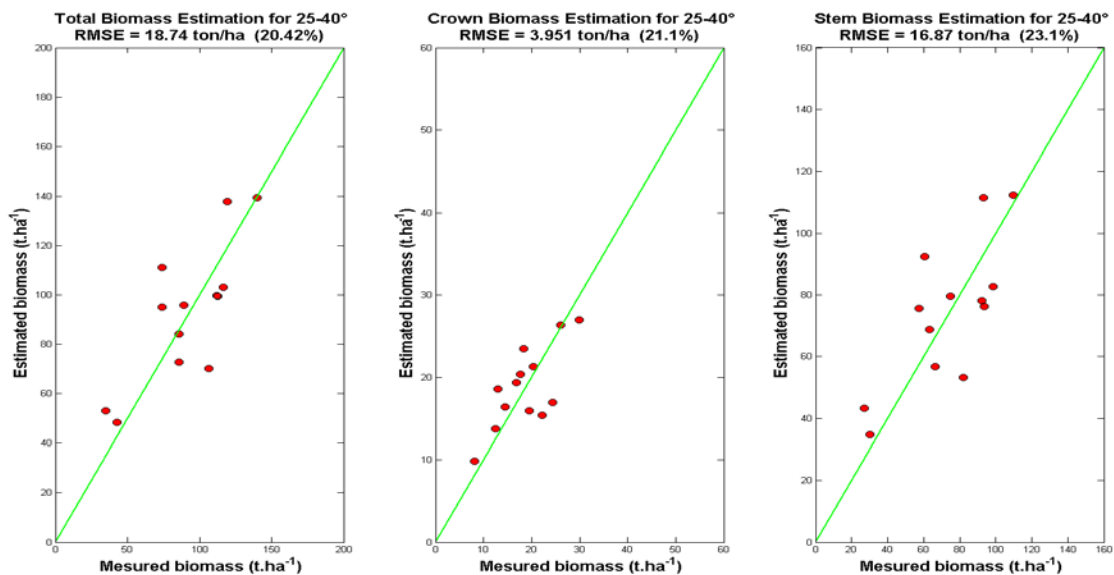
When data from a restricted radar look angle $25^\circ - 40^\circ$ are used, the comparison of estimated and measured biomass is improved. Figure 9 shows the results obtained with the heading 132° image.



Crown	Stem
$a_0 = -18,8602$	$a_0 = -25,3955$
$a_1 = -0,5152$	$a_1 = -0,1016$
$a_2 = -0,0227$	$a_2 = -0,166$
$b_1 = -0,1217$	$b_1 = 1,2345$
$b_2 = -0,751$	$b_2 = 0,0537$
$c_1 = -3,4462$	$c_1 = -6,835$
$c_2 = -0,15$	$c_2 = -0,3184$

Figure 9: Comparison of estimated and measured biomass from data of heading 132° image, with data points restricted to radar incidence angle of $25^\circ - 40^\circ$. Left: total above ground biomass, middle: crown biomass, right: stem biomass. The table lists the corresponding coefficients.

Using the second set of data (from different headings 42° , 133° , 313° et 357°), the following results are obtained:



Crown	Stem
$a_0 = -9,7489$	$a_0 = -25,914$
$a_1 = 0,7291$	$a_1 = 0,0421$
$a_2 = 0,0144$	$a_2 = -0,0327$
$b_1 = 0,5278$	$b_1 = 1,1439$
$b_2 = -0,1437$	$b_2 = 0,047$
$c_1 = -3,7664$	$c_1 = -6,7439$
$c_2 = -0,1685$	$c_2 = -0,3067$

Figure 10: Comparison of estimated and measured biomass from data of different headings 42°, 133°, 313° et 357°, with data points restricted to radar incidence angle of 25°-40°. Left: total above ground biomass, middle: crown biomass, right: stem biomass. The table lists the corresponding coefficients.

All the above results show that the sets of coefficients differ significantly one another.

Test of robustness of the empirical coefficients:

Using the coefficients of the first set of data (table in figure 9) to the second set of data provides the following results:

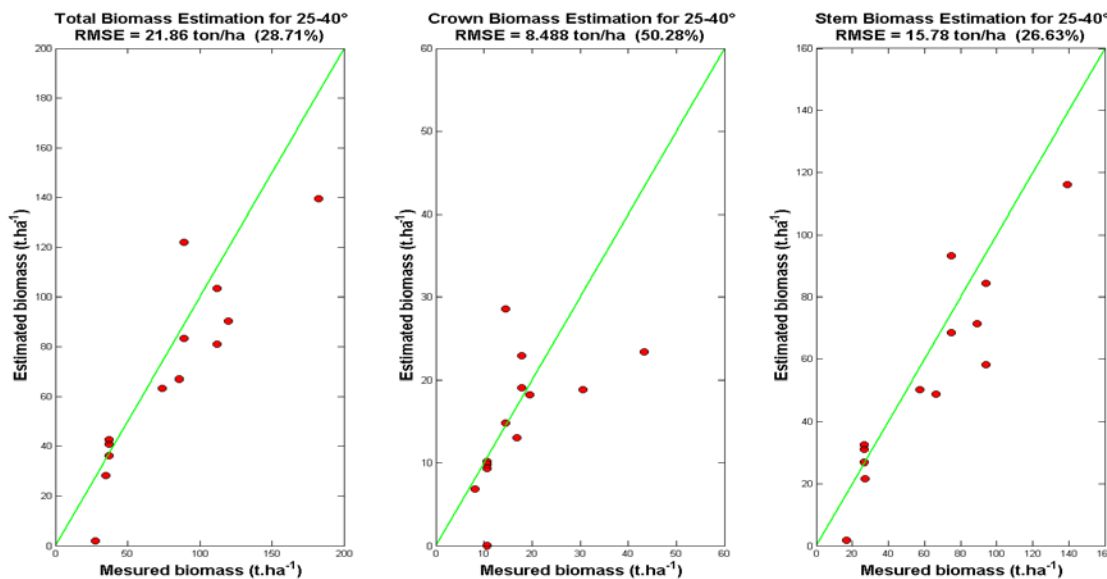


Figure 11: Comparison of estimated and measured biomass from data of different headings 42°, 133°, 313° et 357°, with data points restricted to radar incidence angle of 25°-40°. Left: total above ground biomass, middle: crown biomass, right: stem biomass. The coefficients used in the inversion are derived from data of heading 132° (Table in Figure 9)

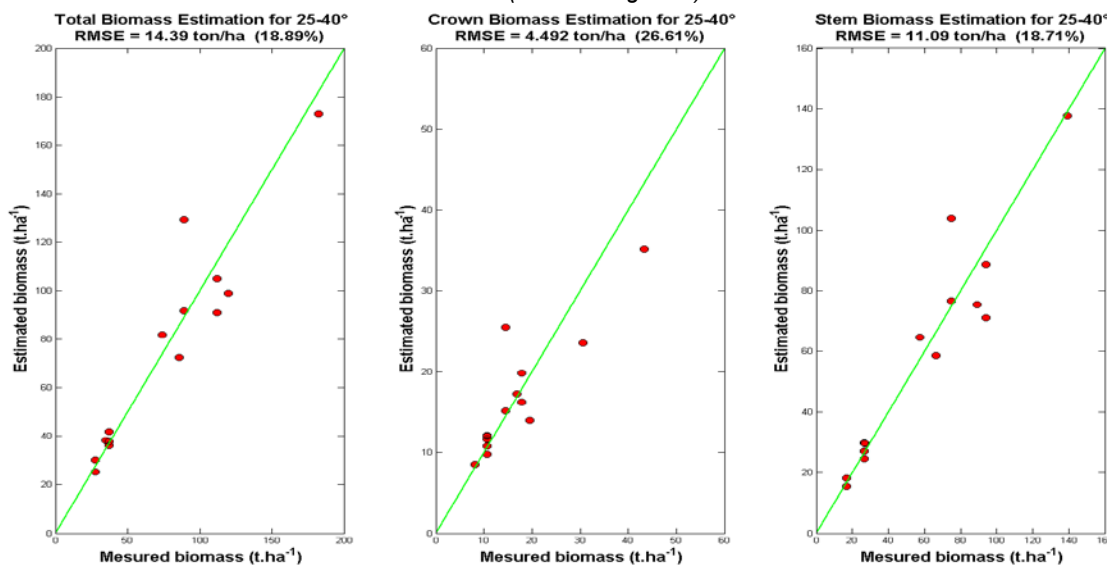
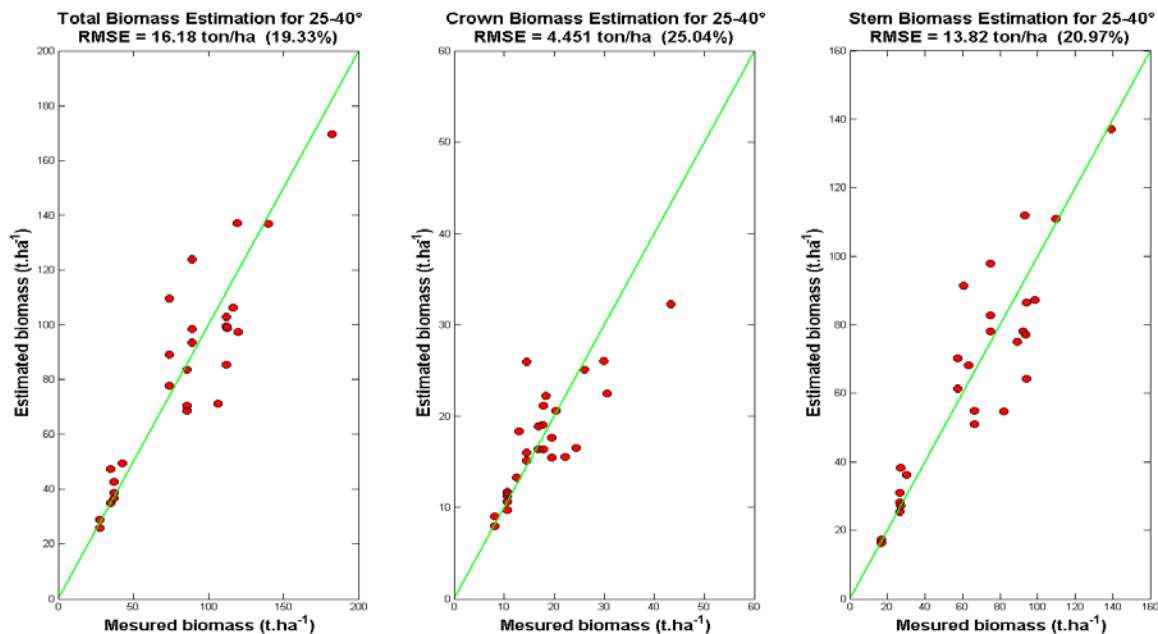


Figure 12: Comparison of estimated and measured biomass from data of different heading 132°, with data points restricted to radar incidence angle of 25°-40°. Left: total above ground biomass, middle: crown biomass, right: stem biomass. The coefficients used in the inversion are derived from data of heading 42°, 133°, 313° et 357° (Table in Figure 10)

Inversion using all the headings:

Finally, for BIOSAR –II, the forest stands observed from all the headings are used in an integrated datasets to assess the inversion.

Figure 13 shows the result obtained.



Crown	Stem
$a_0 = -12,6097$	$a_0 = -25,6846$
$a_1 = 0,1079$	$a_1 = 0,0202$
$a_2 = -0,0046$	$a_2 = -0,0363$
$b_1 = 0,4668$	$b_1 = 1,384$
$b_2 = -0,1423$	$b_2 = 0,0607$
$c_1 = -3,2972$	$c_1 = -6,9641$
$c_2 = -0,144$	$c_2 = -0,3206$

Figure 13: Comparison of estimated and measured biomass from data of different headings 132°, 42°, 133°, 313° et 357°, with data points restricted to radar incidence angle of 25°-40°. Left: total above ground biomass, middle: crown biomass, right: stem biomass. The coefficients used in the inversion included in the table.

The following table presents the data used to derive the results in Figure 11.

Heading	Stand	Biom Total	Biom Crown	Biom Stem
132	4115	89,31	14,43	74,88
	4038	85,6	22,18	63,42
	4035	35,08	8,19	26,89
	3628	74,28	16,83	57,45
	36169	112,82	20,42	92,4
	3689	86,03	19,5	66,53
	3611	116,46	17,74	98,72
	31818	73,8	13,02	60,78
	30097	111,96	18,3	93,66
	2629	139,76	29,9	109,86
	2625	119,13	26,08	93,05
	2626	106,24	24,41	81,83
	21577	42,71	12,49	30,22
m47	36979	37,12	10,7	26,42
	32398	27,46	10,67	16,79
	2269	182,54	43,36	139,18
	18147	119,8	30,51	89,29
42	4451	111,74	17,82	93,92
	4115	89,31	14,43	74,88
133	3628	74,28	16,83	57,45
	4035	35,08	8,19	26,89
	4451	111,74	17,82	93,92
	4115	89,31	14,43	74,88
	3689	86,03	19,5	66,53
313	36979	37,12	10,7	26,42
	32398	27,46	10,67	16,79
357	36979	37,12	10,7	26,42

9.2.5 Inversion using intensity and height

In order to assess the use of forest height in the inversion, a term of forest height is added in the Saatchi equation for Stem biomass and Crown biomass. Two tests have been made: adding one or two terms accounting for the stand height.

d.H , or adding

d1H+ d2H2

The test uses H for the stand Height from a) Lidar Height, b) L-band Pol-InSAR derived Height, and c) P-band Pol-InSAR derived Height. The three sets of stand heights are provided for BIOSAR-II.

Figure 14 presents the preliminary results using linear term for stand height. In figure 16, it can be noted that the use of the Lidar height improves the result (RMSE from 16.18 ton/ha to 10.84 ton/ha, or 19.33% of biomass versus 12.95%). But the result is expected, since the Lidar height are used to derive biomass in the ground datasets.

The improvement provided by L-band Pol-InSAR height is smaller, but still noticeable (RMSE= 12.78 ton/ha, or 15.27%), as for P-band Pol-InSAR, the improvement is marginal (15.12 ton/ha or 18.07%).

It can be added that the results using both linear and second order terms do not differ from the single linear term.

Further assessment still needs to be done to document on the joint use of intensity and height in BIOSAR-II datasets.

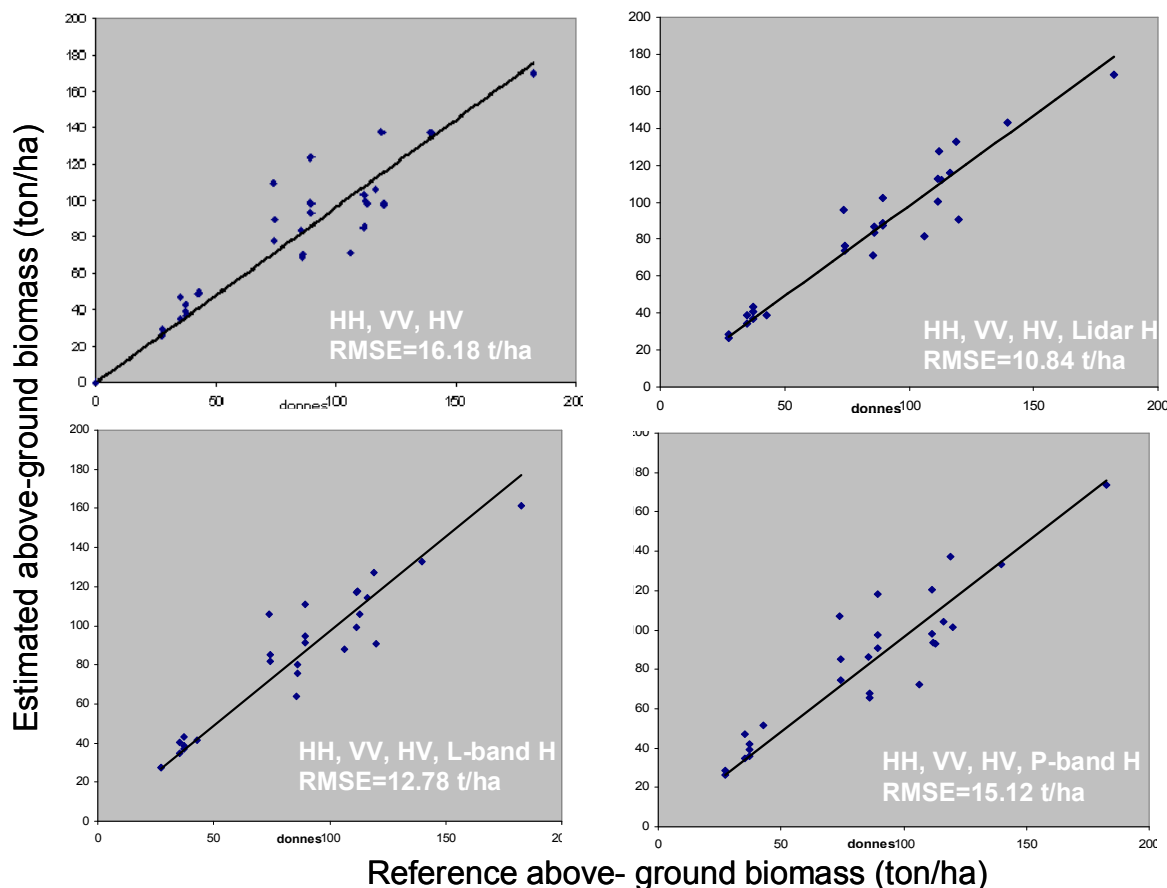


Figure 14: Top left: Inversion using HH, VV, HV (same as in figure 13 left), Top right: inversion using HH, VV, HV and Lidar Height. Bottom left: inversion using HH, VV, HV and L-band derived height, bottom right: inversion using HH, VV, HV and P-band derived height.

9.2.6 Summary and further works

1. Quantify the impact of topography on the biomass intensity relationship and identify methods for mitigation:

The backscatter intensity is strongly affected by topography. When expressed in local-incidence angle normalized γ° , the topographic effect is reduced in particular for HV and VV. Within the scene remaining effects are still visible (e.g. border effect from double bounce scattering).

γ° extracted from forest stands are analysed as a function of stand biomass from images of different headings (for different local angles). The values of the backscatter at HV are of the same order than observed in previous studies, but presenting some dispersion which increases with the local incidence angle.

In addition, the dispersion should be reduced when the radar angle is in a small range (comparable to the range in spaceborne SAR).

2. The biomass intensity retrieval algorithms have been assessed for the BIOSAR-II high-latitude boreal forests and their performance for this ecosystem has been quantified:

- the use of HV intensity provide an unsupervised inversion. The validation using stand values provides a RMSE of 35 ton/ha (41.8% of biomass)

- the use of HV, VV, HH based on Saatchi algorithm provides, using training stands in a scene provide very good results (RMSE=23.86 ton/ha). Attempts to perform the training of one part of the data sets (with different headings) to other data sets provide also good results (18;74 ton/ha and 21.86 ton/ha in two examples)

A biomass map has been derived to present the prototype Level-2 product. Further validation need to be performed.

3. Extend analysis to multi-channel retrieval (including integration of height information) and L-Band for selected datasets

Preliminary analysis incorporating forest height from Lidar, from L-band Pol-InSAR and P-band Pol-InSAR has been performed. The results which need further investigations, did not show very significant improvement in the inversion.

Further works

Further assessment of the datasets, in particular for the use of integrated intensity and heights,

Using Bayesian inversion approach to improve the inversion scheme, in particular when unsupervised methods are used;

Investigating the use of Pol-InSAR derived measurements, including coherence in the inversion

9.3 Assessment of forest height retrieval by DLR

This chapter deals with forest parameters estimation using a model based multi-baseline approach developed at the Microwaves and Radar institute. Forest height is one of the main parameter that this chapter is focusing on and specifically on the validation of the retrieval algorithms for high-latitude boreal forests and the quantization of the performance for this ecosystem. The impact of topography on forest height retrieval has been studied and quantified. The work has been carried out with L- / P-band airborne SAR data and simulated P-band spaceborne data acquired within the BIOSAR 2008 project.

9.3.1 Data Selection

In order to investigate the impact of topography on forest height retrieval with multi-baseline Pol-InSAR two differently derived digital elevation models (DEM) were selected. One derived from repeat pass L-band and the other one derived from Lidar measurements. Both digital elevation models were used to estimate the surface slopes with respect to the radar geometry. In this study the following Pol-InSAR data were used:

- The area coverage is about 3 (range) X 10 (azimuth) km
- Flights in two different flight directions were used for data processing: 314 and 134 degree
- Two different frequency were used for forest height inversion: L- and P-band
- For a better performance a multi-baseline approach was chosen for forest height inversion using L-band with 0,6,12,18,24,30m baselines and P-band with 0,8,16,24,32,40m baselines

The P-band E-SAR airborne data were simulated corresponding to the specification of the ESA's Earth explorer BIOMASS mission. The impact of these parameters is investigated using the filtered 6 MHz P-band data. A comparison of the inversion results between 94 MHz and 6 MHz bandwidth at P-band is performed and discussed. The estimated and obtained Pol-InSAR results were validated and compared with ground measurement, Lidar canopy height and field survey data in the Krycklan forest.

9.3.1.1 Slope Estimation

The main objective of this section is to quantify and estimate the impact of topographic slopes on height retrieval algorithms and to identify potential methods for their mitigation in Pol-InSAR modeling. Two differently derived digital elevation models were used for the estimation of the slope:

- Lidar derived DEM: The test site was mapped using an airborne laser instrument with a spatial resolution of 0.5 x 0.5 m. In **Fig. 9.2.1** on the left the Lidar DEM in E-SAR airborne coordinates is shown. The topographic variation is between 100 m to 350 m.
- L-band derived DEM: The L-band DEM is derived from multi-baseline Pol-InSAR data by using phase calibration and coherence scatterer (CS) techniques displayed in the middle in Fig. 9.2.1. On the right a comparison of both DEMs plotted against each other is presented. There is no significantly difference between L-band and Lidar DEMs from low to high elevation.

Fig. 9.2.2 show a slope map in the Krycklan forest estimated with the Lidar digital terrain model (DTM), scaled from -20° to 20° degree. This slope image was calculated considering radar geometry (flight direction 314° from north and south-west radar look direction). Positive slopes can be defined as an incline plane towards the radar sensor (see **Fig. 9.2.2** left). The other flight direction is exactly 180° opposite with 134° and a radar north-east look direction. The slopes north-east looking have a opposite sign and same absolute slope values.

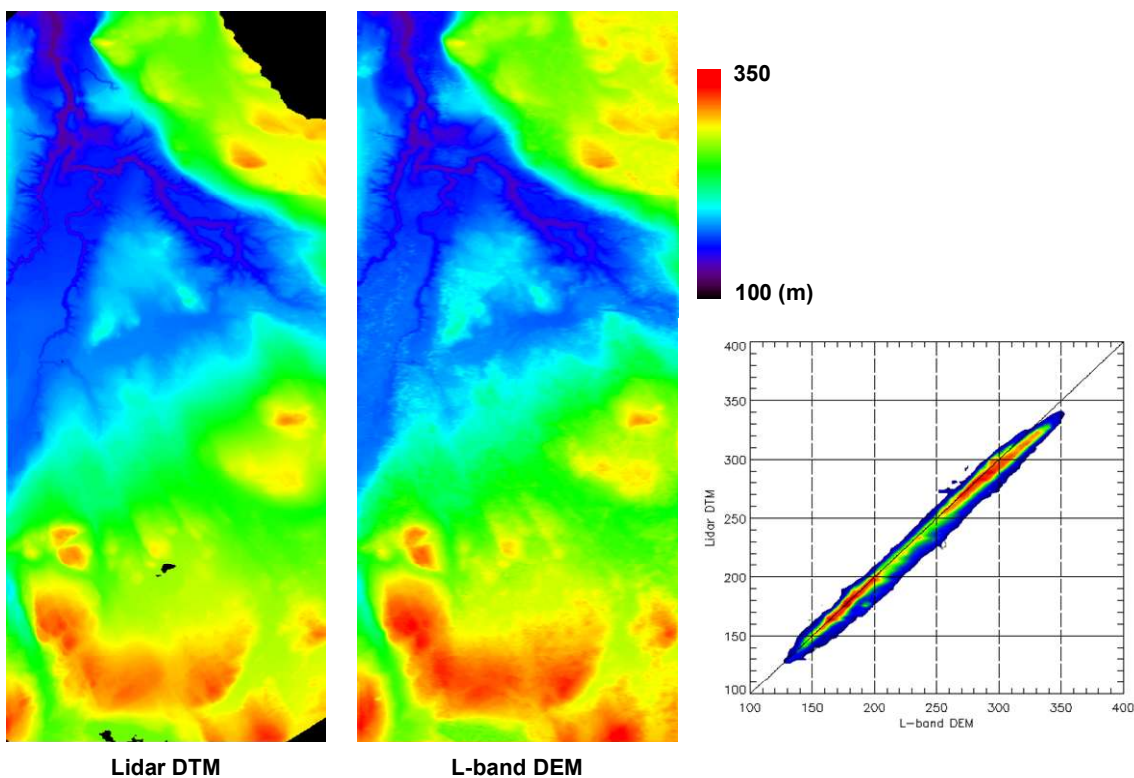


Fig. 9.2.1. DEM of the Krycklan test site: (Left) Lidar DEM, scaled from 100 to 350m. (Middle) L-band DEM. (Right) Comparison of Lidar DEM and L-band DEM.

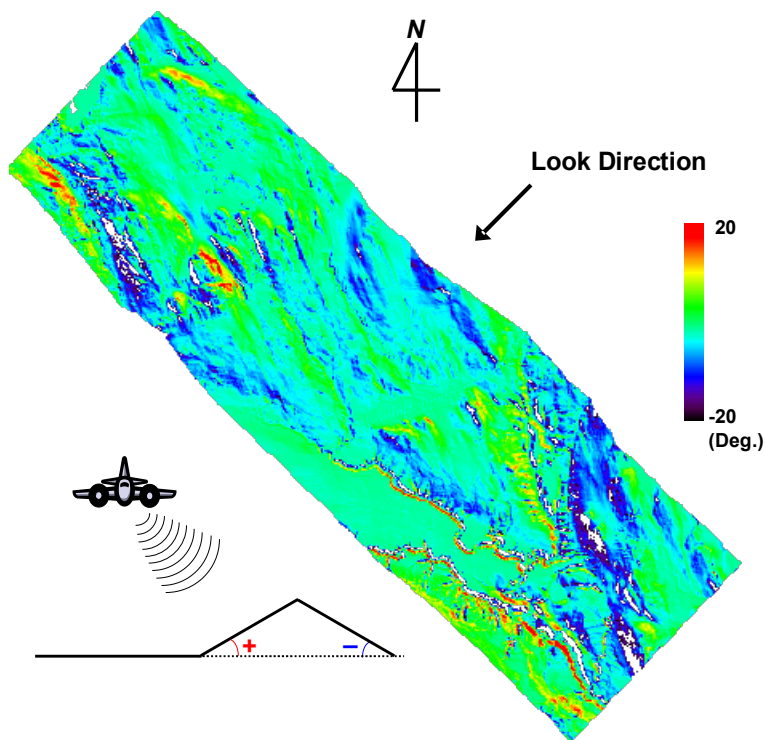


Fig. 9.2.2. Topographic slopes in the south-west look direction scaled between -20° to 20° .

9.3.1.2 Summary of vertical wave number (kz)

Table 1 provides a summary of the Pol-InSAR data sets used for this study. SAR data were acquired in two flight direction (314 ° and 134 °) with a left looking system at L- and P-band.

L-band: L-band records were done with a 6, 12, 18, 24, 30 m spatial baseline in both flight directions. The vertical wavenumber (kz) varies from 0.069 to 0.346 for the 314° heading and 0.074 – 0.353 for the 134° heading.

P-band: The spatial baselines at P-band vary from 8 to 40 m with a spatial spacing of 8m also in both flight directions. The vertical wavenumber changes from 0.028 to 0.136 and 0.022 to 0.128 in each track. P-band has a relatively smaller kz range than L-band.

BIOMASS simulation data: Simulated spaceborne BIOMASS SAR data were generated from one flight direction (314°) of the P-band data. P-band spatial baselines were considered to have critical baselines for the simulated 6 MHz bandwidth.

In Table 1 the spatial baselines and vertical wave numbers for all used data are listed. The BIOMASS simulated data are marked in red.

Table 1. Pol-InSAR data set used for forest height estimation.

<i>Frequency</i>	<i>Flight Direction</i>	<i>Baseline [m]</i>	<i>Mean Kz [rad./m]</i>
L-band	314 °	6	0.069
		12	0.142
		18	0.207
		24	0.286
		30	0.346
	134 °	6	0.074
		12	0.143
		18	0.207
		24	0.285
		30	0.353
P-band	314 °	8	0.028
		16	0.056
		24	0.086
		32	0.111
		40	0.136
	134 °	8	0.022
		16	0.048
		24	0.078
		32	0.100
		40	0.128

9.3.1.3 Ground measurements data

The objective is to have a validation of the estimated Pol-InSAR forest heights. For comparison and validation of inverted forest heights, airborne Lidar measurements and field inventory data are used.

Fig. 9.2.3 shows the height estimations from Lidar measurements in UTM 34. It is scaled 0 to 35 m. As the reference height for validation, the so-call 'H100' from forest measurements [2] were used, which is defined as mean height of the H100 highest trees per hectare [3] . The H100 was estimated from Lidar data by taking the highest trees within a 10m by 10m average window. The H100 is a forestry standard canopy top height measure and corresponds quite well to forest heights seen by the radar, it is calculated out of the trees forming the canopy.

In this study the comparison of inversion heights from two flights track's against ground measurement were done in UTM 34 coordinate on polygon basis. Two types of polygons were available:

- Individual selected homogenous polygons from the original Lidar height map (see Fig. 9.2.3 right): 229 homogenous polygons over the test site were selected that covers an area of 834 hectare corresponding to about 30 % of inversion forest height maps at L- and P-band. The polygons are less effected by the local topographic variation as the individual polygon size is smaller and only homogenous areas were selected.
- Field survey selected polygons (see Error! Reference source not found.): In total, 31 forest stands were surveyed for in-situ measurements in the Krycklan forest and covers an area of about 260 hectare. It has the advantage of using field survey information data for comparison and validation. The individual sizes of the polygons are much bigger and therefore more affected by the local topography. In addition the polygons are not homogenous in terms of forest height variation.

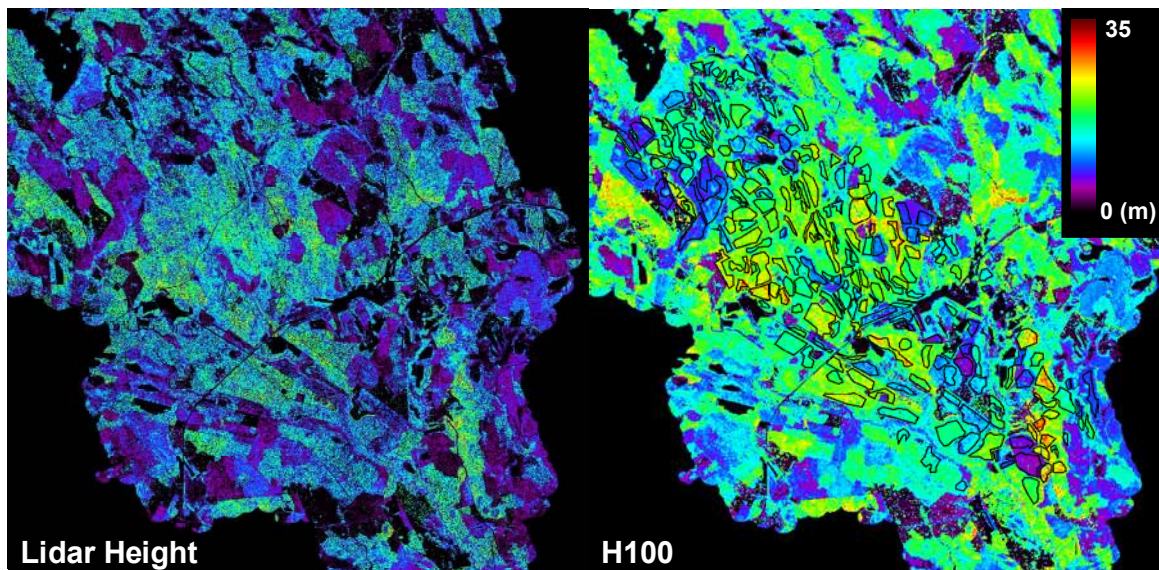


Fig. 9.2.3. Krycklan laser forest height map. (Left) Original vegetation height map. (Right) Lidar H100 measurements, scaled from 0 to 35 m.

9.3.1.4 Pol-InSAR data Quality

Interferometric coherence and phase images were **already shown in section** Error! Reference source not found.. In this section the coherence level of L- and P-band acquired in both flight tracks is investigated.

Fig. 9.2.4 shows coherence histograms of HH, HV and VV polarizations in 314° and 134° flight headings. The displayed colors represent the average values of the vertical wave number (kz) summarized in Table 1. As expected with increasing the spatial baseline the volume decorrelation is also increasing in forest areas and decreases the interferometric coherence level. The HV coherence is the lowest as their contribution to the volume decorrelation is assumed to be the highest.

P-band coherence histograms are shown in Fig. 9.2.5, where the coherence ranges from 0.4 to 1.0. Even P-band HV polarization shows lower coherence level because of volume decorrelation in forest areas. Comparing with L-band, P-band has in general higher coherence levels. There are two reasons; at first for 6MHz simulation data the spatial baselines (kz) in P-band were designed smaller due to the critical baseline. Small P-band kz makes less volume decorrelation and keeps high coherence levels. Secondly the repeat pass acquisitions with 10 to 60 minutes causing temporal decorrelation contributions. With the BioSAR-1 data it could be shown that P-band was stronger against temporal decorrelation than L-band [1]. Hence, P-band was less affected by temporal decorrelation.

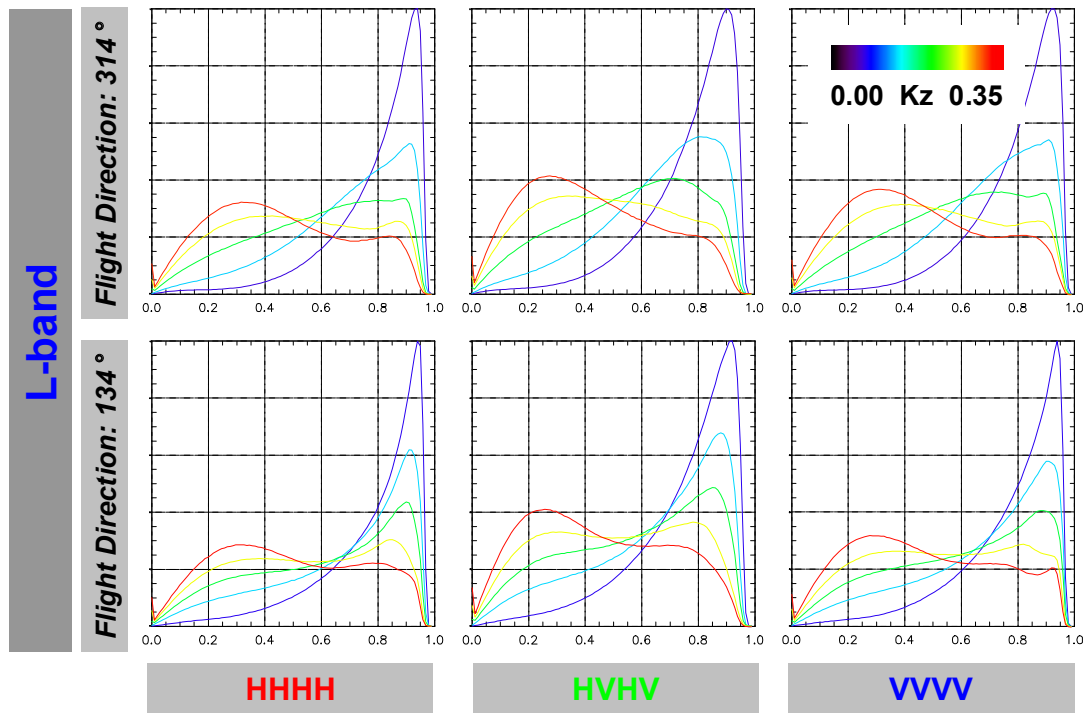


Fig. 9.2.4. Coherence histograms at L-band. (Upper) Flight direction 314 deg., look direction: south-west. (Bottom) Flight direction 134 deg., look direction: north-east. Color represents the vertical wavenumber.

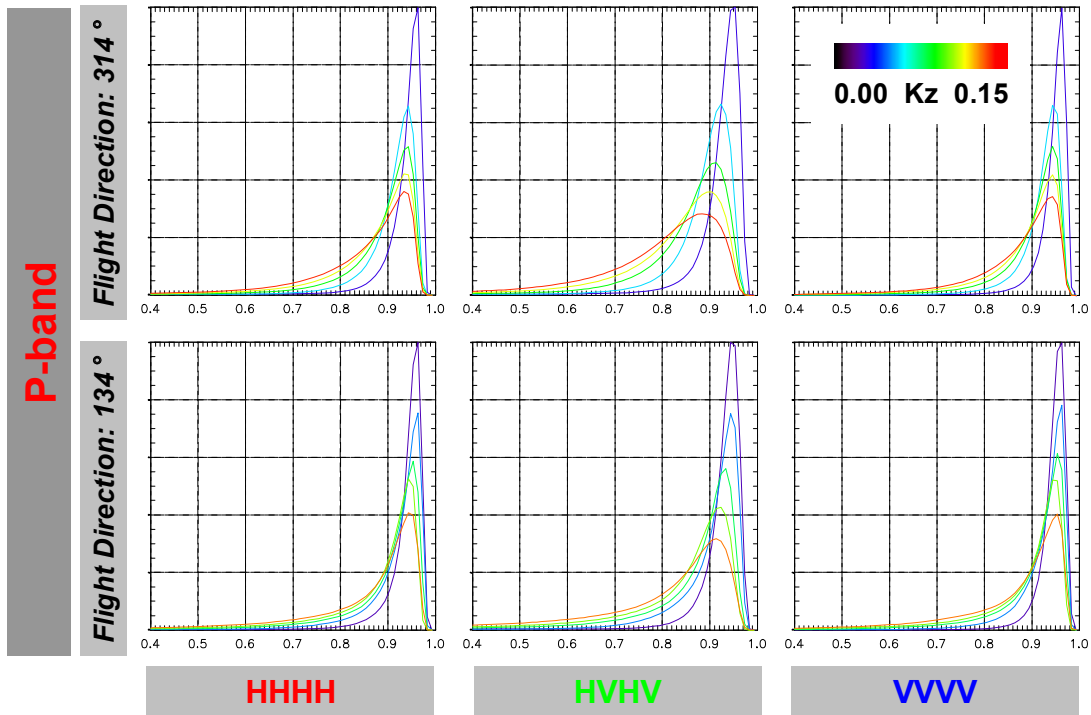


Fig. 9.2.5. Coherence histograms at P-band. (Upper) Flight direction 314 deg., look direction: south-west. (Bottom) Flight direction 134 deg., look direction: north-east. Color represents the vertical wavenumber.

9.3.1.5 Pol-InSAR Parameter Inversion

<Pol-InSAR forest height inversion model>

The key observable used in Pol-InSAR application is the complex interferometric coherence $\tilde{\gamma}$ estimated at different polarizations. The estimated coherence depends on instrument and acquisition parameters as well as on dielectric and structural parameters of scatterers. After calibration of system-induced decorrelation in azimuth and range, the estimated coherence can be composed into different decorrelation contributions [4].

$$\tilde{\gamma} = \tilde{\gamma}_{temporal} \gamma_{SNR} \tilde{\gamma}_{volume} \quad (1)$$

Volume decorrelation $\tilde{\gamma}_{volume}$ is the decorrelation caused by the different projection of the vertical component of the scatterer into two SAR images. $\tilde{\gamma}_{volume}$ is directly linked to the vertical distribution of scatterers $F(z)$ through a (normalized) Fourier transformation relationship. A widely and successfully used model for $F(z)$ is the so-called Random Volume over Ground (RVoG), a two-layer model. It is a two-layer model composed by a vegetation layer (canopy + trunks) and a ground component. The vegetation layer is modeled as a layer (volume) of given thickness containing randomly oriented particles characterized by scattering amplitude per unit volume. The random volume is located over an impenetrable ground scatterer characterized by its own scattering amplitude.

The volume decorrelation caused by the vegetation layer only can be described as

$$\tilde{\gamma}_{V_0} = \exp(i\kappa_z z_0) \frac{\int_0^{h_v} \exp(i\kappa_z z') \exp\left(\frac{2\sigma z'}{\cos\theta_0}\right) dz'}{\int_0^{h_v} \exp\left(\frac{2\sigma z'}{\cos\theta_0}\right) dz'} \quad (2)$$

where h_v is the height of the volume and κ_z the effective vertical (interferometric) wave-number that depends on the imaging geometry and the radar wavelength λ . θ_0 is the incidence angle and σ is a mean extinction coefficient.

Assuming no response from the ground in one polarization channel, the inversion problem has a unique solution and is balanced with five real unknowns ($h_v, \sigma, m_{1-2}, \phi_0$) and three measured complex coherences [$\tilde{\gamma}(\vec{w}_1)$ $\tilde{\gamma}(\vec{w}_2)$ $\tilde{\gamma}(\vec{w}_3)$] each for any independent polarization channel [5]

$$\min_{h_v, \sigma, m_i, \phi_0} \left\| \left[\tilde{\gamma}(\vec{w}_1) \quad \tilde{\gamma}(\vec{w}_2) \quad \tilde{\gamma}(\vec{w}_3) \right]^T - \left[\tilde{\gamma}_V(h_v, \sigma, m_1) \quad \tilde{\gamma}_V(h_v, \sigma, m_2) \quad \tilde{\gamma}_{V_0} \exp(i\phi_0) \right]^T \right\| \quad (3)$$

Equation (3) is used to invert the Pol-InSAR data sets at L- and P-band. The same regularization ($m_3 = 0$) has been used at L-band as well as at P-band. Because of dense vegetation layer, a modified regularization at P-band is not required. Note that the assumption for no ground response is not necessarily linked to HV channel.

<Slope correction in Pol-InSAR>

Two parameters in Pol-InSAR model are affected by the topographic slope:

- Effective **ground-to-volume amplitude ratio** (m) is the function of polarization and slope. The strong polarized behaviour of ground scattering combined with the directivity of the dihedral scattering component make the type and amount of ground scattering strongly dependent on the terrain slope in range [6].
- The **vertical wavenumber** is a function of the incidence angle that makes a terrain correction necessary [6]. **Fig. 9.2.6** shows the geometry of radar interferometry with slope. The vertical wavenumber can be corrected and shown in equation (4).

$$k_z = \frac{4\pi}{\lambda} \frac{\Delta\theta}{\sin(\theta_0 - \alpha)} \quad (4)$$

where $\Delta\theta$ is the apparent angular separation of the baseline from the scattering point, θ is incidence angle, and α is slope. Positive slope makes k_z larger while negative slope makes k_z smaller. As an example, the vertical wavenumber images are shown in **Fig. 9.2.6** before (middle) and after terrain correction (right).

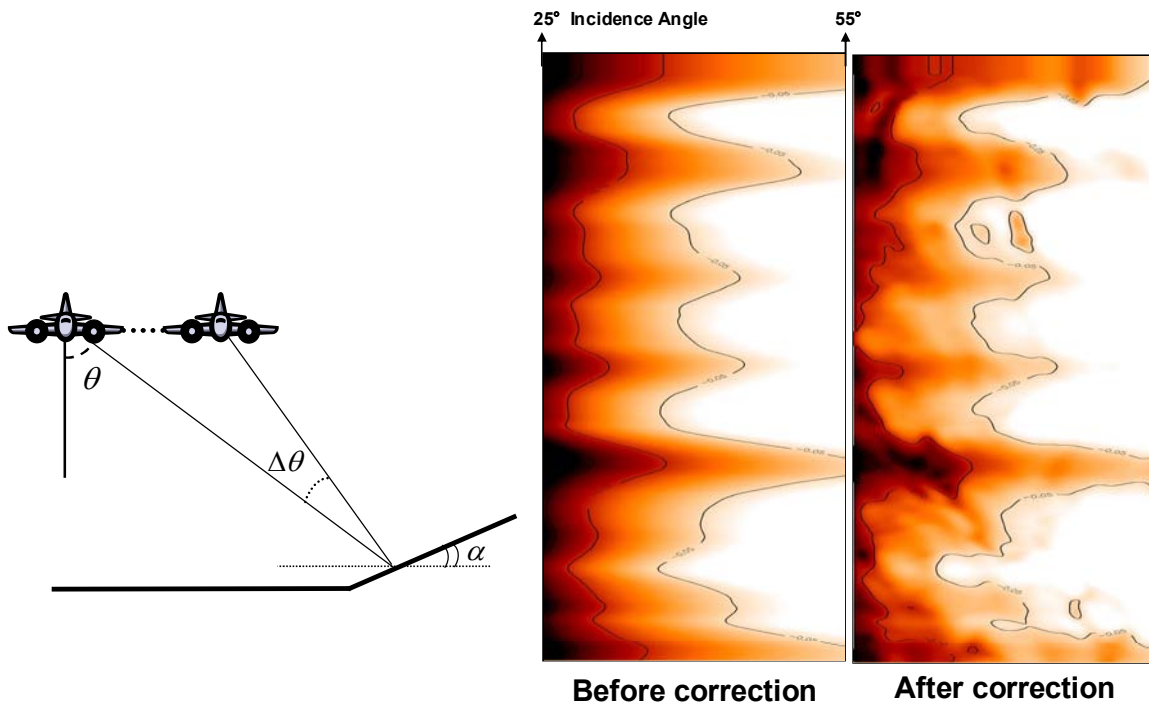


Fig. 9.2.6. (Left) Acquisition geometry, θ =incidence angle, $\Delta\theta$ =difference in incidence angle, α =terrain slope. (Right) Example of vertical wavenumber terrain correction at L band.

9.3.2 Data Processing for Pol-InSAR

In general, airborne SAR systems have strong variations of incidence angles (and thus the effective baseline) from near to far range. Therefore, the inversion performance is also varying with slant range. For a good inversion ill-conditioned regions have to be masked out.

At large effective baselines (i.e. large absolute kz values; $kz > 0.15$) the sensitivity of the coherence to forest height can saturate at heights lower than the forest heights in the scene. The overall coherence level is too low for valuable inversion. Such areas are masked out. The large kz mask acts primarily in near range. On the other hand, at small effective baselines (i.e. small absolute values; $kz < 0.05$) the favourable coherence to height scaling leads to high heights errors for small residual non-volumetric decorrelation, for example, temporal decorrelation. Such areas are excluded by kz mask. The small kz mask acts primarily in far range.

Low coherences make accurate inversion at a reasonable spatial resolution impossible. Therefore, areas with coherences lower than 0.3 have been also excluded.

After masking out of non-valid coherence areas and applying the forest height inversion model, forest maps are obtained in each spatial baseline at L- and P-band. These inversion results can be combined with considering the polarimetric conditions [6].

9.3.2.1 Impact of Topography

Fig. 9.2.7 shows multi-baseline Pol-InSAR inversion results using 6 flight tracks (134° heading), scaled from 0 to 35m baseline, where left the forest height map without terrain correction and adjacent the forest

height using slope corrected k_z as in equation (4) is displayed. Difference heights before and after terrain correction is shown in Fig. 9.2.7 on the right. Non-slope-corrections causing an underestimation/overestimation of forest heights in hilly terrain areas. The over-/underestimation rates are related to an angle of inclination see **Fig. 9.2.2**.

Height errors can be estimated by subtracting the reference height, H100. Three estimated forest heights are plotted against the terrain slope (on pixel basis in **Fig. 9.2.8**). There is a tendency that positive slopes makes inversion results overestimated while negative slopes lead to underestimation. Height errors increase with the rate of inclination. An angle of +/- 20 degree results in about +/- 10 m height error. Using the Lidar DEM and evaluated as in Equation (4), the impact of topography in Pol-InSAR performance was corrected or mitigated successfully and is shown in **Fig. 9.2.8** in the middle. There is no tendency of overestimation or underestimation on positive and negative slopes visible. Also for the L-band derived DEM (**Fig. 9.2.8** on the right) no trend is seen. Thus, in the absence of an external ground DEM, the impact of topography in Pol-InSAR model can be corrected or reduced by itself.

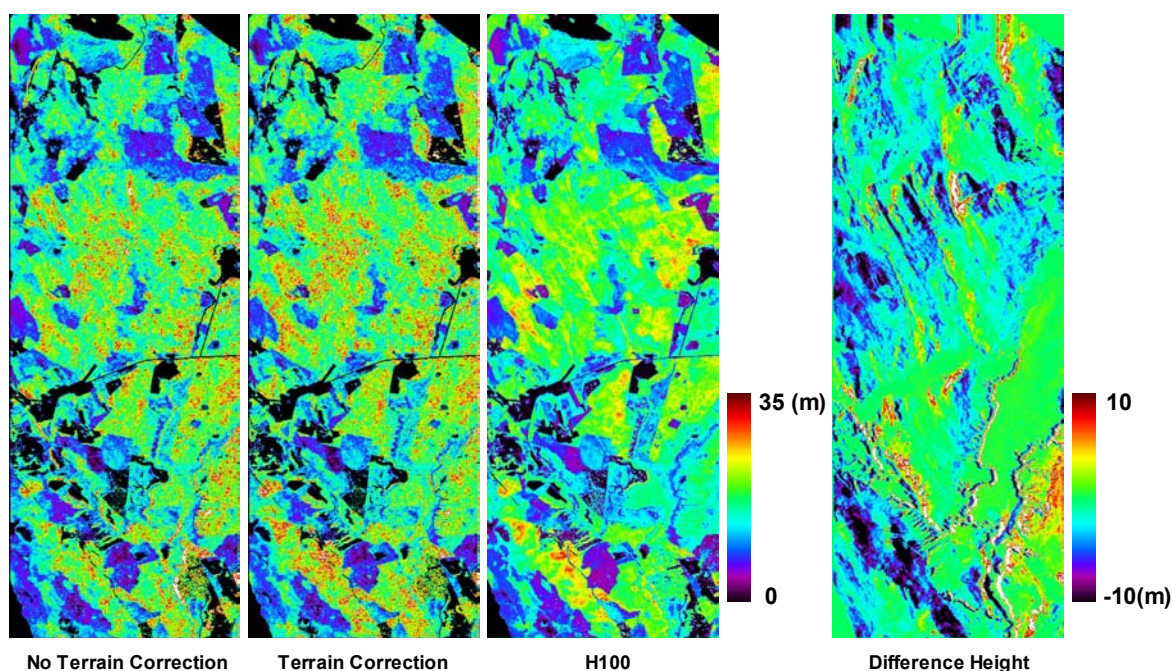


Fig. 9.2.7. Krycklan forest height maps. 1) inversion height without terrain correction. 2) inversion height with terrain correction, 3) Lidar H100 measurements, and 4) difference height between 1) and 2).

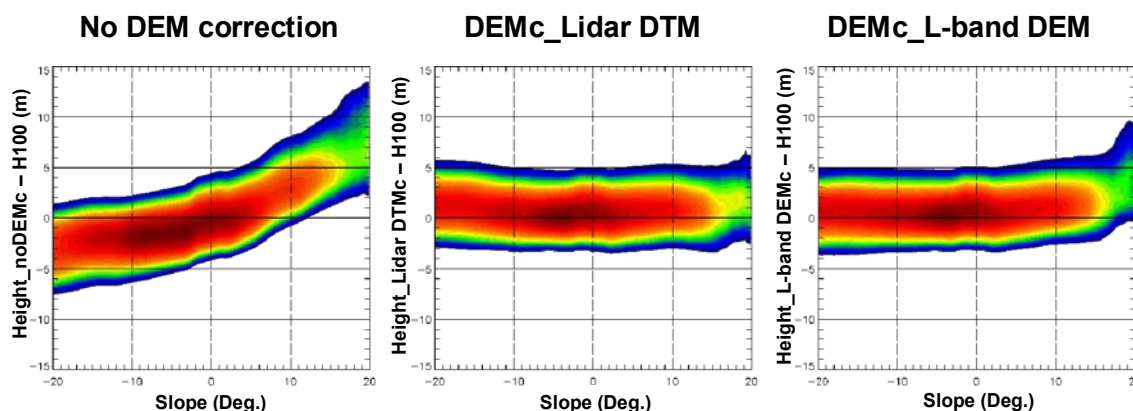


Fig. 9.2.8. The impact of topography. (Left) slope versus height difference between L-band inversion result without correction and Lidar H100. (Middle) Slope versus height difference between L-band inversion result with terrain correction derived from Lidar DEM and Lidar H100. (Right) Slope versus height difference between L-band inversion result with terrain correction derived from L-band DEM and Lidar H100.

9.3.2.2 Pol-InSAR inversion results at L-band and P-band

Forest heights from radar data were inverted using the Random Volume over Ground (RVoG) model [5] and slope correction with Lidar DEM. For comparison and validation of forest height estimates for both flight tracks, inversion results were transformed from slant range geometry to the UTM 34 coordinate. Three types of inversion height maps at L- and P-band were derived. At first, two Pol-InSAR inversion heights were estimated by two different flight tracks (314° and 134° from north). Then this height estimates were merged into one forest height map.

<L-band>

Fig. 9.2.9 shows forest height maps derived from L-band data where the height is scaled between 0 to 35m. Upper left image shows the result from 314° heading and upper right the results from 134° flight heading and on the bottom left the forest height merged by the upper two images is displayed. Lidar H100 is used for validation shown in the bottom right of Fig. 9.2.9 and is overlaid by polygons that were individually selected.

One flight track is exactly 180 degree different to the other one therefore the upper two images have the inclinations of the same absolute slope values but different signs (positive and/or negative).

Upper two forest estimates make clear that Pol-InSAR forest height inversion with terrain correction provides consistent forest height maps at different slopes. Only small parts of the forest areas for the 134° flight direction height map (red circle) were overestimated owing to small local incidence angle (≈ 0). This occurs to near range, small incidence angle and to steep positive gradient data. It makes local incidence angle closed to zero and Pol-InSAR non-valuable. The combination of both track's reduces the variation of estimates and improves forest height inversion.

The comparisons at L-band estimates versus the Lidar H100 with 229 polygons are shown in Fig. 9.2.10. The colour of each plotted point represents the mean slopes of each stand, scaled between -15° and 15°. Inversion heights from 314° and 134° heading reach an γ^2 of 0.91 / 0.92 and with RMSE of 2.16 / 2.23 m for a height range from 5 to 30 m. The correlation coefficient with an γ^2 of 0.94 for a combination of both flight direction estimates is a bit higher, and the RMSE is just 1.32 m (see Fig. 9.2.11 right).

Here, the impact of topography was estimated and quantified by comparing height estimates for both flight directions. The comparison of 314 ° and 134 ° heading results are plotted in **Fig. 9.2.11** left. It is characterized by an γ^2 of 0.91 and an RMSE of 1.69 m for a slope range between -15 ° and 15 °. The estimation accuracy is better than 10 % of mean forest height in hilly terrain area.

In **Fig. 9.2.12** the height validations with the inventory polygons providing 31 stands are plotted also against Lidar H100 height. Compared to the former validation plots, the average in the slope values was reduced because of the larger areas. A γ^2 of 0.88 / 0.89 and an RMSE of 2.11 m / 1.91 m for a height range of 8 to 25 m also prove a good estimation performance at L-band in a hilly boreal forest area.

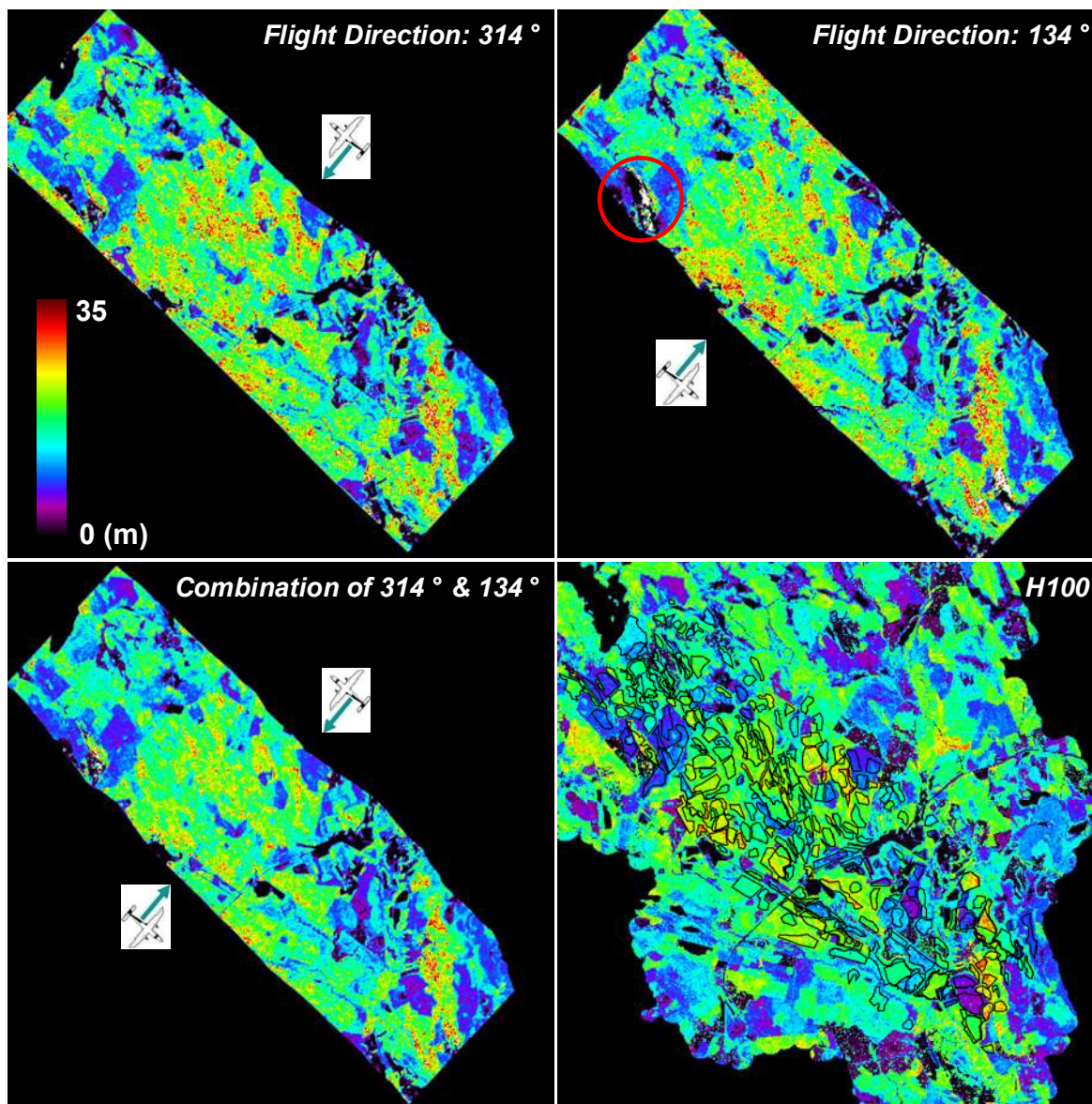


Fig. 9.2.9. Forest height maps at L-band, scaled from 0 to 35 m. (Upper left) L-band inversion height in 314 deg. flight direction, (Upper right) L-band inversion height in 134 deg. flight direction, (Bottom left) combination height, and (Bottom right) Lidar H100 measurements with polygons.

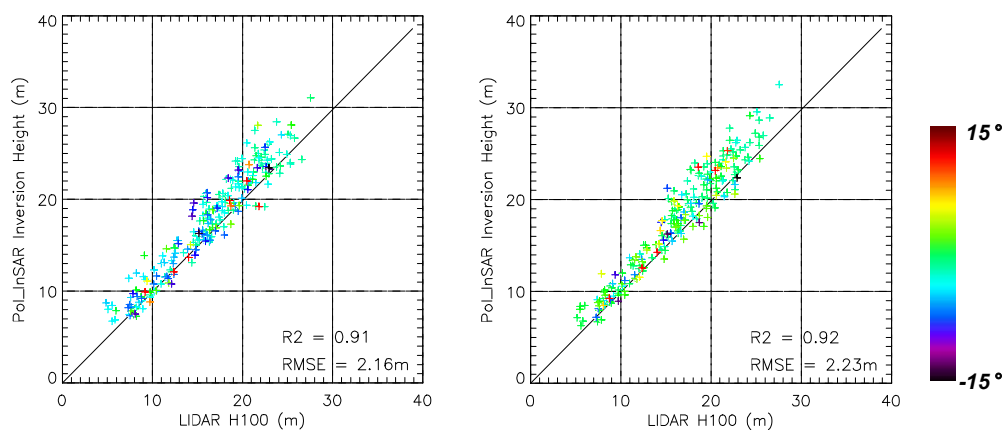


Fig. 9.2.10. *Pol_InSAR* height estimates at L-band versus Lidar H100 validation plots for Krycklan forest. (Left) 314 deg. flight direction, and (Right) 134 deg. flight direction.

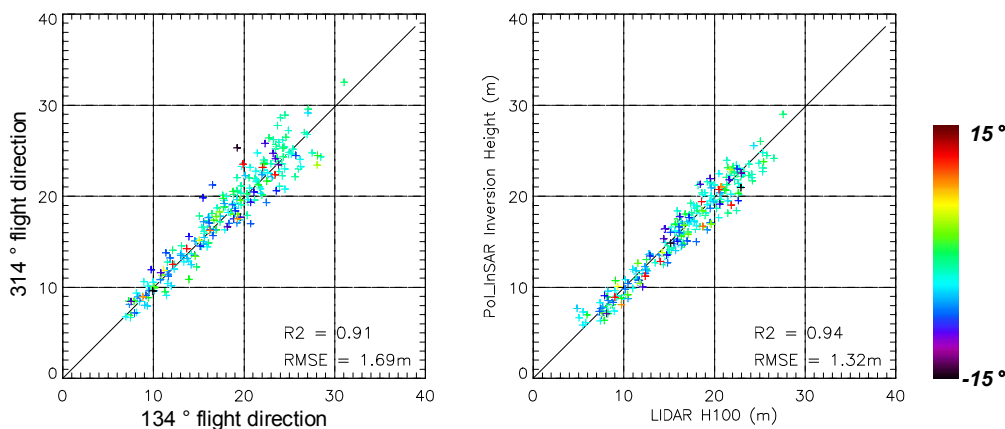


Fig. 9.2.11. (Left) Comparison of 314 deg. and 134 deg. flight directions results. (Right) Combined *Pol_InSAR* estimates at L-band versus Lidar H100 validation plot for Krycklan forest.

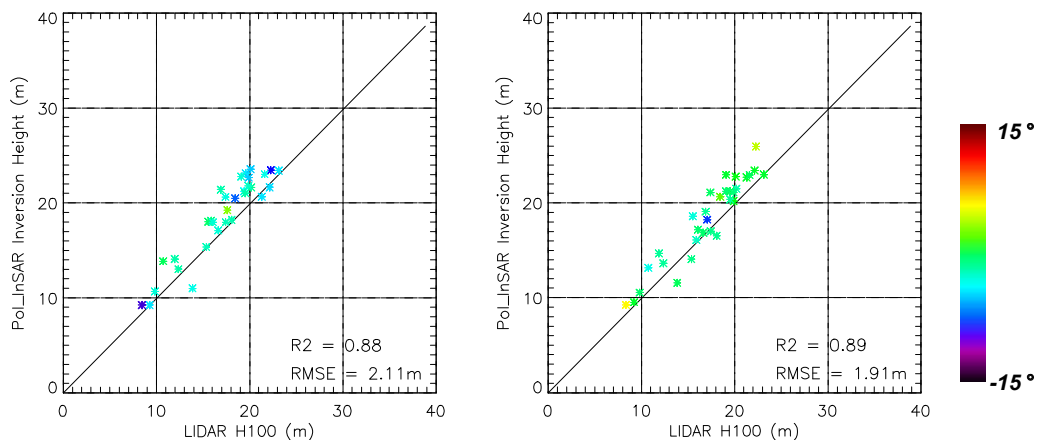


Fig. 9.2.12. *Pol_InSAR* height estimates at L-band versus Lidar H100 validation plots with 31 stands which were used for field survey. (Left) 314 deg. flight direction, and (Right) 134 deg. flight direction

<P-band>

Similar to L-band, P-band estimates were validated by Lidar H100 and compared with both flight tracks.

In **Fig. 9.2.13** from P-band forest height derived maps are displayed. On the upper left the forest height map derived from the 314 ° and upper right from the 134 ° flight heading are presented. In the bottom left the combined height map of both flight headings is shown. Finally on the bottom right the Lidar H100 overlaid with the selected polygons, scaled from 0 to 35 m is presented.

Forest heights were estimated using a multi-baseline inversion approach. The reason for it is the strong variation of the radar look angle in the airborne case. The variation of the look angle goes along with a change of baseline, implying an inversion performance that varies along range [6] . In general, the effective baseline decreases along range in consequence regions in far range with small spatial baselines have a too high sensitivity to volume. Large spatial baselines are useful to recover this kind of variation. However, the P-band acquisitions have a relatively small vertical wave number (mean k_z : 0.022 – 0.136) due to the simulation of 6 MHz spaceborne data. In upper images of **Fig. 9.2.13**, forest heights were slightly overestimated in far range. After combining two forest height maps a stable forest height map in spite of limited small k_z range is obtained.

P-band results were also validated against the Lidar H100 stands. The comparisons against H100 are shown in **Fig. 9.2.14**. The plots showing P-band estimates for each flight track with γ^2 of 0.62 / 0.61 and an RMSE of 4.07 m / 4.05 m in 314° / 134° heading, for height ranges between 5 and 30m. Compared to L-band P-band estimates have a lower correlation coefficient and higher RMSE. Recent P-band experiments in boreal like forest showed underestimation of forest height estimates. The reason for this is supposed to be in the deviations of the real vertical forest structure from the one assumed by the Random-Volume-over-Ground (RVoG) model [7] . Using the combination of both flight headings improves a bit the correlation coefficient and the RMSE (0.65 / 3.85m) shown in **Fig. 9.2.15** left. This result proves that topographical effects can be also corrected and mitigated at P-band.

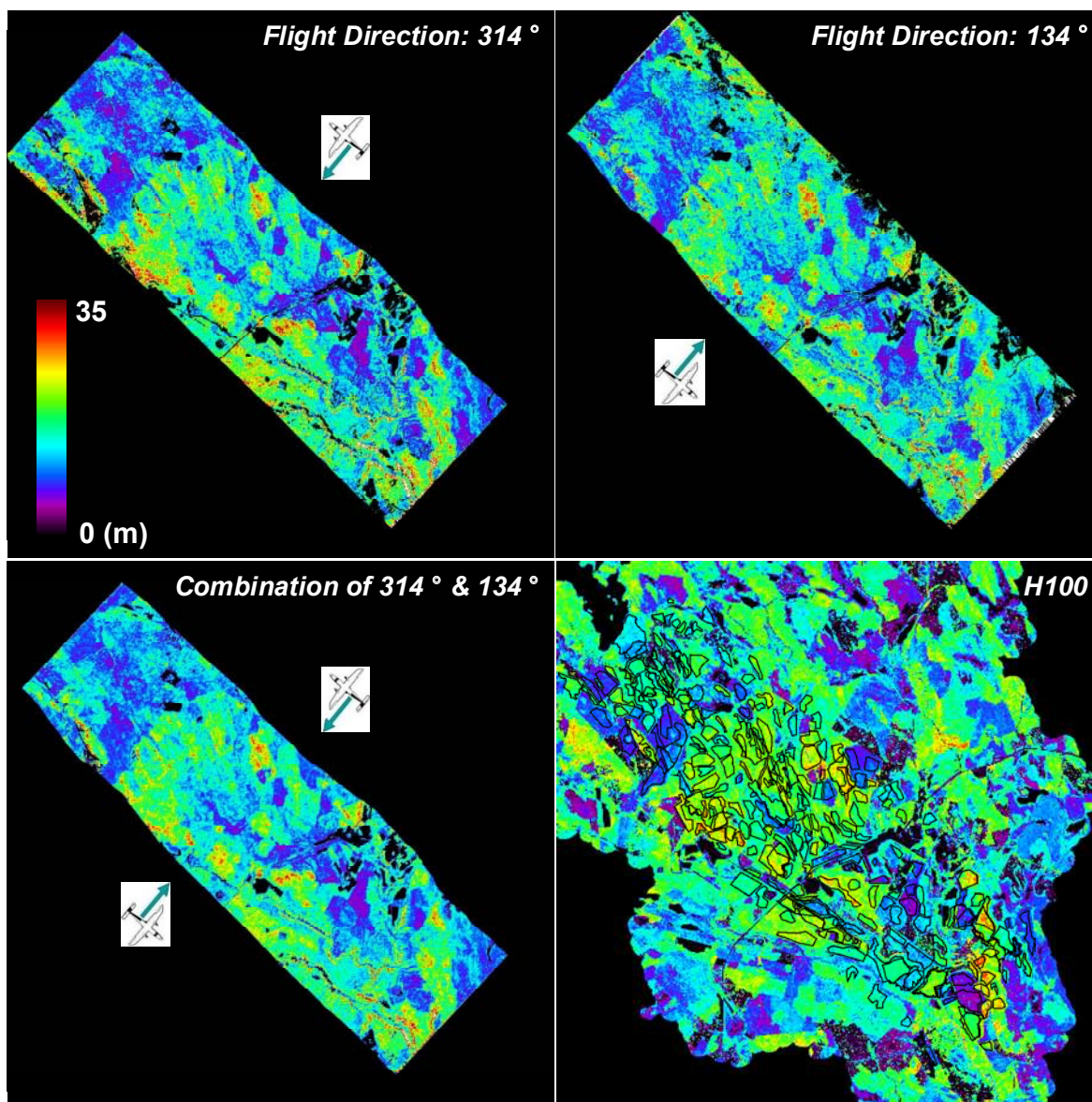


Fig. 9.2.13. Forest height maps at P-band, scaled from 0 to 35 m. (Upper left) P-band inversion height in 314 deg. flight direction, (Upper right) P-band inversion height in 134 deg. flight direction, (Bottom left) combination height, and (Bottom right) Lidar H100 measurements with polygons.

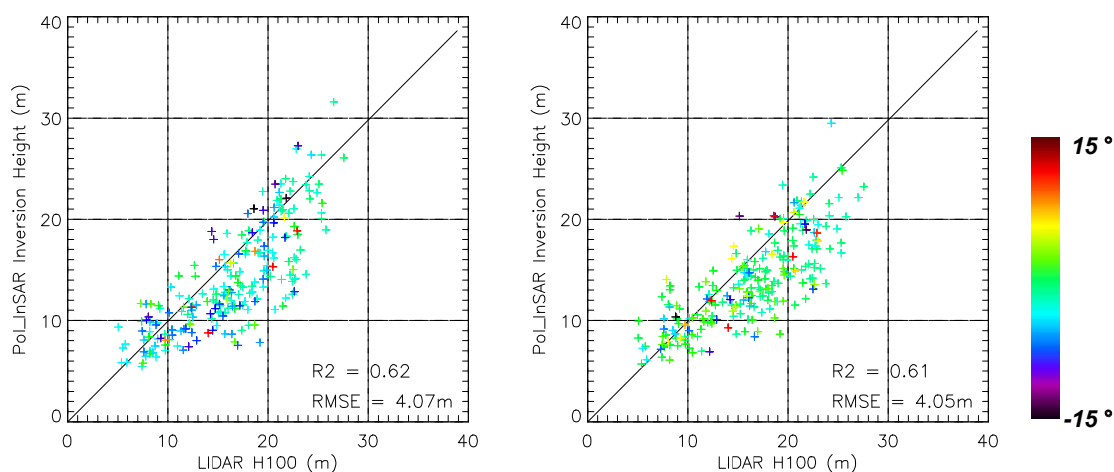


Fig. 9.2.14. Pol-InSAR height estimates at P-band versus Lidar H100 validation plots for Krycklan forest. (Left) 314 deg. flight direction, and (Right) 134 deg. flight direction.

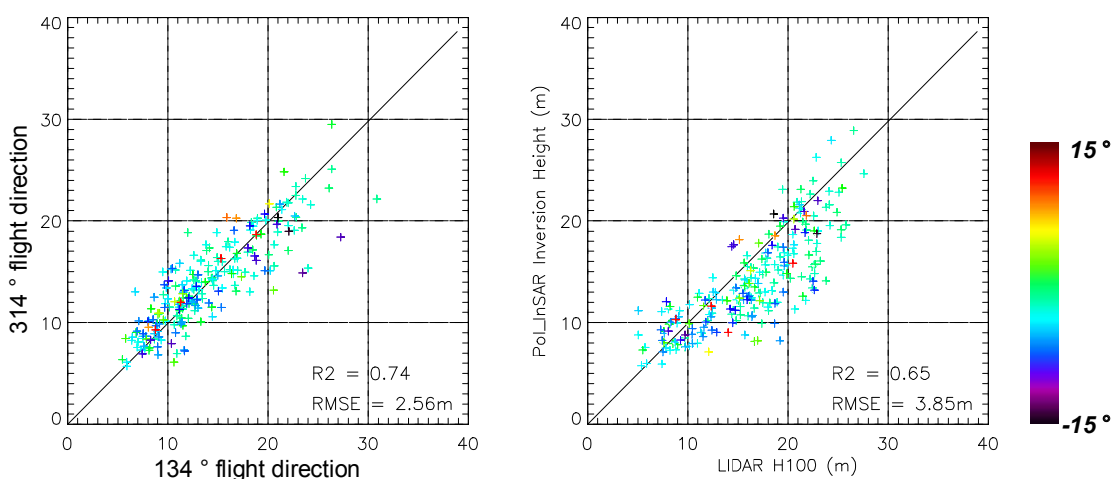


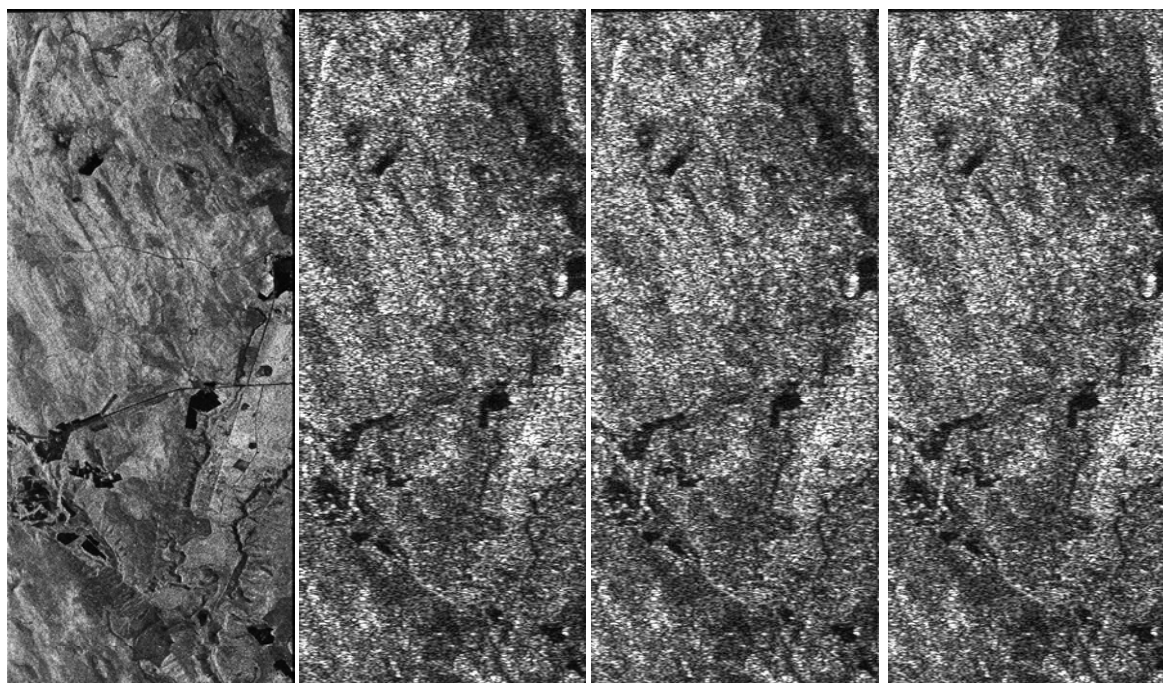
Fig. 9.2.15. (Left) Comparison of 314 deg. and 134 deg. flight directions results. (Right) Combined Pol-InSAR estimates at P-band versus Lidar H100 validation plot for Krycklan forest.

9.3.3 Spaceborne simulation data at P-band

The estimation of forest height (and its close relation to forest biomass) becomes important in the frame of the ESA’s Earth explorer BIOMASS mission. In this study the impact of sensor related parameters (bandwidth (6 MHz), NESZ, range/azimuth ambiguities) on the Pol-InSAR inversion performance is assessed.

The performance analyses are done on the BioSAR 2008 acquired data. The P-band 314° flight heading was selected (Table 1) for reprocessing the SAR data in order to obtain the simulated spaceborne data with the BIOMASS mission specification [8]. The impact of the longer wavelength and the repeat pass time is investigated using the filtered 6 MHz P-band data. A comparison of the inversion results between 94 MHz and 6 MHz bandwidth in P-band data is performed and discussed.

Fig. 9.2.16 shows HH amplitude images and three levels (spatial resolution, NESZ, and Rg/Az ambiguities) simulation data. The simulation starts with the full resolution polarimetric scattering matrix data of airborne acquisition. The output of each simulation step serves as input to the next steps [8] .



Airborne (Bw=94MHz) Spaceborne (Bw=6MHz) Spaceborne (NESZ=-28dB) Spaceborne (Rg/Az Amb)

Fig. 9.2.16. HH polarization amplitude images of Krycklan forest. 1) P-band airborne SAR data. Simulation data after 2) reducing the resolution, 3) increasing the Noise-Equivalent- Sigma-Zero (NESZ), and 4) inserting ambiguities.

9.3.3.1 Coherence

Fig. 9.2.17 shows the HH coherence amplitude images corresponding to E-SAR airborne SAR data and there levels (spatial resolution, NESZ, and ambiguities) of reprocessed data for a 16m spatial baseline. Resolution was changed in a first step by reducing the range and azimuth signal bandwidth. The reprocessed SAR products have a spatial resolution of 25 x 12.5 m while the airborne SAR data having 1.49 m range resolution. In general it can be stated that the interferometric coherences of the simulated data have lower coherence levels comparing to the airborne data. Especially, in hilly terrain the coherences decreasing stronger due to the increase of range decorrelation for small bandwidth.

Histograms of coherences at different polarization for the simulated data are plotted in **Fig. 9.2.18**. To avoid the strong range decorrelation effect, spatial baselines were designed to have small k_z . Therefore, airborne SAR data show high coherence levels (HH: 0.94 / HV: 0.90 / VV: 0.95). After reducing the bandwidth coherence level drops to 0.85 in HH polarization. Decreasing homogeneity in large window size (about 100 X 100 m) mainly affects to coherence. The NESZ and the ambiguity changes affect also the coherence level but lower than the changes in the bandwidth. However, higher NESZ and ambiguity levels leads to decrease the coherence level comparable to the coherence level of airborne cross-polarised coherences.

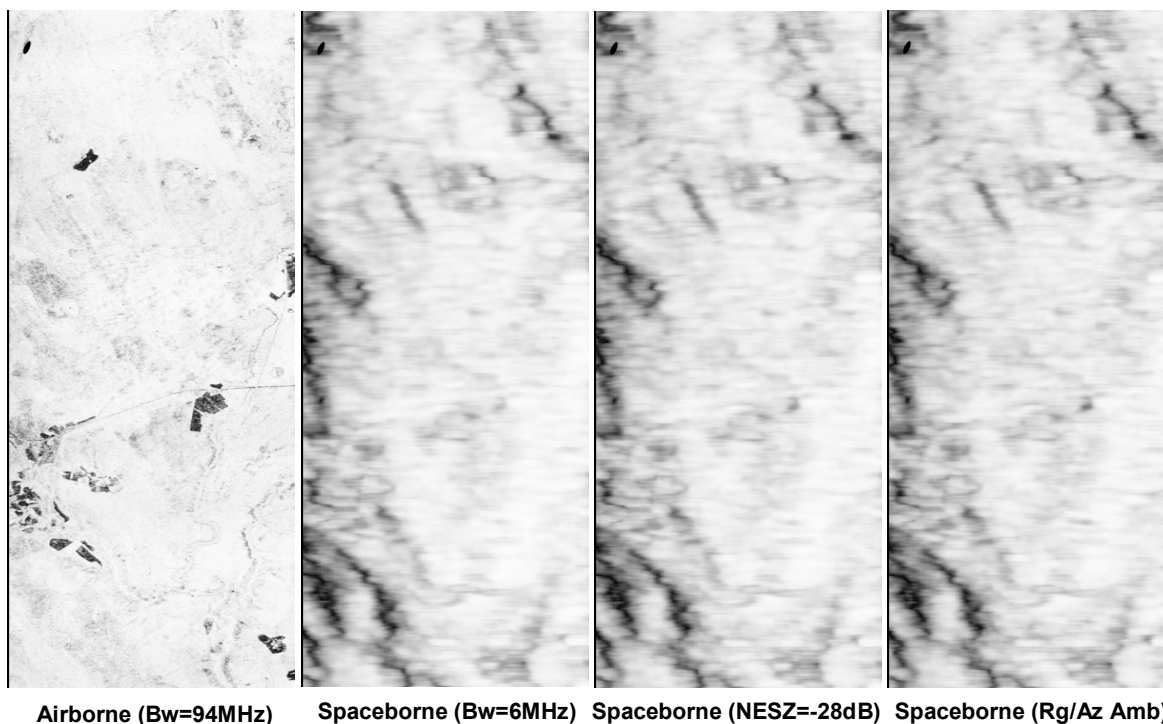


Fig. 9.2.17. HH polarization coherence maps of Krycklan forest: E-SAR airborne SAR (Left) and three levels of simulation steps (resolution, NESZ, and Rg/Az ambiguities), scaled 0 to 1.

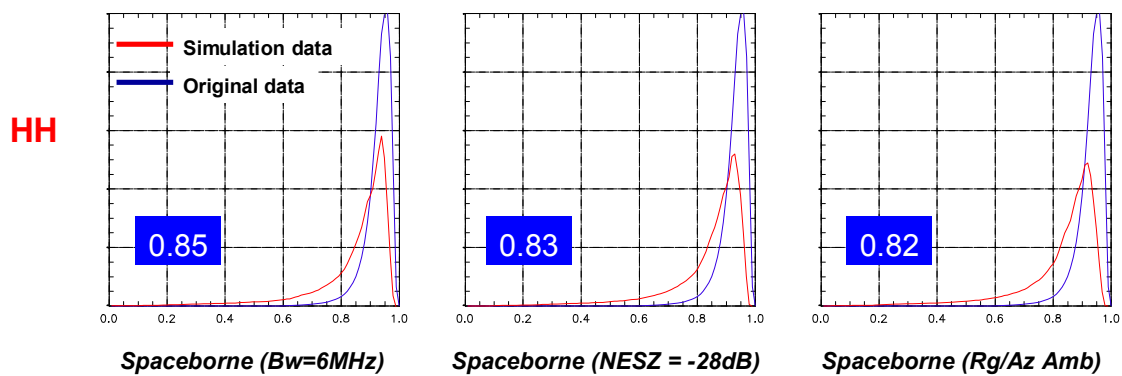
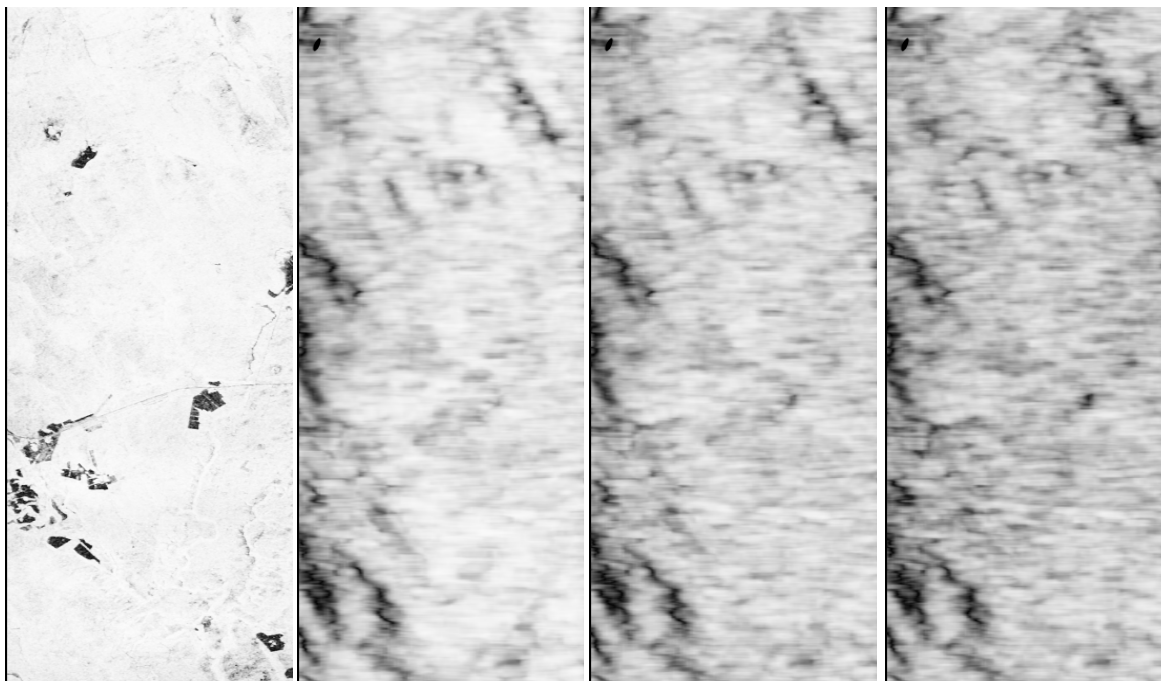


Fig. 9.2.18. HH Coherence histograms (blue: E-SAR, red: simulation data). (Left) Resolution, (Middle) NESZ, and (Right) range and azimuth ambiguities.



Airborne (Bw=94MHz) Spaceborne (Bw=6MHz) Spaceborne (NESZ=-28dB) Spaceborne (Rg/Az Amb)

Fig. 9.2.19 HV polarization coherence maps of Krycklan forest: E-SAR airborne SAR (Left) and three levels of simulation steps (resolution, NESZ, and Rg/Az ambiguities), scaled 0 to 1.

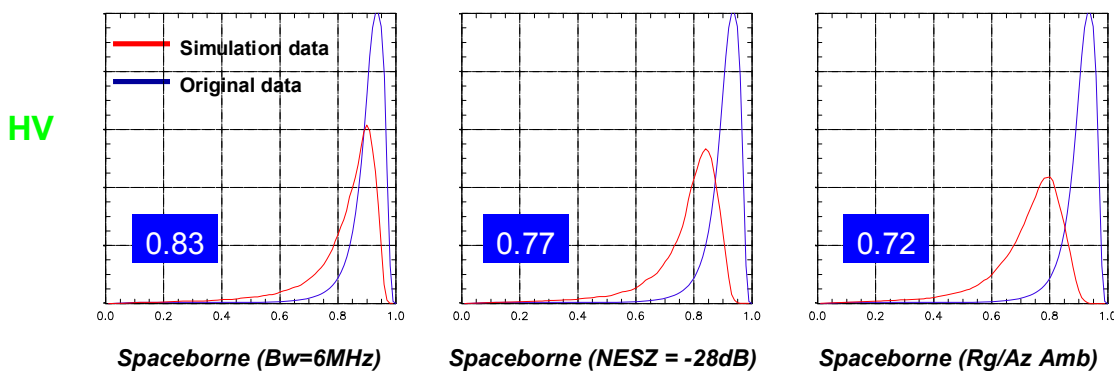
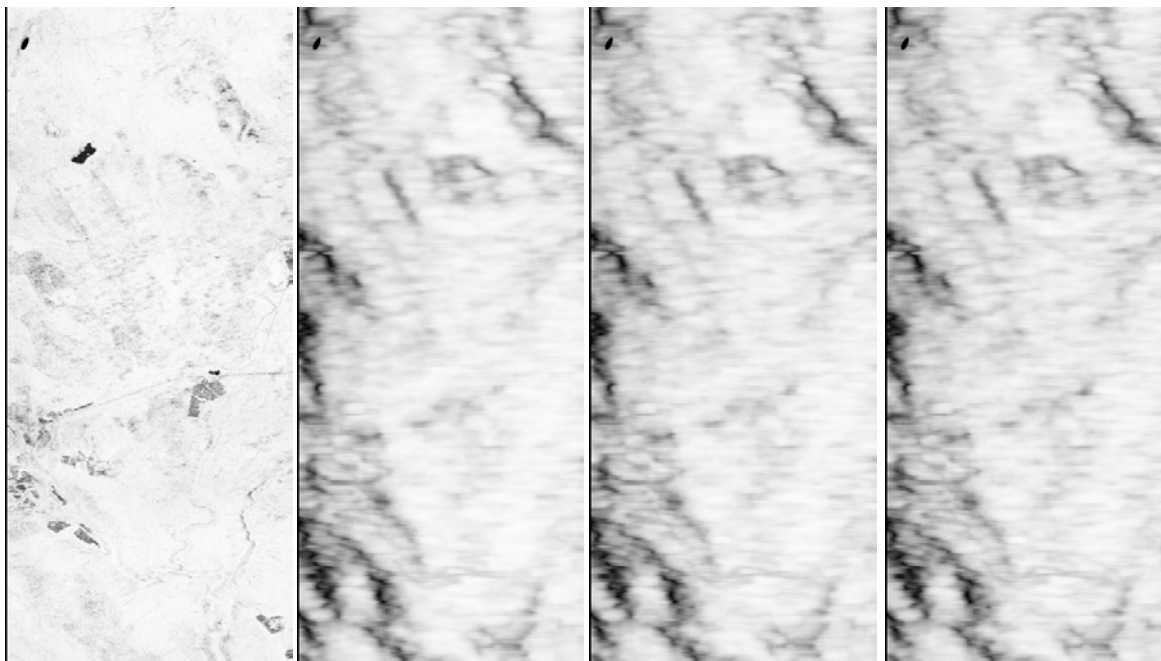


Fig. 9.2.20. HV Coherence histograms (blue: E-SAR, red: simulation data). (Left) Resolution, (Middle) NESZ, and (Right) range and azimuth ambiguities.



Airborne (Bw=94MHz) Spaceborne (Bw=6MHz) Spaceborne (NESZ=-28dB) Spaceborne (Rg/Az Amb)

Fig. 9.2.21. HH polarization coherence maps of Krycklan forest: E-SAR airborne SAR (Left) and three levels of simulation steps (resolution, NESZ, and Rg/Az ambiguities), scaled 0 to 1.

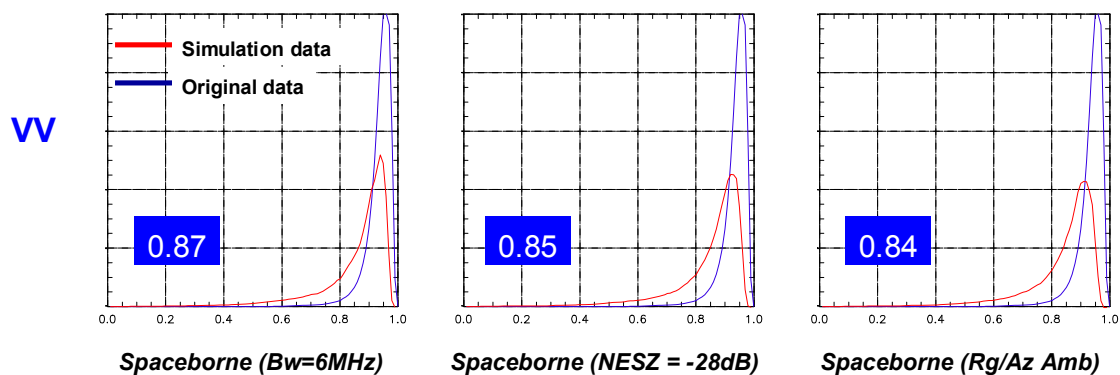


Fig. 9.2.22. VV Coherence histograms (blue: E-SAR, red: simulation data). (Left) Resolution, (Middle) NESZ, and (Right) range and azimuth ambiguities.

9.3.3.2 Pol-InSAR inversion

Forest height inversion with the reprocessed SAR data according to the BIOMASS specification is performed and is shown in **Fig. 9.2.23** middle. The forest height derived from the simulated heights is higher than the height estimates using the airborne data. Especially, forest heights in hilly area are higher. After changing the scale of the forest height (10 to 45 m), inversion result becomes similar to airborne SAR case. In spite of low resolution, noise, and ambiguities Pol-InSAR inversion result have still certain sensitivity to forest structure in the Krycklan forest.

Fig. 9.2.24 shows the comparison of Pol-InSAR inversion results obtained from airborne data and simulated data. There is a tendency that the inverted forest heights from the simulated data are higher than obtained from the airborne data. After normalizing by the total number of samples for a given airborne Pol-InSAR inversion height, it can be shown that low forests areas are more affected by the imposed constraints from the mission design than higher forests (see normalized 2-D histograms in Fig. 9.2.24). This can be seen as uncompensated decorrelation effects that causes more overestimation in lower forests [6].

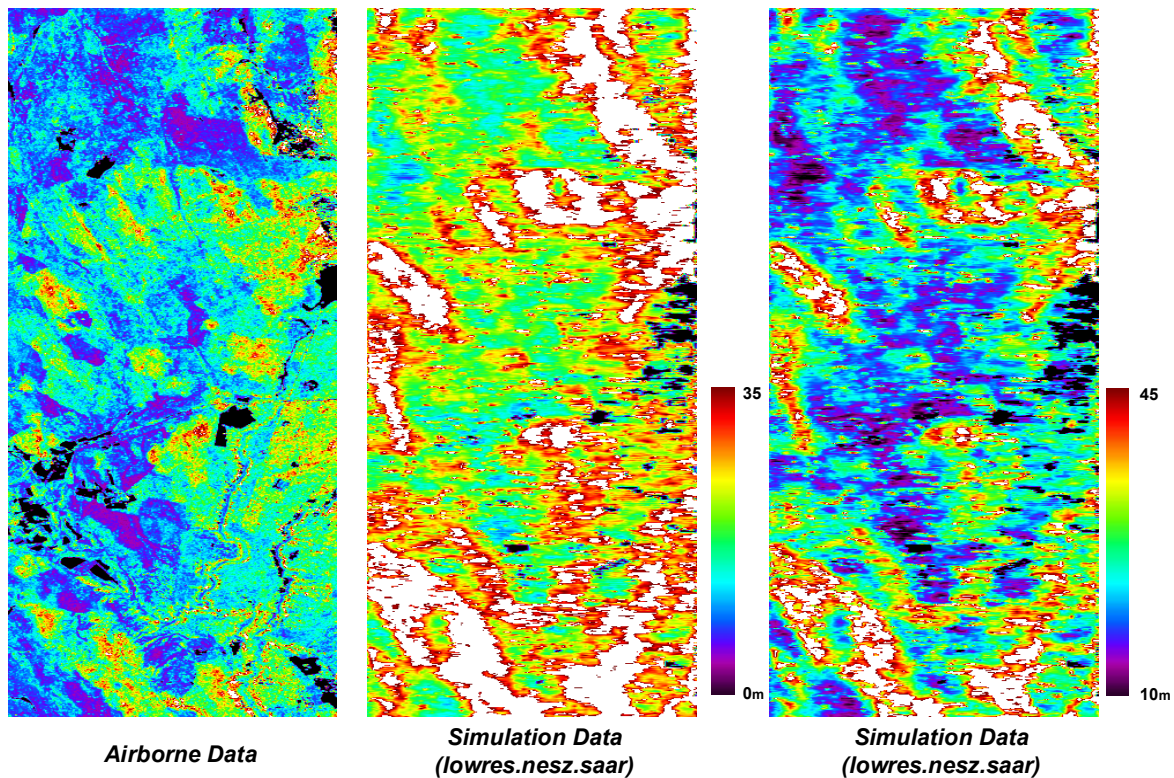


Fig. 9.2.23. Forest height maps for Krycklan forest. (Left) E-SAR airborne SAR inversion result, scaled 0 to 35 m, (Middle) simulation data inversion height, scaled 0 to 35 m, (Right) simulation data inversion height, scaled 10 to 45 m.

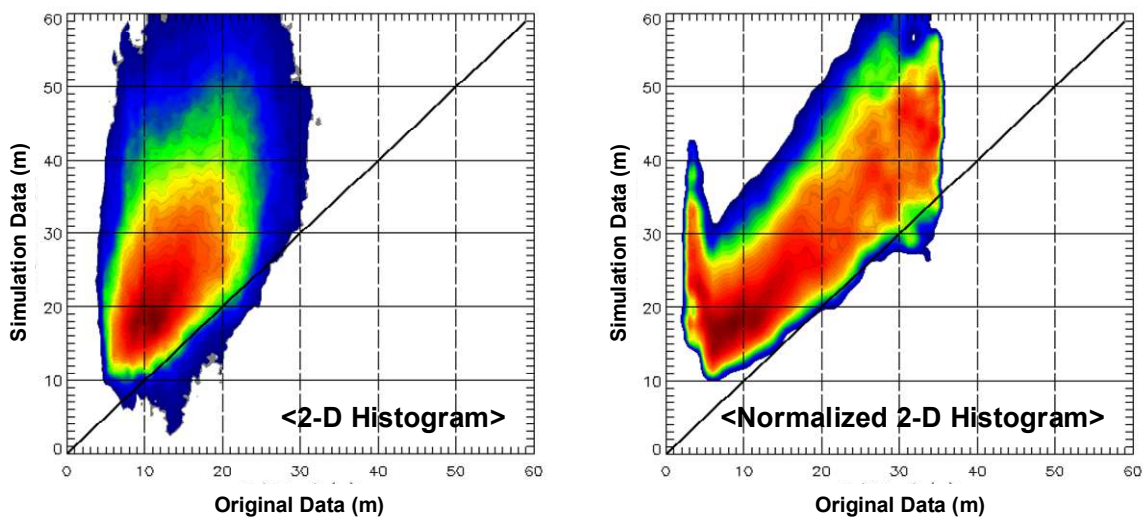


Fig. 9.2.24. Pol-InSAR inversion height comparison between airborne data (94 MHz bandwidth) and simulation data (6 MHz bandwidth plus additional noise and ambiguities). (Left) 2-D histogram, (Right) normalized 2-D histogram.

9.3.4 Summary and Recommendation

The data have been abundantly acquired by L- and P-band on various spatial baselines and in two flight tracks considering to ascending and descending modes. Field survey data and Lidar measurements were also obtained and used for validation and comparison. In addition to those, P-band spaceborne simulation data were generated by the simulation strategy according to the BIOMASS (P-band) mission specification.

Impact of slope: The impact of topography in forest height retrieval performance was investigated using two differently derived digital elevation models: the high resolution Lidar DEM and the repeat pass derived airborne L-band DEM. Both data sets were helpful for slope correction in Pol-InSAR inversion model. Vertical wavenumber (kz) corrected by slope for two DEMs did not introduce any bias in forest height estimation. In addition, corrected inversion results were double-checked by the comparison of two flight directions. For both flight headings introducing different local incidence angles the same quality of forest height at L- and P-band could be obtained. The correlation coefficient and RMSE were just 0.91 / 1.69 m at L-band and 0.74 / 2.56 m at P-band, height ranges from 5 to 30 m. These results show that topography effects can be corrected and mitigated using Pol-InSAR model-based inversion processing.

Pol-InSAR inversion & validation: The forest height retrieval for high-latitude boreal forests was estimated and verified for ascending and descending modes at L- and P-band. Especially, in L-band a wider range of spatial baselines were available.

For the Krycklan test-site, the Pol-InSAR forest height estimates have been validated against H100 values derived from Lidar measurements and field inventory data. For forest heights ranging from 5 to 30 m, L- and P-band estimates were stable even in hilly terrain. L-band estimates were characterized by an γ^2 of 0.94 with an RMSE of 1.32 m, while P-band estimates showed an γ^2 of 0.65 with an RMSE of 3.85 m. The overall estimation accuracy in Krycklan was better than 10% for L-band (but, 20 % for P-band). L-band result presented higher correlation coefficient and lower RMSE than P-band. This is probably caused by a smaller available P-band kz range and the less sensitivity of the longer wavelength.

P-band simulation data: The P-band spaceborne simulation data according to the BIOMASS mission design were used for this study. The simulation started with full resolution of airborne SAR data and reduced range-azimuth resolutions of 25 X 12.5 m. The key limiting factor in coherence estimation for HH-, VV-, and HV-polarizations appears to be the reduced spatial resolution. The interferometric coherence levels dropped about 0.1. The higher NESZ and ambiguities affected definitely HV coherence level while co-polarization kept their coherence level.

However, for the forest height inversion the simulated data kept enough coherence level to apply forest inversion. A first comparative analysis for simulated P-band data applying forest height inversion has been presented. Inversion results were several meter higher and had larger variation than airborne SAR estimates.

The impact of parameters relating to the propagation path (ionosphere) and to temporal decorrelation should be considered and further studied.

9.3.5 References

- [1] BioSAR, Final Reprot, ESTEC Contract No. RFQ/3-20755/07/NL/CI.
- [2] T. Mette, K. P. Papathanassiou, I. Hajnsek, "Biomass estimation from polarimetric SAR interferometry over heterogeneous forest terrain", Proceeding of IEEE Geoscience and Remote Sensing Symposium (IGARSS 2004), 20. - 24. September, Anchorage, Alaska, 2004.
- [3] H. Kramer, A. Akca, "Leitfaden zur Waldmesslehre", Sauerländer, Frankfurt, 1995 p. 145.
- [4] R. Bamler, P. Hartl, "Synthetic aperture radar interferometry", *Inverse Problems*, vol.14, no. 4, pp. R1-R54, 1998.
- [5] S.R. Cloude and K.P., Papathanassiou, "Three-stage inversion process for polarimetric SAR interferometry", *IEE Proceedings - Radar Sonar and Navigation*, vol. 150, no. 3, pp. 125-134, 2003.
- [6] I. Hajnsek, F. Kugler, S.-K. Lee, K. P. Papathanassiou, "Tropical-Forest-Parameter Estimation by means of Pol-InSAR: The INDREX II Campaign, *IEEE Transactions on Geoscience and Remote Sensing*, vol. 47, no. 2, pp. 481 – 493, February 2009.
- [7] F. Kugler, S. K. Lee and K. P. Papathanassiou, "Estimation of forest vertical structure parameter by means of POL-InSAR", *IEEE Geoscience and Remote Sensing Symposium (IGARSS)*, Cape town, South Africa, July 2009
- [8] Scheiber, R., Lee, S.-K., Papathanassiou, K.P. and Floury, N., "Extrapolation of Airborne Polarimetric and Interferometric SAR Data for Validation of Bio-Geo-Retrieval Algorithms for Future Spaceborne Missions", *Proc. IGARSS 2009*, Cape Town, South Africa, July 2009.

9.4 Assessment of tomography by POLIMI

9.4.1 Work objectives

This work addresses the development and assessment of processing techniques aimed at the retrieval of the three dimensional (3D) structure of forested areas through the coherent exploitation of multi-polarimetric and multi-baseline (MPMB) SAR surveys.

Possible incoming spaceborne SAR systems such as BioMass [1], Tandem-L [2], and SAOCOM [3], pose the bases for unprecedented capabilities as for the investigation of the Earth's surface at longer wavelengths. In particular, the enhanced interferometric capabilities of such systems will provide for the first time the concrete possibility to investigate the 3D structure of forested areas, therefore constituting major tools for providing the Scientific Community with a new kind of information about Radar scattering from forested areas at vast scales.

For these reasons, the data-set available in the framework of BioSAR 2008 constitutes an extremely important opportunity for the experimental assessment of the potentials and limitations relative to the inference of the 3D structure from SAR observations. In particular, this work has been carried out with the following purposes in mind:

- Validation of the proposed processing techniques for application at P-Band and L-Band;
- Comparison and discussion of the results obtained at different wavelengths;
- Analysis of the results achieved basing on low resolution P-Band data emulating BioMass spaceborne acquisitions.

As agreed at KOM, the following points have been specifically addressed:

- Validation of Phase Calibration techniques required for Tomographic analyses;
- Identification of bald and forested areas;
- Retrieval of Terrain and canopy elevation;
- Separation of the backscattered powers associated with ground and volume contributions;
- Study and interpretation of the topographical effects on the tomographic signature

9.4.2 Description of the Data

The test site selected for the BIOSAR 2008 campaign is the forested area within the Krycklan River catchment, Northern Sweden. The data available for WP 44 is represented by 5 sets of single look complex (SLC), fully polarimetric, SAR images in Radar Geometry (RGI products). Each data-set is constituted by 6 interferometric tracks (five baselines) for each polarimetric channel. The test site has been imaged from two opposite points of view at both P-Band and L-Band, as the SAR sensor has been flown with look direction South-West (SW) or North-East (NE). Additionally, a new data-set emulating BioMass data has been obtained by processing the SW P-Band data-set. The acquisition campaign has been carried on October 14 (P-Band) and October 15 (L-Band) 2008. The parameters of the acquisition system are briefly summarized in Table 2, Table 3, and Table 4.

P-Band		
Look Directions	<i>South-West</i> <i>North-East</i>	
Carrier Frequency	f_0	350 [MHz]
Carrier Wavelength	λ	0.86 [m]
Sampling Frequency	f_s	100 [MHz]
Slant Range Resolution	dr	2.12 [m]
Azimuth Resolution	da	1.6 [m]
Horizontal Baseline Spacing	db	8 [m]
Total Horizontal Baseline Aperture	A	40 [m]
Look Angle	θ	25° (Near Range) – 55° (Far Range)
Flight Height	H	3900 [m]

Table 2: Parameters of the acquisition system: P-Band

L-Band		
Look Directions	<i>South-West</i> <i>North-East</i>	
Carrier Frequency	f_0	1.300 [MHz]
Carrier Wavelength	λ	0.23 [m]
Sampling Frequency	f_s	100 [MHz]
Slant Range Resolution	dr	2.12 [m]
Azimuth Resolution	da	1.2 [m]
Horizontal Baseline Spacing	db	6 [m]
Total Horizontal Baseline Aperture	A	30 [m]
Look Angle	θ	25° (Near Range) – 55° (Far Range)
Flight Height	H	3900 [m]

Table 3: Parameters of the acquisition system: L-Band

BIOMASS Emulation		
Look Direction	<i>South-West</i>	
Carrier Frequency	f_0	350 [MHz]
Carrier Wavelength	λ	0.86 [m]
Sampling Frequency	f_s	100 [MHz]
Slant Range Resolution	dr	25 [m]
Azimuth Resolution	da	16 [m]
Horizontal Baseline Spacing	db	8 [m]
Total Horizontal Baseline Aperture	A	40 [m]
Look Angle	θ	25° (Near Range) – 55° (Far Range)
Flight Height	H	3900 [m]

Table 4: parameters of the acquisition system: BioMass Emulation

Data focusing, amplitude calibration, motion compensation, and co-registration has been performed by DLR, according to standard procedures used for pre-processing PolInSAR data. The data-set emulating BioMass acquisitions have been provided by DLR.

Along with the SLC RGI data, the following ancillary products have been exploited for the analyses:

- Coefficients for height to phase conversion (kz); provided by DLR.
- Reference Phases corresponding to flat terrain; provided by DLR.
- Warping maps used for geocoding each data-set on a common reference grid; provided by DLR.
- Calibrating Phases (P-Band only); provided by DLR.
- LIDAR measurements relative to canopy elevation; provided by FOI.
- LIDAR measurements relative to terrain elevation; provided by FOI.

OK for data downloading has been released on March 19 2009

9.4.3 Preliminary Analysis

This section is devoted to providing a qualitative analysis of the characteristics of the BioSAR 2008 data-sets, in dependence of terrain topography and canopy height.

Figure 1 shows a map of the forest height in the geometry of the the P-Band SW data-set. Forest height has been obtained from LIDAR measurements provided by FOI, by evaluating the H100 height [4] in ground geometry and resampling the result into SAR geometry. To this aim, accurate geocoding and inverse geocoding procedures have been defined, in order to modify the warping maps provided by DLR in such a way as to account for volume height above the ground.

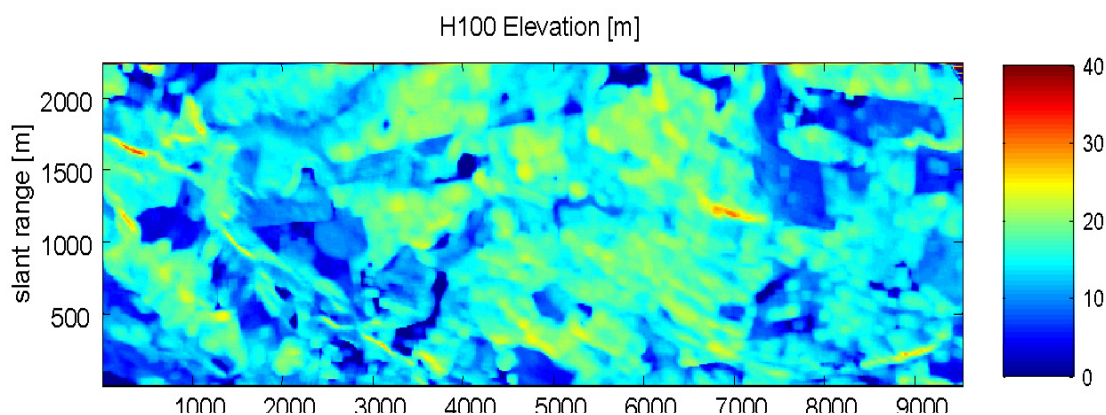


Figure 1: H100 Elevation in RGI Geometry

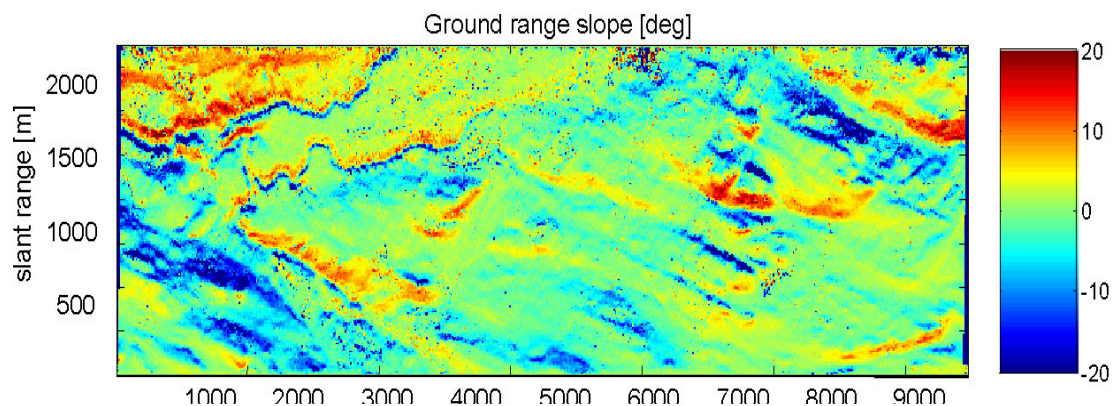


Figure 2: Ground Range Slopes. Positive values occur when terrain is tilted toward the SAR sensor

The imaged scene presents a hilly topography, with elevation over the sea level ranging to 150 m to 400 m. Figure 2 reports the map of ground slopes in the geometry of the P-Band SW data-set. The map shown in such a figure has been derived from the P-Band SW data-set itself, after retrieving terrain elevation through a joint processing of all tracks. Further details about DEM retrieval are provided in the remainder.

Figure 3 reports the mean reflectivity in polarization HH, averaged over all tracks, for data-sets P-Band SW and L-Band SW. As expected at longer wavelengths, open areas, or areas characterized by the

presence of low vegetation, exhibit a lower intensity than forested areas. This phenomenon is more visible at P-Band, where backscattering in forested areas dominates by about 20 dB.

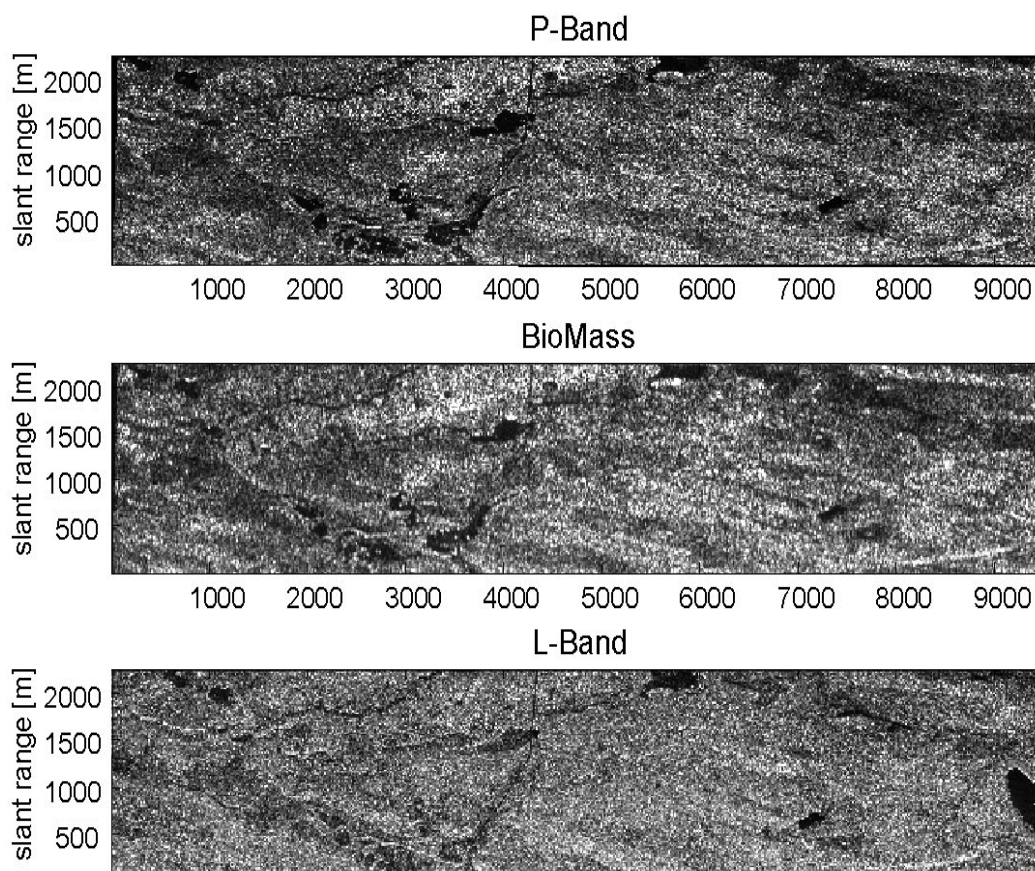


Figure 3: Mean Reflectivity in Polarization HH for the P-Band SW, L-Band SW, and BioMass data-sets.

9.4.3.1 Interferometric Coherence and Phase

Figure 4, Figure 6, Figure 7 report the interferometric coherence and phase observed in polarization HH for the P-Band SW, L-Band SW, and BioMass data-sets, evaluated by exploiting a spatial averaging window as large as 60 x 60 m (ground range, azimuth). All cases are relative to the maximum baseline available, corresponding to 30 m at L-Band at 40 m at P-Band. All interferograms have been phase-flattened by exploiting the reference phases corresponding to flat terrain, provided by DLR.

As for the P-Band SW data-set, in first place it may be observed that decorrelation mainly occurs in non vegetated areas, consistently with the weak surface scattering contributions that are expected to occur at P-Band. Forested areas, instead, exhibit quite high coherence values. Accordingly, the P-Band data-set is loosely affected by volume decorrelation. This phenomenon is partly due to the fact that the overall baseline aperture does not provide a large sensitivity to height at P-Band. On the other hand, however, it is also an indicator of weak volume contributions with respect to ground scattering. In order to provide a more quantitative kind of argument, Figure 5 reports the theoretical value of the interferometric coherence for the P-Band SW data-set at a baseline of 40 m, evaluated in correspondence of the vegetation height map in Figure 1. Volume scattering has been modeled as being constituted by a uniform layer of a certain height within the SAR resolution cell.

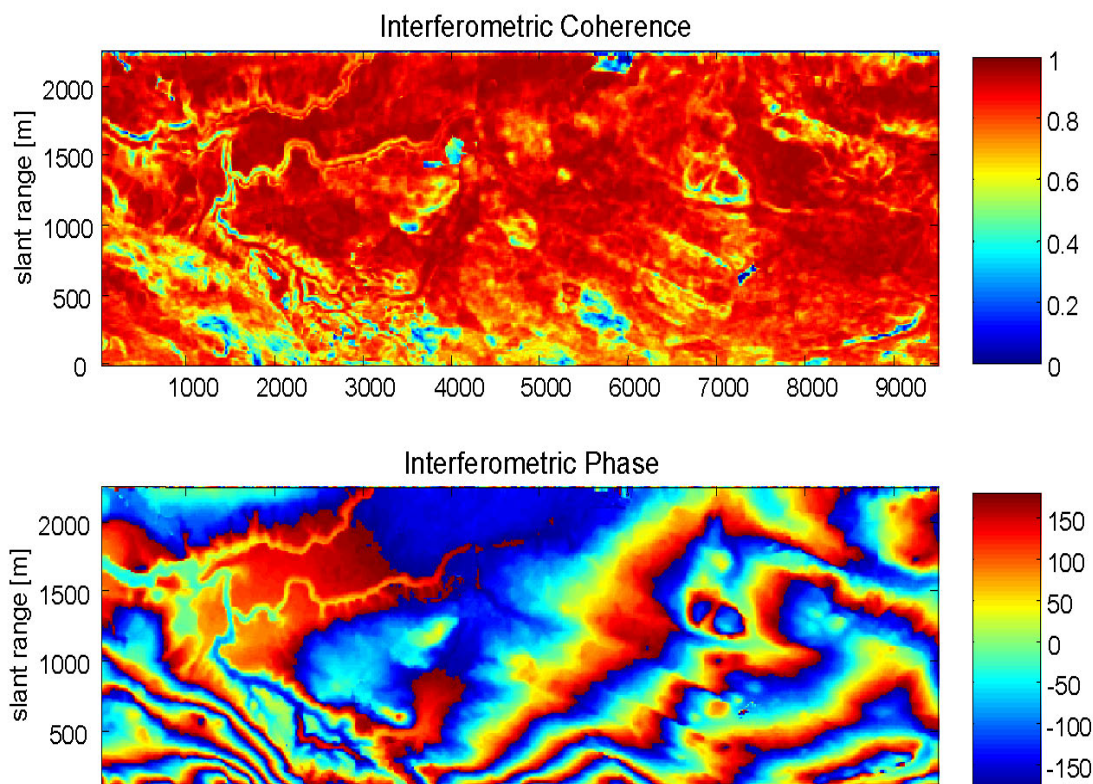


Figure 4: Interferometric Coherence (top) and Phase (bottom) for the P-Band SW data-set, polarization HH. Horizontal baseline is equal to 40 m.

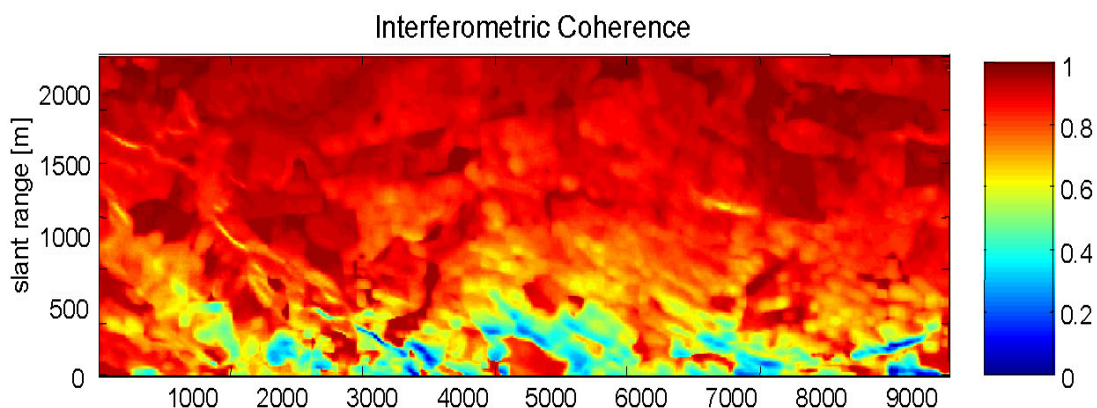


Figure 5: Theoretical Interferometric Coherence at a baseline of 40 m for the P-Band SW data-set, assuming uniform volume scattering.

It may be appreciated that sensitivity to volume decorrelation is a strongly varying function of the slant range coordinate, due to the large variation of the look angle from near to far range. Sensitivity to volume decorrelation is almost lost at far range, but it is sufficient at near range to reveal the presence of volumetric scatterers. Comparing Figure 4 to Figure 5 it may be easily recognized that the observed

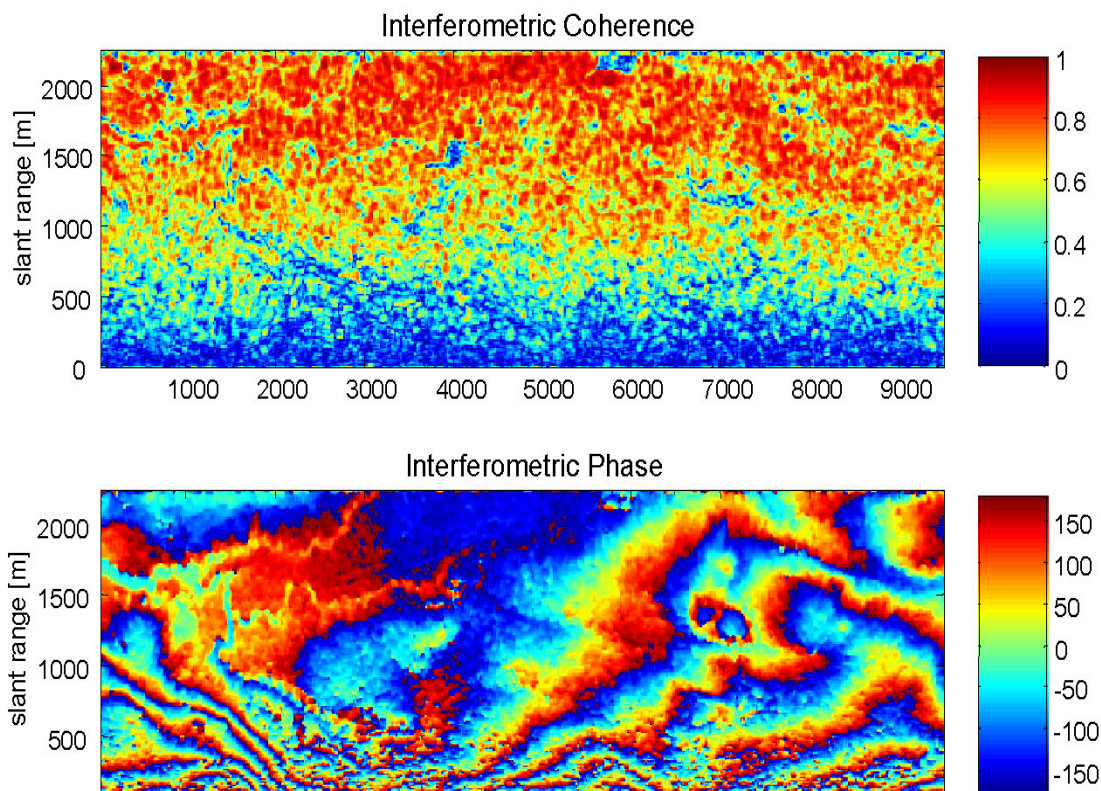


Figure 6: Interferometric Coherence (top) and Phase (bottom) for the BioMass data-set, polarization HH. Horizontal Baseline is equal to 40 m.

interferometric coherence in forested areas are often much higher than the theoretical values, thus providing evidence in support of the presence of significant ground contributions in HH at P-Band,.

Also note that the coherence of the P-Band SW data-set shows a good correlation with ground slopes, which supports the idea of strong ground contributions. The interferometric phase, see Figure 4, bottom row, appear to be loosely affected by noise, and thus suited for the estimation of phase center elevation through standard InSAR techniques.

In the BioMass case, the interferometric coherence is dominated by Spectral Shift decorrelation [5], as shown by the rising trend with respect to the slant range coordinate, see Figure 6, top row. The interferometric phases appear to be more affected by noise with respect to the E-SAR case in Figure 4. Besides the aforementioned Spectral Shift decorrelation, this phenomenon is also due to the huge resolution unbalance between BioMass and E-SAR in both range and azimuth directions, see Table 2 and Table 4, resulting in a resolution loss factor of about 125. As a consequence, at 30° the number of independent sample within a 60 x 60 m estimation window drops down to just 5, resulting in phase noise to increase [6], [7], [8].

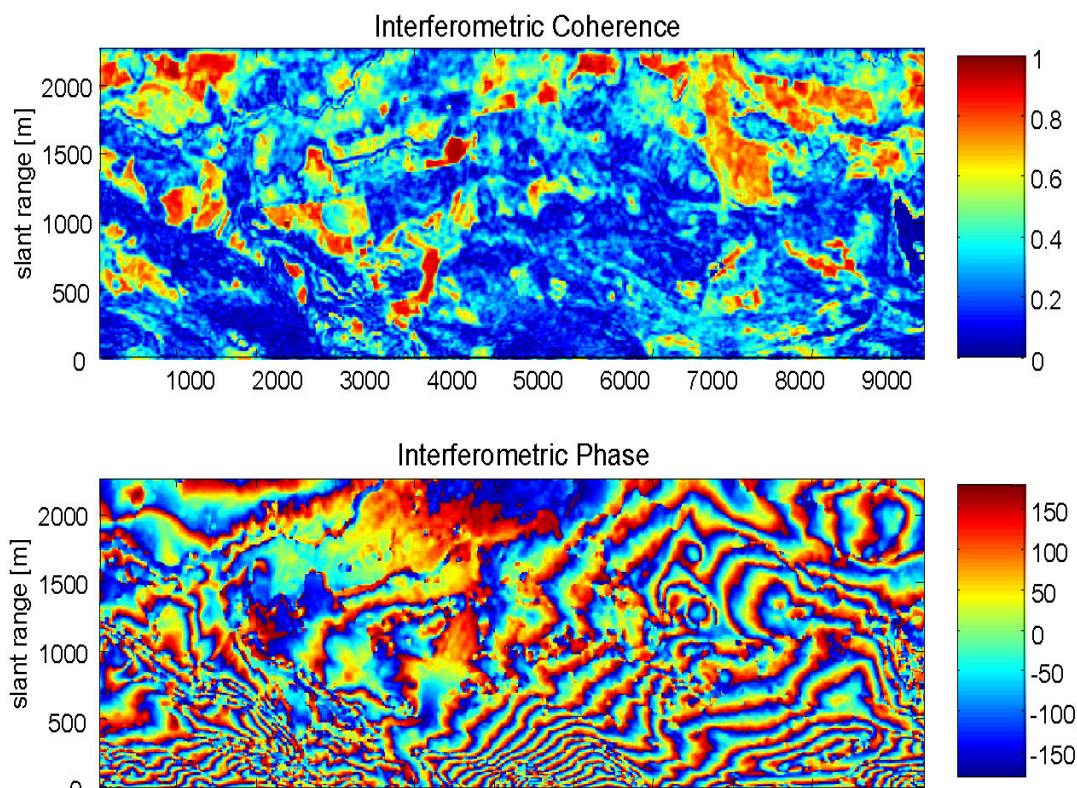


Figure 7: Interferometric Coherence (top) and Phase (bottom) for the L-Band SW data-set, polarization HH. Horizontal-Baseline is equal to 30 m.

The behaviour of the interferometric coherence at P-Band is exactly the opposite as the one observed at L-Band, see Figure 7, where the coherence is remarkably higher in open areas. As for forested areas, this phenomenon is to be imputed to stronger volume contributions and larger height sensitivity at L-Band with respect to P-Band. As for open areas, instead, the higher coherence observed at L-Band is consistent with the Small Perturbation Model (SPM) for surface scattering [9], after which surface scattering contributions

are expect to decrease as the wavelength increases, resulting in the interferometric coherence to be more affected by noise and clutter contributions at P-Band than at L-Band.

9.4.3.2 Statistics of the co-polar channels

The information carried by the co-polar channels has been analyzed by averaging the signal energies and the co-polar interferograms over all the tracks and inside an estimation window as large as 60×60 m (ground range, azimuth).

The maps of the co-polar coherence and phase for the P-Band SW data-set are reported in Figure 8. Comparing the bottom row of Figure 8 with Figure 1 it is easy to recognize a strong correlation between the spatial distribution of the co-polar phase with that of open and forested areas. Open areas are characterized by a co-polar phase of about -20° , whereas the most likely co-polar phase in forested areas is about 50° . A further analysis reveals a clear rising trend has been observed between the co-polar phase and forest height, as shown in Figure 9, top left panel. Such a result seems to suggest the presence of dihedral contributions, as the co-polar phase of surface and volumetric scattering is expected to be null [10].

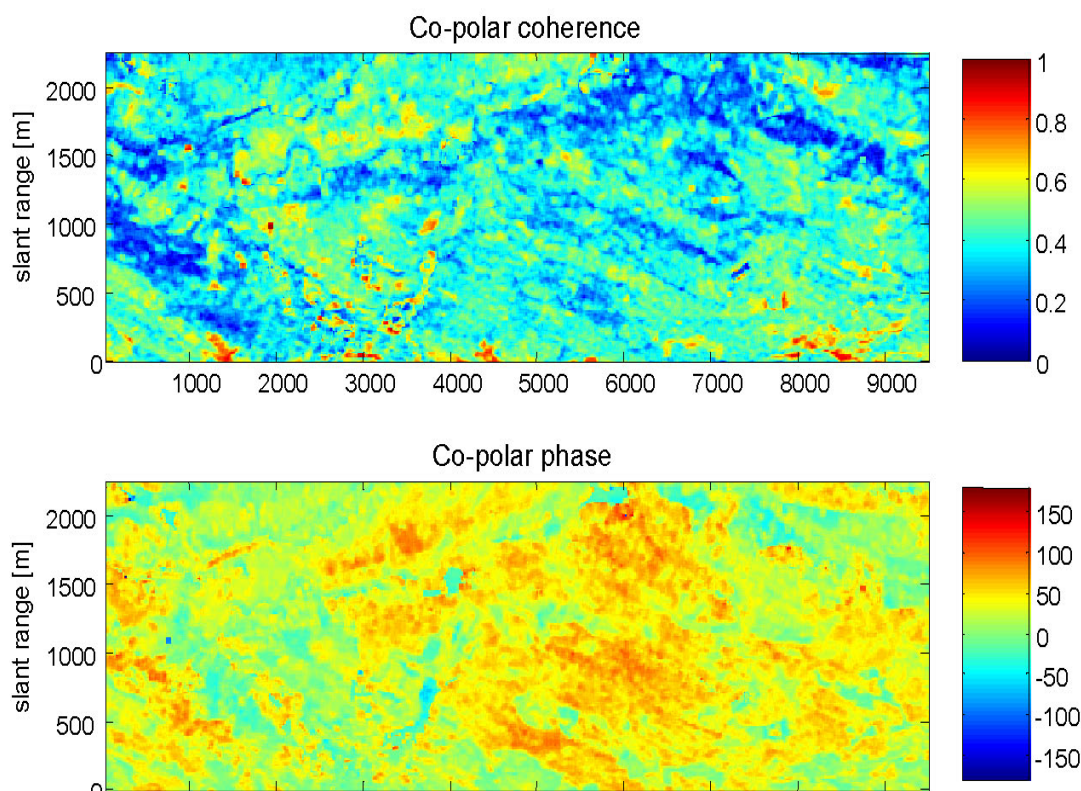


Figure 8: Co-polar Coherence (top) and Phase (bottom) for the P-Band SW data-set, averaged over all tracks.

The co-polar coherence, instead, appear to be anti-correlated with forest height, see Figure 9, bottom left panel. It is worth noting that high values of co-polar coherence are seldom found, even in areas where vegetation is very low or absent.

The total co-polar energy, defined as the sum of the energies associated with HH and VV, has been observed to give rise to a rising trend with respect to canopy elevation, see Figure 9, top right panel. The

joint distribution of the total energy and the co-polar phase has turned out to be substantially bimodal, low and high energies being concentrated around and 50° and -20°, respectively, see Figure 9, bottom right panel.

An analysis of the co-polar signature with respect to ground range slope is shown in Figure 10. In all panels, positive slopes correspond to areas tilted toward the sensor. The top row reports the joint distribution of the total energy and ground range slope. The two panels correspond to the cases where signal energy has been compensated (right panel) or not (left panel) for ground range slope. Energy compensation has been carried out by normalizing the signal energy by the ground range extent of the SAR resolution cell- In formula:

$$E_{comp} = E \cdot \sin(\theta - \alpha) \tag{Eq 1}$$

where: E is the (uncompensated) total signal energy; θ is the look angle; α is the ground range slope.

Comparing the two panels it may be appreciated that the total energy is indeed correlated with terrain topography, even though the compensation in Eq 1 does not manage to flat the energy distribution completely.

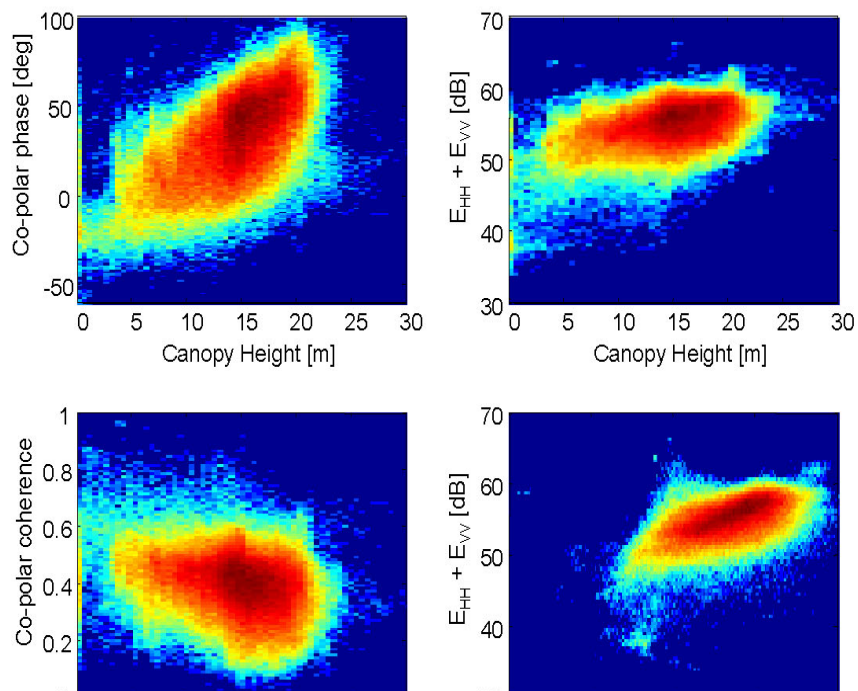


Figure 9: 2D histograms relative to the co-polar signature of the P-Band SW data-set. Top left: Co-polar phase vs. Canopy height. Top right: Total Energy vs. Canopy Height. Bottom Left: Co-polar coherence vs. Canopy height. Bottom right: Total Energy vs. Co-polar phase. The color scale in each panel is proportional to the logarithm of the number of counts within each bin.

The bottom row of Figure 10 reports the joint distributions of co-polar phase (right panel) and coherence (left panel) with respect to ground range slope. Forward slope areas ($\alpha > 0$) have been observed to correspond to high co-polar coherence and low co-polar phase, whereas back slope areas ($\alpha < 0$) have been observed to correspond to low co-polar coherence and dispersed co-polar phase.

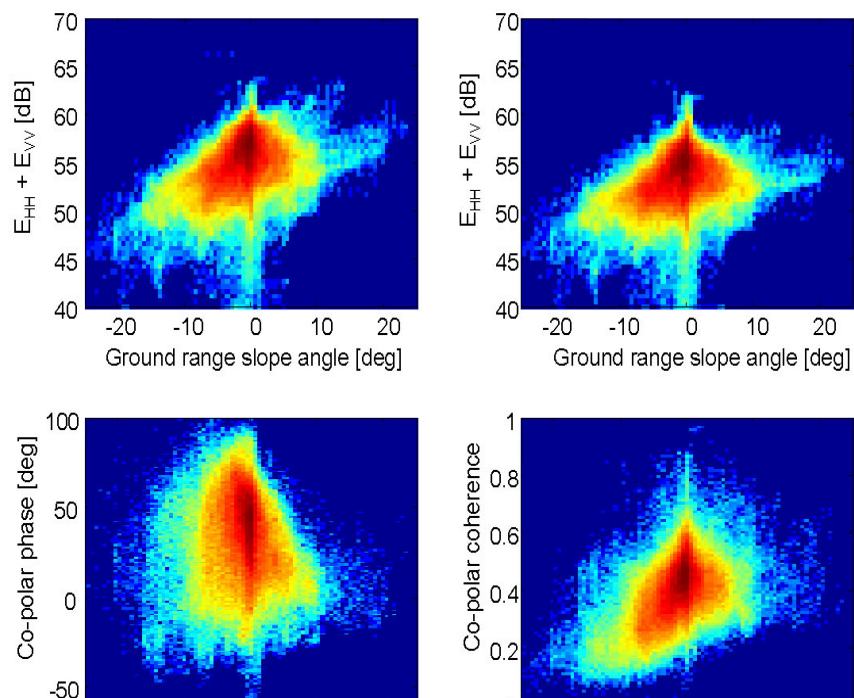


Figure 10: 2D histograms relative to the co-polar signature of the P-Band SW data-set. Top left: Total Energy vs. Ground range slopes. Top right: Corrected Total Energy vs. Ground range slopes. Bottom Left: Co-polar phase vs. Ground range slopes. Bottom right: Co-polar coherence vs Ground range slopes. The color scale in each panel is proportional to the logarithm of the number of counts within each bin.

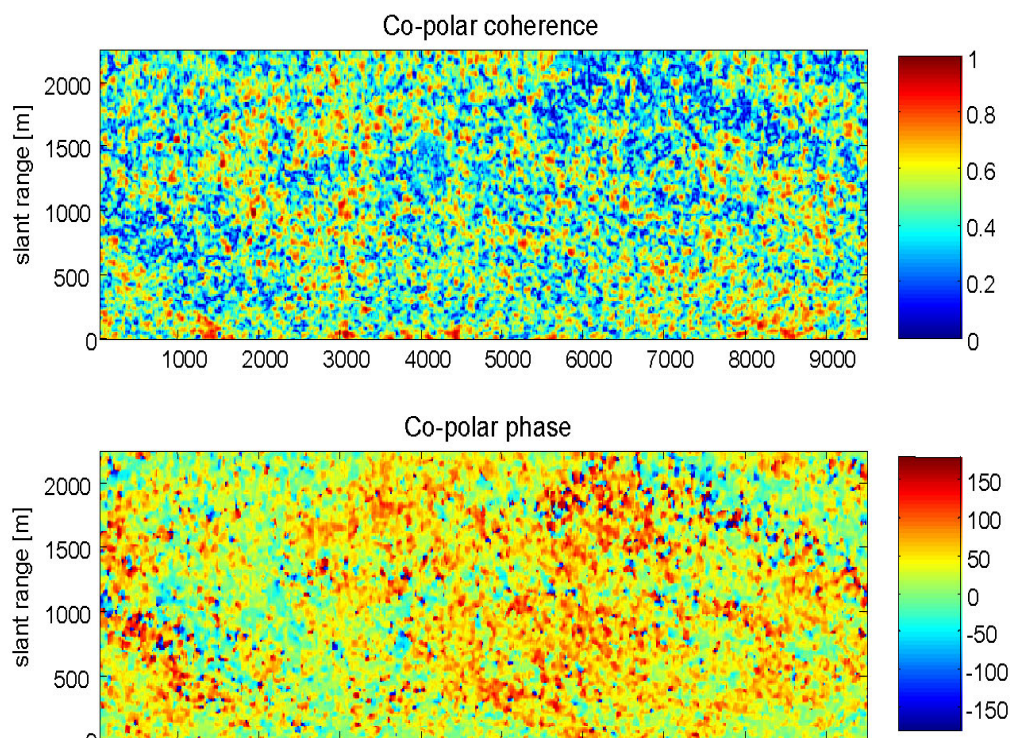


Figure 11: Co-polar Coherence (top) and Phase (bottom) for the BioMass data-set, averaged over all tracks

The analysis of the co-polar signature of the BioMass data-set has yielded similar results as the ones discussed above relatively to the full bandwidth P-Band case, see Figure 11, Figure 12, Figure 13. The only noticeable difference is relative to the higher dispersion observed. This is consistent with the resolution unbalance between the BioMass and E-SAR systems, resulting in much fewer independent samples being employed in statistics evaluation in the BioMass case.

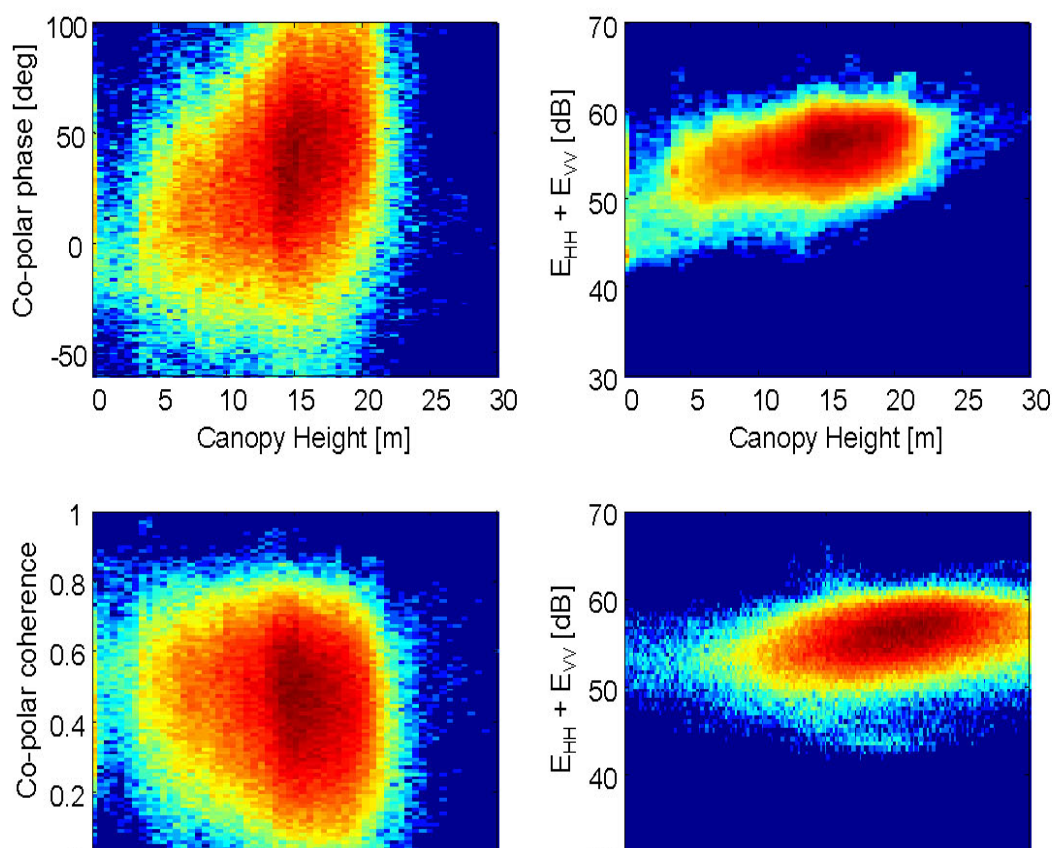


Figure 12: 2D histograms relative to the co-polar signature of the BioMass data-set. Top left: Co-polar phase vs. Canopy height. Top right: Total Energy vs. Canopy Height. Bottom Left: Co-polar coherence vs. Canopy height. Bottom right: Total Energy vs. Co-polar phase. The color scale in each panel is proportional to the logarithm of the number of counts within each bin..

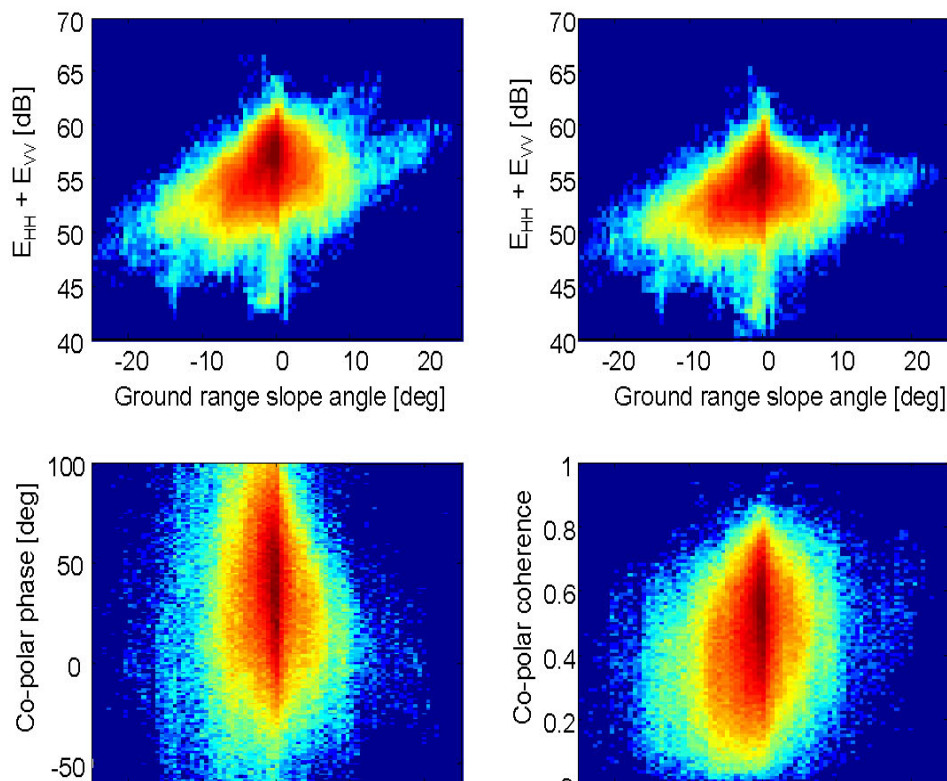


Figure 13: 2D histograms relative to the co-polar signature of the BioMass data-set. Top left: Total Energy vs. Ground range slopes. Top right: Corrected Total Energy vs. Ground range slopes. Bottom Left: Co-polar phase vs. Ground range slopes. Bottom right: Co-polar coherence vs. Ground range slopes. The color scale in each panel is proportional to the logarithm of the number of counts within each bin.

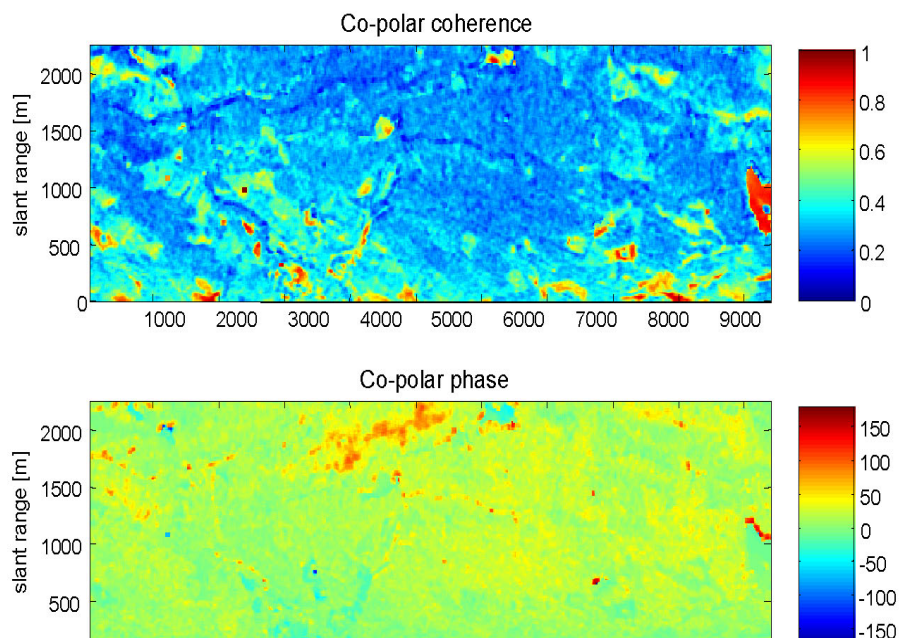


Figure 14: Co-polar Coherence (top) and Phase (bottom) for the L-Band SW data-set, averaged over all tracks.

The analyses of the co-polar signature for the L-Band SW data-set are reported in Figure 14, Figure 15, Figure 16. All of the results are not qualitatively different than those obtained at P-Band, in that the same kinds of trend (i.e.: increasing or decreasing) are observed at –Band as well as at L-Band. However, such trends are characterized at L-Band by a lower dynamic. The co-polar phase has been observed to vary from about -20° in open areas to about 20° in most of forested areas. Similarly, co-polar coherence has been observed to be anti-correlated with forest height, even though not so much as at P-Band. Both the co-polar coherence and phase show only minor variations with respect to ground range slope. The total energy has been observed to increase with forest height, but not so much as at P-Band. Also at L-Band, the total energy has turned to be correlated with terrain topography, even though a residual trend is visible even after compensating for ground range slope.

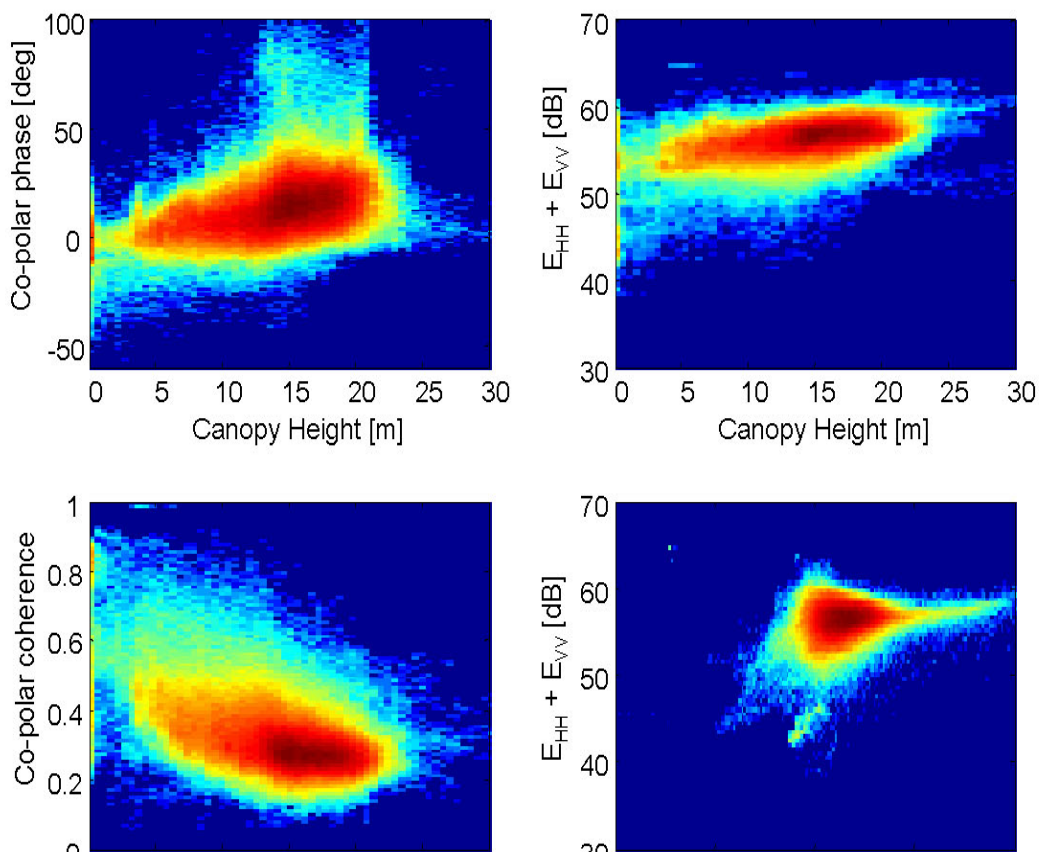


Figure 15: 2D histograms relative to the co-polar signature of the L-Band SW data-set. Top left: Co-polar phase vs. Canopy height. Top right: Total Energy vs. Canopy Height. Bottom Left: Co-polar coherence vs. Canopy height. Bottom right: Total Energy vs. Co-polar phase. The color scale in each panel is proportional to the logarithm of the number of counts within each bin.

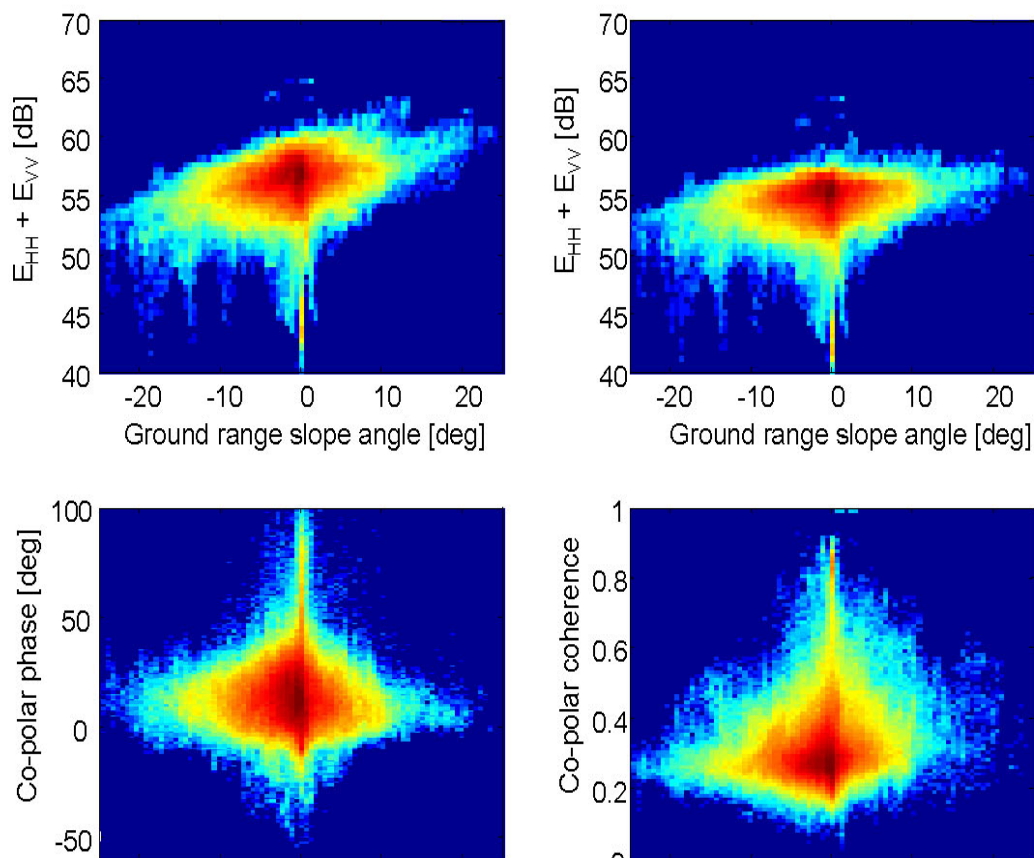


Figure 16: 2D histograms relative to the co-polar signature of the L-Band SW data-set. Top left: Total Energy vs. Ground range slopes. Top right: Corrected Total Energy vs. Ground range slopes. Bottom Left: Co-polar phase vs. Ground range slopes. Bottom right: Co-polar coherence vs. Ground range slopes. The color scale in each panel is proportional to the logarithm of the number of counts within each bin.

9.4.3.3 Amplitude Stability

Differently from the previous sections, where the properties of the data-sets have been investigated by evaluating statistics inside an averaging window, the aim of this section is to provide a pixel scale analysis of the investigated data-sets. In order to do this, each pixel in the image stack will be analyzed as for its amplitude stability features. Such an approach is commonly used in spaceborne Permanent Scatterers Interferometry (PSI) for the identification of the most coherent targets within the whole data stack [11].

9.4.3.3.1 Data Amplitude Stability

Accordingly with PSI literature, we define amplitude stability of a pixel in an image stack as the ratio μ/σ , where μ and σ are the mean and the standard deviation of the SLC data amplitudes [11].

Figure 17 reports the histograms of the μ/σ index obtained by analyzing the HH and VV channels of data-sets P-Band SW, L-Band SW, and BioMass.

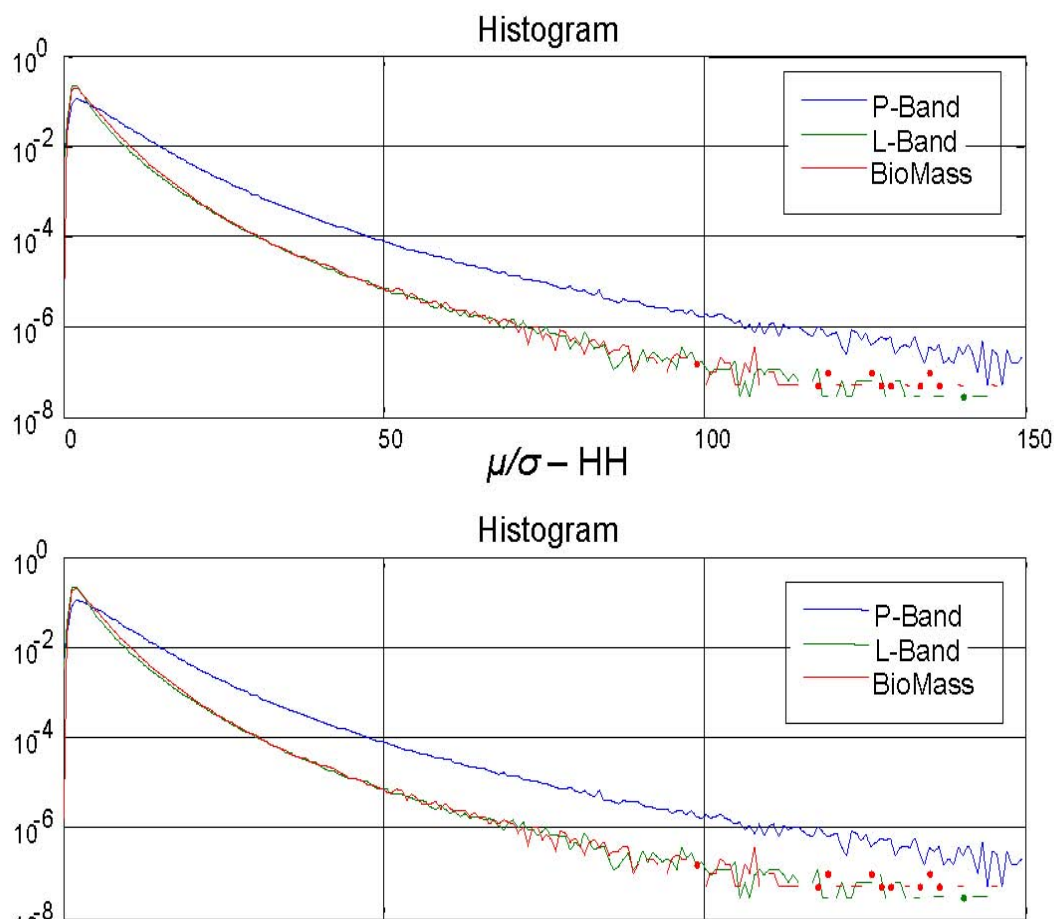


Figure 17: Histograms of the μ/σ index in HH (top row) and VV (bottom row) for the following data-sets: P-Band SW, L-Band SW, BioMass. Histograms have been normalized such that their sum is unitary.

It may be appreciated that in all cases a very high number of samples is associated with very high values of the μ/σ index compared to spaceborne InSAR applications, where a target is considered coherent for $\mu/\sigma > 4$, see [11].

However, it has to be considered that the probability that an incoherent target (i.e., clutter) results in high μ/σ values is a function of the number of tracks. It follows that the choice of a proper threshold for reliable identification of coherent targets through the usage of the μ/σ index is dependent on the number of available tracks as well. Figure 18 reports the graph of the probability that μ/σ for an incoherent target exceeds a certain threshold with $N = 6$ tracks. Such a graph has been obtained with Monte-Carlo simulations over 105 trails.

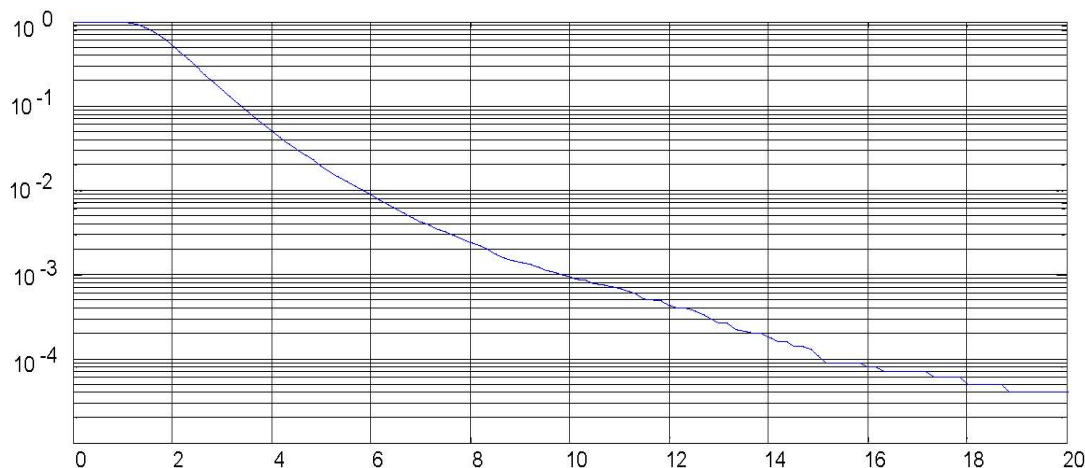


Figure 18: Probability of False Alarm for an incoherent target with $N = 6$ tracks

It may be appreciated that the probability that an incoherent target gives rise to $\mu/\sigma > 4$, which may be thought of as a probability of false alarm (pfa), is not negligible if only 6 tracks are employed. Instead, a far more significant threshold for the identification of coherent targets basing on the BioSAR 2008 data-sets can be assessed in $\mu/\sigma > 15$, corresponding to a pfa lower than 10^{-4} . Accordingly, a value of μ/σ about 15 may be thought of as a threshold beyond which a target is at least partially coherent in the whole image stack.

9.4.3.3.2 Target Identification

Whereas the analysis presented in the previous section allows the identification of partially coherent targets, in this section we investigate the possibility of identifying point-like targets within the imaged scene. The main goal of such an investigation is to provide elements in support of the presence of dihedral contributions in forested areas, with particular attention to P-Band data. In the framework of multibaseline SAR analyses, an important element for the separation of point-like and volumetric targets is represented by the statistical behaviour of the targets in the image stack. Point-like targets are supposed to stay coherent in all acquisitions, giving rise to high values of the μ/σ index, whereas volumetric targets undergo a correlation loss due to baseline decorrelation [12], [13], resulting in lower μ/σ values. Differently from the previous case of incoherent targets, however, it is difficult to establish a threshold for assessing whether a target is to be considered point-like or not. The reason for this statement is that spatial decorrelation mainly depends on carrier wavelength, effective normal baseline, pulse bandwidth, and finally on volume height [12], resulting in a wide variety of possible thresholds for the μ/σ index. As an example, Figure 19 reports the values of μ/σ corresponding to a pfa = 10^{-3} for a uniform volumetric target as high as 10 m, generated assuming uniform volume scattering. The graphs have been obtained through Monte-Carlo simulations, with reference to the parameters of the acquisition systems reported in section 9.4.2.

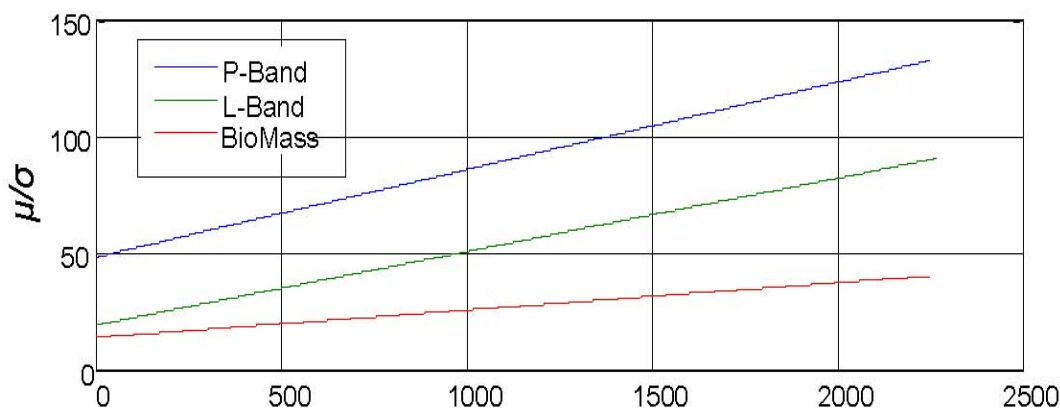


Figure 19: threshold for the μ/σ index corresponding to $pfa = 10^{-3}$ for a uniform volumetric target as high as 10 m.

The most critical case is associated with the P-Band, full bandwidth, data, where baseline diversity is not enough to provide discrimination capabilities between point-like and volumetric targets. Even in the L-Band and BioMass cases, however, the threshold with $pfa = 10^{-3}$ is higher than 15 at all slant range locations. The situation is clearly even worse for smaller volumes, as it may be the case of bushes or understory. Accordingly, in all cases there is a concrete possibility that relatively small volumes can give rise to high values of the μ/σ index.

For this reason, it has been decided to exploit further constraints for the identification of point-like targets, by jointly analyzing the μ/σ indexes in both the co-polar channels. The polarimetric behaviour of volumetric targets is expected to be associated with high entropy, resulting in poor correlation between HH and VV, whereas contributions to the co-polar channels are expected to be highly correlated in the case of dihedral or surface scattering, see for example [14], [10].

It follows that the μ/σ index for dihedral, or even surface, scattering is expected to be not only high in magnitude, but also very similar in HH and VV, therefore resulting in a further constraint to exclude volumetric targets from the set of amplitude stable targets. Accordingly, two criteria have been established for point selection. The first is the requirement that the difference between the μ/σ indexes in the co-polar channels does not exceed a certain threshold, T_d ; the second is that both indexes are required to be higher than another threshold, T_m . In formula:

$$\begin{aligned}
 \mu/\sigma(HH) &> T_m \\
 \mu/\sigma(VV) &> T_m \\
 |\mu/\sigma(HH) - \mu/\sigma(VV)| &< T_d
 \end{aligned}
 \tag{Eq 2}$$

Figure 20 reports the curves for threshold T_m corresponding to a $pfa = 10^{-3}$ for a uniform target as high as 1 m. The graphs have been obtained through Monte-Carlo simulations, with reference to the parameters of the acquisition systems reported in section 9.4.2. In all cases the threshold T_d has been set to $T_d = 5$.

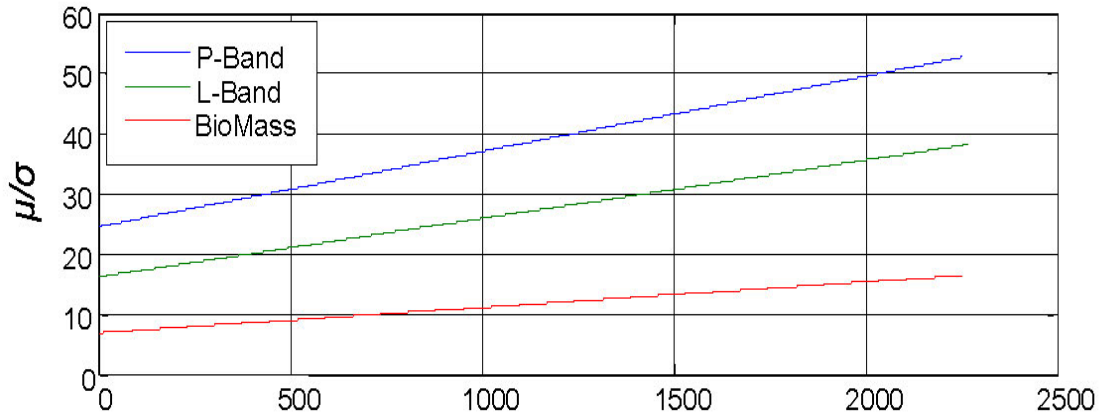


Figure 20: threshold for the μ/σ index corresponding to $pfa = 10^{-3}$ for a uniform volumetric target as high as 1 m, under the constraints in Eq 2. Threshold T_d is set to $T_d = 5$.

It may be appreciated that the application of the constraints in Eq 2 results in much lower thresholds for the μ/σ index with respect to the graphs in Figure 19, especially in light of the fact that Figure 20 is relative to a volumetric as high as just 1 m. Accordingly, the application of the constraints in

Eq 2 allows the selection of higher number of targets, while ensuring the rejection of volumetric targets higher than 1 m with a probability higher than 0.999.

The results relative to point selection for data-sets P-Band SW, BioMass, and L-Band SW are reported in Figure 21, Figure 22, Figure 23. Threshold T_d has been set to $T_d = 5$ in all cases, whereas threshold T_m has been determined adaptively with reference to a volumetric target as high as 1 m, according to the graphs in Figure 20. Accordingly, the selected points are to be intended as corresponding to targets whose amplitude stability across 6 tracks is better than what is expected for a volumetric target constituted by a uniform layer as high as 1 m within the SAR resolution cell. Still, high values of the μ/σ index could originate from targets that are not uniformly distributed within the SAR resolution cell. It follows that the selected targets are to be interpreted as being associated with ground-trunk interactions, surface scattering, and volumetric targets that are small compared to the SAR resolution cell.

Comparing Figure 1 to Figure 21 it is easy to see that the selected points in the P-Band SW data-set correspond to forested areas or to isolated peaks in bald areas, indicating that they might be regarded as double bounce contributions resulting from ground-trunk interactions. This hypothesis is supported by the corresponding co-polar phases, whose histogram shows a peak about 50° , see Figure 21, bottom left panel. Yet, it has to be remarked that the co-polar phase is slightly less than 0° for a non negligible number of points. Such points might correspond to dielectric losses of either the ground or the tree trunks. However, they could as well be associated with scattering from surfaces or small volumes, whose identification is not possible through the kind of analysis within this section. The vast majority of the selected points occur in areas where the ground slope is within $\pm 5^\circ$, Figure 21, bottom right panel. Though, very stable points have been found in areas with relevant ground slopes as well. Excluding the presence of double bounce contributions at slopes higher than 5° , see for example [15], such points are likely to be associated to small volumetric targets. Finally, a decreasing trend of the density of the selected points with respect to the slant range coordinate is clearly visible. This phenomenon is due to the fact that baseline diversity at far ranges is not enough to provide discrimination capabilities between point-like and volumetric targets basing on amplitude only information.

Mean Reflectivity - HH

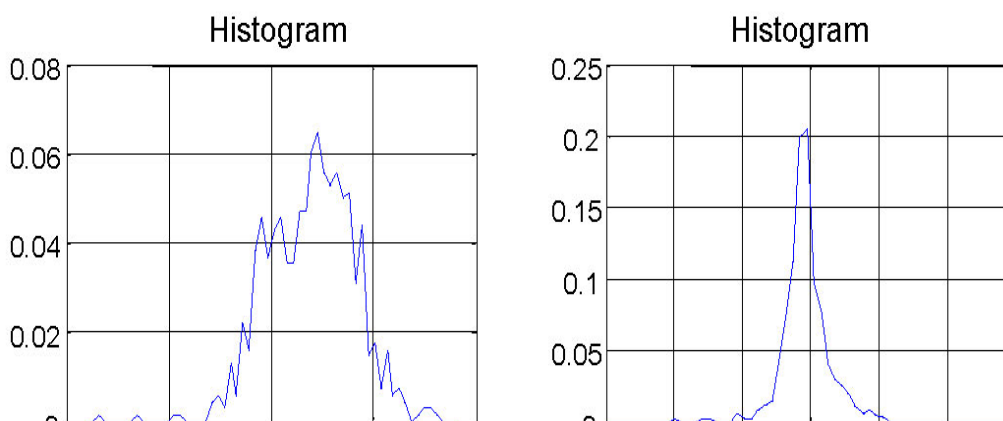
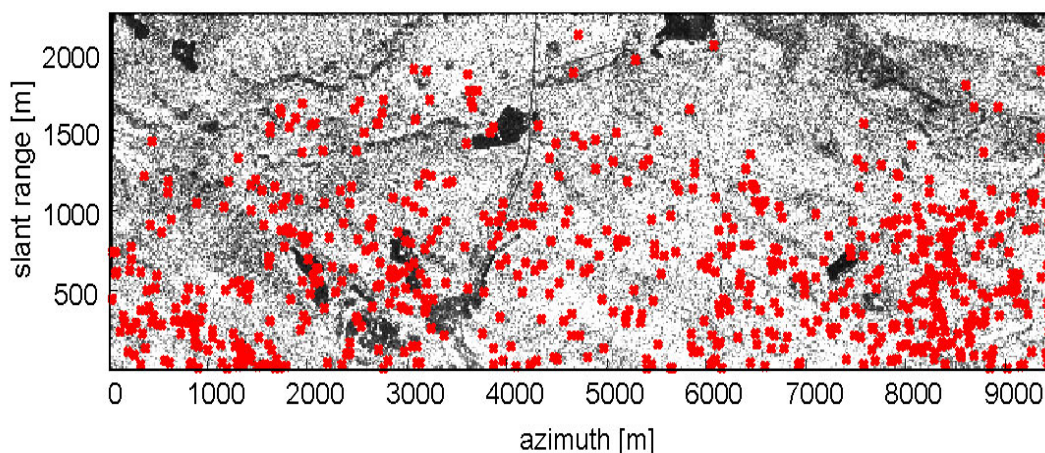
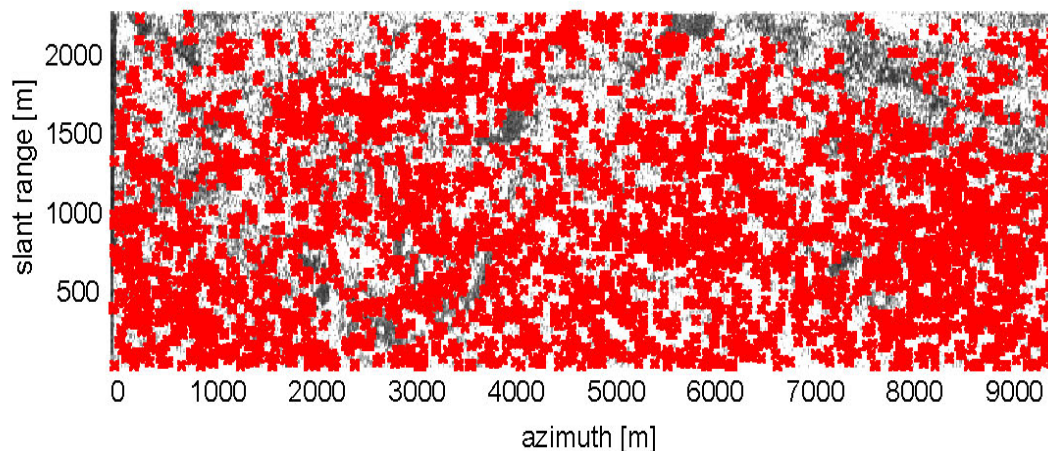


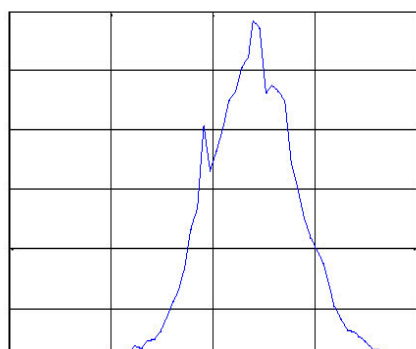
Figure 21: Point selection for the P-Band SW data-set. Top row: mean reflectivity for the HH channel; the selected points are identified by the red marks. Bottom row: histogram of the co-polar phase (left) and ground slope (right) for the selected points.

Considering the BioMass case, reported in Figure 22, no rising trend is visible between the slant range coordinate and point density. This is due to the fact that a much smaller pulse bandwidth is employed in the BioMass case with respect to the E-SAR case, resulting in a much larger extent of spatial decorrelation phenomena. Accordingly, uniform volumetric targets are less likely to give rise to high value of the μ/σ index, which makes it easier to exclude them from point selection. Nevertheless, there is a concrete possibility that many selected points correspond to volumetric targets whose extent is smaller than the resolution cell, due to the 25 m slant range resolution of BioMass. However, it is worth noting that the selected points are found in forested areas, and that the most likely co-polar phase has been observed to be about 50° . As discussed in the previous case, such arguments indicate the presence of double bounce contributions resulting from ground-trunk interactions among the set of the selected points.

Mean Reflectivity - HH



Histogram



Histogram

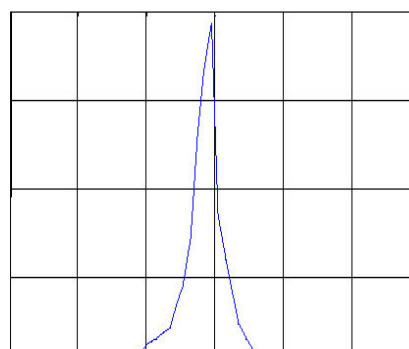


Figure 22: Point selection for the BioMass data-set. Top row: mean reflectivity for the HH channel; the selected points are identified by the red marks. Bottom row: histogram of the co-polar phase (left) and ground slope (right) for the selected points

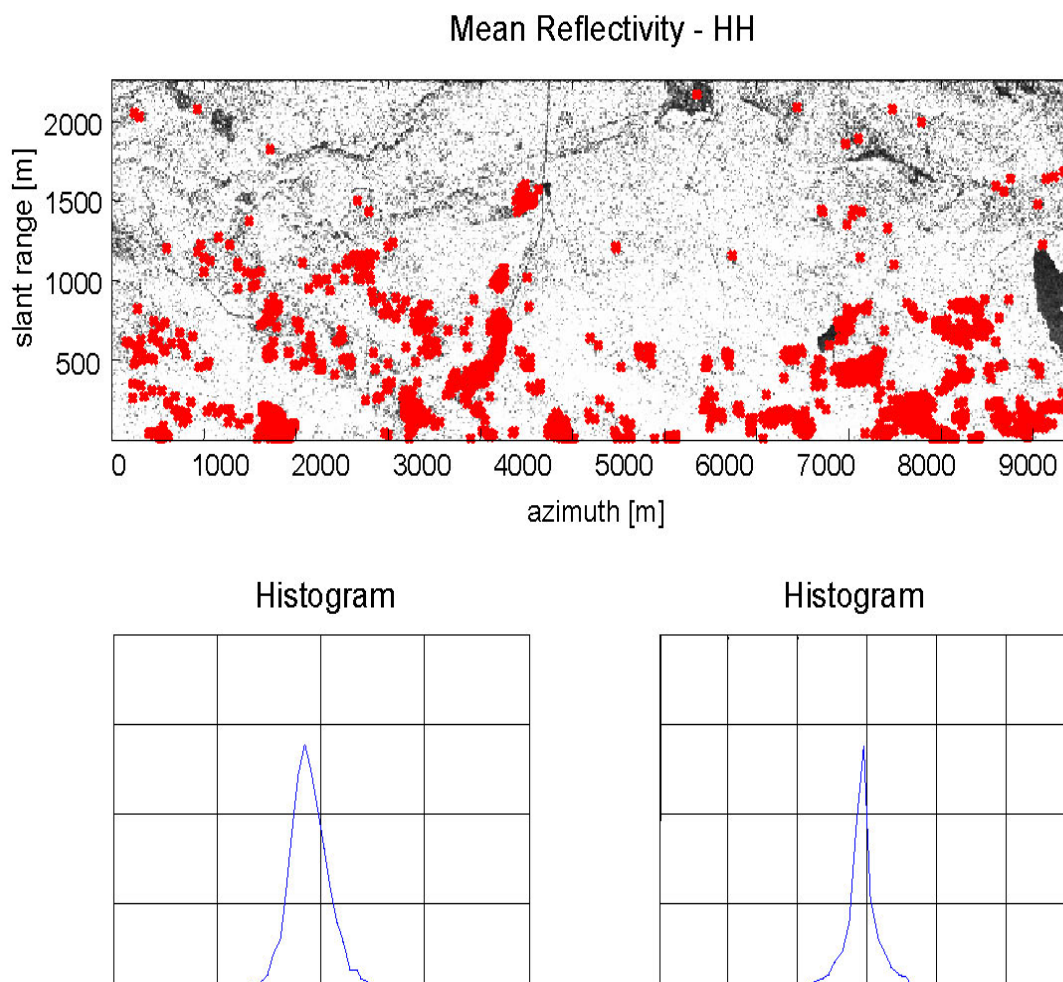


Figure 23: Point selection for the L-Band SW data-set. Top row: mean reflectivity for the HH channel; the selected points are identified by the red marks. Bottom row: histogram of the co-polar phase (left) and ground slope (right) for the selected points.

Finally, the outcomes of point selection at L-Band have turned out to be the opposite of those obtained at P-Band, as the vast majority of selected points is found in open areas. Such points are likely to correspond to surface targets, whereas the presence of dihedral scattering seems to be excluded. This conclusion is supported by the co-polar phases of the selected points, whose histogram exhibits a peak about -18° .

9.4.3.4 Summary

So far, this section has presented different kinds of preliminary analyses, aimed at providing a first-order characterization of the BioSAR 2008 data-sets.

Due to limited baseline diversity, the P-Band SW data-set is loosely affected by volume decorrelation, except at near range. Nevertheless, the high values observed as for the interferometric coherence suggest the presence of strong ground contributions, at least in the co-polar channels, as confirmed by the correlation with respect to terrain topography.

A significant number of amplitude stable points has been found in forested areas at near range. As discussed, there are no elements to identify such points with dihedrals rather than with small volumetric targets. In any case, however, the presence of such points is an indicator that most contributions do not come from canopy backscattering.

A value of 50° has been observed for the co-polar phase in forested areas. This result can be interpreted as an index of the presence of a dihedral contribution, with loss with respect to the ideal value of 180° due to the dielectric properties of the ground-trunk ensemble [10], [16]. However, low values of the co-polar coherence have been observed, whereas dihedral contributions are usually assumed to be highly correlated [10]. One possible explanation is that a significant contribution from canopy backscatter is present, which would explain both the low co-polar coherence and the reduction of the co-polar phases from the ideal value of 180° to 50° . This interpretation, however, would neither be consistent with the presence of highly amplitude stable targets, nor with the rather high geometric coherences exhibited by the co-polar channels throughout the imaged scene. A better explanation seems to be that to consider scattering from forested areas in co-polar channels as being contributed by a dominant scattering mechanism, responsible for (most of) the coherence loss between the co-polar channels but highly coherent with respect to geometrical variations. From a physical point of view, it makes sense to relate such scattering mechanism to the ensemble of trunk-ground and canopy-ground interactions, eventually perturbed by the presence of understory and trunk-ground dielectric losses.

It has to be remarked that similar has been observed relatively to the Remningstorp test site investigated in the framework of the BioSAR 2007 campaign.

Despite the higher dispersion, no relevant difference is observed as for the BioMass data-set. High numbers of amplitude-stable points are found in forested areas, and similar values are observed relatively to the co-polar coherence and phase.

As expected, things change at L-Band, especially as for the interferometric behavior of the data-sets. In this case a significant volume decorrelation has been observed, witnessing the large sensitivity, as compared to P-Band data, of L-Band data to volume scattering. A different behavior is also observed for open areas, whose interferometric coherence is much higher. As a result, amplitude stable points are now found in open areas. Analog to P band, the co-polar signatures at L-Band grow with vegetation height, even though to a less extent. Most likely, specular reflections from the ground level are present at L-Band as well, even though their contribution to the received signal is much weaker compared to the P-Band case.

9.4.4 SAR Tomography

The idea behind the concept of 3D reconstruction is rather simple. Consider a multi-baseline SAR system, where several SAR sensors, flown along parallel tracks, image a scene from different points of view, as depicted in Figure 24.

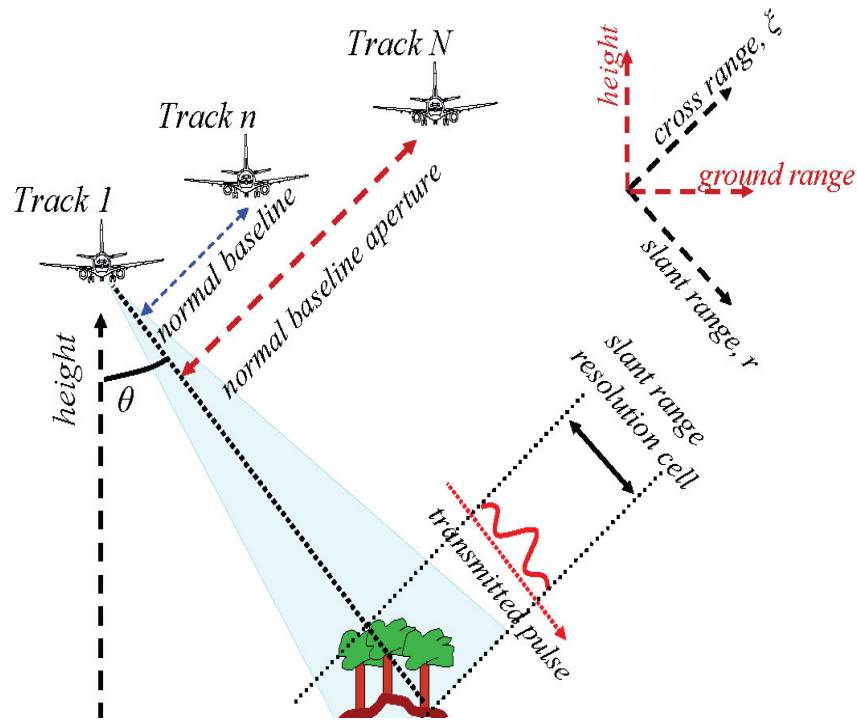


Figure 24: Acquisition geometry for a multi-baseline SAR system.

Such a system offers the possibility to gather the backscattered echoes not only along the azimuth direction, but also along the cross-range direction, defined by the axis orthogonal to the Line Of Sight and to the orbital track. Accordingly, the backscattered echoes can be focused not only in the slant range, azimuth plane, but in the whole 3D space. It follows that, if the carrier frequency is such that the penetration in the scattering volume is guaranteed, the vertical profile of the scatterers is retrieved by separating their contributions in multiple layers. Therefore, multi-baseline SAR system may be thought of as a fully 3D imagery tool, where the size of the 3D resolution cell is determined by the pulse bandwidth along the slant range direction, and by the lengths of the synthetic apertures in the azimuth and cross range directions, see Figure 25.

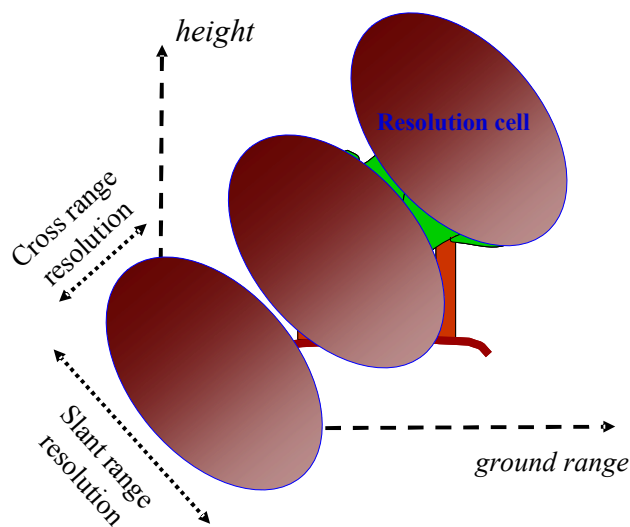


Figure 25: Slant range, cross range extension of the Tomographic resolution cell.

In formula, the extent of the resolution cell along the slant range and cross range directions is given by:

$$\Delta r = \frac{c}{2B} \quad \text{Eq 3}$$

and:

$$\Delta e = \frac{\lambda r}{2A} \quad \text{Eq 4}$$

where:

- Δr is the resolution along the slant range direction
- c is the speed of light
- B is the system bandwidth
- Δe is the resolution along the cross range direction
- A is the total normal baseline aperture
- λ is the carrier wavelength
- r is the distance between the target and the sensor of the Master image.

Both 2D and 3D focusing of SAR data may be regarded as specializations to the SAR case of the more general concept of Diffraction Tomography, widely exploited in seismic processing [18]. As such, 3D focusing is analogous to the basic formulation of T-SAR, in which no assumption is made about the imaged scene. See, for example, the work by Reigber and Moreira in [19].

9.4.4.1 Mathematical Formulation

Consider a data-set constituted by N focused SAR images, and let y_n denote a complex valued pixel from the n -th image, the dependence on the slant range, azimuth location being made implicit to simplify the notation. After proper phase corrections compensating for flat terrain terms, each image can be represented as [7], [20]:

$$y_n = \int P(e) \exp\left(-j \frac{4\pi b_n}{\lambda r} e\right) de \quad \text{Eq 5}$$

where:

- e is the cross range coordinate
- b_n is the normal baseline for the n -th track, with respect to a reference Master track
- $P(e)$ represents the complex reflectivity for the target at cross range location e , averaged within the SAR slant range, azimuth resolution cell.

The equation above is the key to the mathematical formulation of T-SAR. It states that the SAR multi-baseline data and the cross range distribution of the targets form a Fourier pair. Hence, $P(e)$ can be retrieved by taking the Fourier Transform of the data with respect to the normal baseline.

In case of vegetated scenarios, the quantity $P(e)$ is better described as a stochastic process, due to the variability of the sub-scatterers within the SAR resolution cell [7]. For this reason, it follows that in the analysis of forested areas the interest is in the evaluation of the backscattered power at each cross range location, defined as:

$$S(e) = E\left[|P(e)|^2\right] \quad \text{Eq 6}$$

Where $E[\]$ is the Expected Value operator. Accordingly, it may be stated that T-SAR is, in its essence, a Spectral Estimation problem, where the Spectrum of the data is given by the backscattered power distribution of the target along the cross range direction. Operationally, the estimation of $S(e)$ is carried out basing on the second order moments of the data, which are measured by evaluating the interferometric pairs. To better formalize the problem, define:

$$\mathbf{y} = [y_0 \quad y_1 \quad \cdots \quad \cdots \quad y_{N-1}]^T \quad \text{Eq 7}$$

as the stack of the multi-baseline data at a given slant range, azimuth location. Given this definition, the ensemble of all the available interferograms may be represented in a compact form by considering the data covariance matrix, namely:

$$\mathbf{R} = E[\mathbf{y}\mathbf{y}^H] \quad \text{Eq 8}$$

where H means transposed and complex conjugate.

It follows after well known results from the Theory of Spectral Estimation, see for example [21], that the information about the Spectrum of the data is carried by the data covariance matrix. Accordingly, T-SAR may be rephrased as the problem of estimating the backscattered power distribution of the target given a sample estimate of the data covariance matrix:

$$\hat{\mathbf{R}} \xrightarrow{T-SAR} \hat{S}(e) \quad \text{Eq 9}$$

9.4.4.2 On the role of terrain topography

Once the cross range distribution of the backscattered power has been retrieved at each slant range bin, an interpolation step is required in order to pass from the slant range, cross range coordinates to the ground range, height coordinates. This operation is conceptually not different from standard geocoding of SAR images, with the only exception that the cross range location of the targets has to be accounted for as well, resulting in the increase of dimensionality of the interpolation step. Accordingly, the correct

implementation of such an interpolation step requires the knowledge of terrain topography, analogously to conventional geocoding. This concept is pictorially depicted in Figure 26.

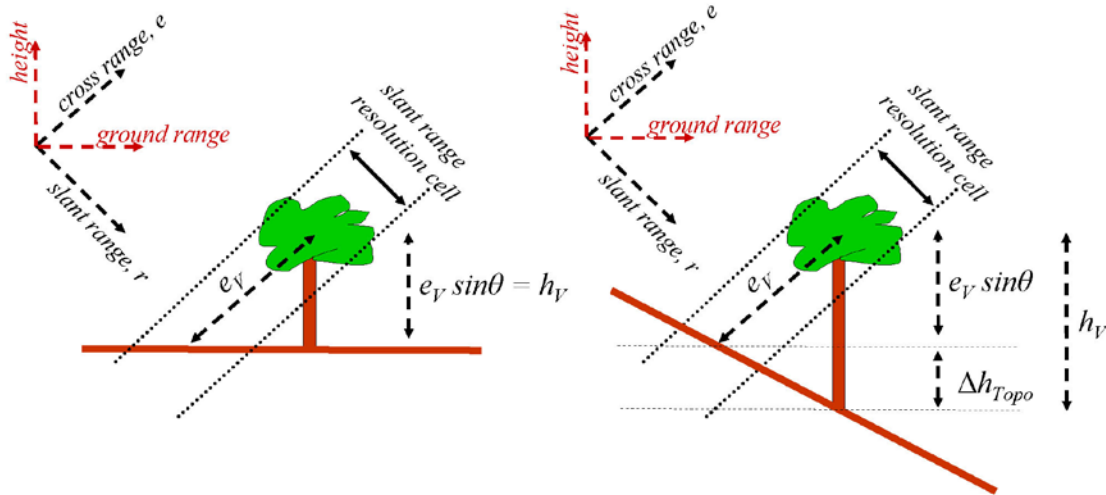


Figure 26: relation between cross range and height in case of a flat (left) or tilted (right) topography.

In case of a flat topography, the vertical location of the tree canopy may be derived directly from its cross-range location, according to the rule:

$$h_V = e_V \sin \theta \quad \text{Eq 10}$$

where θ is the look angle. In general, however, it must be considered that two targets at the same slant range location correspond to different ground range locations, if they are displaced along the cross range axis. Accordingly, the variation of topography along the ground range axis has to be taken into account when evaluating the height difference between such two targets.

For example, with reference to the right panel of Figure 26, the distance between the ground and the tree canopy along the vertical direction is given by:

$$h_V = e_V \sin \theta + \Delta h_{Topo} \quad \text{Eq 11}$$

where Δh_{Topo} is the topographic variation along the ground range coordinate.

Therefore, knowledge of terrain topography is strictly required for the correct evaluation of target elevation above the ground.

Finally, assuming a planar topography with slope angle α it follows that Eq 11 can be conveniently simplified to:

$$h_V = e_V \frac{\sin(\theta - \alpha)}{\cos \alpha} \quad \text{Eq 12}$$

where a positive value of α corresponds to a terrain tilted towards the sensor. Eq 12 allows a straightforward evaluation of the sensitivity of forest height with respect to ground slope inaccuracies, see Figure 27.

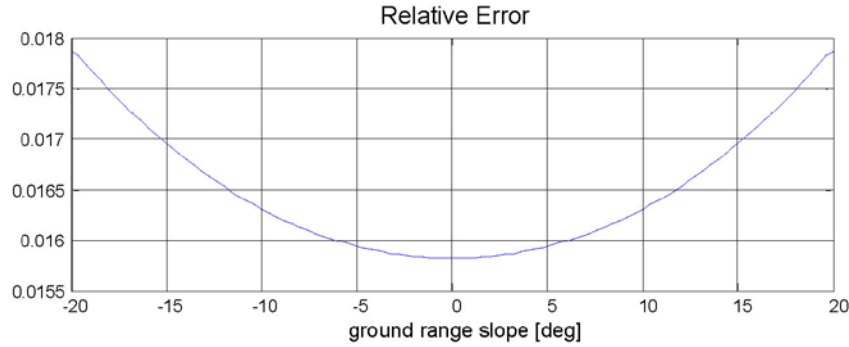


Figure 27: Relative error on forest height due to a ground slope inaccuracy of 1° for a look angle of 25°.

9.4.4.3 Spatial resolution

The condition for the separation between the ground and the canopy can be performed provided that either the ground or the canopy are present in each Tomographic resolution cell, whose extent is determined by both baseline aperture and pulse bandwidth. It follows that two limits arise as for the vertical resolution capabilities of a Tomographic SAR system in the analysis of vegetated areas. One is relative to baseline aperture, and it may be derived after Eq 4 and Eq 12:

$$\Delta h_{ba} = \Delta e \frac{\sin(\theta - \alpha)}{\cos \alpha} = \frac{\lambda r \sin(\theta - \alpha)}{2A \cos \alpha} \quad \text{Eq 13}$$

The other limit arises as a consequence of pulse bandwidth, and it may be derived after Eq 3:

$$\Delta h_{pb} = \Delta r \frac{\cos(\theta - \alpha)}{\cos \alpha} = \frac{c \cos(\theta - \alpha)}{2B \cos \alpha} \quad \text{Eq 14}$$

Figure 28 reports the graphs of the most stringent among the two limits to vertical resolution discussed above for the BioSAR 2008 data-sets, as a function of the ground range coordinate. For both the P-Band and the L-Band data-sets, the lower bound is the one given by baseline aperture, see Eq 13. For BioMass, instead, the lower bound is given by baseline aperture at middle and far range, whereas the limit due to pulse bandwidth determines the lower bound at near range.

It has to be remarked that such limits are to be intended as lower bounds only in the case where T-SAR is implemented as a simple focusing along the cross-range direction, namely by taking the Fourier Transform of the data with respect to the normal baseline. However, several methods have been developed in literature to achieve super-resolution capabilities with respect to the limits here discussed.

As for the limit due to baseline aperture, several techniques have been proposed in the Direction of Arrival (DOA) literature, such as Capon Filtering, MUSIC, APES, ESPRIT, or more sophisticated Maximum Likelihood (ML) solutions. All these techniques assume the received signal to be constituted by a number of sinusoids plus noise. Basing on this assumption, the signal parameters are estimated exploiting the concepts of array manifold and spaces of signal and noise [22], [23], [24], [25]. A different solution may be found in the works by Fornaro et al., [26], [27], focused on the analysis of urban areas, and in those relative to Polarization Coherence Tomography (PCT), due to Cloude, [28], [29], focused on the analysis of forested areas. The common trait of those works is that super-resolution is achieved by exploiting a

priori information about target location. In the case of forested areas, for example, the a priori information is represented by ground topography and canopy top height [29].

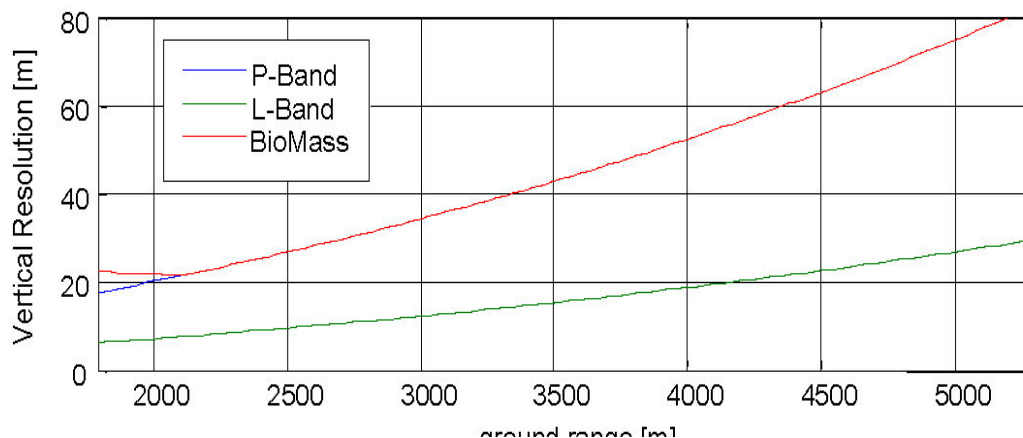


Figure 28: Vertical resolution achievable through 3D focusing for the P-Band SW, L-Band SW, and BioMass data-sets.

As for the limit due to pulse bandwidth, a possible countermeasure is to resort to a model based approach, in such a way as to rephrase T-SAR as a parametric estimation problem. This is the approach we proposed in the framework of the BioSAR 2007 campaign, see [30], [31], [32].

An alternative approach, which has the nice property of being substantially model free, has been proposed in [20], [33], starting from the consideration that the limit due to pulse bandwidth has an equivalent statistical interpretation in terms of terrain decorrelation.

The only assumption within this approach is that the vegetation layer is identified as being uniform along the ground range coordinate. Under this hypothesis the contributions of terrain decorrelation to the interferometric coherence may be compensated for by forming the interferograms after Common Band Filtering (CBF) [5], [17], [33].

Accordingly, the basic idea of the proposed approach is to replace the sample covariance matrix with the matrix of the interferograms formed after CBF. In [20], [33] it is shown that this operation results in a vertical resolution enhancement by a factor 2. The price to be paid is the loss of positive definiteness of the sample covariance matrix, resulting in the need to adopt proper countermeasures to stabilize the results, such as water filling or diagonal loading [34].

Still, in the BioMass case such an approach allows to improve the resolution from a value of about 20 m to about 10 m, therefore bringing a remarkable advantage as for the analysis of forested areas.

9.4.4.4 A note on baseline design

After Eq 5, the design of the baseline set for Tomographic application may be performed basing on standard results from Signal Theory [35]. In particular, as the aim is to correctly represent the power spectrum of the data, the baseline set has to be designed in such a way as to avoid the arising of aliasing phenomena. Letting N be the number of tracks, and assuming a uniform baseline sampling with baseline spacing Δb , the cross range of ambiguity (corresponding to the Nyquist frequency of the multi-baseline SAR system) is given by:

$$e_a = \frac{\lambda r}{2\Delta b} \quad \text{Eq 15}$$

which converts into the height of ambiguity as:

$$h_a = \frac{\lambda r \sin(\theta - \alpha)}{2\Delta b \cos \alpha} \quad \text{Eq 16}$$

Considering the resolution loss due to pulse bandwidth, the condition to avoid spectral aliasing is given by:

$$h_a > 2\Delta h_{pb} + h_v \quad \text{Eq 17}$$

where h_v is the vegetation height. Considering a vegetation layer as high as 30 m at a look angle of 25°, the condition in Eq 17 results in the requirement $h_a > 70$ m, corresponding to a baseline spacing $\Delta b = 11$ m. Note that the resolution limit due to pulse bandwidth varies as a function of terrain slope, and thus some extra margin has to be considered in the case of hilly topographic. Accordingly the choice of a 8 m horizontal baseline sampling has to be considered as a prudential trade-off between the needs to keep baseline aperture as large as possible and avoid spectral aliasing at near range, even in presence of topographic slopes.

9.4.4.5 Propagation Disturbances

The phase of SAR data is affected by two kinds of error. The first kind is related to the uncertainty about the sensor positions, due to unknown deviations of the platforms with respect to the nominal trajectories [36]. The second kind of error is due to the presence of atmospheric disturbances, which results in stochastic fluctuations of the propagation delay [37]. Although the physical origins of these two kinds of error are quite different, their impact on SAR data is rather similar, in that: both kinds of error are the result of uncompensated delays of the RADAR echoes as they travel back to the SAR sensor; both kinds of error are characterized by a large spatial decorrelation length with respect to the extent of the SAR slant range, azimuth resolution cell. Therefore, in this analysis both kinds of error will be simply referred to as Propagation Disturbances (PDs). As highlighted in many papers, the presence of PDs may easily turn out to be critical for multi-image SAR applications, preventing the exploitation of the phase information. For this reason, both InSAR and TSAR require a phase calibration step at a preprocessing stage, in order to mitigate as much as possible the impact of PDs on the data. Although the problem of phase calibration has been widely considered in SAR literature, see for example [38], [26], the only formal analysis of the impact of PDs on T-SAR has been provided in [39] and [40], at least to our knowledge.

To better detail the analysis, define the SAR data affected by PDs as:

$$y_n^{(pd)} = y_n \exp(j\alpha_n) \quad \text{Eq 18}$$

where α_n is the PD affecting the n -th acquisition.

Since PDs act as a multiplicative noise for the SAR signal, they result in a convolutive distortion affecting the Tomographic reconstruction. In other words, the macroscopic effect of PDs is to defocus the reconstructed scene along the cross range direction, due to the convolution with the Fourier Transform of $\exp(j\alpha_n)$. In case of propagation disturbances that are caused by the presence of the atmosphere, it makes sense to assume that the resulting defocusing of the reconstructed scene depends almost totally on the temporal spacing between one acquisition and another. Since the decorrelation time of the atmospheric conditions is shorter than one day, it follows that the worst case is found when the SAR images are acquired with a temporal interval of at least one day with one another, as it happens in spaceborne applications. In order to characterize this important case from a quantitative point of view, PDs

will be assumed to be a set of stochastic variables, independent and identically distributed. This hypothesis allows to treat the PDs by introducing the quantity:

$$\gamma_\alpha = E[\exp(j\alpha_n)] \quad \text{Eq 19}$$

Whatever the distribution of the PDs, it is easy to see that γ_α must be a decreasing function of the variance of the PDs. For this reason, γ_α will be interpreted as a measure of phase stability.

A viable approach to characterize quantitatively the impact of PD on the tomographic reconstruction is to assume that a large number of tracks is available, in such a way that the baseline spacing is sufficiently small to avoid aliasing problems and the cross range resolution is arbitrarily small. Under these hypotheses the backscattered power distribution can be easily retrieved by using the Periodogram estimator, whose statistical properties have been widely investigated in literature, see for example [21]. The Periodogram estimator is defined as:

$$\hat{S}(e_k) = \frac{1}{N} \left| \sum_n y_n \exp\left(j \frac{2\pi}{N} nk\right) \right|^2 \quad \text{Eq 20}$$

where $e_k = k \cdot \text{ea}/N$. The total backscattered power is then obtained as

$$\sigma_s^2 = E[|y_n|^2] = \frac{1}{N} \sum_k E[\hat{S}(e_k)] \quad \text{Eq 21}$$

It is shown in [39] that the expected value of the Periodogram in presence of PDs may be written as:

$$E[\hat{S}(e_k)^{(pd)}] = E[\hat{S}(e_k)] + \frac{1 - \gamma_\alpha^2}{\gamma_\alpha^2} \sigma_s^2 \quad \text{Eq 22}$$

Accordingly, PDs have the effect of increasing the noise floor of the Periodogram, analogously to thermal noise. Clearly, this phenomenon impacts not only on the expected value of the Periodogram, but also on its variance, so that it becomes necessary to discuss the impact of noise on the random oscillations that affect the Periodogram. In order to do this, the concept of Tomographic SNR (TSNR) has been proposed in [39]:

$$TSNR = \frac{E[\hat{S}(e_k)^{(pd)}] - E[\hat{S}(e_{k \min})^{(pd)}]}{\sqrt{V(\hat{S}(e_{k \min})^{(pd)})}} \quad \text{Eq 23}$$

Where $e_{k \min}$ is the cross range location corresponding to the minimum of the expected value of the Periodogram and $V()$ is the variance operator. Such a definition provides a direct comparison of the dynamic range of the Periodogram with respect to the amplitude of the oscillations, therefore constituting an useful tool for the evaluation of the impact of disturbances. As a rule of the thumb, the condition for obtaining reliable results can be assessed in $TSNR > 15$ dB [39]. Finally, recalling that that the square root of the variance of the periodogram is approximately equal to the expected value of the Periodogram [21], and assuming no signal contributions from cross range location $e_{k \min}$, Eq 23 simplifies to:

$$TSNR = \frac{E[\hat{S}(e_k)]}{\sigma_s^2} \frac{\gamma_\alpha^2}{1 - \gamma_\alpha^2} \quad \text{Eq 24}$$

Consider now, for sake of simplicity, a uniform vegetation layer, characterized by a constant cross range backscattered power distribution within a certain cross range support eV , which may be roughly derived as $eV = hV/\sin\theta$, being hV the vegetation height.

Assuming that the number of acquisition, N , is large Periodogram bias can be neglected, and thus the expected value of the Periodogram can be assumed as being constant inside the cross range support and null outside of it. It then follows after Eq 21 that the expected value of the Periodogram – unaffected by PDs –inside the cross range support is given by:

$$E[\hat{S}(e_k)] = \frac{e_a}{e_v} \sigma_s^2 = \frac{h_a}{h_v} \sigma_s^2 \quad \text{Eq 25}$$

Where e_a is the cross range of ambiguity and h_a is the height of ambiguity. At this point the TSNR for a uniform volumetric target may be written as:

$$TSNR = \frac{h_a}{h_v} \frac{\gamma_\alpha^2}{1 - \gamma_\alpha^2} \quad \text{Eq 26}$$

Eq 26 reveals an important concept: the higher the vegetation height, the larger is the impact of PDs on the Tomographic reconstruction. In order to state an explicit phase stability requirement, it is convenient to further assume the PDs to be Normally Distributed with standard deviation σ_α . Under this hypothesis phase stability can be directly related to σ_α via the equation:

$$\gamma_\alpha = \exp\left(-\frac{\sigma_\alpha^2}{2}\right) \quad \text{Eq 27}$$

For example, assuming that $h_a = 2 h_v$, it follows that for the TSNR to be higher than 15 dB the standard deviation associated with the PDs must be 10° or better for the correct focusing of a uniform volumetric target. Though, more stringent calibration requirements must be assumed for the 3D imaging of non uniform scenarios, as it may be the case of forested areas if strong terrain contributions occur.

It is worth noting that the TSNR can be enhanced by averaging the Periodogram over neighboring looks. In this case, it may be shown [39], [40] that, provided that the number of looks employed in the average is large, the TSNR is enhanced by a factor that is roughly proportional to the square root of the ratio between the maximum normal baseline and the critical baseline. As a consequence, the impact of PDs can be recovered by adding new acquisitions beyond the critical baseline.

9.4.4.6 Phase Calibration

The urgency for the establishment of reliable Phase Calibration techniques has been pointed up since the advent of multi-baseline SAR Interferometry (InSAR). InSAR Phase Calibration techniques typically rely on the hypothesis that a sufficiently dense set of PS is found within the imaged scene, [11], or that it is possible to reconstruct a reliable set of calibrating phases basing on small normal and temporal baselines, [26]. A phase calibration techniques that explicitly accounts for the presence of volumetric scattering has been proposed in [41]. Such a methodology is based on the concepts of Algebraic Synthesis [42], [43], and Phase Linking [44], [20]. The Algebraic Synthesis technique allows the retrieval of ground contributions within the data. Such a technique constitutes a key element of the Tomographic processing proposed in the present work, and will be detailed in the next section. The Phase Linking algorithm, instead, is a Maximum Likelihood technique for the estimation of the interferometric phases in N tracks, under the hypothesis of scattering from a single target. The result is a three step Phase Calibration procedure, detailed as follows:

1. The data covariance matrix relative to ground only contributions, R_g , is retrieved via the Algebraic Synthesis technique.

2. The matrix R_g is analyzed through the Phase Linking algorithm, which produces the estimates of the N interferometric phases associated with the optical paths from the ground level to the N SAR sensors.
3. Basing on such estimates, Phase Calibration is performed through standard techniques from PS interferometry.

For brevity, such a technique will be hereinafter referred to as AS-based calibration technique.

The validity of this approach with respect to the conventional PS-based approach has been discussed in [41], basing on the BioSAR 2007 data-set. As a result, it has been observed that the AS-based calibration technique performs as well as the PS-based approach, if not even better, resulting in the possibility to obtain an accurate Tomographic reconstruction. Details are provided in [41].

9.4.5 Disjoint Tomographic Imaging of Ground and Volume: Algebraic Synthesis

The Algebraic Synthesis (AS) technique [42], [43], [41], has recently been developed to the aim of merging the advantages of the PolInSAR technique with the vast range of products deliverable through multi-baseline Tomographic techniques. The result is an algebraic decomposition technique, which allows to proceed to Scattering Mechanism (SM) separation by employing not only model based approaches, generally retained in literature, but also model free and hybrid approaches, while yielding the best Least Square solution for any given number of SMs.

The AS here discussed provides important advantages with respect to the COMET approach exploited in the framework of BioSAR 2007. In first place, the AS technique is easier to implement: the algorithm works in a totally blind fashion, without the need for initialization and constraining. Furthermore, the exploitation of algebraic decomposition techniques results in a substantial reduction of the computational burden with respect to the COMET. However, the most important advantage of the AS technique over the COMET is its capability to work in absence of an a-priori physical model for the targets. Finally, it is worth noting that the results yielded by the COMET can be reproduced in the framework of the AS technique as well, simply by choosing the proper solution for the retrieval of the volume structure.

9.4.5.1 Mathematical Formulation:

The AS technique relies on three basic hypotheses:

- H1) statistical uncorrelation of the different scattering mechanisms (SMs), such as ground, volume, and ground-trunk scattering;
- H2) independence of volumetric and temporal coherence losses of each SM alone on the choice of the polarimetric channel;
- H3) invariance (up to a scale factor) of the average polarimetric signature of each SM with respect to the choice of the track.

The validity of hypothesis H1 is supported by the fact that distinct SMs are associated with distinct physical objects, or with different wave directions in case of multiple scattering (such as ground-trunk or ground-volume scattering). Considering only spatial decorrelation phenomena, the validity of hypothesis H2 is subjected to the condition that the spatial structure of each SM can be described independently on the choice of the polarimetric channel. This is surely true as long as geometrical descriptors are used, such as terrain slope or volume top height, for example. However, this hypothesis is not strictly verified if electromagnetic descriptors are considered, such as subsurface penetration or volume extinction, since such parameters may undergo a variation from one polarimetric channel to another. Accordingly, retaining hypothesis H2 is equivalent to considering only the average electromagnetic properties of each SM across the three polarimetric channels. An analogous conclusion can be drawn as for temporal decorrelation. Hypothesis H3 is equivalent to assuming that the temporal and geometrical separation among different tracks result in at most a variation of the total backscattered power associated with each SM. The validity of this hypothesis is clearly subjected to the conditions that: a proper polarimetric calibration has been performed [10]; only a small variation of the look angle occurs from one track to another; the average polarimetric signature of each SM is temporally homogeneous. The latter point entails that the cases where events like floods, fires, frosts, deforestation occur only in some of the acquisitions are to be considered out of the range of validity of the AS technique, as well as the case where acquisitions from different seasons have to be processed jointly. It is important to note that hypotheses H1, H2, H3 are fully consistent with the Random Volume over Ground (RvoG) model often assumed in single baseline PolInSAR applications [13], [45].

Consider now a data constituted of 3N fully polarimetric SAR images acquired along N distinct tracks, and let $y_n(w_i)$ denote a complex valued pixel from the n-th track in the polarimetric channel identified by the polarimetric projection vector w_i [14], the dependency on the slant range, azimuth coordinates being made implicit to simplify the notation. Further define the multi-polarimetric multi-baseline (MPMB) data vector as:

$$\mathbf{y} = [\mathbf{y}^T(\mathbf{w}_1) \quad \mathbf{y}^T(\mathbf{w}_2) \quad \mathbf{y}^T(\mathbf{w}_3)]^T \quad \text{Eq 28}$$

where $y(w_i)$ is the stack of the multi-baseline data in polarization w_i .

It follows after the three hypotheses discussed above that the covariance matrix of the MPMB data can be expressed as a Sum of Kronecker Products (SKP). In formula:

$$\mathbf{W} = E[\mathbf{y}\mathbf{y}^H] = \sum_k^{K_T} \mathbf{C}_k \otimes \mathbf{R}_k \quad \text{Eq 29}$$

where:

- \mathbf{W} is the covariance matrix of the MPMB data [3Nx3N]
- K_T is the total number of SMs that contribute to the SAR signal, such as ground scattering, volume scattering, ground trunk scattering, or other.
- \mathbf{C}_k is the polarimetric covariance (among different polarizations) matrix associated with the k -th SM [3x3].
- \mathbf{R}_k is the interferometric covariance matrix (among different tracks) associated with the k -th SM [NxN]

Therefore, Eq 29 states that each SM is represented by a Kronecker Product between two matrices, one, C_k , accounting for the electromagnetic properties and the other, R_k , for the spatial structure of that SM. By virtue of their physical meaning, the matrices C_k and R_k will be hereinafter referred to as polarimetric signatures and structure matrices, respectively. It is important to note that both the polarimetric signatures and the structure matrices are by definition positive definite, since they are obtained by taking the correlations between different tracks and/or different polarizations.

The key to the exploitation of the SKP structure is the important result, due to Van Loan and Pitsianis [46], after which every matrix can be represented as a weighted SKP, the weight representing a measure of the contribution of each Kronecker Product. In other words, the matrix W can always be rewritten as:

$$\mathbf{W} = \sum_k^{K_T} \lambda_k \mathbf{U}_k \otimes \mathbf{V}_k \quad \text{Eq 30}$$

Where:

- λ_k is the weigh associated with each of the Kronecker Products. All weights are positive valued by construction. By convention it will be assumed that:

$$\lambda_1 \geq \lambda_2 \geq \dots \geq \lambda_{K_T} \quad \text{Eq 31}$$

- $\mathbf{U}_k, \mathbf{V}_k$ are two sets of matrices that can be obtained in closed form directly from \mathbf{W} . The dimensionalities of $\mathbf{U}_k, \mathbf{V}_k$ is the same as \mathbf{C}_k and \mathbf{R}_k , respectively.

Two important results follow:

- R1) The best Least Square approximation of the data covariance matrix with $K < K_T$ Kronecker Products is obtained by truncating the sum in Eq 31 to the K-th term.

R2) The two sets of matrices U_k and V_k , which are known via the SKP Decomposition of W , can be transformed into the two sets of matrices C_k, R_k , which carry the information about the physics of each SM. Such a transformation is linear, invertible, and it is determined by exactly $K(K-1)$ real numbers.

Proofs: see [42], [43].

An interesting corollary of the second of the results above is found when only $K=2$ SMs are present, corresponding to the assumption of ground and volume scattering. In this case the transformation that links the matrices U_k and V_k to the polarimetric signatures and structure matrices of ground and volume scattering is determined by just 2 real numbers, and may be cast in the form:

$$\begin{aligned}
 \mathbf{R}_g &= a\mathbf{V}_1 + (1-a)\mathbf{V}_2 \\
 \mathbf{R}_v &= b\mathbf{V}_1 + (1-b)\mathbf{V}_2 \\
 \mathbf{C}_g &= \frac{1}{a-b}(b\lambda_1\mathbf{U}_1 - (1-b)\lambda_2\mathbf{U}_2) \\
 \mathbf{C}_v &= \frac{1}{a-b}(-a\lambda_1\mathbf{U}_1 + (1-a)\lambda_2\mathbf{U}_2)
 \end{aligned}
 \tag{Eq 32}$$

It is worth pointing out the cross-relation existing between the structure matrix of one SM and the polarimetric signature of the other: the parameter a determines the ground structure matrix and the volume polarimetric signature (up to a scale factor), whereas the parameter b determines the volume structure matrix and the ground polarimetric signature (up to a scale factor).

On this basis, the AS technique has been developed as an operational tool for the separation of ground and volume scattering even in absence of a physical model, while ensuring the physical validity of the solution and yielding the best Least Square solution given the hypothesis of two SMs. The procedure can be summarized as follows:

1. Truncate the SKP Decomposition of the sample covariance matrix of the data by retaining the first two terms. This operation ensures the best Least Square fit given the hypothesis of two SMs.
2. Determine the range of values for the parameters (a,b) that yields positive definite solutions for C_g, R_g, C_v, R_v . This operation ensures the physical validity of the solutions.
3. Optimize some criterion in order to pick a unique solution among the set of all the physically valid ones.

Different approaches may arise depending on the criteria to be optimized at step 3. In a model based approach the solution is chosen in such a way that the polarimetric signatures and/or the structure matrices are as close as possible to some physically based model. Otherwise, the solution can be chosen in a model free fashion, through the optimization of some algebraic criterion.

9.4.5.2 Geometrical Interpretation

The AS technique may be given a straightforward geometrical interpretation, providing useful insights about how this methodology works.

Consider the problem of the separation of ground and volume scattering, basing on single baseline ($N = 2$), fully polarimetric acquisitions, and assume, for sake of simplicity, that the data is stationary, so that the structure matrix of each SM has unitary entries on the main diagonal. This property is inherited by the matrices V_1, V_2 in Eq 32, resulting in the possibility to recast the equations relative to the

structure matrices in Eq 32 by considering only the off-diagonal terms, which represents the interferometric coherences. In formula:

$$\begin{aligned} \gamma_g &= a\gamma_1 + (1-a)\gamma_2 \\ \gamma_v &= b\gamma_1 + (1-b)\gamma_2 \end{aligned} \quad \text{Eq 33}$$

Accordingly, the interferometric coherences associated with ground and volume scattering are bound to lie on the line l in the complex plane that passes through γ_1, γ_2 . The positive definitiveness condition for the structure matrices is satisfied by requiring that $|\gamma_g| \leq 1, |\gamma_v| \leq 1$, and thus only the portion of l inside the unitary circle has to be considered. Further requiring the positive definitiveness condition for the polarimetric signatures, it follows that the physical solutions for γ_g, γ_v are bound to belong to two branches s_a, s_b along the line l , as depicted in Figure 29, left panel. Accordingly, the problem of identifying two SMs basing on multi-polarimetric, single baseline data is equivalent to the problem of finding two points along the segments s_a, s_b . This conclusion is exactly the same as the one drawn by Cloude and Papathanassiou in [45] assuming the RvOG model, although in that paper a totally different methodology is used, and only the single baseline case is considered.

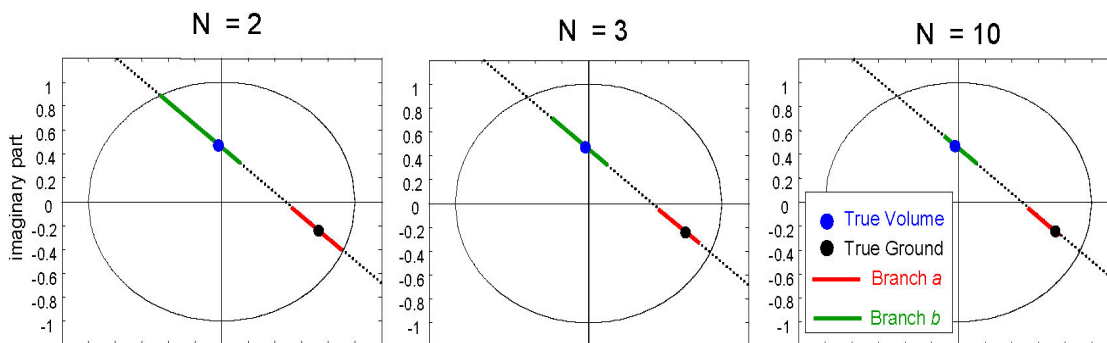


Figure 29: Regions of physical validity for ground and volume interferometric coherence in the interferometric pair between track 0 and track 1. N is the total number of available tracks. Branch a (red) and b (green) are associated with physically valid solutions for ground and volume scattering, respectively. True ground and volume coherence are indicated by the black and blue points, respectively.

As new acquisitions are gathered, instead, the positive definitiveness constraint results in the regions of physical validity to shrink, depending on the total number of available tracks, see Figure 29, middle and right panels. Accordingly, the larger the number of available tracks, the easier it is to pick the correct solutions.

By virtue of this result, the AS technique here proposed can be thought of as a multi-baseline extension of the procedures usually exploited in single-baseline PolInSAR that is able to jointly exploit all the available interferograms, in such a way as to ensure the physical validity of the solution and optimize the desired criteria by considering the whole data-set at once.

9.4.5.3 Choice of the solutions

Despite the availability of multiple baselines, the problem of SM separation is always affected by an ambiguity, corresponding to the extent of the region of physical validity. In fact, it is important to remark that the choice of the parameters (a,b) does affect the solution in terms of retrieving the polarimetric and structure matrices for ground and volume scattering, but the sum of their Kronecker products is invariant to

choice of the solutions, being identically equal to the best approximation of the data covariance matrix in the Least Square Sense, by virtue of result R1 in section 9.4.5.1. It follows that all the solutions in the region of physical validity are physically valid and give rise to exactly the same data covariance matrix, and thus there is no way to assess algebraically which solution is correct.

It is then important to characterize the different possibilities from a physical point of view, in order to provide a correct interpretation of the results and drive the choice of the criterion for the retrieval of the structure matrix associated with volume scattering.

To do this, a forest scenario has been simulated with the following features:

- Ground coherence losses, accounting for possible decorrelation sources (temporal, noise, or others);
- Volume contributions from the ground level, accounting for the presence of undestorey and scattering from lower branches
- Presence of ground contributions in HV, accounting for 10% of the total energy in HV.
- Variable number of tracks, ranging from $N = 2$ to $N = 10$. The baseline spacing is the same in all cases, so that the overall baseline aperture increases with N .

Two solutions have been evaluated for each branch, corresponding to the inner and outer boundaries of the region of physical validity, see Figure 30.

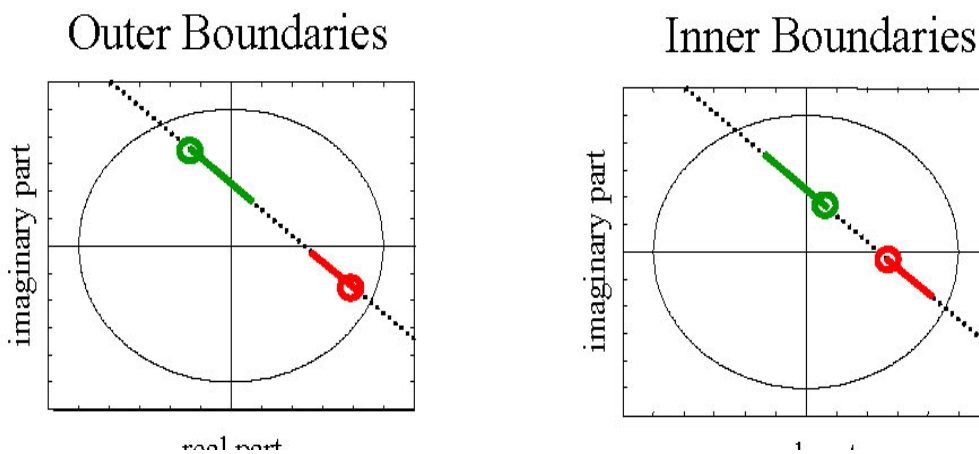


Figure 30: Outer and Inner Boundary solutions. Branches a and b are drawn in red and green, respectively.

The resulting backscattered power distributions for ground and volume scattering are reported in Figure 31 and Figure 32. It is important to recall that the solution on branch a determines the ground structure matrix and the volume polarimetric signature, whereas the solution on branch b determines the volume structure matrix and the ground polarimetric signature, see Eq 32 . Accordingly, the meaningfulness of each solution has to be discussed by taking into account its outcomes relatively to both the structures matrix of one SM and the polarimetric signature of the other. The results have been summarized as follow.

The inner boundary solution on branch a results in the volume polarimetric signature to be rank-deficient, after which it follows that, this solution is not consistent with physical model for forest scattering. Independently on the number of tracks, the estimate the ground structure is contaminated by volume contributions, resulting in apparent components from above the ground. Accordingly, such a solution is to be discarded.

The outer boundary solution on branch a results in the volume polarimetric signature to be full rank, consistently with physical model for forest scattering. The resulting ground structure matrix is maximally coherent. Due to the presence of coherence losses, the effective ground phase center is under-estimated in the case where few tracks are employed. Despite the presence of ground coherence losses, however, the resulting ground backscattered power distribution converges to the true one as the number of available baselines increases.

The inner boundary solution on branch b results in the ground polarimetric signature to be rank-deficient, consistently with the hypothesis that there exists one polarization where volume only contributions are present. If this is true, resulting volume structure corresponds to the true one. Otherwise, the result is systematically contaminated by ground contributions, resulting in apparent volume contributions close to the ground.

The outer boundary solution on branch b results in the ground polarimetric signature to be full rank, consistently with the presence of ground contributions in all polarizations. The resulting volume structure matrix is maximally coherent. If few tracks are employed, this solution acts as a high-pass filter, resulting in the volume to appear thinner than it is. As the number of available baselines increases, this solution converges to the true structure for volume contributions above the ground, whereas volume contributions from the ground level are absorbed into the ground structure.

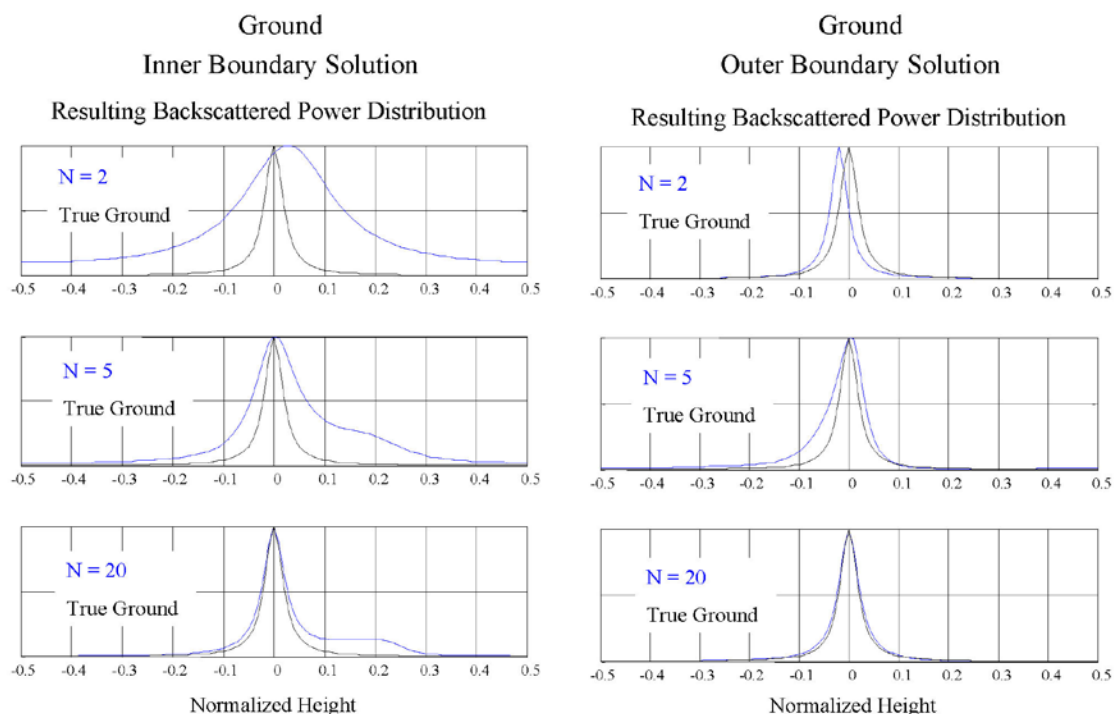


Figure 31: Backscattered power distribution for ground scattering retrieved by taking the Inner Boundary (left) and Outer Boundary (right) solutions.

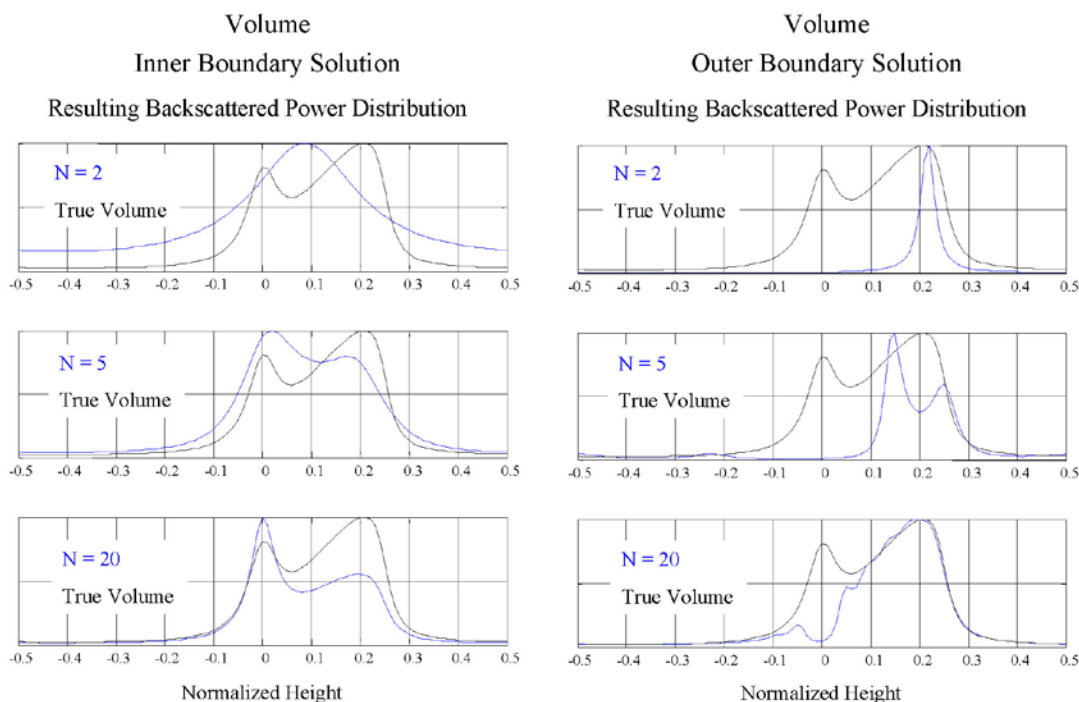


Figure 32: Backscattered power distribution for volume scattering retrieved by taking the Inner Boundary (left) and Outer Boundary (right) solutions.

9.4.5.4 Summary.

The maximal coherence (outer boundary) solution is a suitable criterion for the retrieval of the ground component, implying that the ground contributions are the most stable.

Such a criterion is the one exploited in [41] for the separation of ground contributions to the aim of Phase Calibration. Performances have turned out to be comparable to those of the PS-based approach, therefore providing experimental evidence of its validity. Furthermore, the resulting volume polarimetric signature is full rank, consistently with the hypothesis of a high entropy scattering mechanism.

Considering the volume structure, the maximal coherence solution provides the asymptotical convergence to the true solution for the volume scattering above the ground, but it does not account for volume scattering from the ground level. Thus, the minimal and maximal coherence solutions provide respectively a polarimetry driven and a tomography driven representation of the volume structure. Which representation, or even which combination of the two, is most effective for the aim of forest analyses, with particular regard to biomass estimation, is to be considered an open problem so far.

9.4.6 Tomographic Processing

The Tomographic processing has been implemented as follows.

Covariance Estimation:

The covariance matrix of the multi-polarimetric and multi-baseline SLC RGI data at each slant range, azimuth location is obtained by evaluating all the available interferograms.

In the BioMass case the interferograms have been formed after performing Common Band Filtering (CBF), accordingly to the discussion in section 9.4.4.3.

The size of the estimation window has been set to 60 x 60 m (ground range, azimuth) for all data-sets.

SKP Decomposition

The sample covariance matrix is decomposed into a Sum of Kronecker Products. The first two terms of the SKP Decomposition are retained, in order to identify ground and volume contributions.

Algebraic Synthesis of Ground Structure

Ground structure is retrieved by maximizing the coherence amplitudes in all interferograms under the constraint of physical validity.

Phase Calibration

The Phase Linking algorithm is employed for the estimation of the ground phases, basing on the ground structure matrix retrieved at the previous step. Phase Calibration is performed by compensating the data for the ground phases. Note that this operation automatically zeroes ground phase center elevation, since the information about terrain topography is embedded in the ground phases.

Tomographic Analysis of each polarimetric channel

Estimation of the spatial distribution of the backscattered power associated with each polarimetric channel.

Algebraic Synthesis of Volume Structure

Volume structure is retrieved by looking for the Largest Volume Solution, see details in the following. The polarimetric signatures associated with ground and volume scattering are then evaluated according to Eq 32 in section 9.4.5.1.

Tomographic Analysis of Ground and Volume Structures

Estimation of the spatial distribution of the backscattered power associated with ground and volume scattering.

Retrieval of Terrain Elevation

The ground phases are processed in order to separate topographic contributions from Propagation Disturbances.

The estimation of the spatial distribution of the backscattered powers has been performed in all cases by employing the Capon Spectral Estimator. Such an estimator produces super-resolution capabilities and grating lobes reduction without the need for a-priori information about the targets, see for example [25], [47]. The main drawback associated with the Capon Spectral Estimator is the poor radiometric accuracy, especially in presence of a low baseline aperture. In this sense, conventional Fourier analysis is more accurate. Yet, the resulting spatial resolution would be completely lost at P-Band, as discussed in section

9.4.4.3. A formal treatment of these arguments is found in [34], where both the Fourier and Capon estimators are discussed as special cases of a generalized spectral estimation technique. In particular, it is shown that spatial resolution and radiometric accuracy can not be achieved at the same time, at least in absence of precise a-priori information. Accordingly, the employment of the Capon Spectral Estimator has to be considered as a compromise. Indeed it results in non accurate backscattered power values, but it permits to appreciate details that would not be accessible otherwise with the available baseline set. However, it is very important to remark that the Capon Spectral Estimator has been used only for imaging purposes, whereas the assessment of the backscattered powers associated with ground and volume scattering is carried out through the Algebraic Synthesis technique.

A further remark about Phase Calibration is required. According to the procedure above, Phase Calibration is split into two steps. Firstly, the ground phases are removed, in such a way as to focus the targets above the ground level. This operation clearly results in the loss of the information about terrain topography. Yet, it allows the best focusing of the target along the vertical direction, since Propagation Disturbances are removed as well. Furthermore, this first step has the great advantage of being totally blind. In other words, no a-priori information is required about the scene topography, and no physical modeling of Propagation Disturbances is required either.

A further analysis is then required in order to separate topographic contributions from Propagation Disturbances. In this step, any kind of a-priori information or physical models can greatly enhance the performance, resulting in more accurate topography retrieval.

9.4.7 Tomographic Profiles

In this section the outcomes of the Tomographic analysis of the BioSAR 2008 data-sets are discussed basing on the retrieved backscattered power distributions for a single azimuth cut, selected due to the presence of both open and forest areas. The coordinate (in pixel) for the selected azimuth cut is: 5060 (P-Band SW and BioMass), 8884 (L-Band SW), 7847 (P-Band NE), 12845 (L-Band NE). Terrain topography is characterized by both positive and negative ground range slopes, whose magnitude is up to 8°. Terrain topography for the selected area is shown in Figure 33.

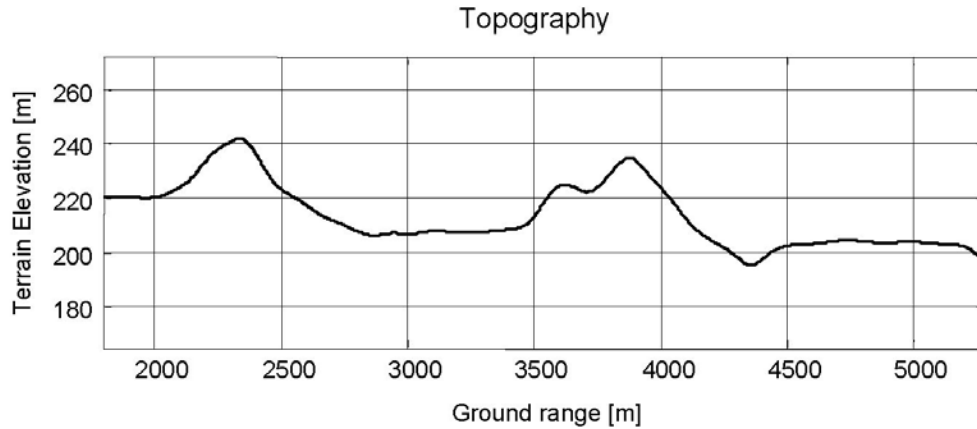


Figure 33: Terrain Topography for the selected azimuth cut.

Each of the panels to follow has been obtained by geocoding the estimated backscattered power distribution from the slant range, cross range coordinates to the ground range, height coordinates, basing on the information about the flight geometry and terrain topography. A further re-sampling operation has then been performed in order to flatten the topography, in such a way as to directly relate the vertical coordinate to the elevation of the targets above the ground. For sake of comparison, each panel reports the graph of the forest height corresponding to the H100 index, which has been evaluated basing on LIDAR-measurements.

9.4.7.1 Tomographic Profiles in HH and HV

The tomographic profiles relative to the HH and HV channels for the five data-sets under analysis are reported in the panels from Figure 34 through Figure 38.

In first place, a loss of vertical resolution from near to far range is clearly visible, due to the reduction of the normal baseline aperture. This phenomenon affects especially P-Band data, where the Fourier resolution is higher than 70 m at far ranges. However, also at far ranges the employment of the Capon spectral estimator manages to retrieve a suitable image of the scene, resulting in a good match with LIDAR measurements.

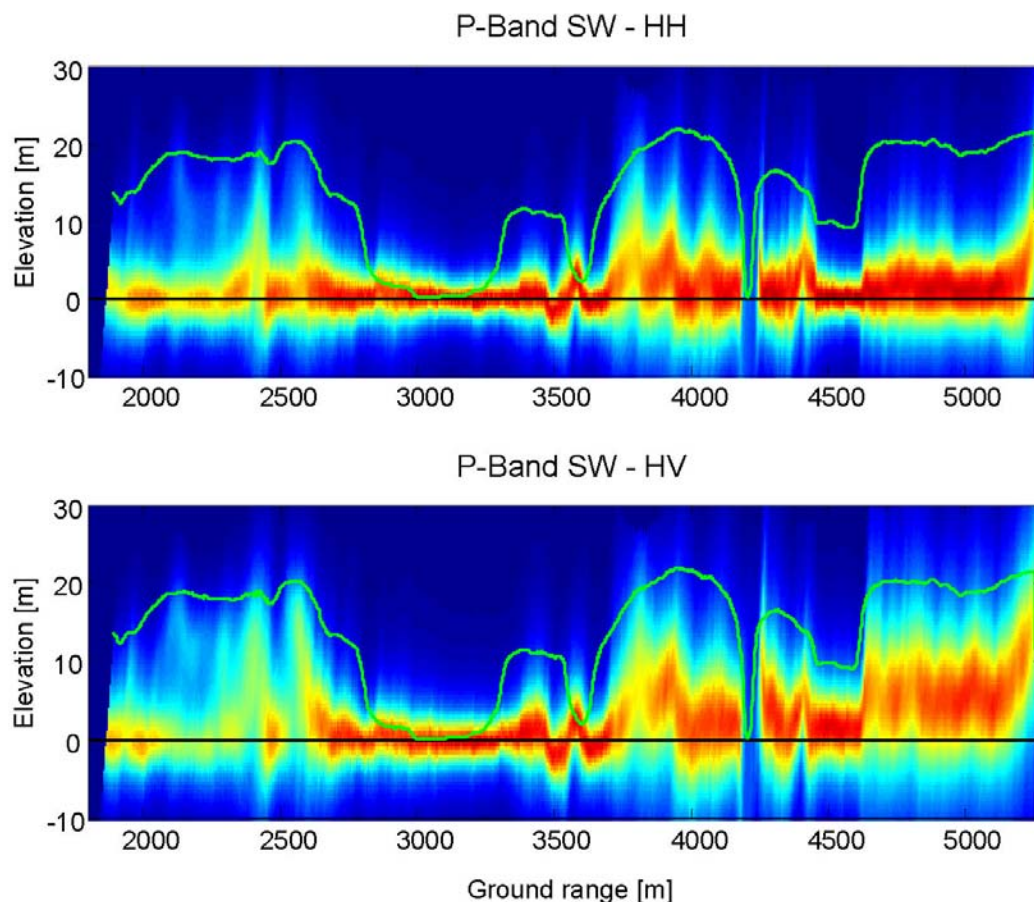


Figure 34: Tomographic Profiles for the selected azimuth cut. Top row: HH. Bottom row: HV. Data-set: P-Band SW.

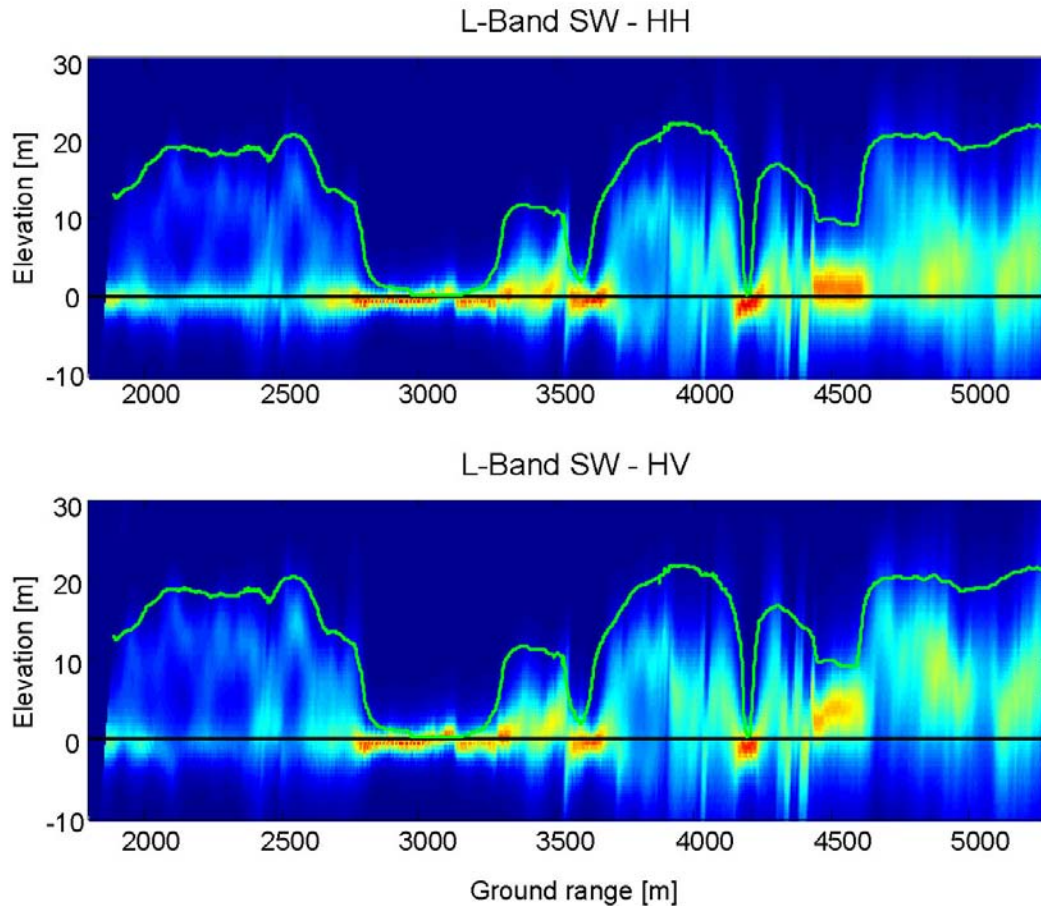


Figure 35: Tomographic Profiles for the selected azimuth cut. Top row: HH. Bottom row: HV. Data-set: L-Band SW.

At P-Band, relevant contributions from the ground level below the forest are found both in HH and HV. It follows that the effective phase center, which corresponds to the location of the maximum of the backscattered power along the vertical direction, is very close to the ground in HH, and only slightly above the ground in HV. Note that this conclusion is not peculiar to the azimuth cut under analysis, as the same behavior of the phase center location along the vertical direction has been observed throughout the whole imaged scene.

As expect, the phase center elevation at L-Band is higher than at P-Band, due to stronger volume contributions from the tree canopies. Nevertheless, a remarkable agreement has been observed between P-Band and L-Band data, as it may be appreciated by comparing Figure 34 and Figure 36 to Figure 35 and Figure 37. It is very important to note contributions from the ground level may be observed at L-Band as well see Figure 35 and Figure 37, even though to a far less extent with respect to P-Band. This phenomenon is well appreciable in the near range areas, where vertical resolution is finer. Accordingly, ground contributions are visible at both wavelengths, independently of polarization.

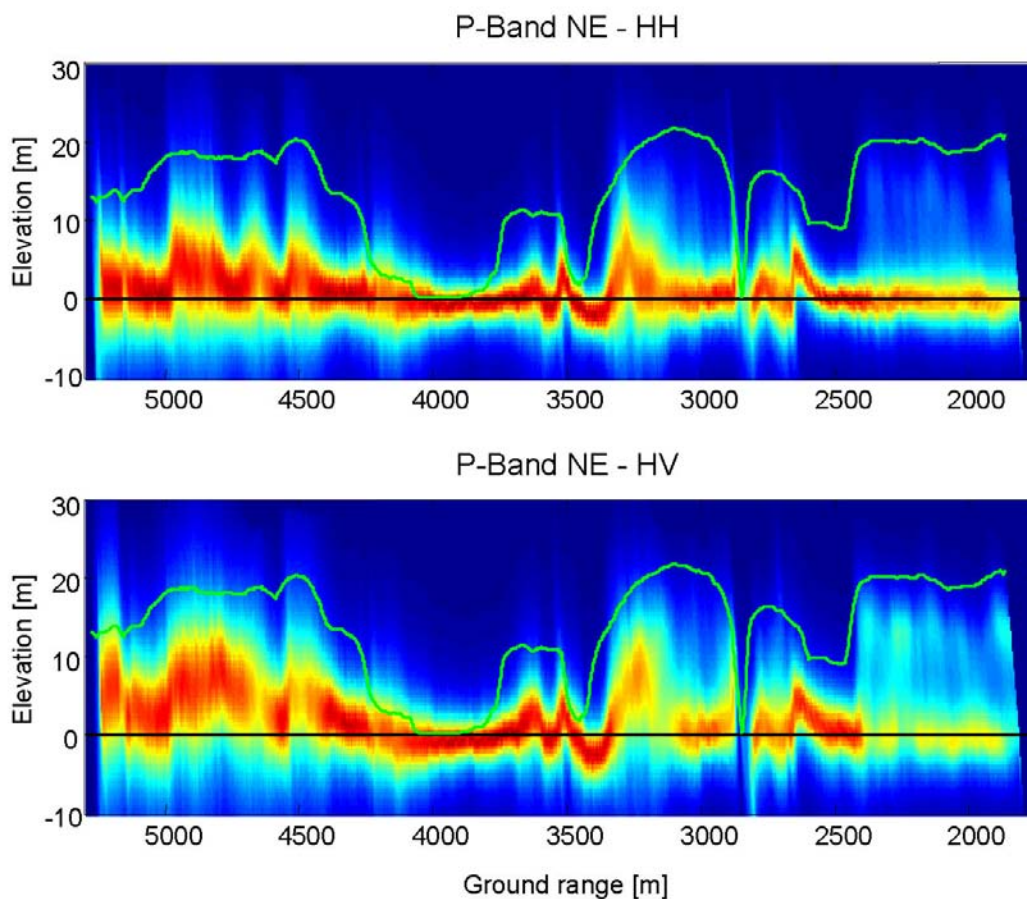


Figure 36: Tomographic Profiles for the selected azimuth cut. Top row: HH. Bottom row: HV. Data-set: P-Band NE.

Besides the resolution loss from near to far range, no remarkable difference is observed between SW and NE acquisitions. This result proves that the impact of ground slopes may be properly compensated for, given the availability of system geometry and terrain topography.

Due to the presence of stronger volume contributions, a better match with LIDAR measurements is observed at L-Band, whereas at P-Band the presence of stronger ground contributions tends to conceal scattering contributions from the tree canopies. Further evidence in support of this conclusion is found by observing that the tomographic profiles in HH and HV are closer to each other at L-Band than at P-Band.

Finally, despite the huge resolution loss with respect to the airborne case, the tomographic profiles obtained by processing the BioMass data-set have turned out to be consistent with those relative to the P-Band SW data-set, see Figure 34 and Figure 38.

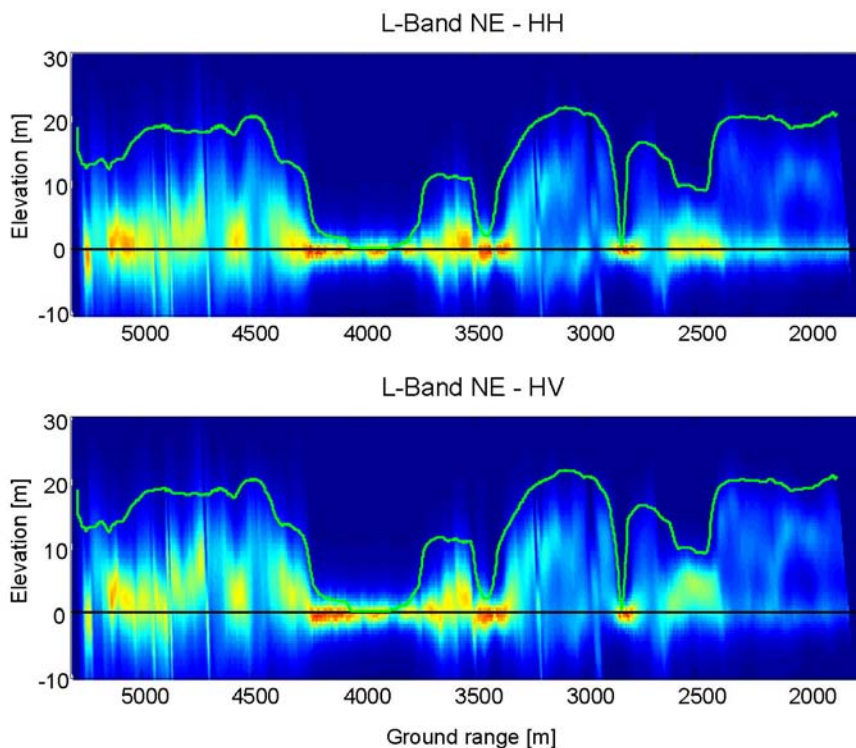


Figure 37: Tomographic Profiles for the selected azimuth cut. Top row: HH. Bottom row: HV. Data-set: L-Band NE.

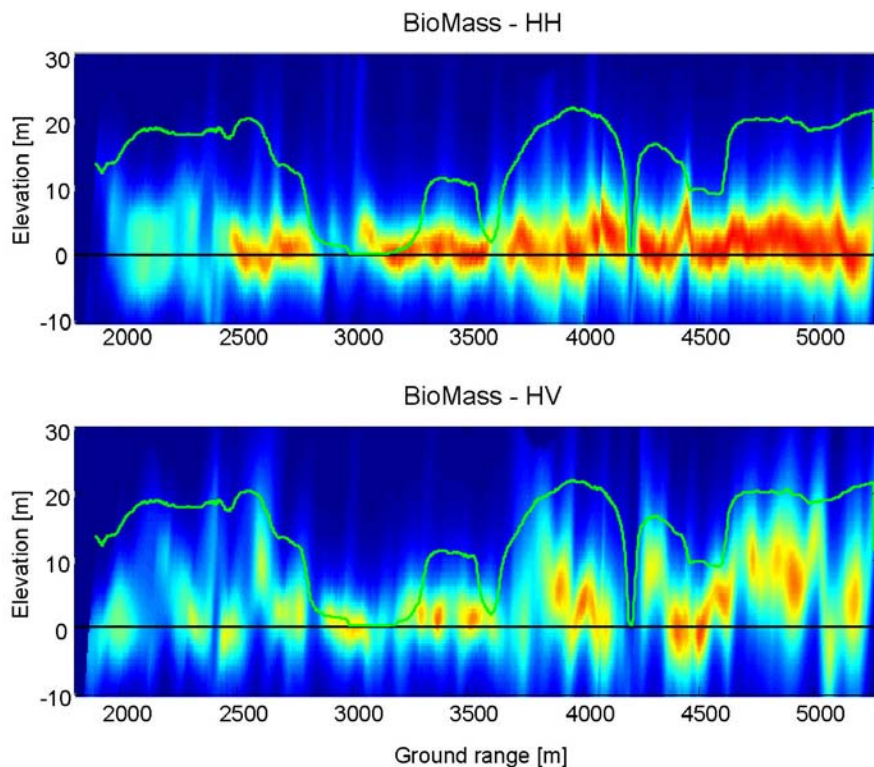


Figure 38: Tomographic Profiles for the selected azimuth cut. Top row: HH. Bottom row: HV. Data-set: BioMass.

9.4.7.2 Algebraic Synthesis

This section is devoted to the tomographic analysis of the SM identified by the AS technique as being associated with ground and volume scattering.

A first important result relative to the application of the SKP Decomposition is reported in Figure 39, which shows the percentage of information that is represented by truncating the SKP Decomposition of the sample covariance matrix at the K-th term, for K ranging from K=1 to K = 5, relatively to the same azimuth cut analyzed in the previous section.

The percentage of information retained has been assessed directly from the data as:

$$I = 1 - \frac{\|\hat{W} - W_K\|_F}{\|\hat{W}\|_F} \quad \text{Eq 34}$$

Where W is the sample covariance matrix, WK is its approximation with K Kronecker products, and F denotes the Frobenius matrix norm.

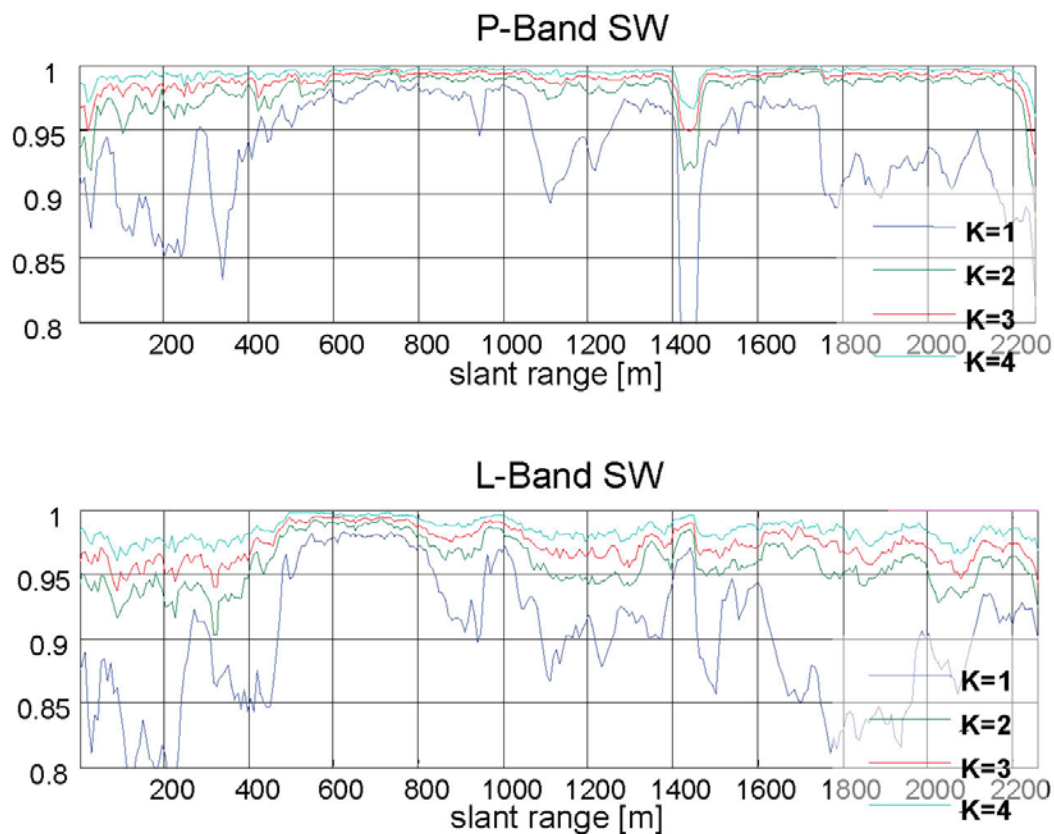


Figure 39: Percentage of information represented by retaining a number of Kronecker products ranging from K=1 to K=5. Top row: P-Band SW data-set. Bottom row: L-Band SW data-set.

Accordingly, the graphs in Figure 39 show that at both P-Band and L-Band more than 90% of the information carried by the data covariance matrix can be correctly represented by retaining just two Kronecker products, after which it follows that the assumption of two SMs is well justified.

At this point, the problem is to properly separate such two SMs, in order to provide a physically meaningful interpretation. In fact, the problem of SM separation is affected by an intrinsic ambiguity, which can not be solved without further hypotheses, see section 9.4.5.

As discussed in section 9.4.5, the ground structure has been determined through maximization of the interferometric coherence amplitudes, under the constraint of positive definitiveness. The results are shown in Figure 40. Especially at P-Band, it may be appreciated that volume contributions have been significantly rejected with respect to the HH and HV tomographic profiles reported in the previous section. Some leakage is present at L-Band as for forested areas, due to the presence of stronger volume contributions.

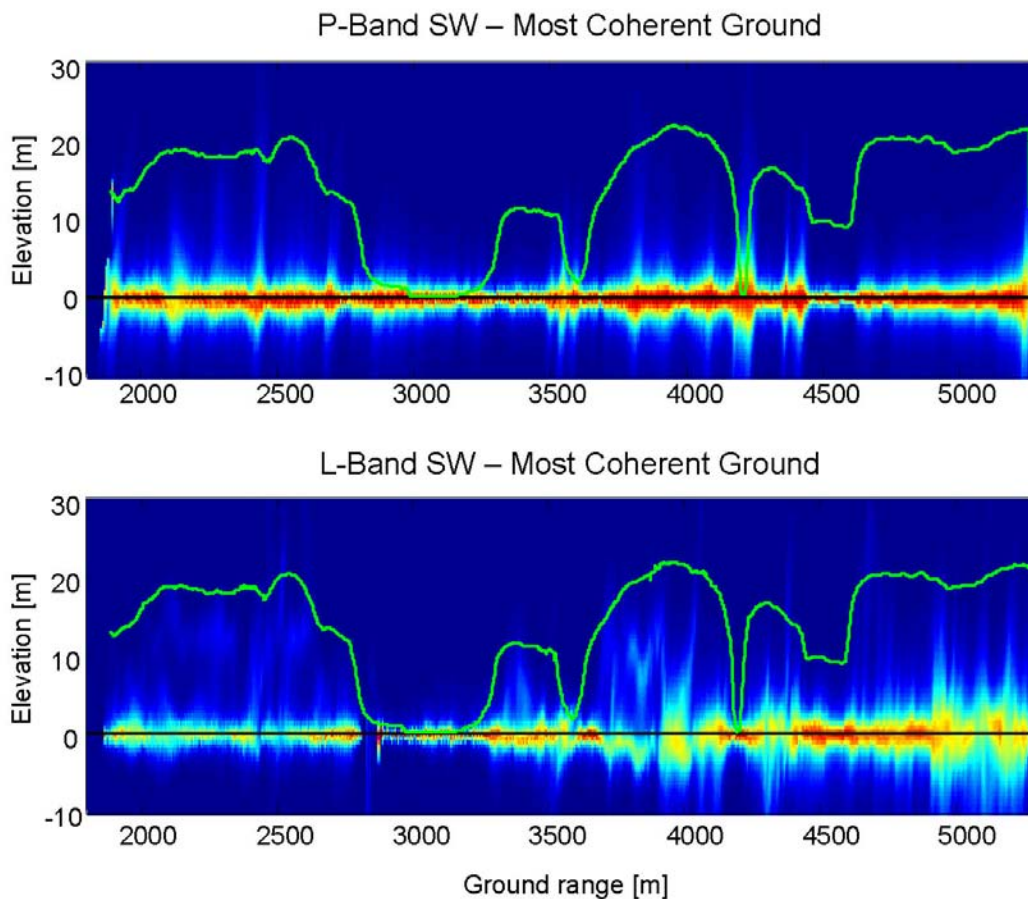


Figure 40: Tomographic profiles for Ground scattering for the selected azimuth cut. Top row: P-Band SW. Bottom row: L-Band SW.

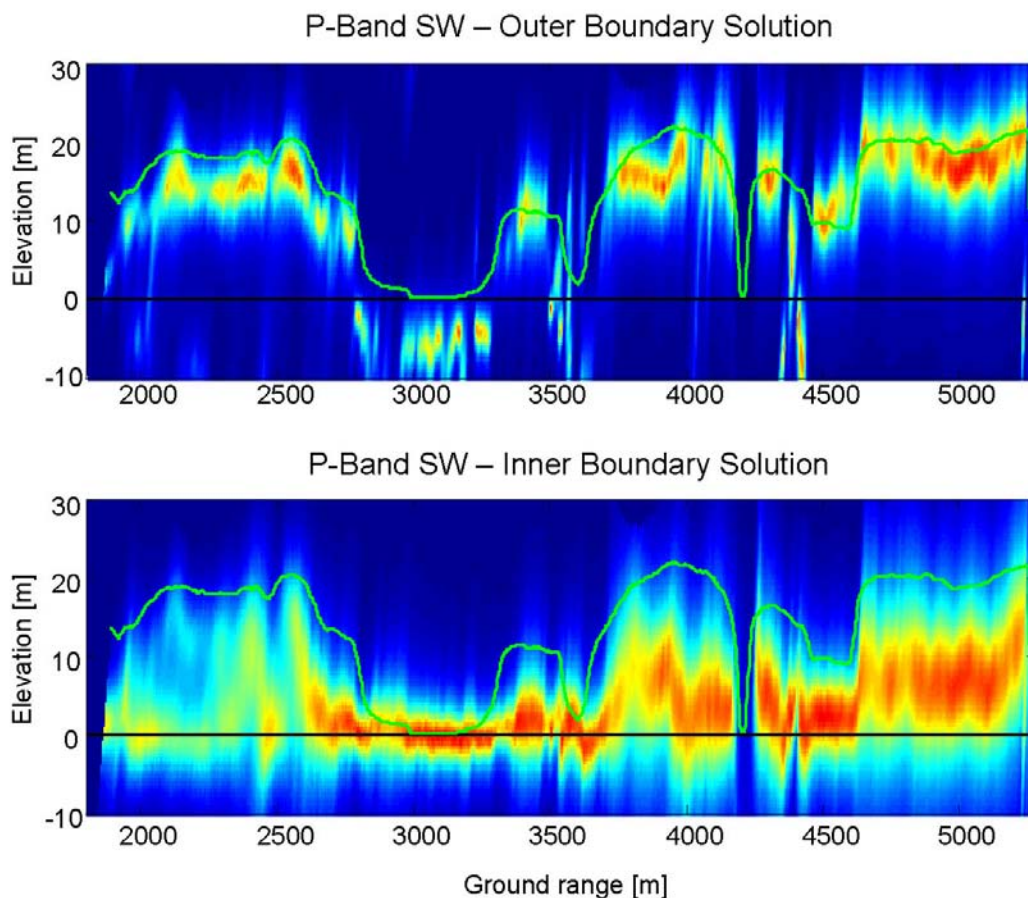


Figure 41: Tomographic Profiles of Volume scattering for the selected azimuth cut. Top row: Outer Boundary Solution. Bottom row: Inner Boundary Solution. Data-set: P-Band SW.

Figure 41 and Figure 42 show the tomographic profiles associated with volume scattering at P-Band and L-Band, retrieved in correspondence with the outer and inner boundary solutions discussed in section 9.4.5. Similar conclusions may be drawn for both wavelengths.

The outer boundary solution results in unlikely thin volumes at a high elevation. This phenomenon is due to the coarse vertical resolution, resulting in the high-pass behavior of the outer boundary solution to have a significant impact, especially at P-Band.

The tomographic profiles yielded by the inner boundary solution are quite similar to those obtained in HV. In particular, relevant contributions from the ground level are observed at both wavelengths. This result has two possible explanations: either the outer boundary solution is wrong, resulting in non-rejected ground components, or contributions from the ground level are to be explained in terms of understory and ground-volume interactions.

It is worthwhile noting that the inner and outer boundary solutions are closer to each other at L-Band, especially in near range. This phenomenon is consistent with the fact that L-Band data are characterized by a better vertical resolution than P-Band, resulting in a reduction of the ambiguity that affects the problem of SM separation.

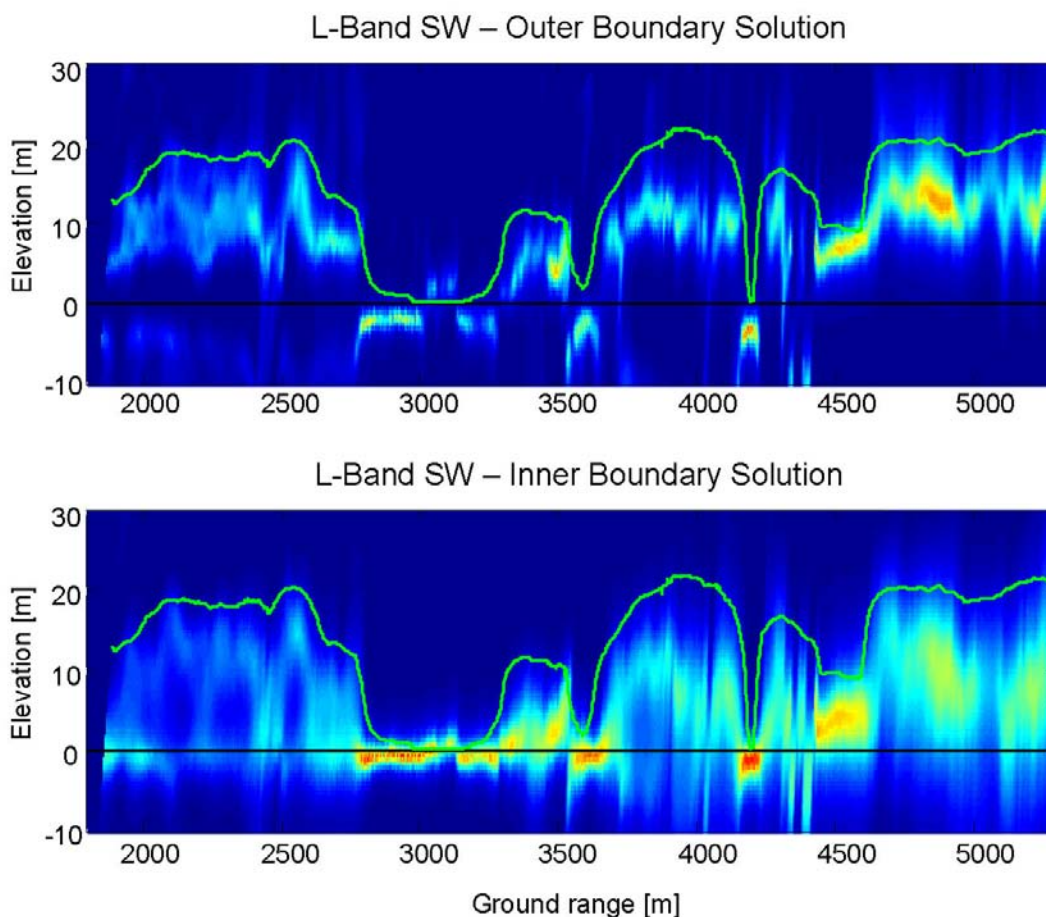


Figure 42: Tomographic Profiles of Volume scattering for the selected azimuth cut. Top row: Outer Boundary Solution. Bottom row: Inner Boundary Solution. Data-set: L-Band SW.

In order to retrieve a suitable solution for describing the structure of volume contributions above the ground while avoiding the high-pass effect of the outer boundary solution, it has been decided to associate volume scattering with the largest SM along the vertical direction. This solution, hereinafter referred to as Largest Volume Solution (LVS), consists in equalizing the backscattered power along the vertical direction, in such a way as to reveal the presence of scattering contributions along the largest vertical extent.

Results are shown in Figure 43. It may be appreciated that the Largest Volume Solution achieves an important improvement at P-Band, resulting in a better match with LIDAR measurements with respect to the tomographic profile in HV. Some improvement is visible at L-Band too, even though there is no significant difference with respect to HV. Accordingly, the Largest Volume Solution appears to be an attractive tool especially at P-Band, as it manages to reject most contributions from the ground level while resulting in a physically sound volume structure. Yet, it has to be remarked that physical soundness is the only argument in support of the Largest Volume Solution, whereas there are no rigorous proofs that it yields the true structure of volume scattering.

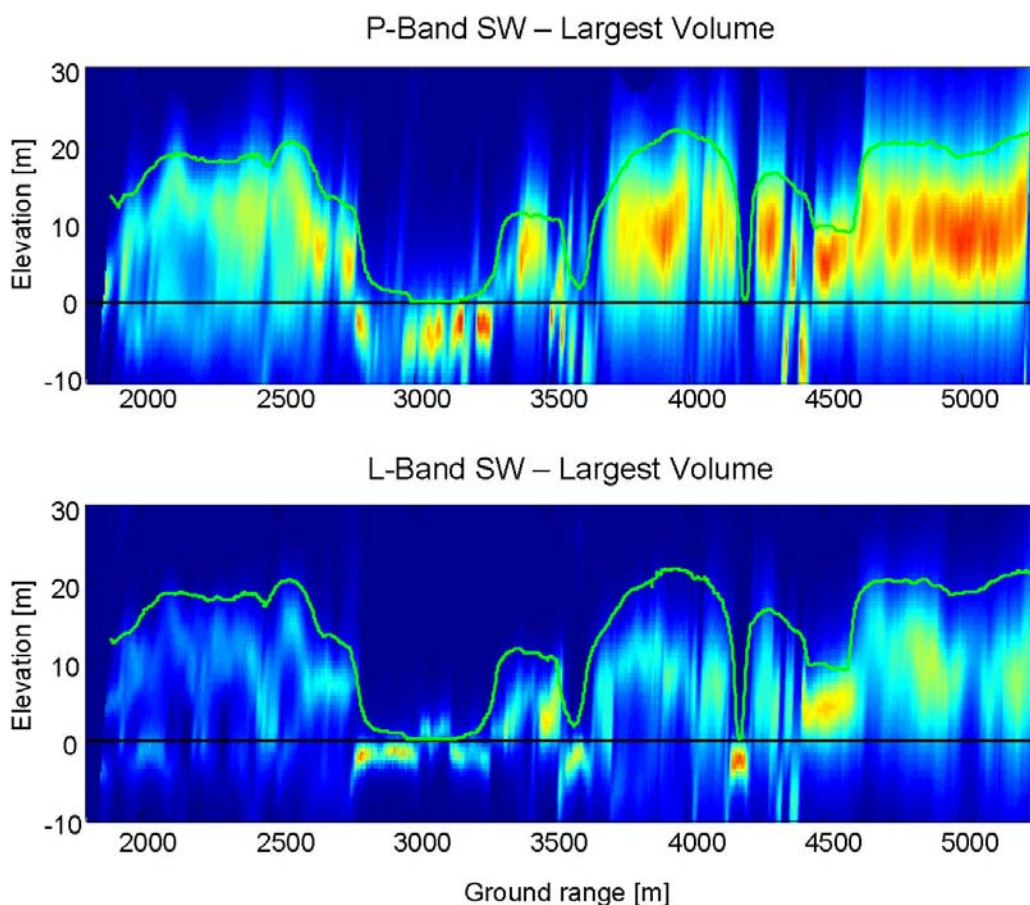


Figure 43: Tomographic Profiles of Volume scattering for the selected azimuth cut. Top row: Largest Volume Solution for data-set P-Band SW. Bottom row: Largest Volume Solution for data-set L-Band SW.

The BioMass case is reported in Figure 44. Even though some improvement is visible, the results appear to be significantly more dispersed than in the full bandwidth case. This phenomenon can be explained in light of the fact that the sample covariance matrix is estimated in the BioMass case with much fewer samples than in the full bandwidth case, resulting in volume optimization to be more sensitive to random oscillations within the data. Furthermore, only minor differences are observed between the profiles associated with the Largest Volume Solution and the HV polarization in the BioMass case with respect to the full bandwidth case. Besides the impact of random oscillations of the data discussed above, this result is due to the vertical resolution loss that arises from pulse bandwidth reduction, discussed in section 9.4.4.3. Such a resolution loss results in the spatial structures associated to the different polarization to be closer to each other, see Figure 38. This limits the range of the physically valid spatial structures that may arise by combining different polarization through the SKP decomposition, resulting in fewer valid choices for the determination of the volume structure.

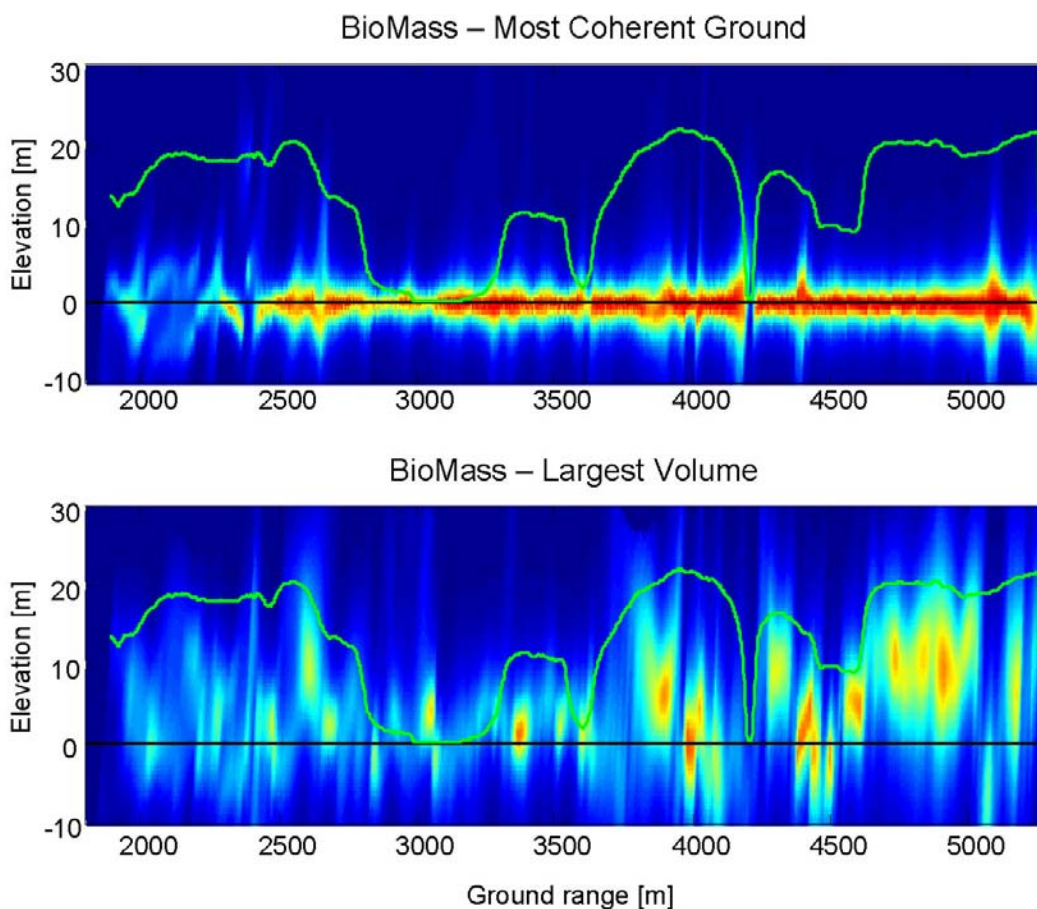


Figure 44: Tomographic Profiles of Ground and Volume scattering for the selected azimuth cut. Top row: Ground. Bottom row: Volume. Data-set: BioMass.

To conclude, it is interesting to note that some areas present volume scattering contributions below the ground level. Such contributions have been observed to occur at the same locations at P-Band and L-Band, mostly in open or very low vegetated areas. Therefore, this result might be an index of the presence of either multiple scattering or subsurface penetration phenomena. So far, however, we have no elements to completely exclude algorithm artifacts, the eventual physical interpretation of this phenomenon being left open for further researches. Still, the presence of a significant backscattered power from beneath the ground is informative in some sense, in that it permits the identification of areas where the signal is not consistent with forest scattering. Accordingly, areas exhibiting a significant backscattered power from beneath the ground have been marked as non vegetated.

9.4.8 Large Scale Tomographic Analysis

This section is devoted to reporting the large scale results of the Tomographic analysis of the BioSAR 2008 data-sets. The following products have been identified as the most representative for the characterization of the imaged scene:

- Tomographic sections associated with the Largest Volume Solution and the HV polarization;
- Volume height;
- Ground to volume backscattered power ratios in different polarizations;
- Average Ground Coherence
- Terrain topography.

In order to facilitate the interpretation of the results to follow, we report hereinafter the maps of the H100 vegetation height and ground range slope angle in the two look directions.

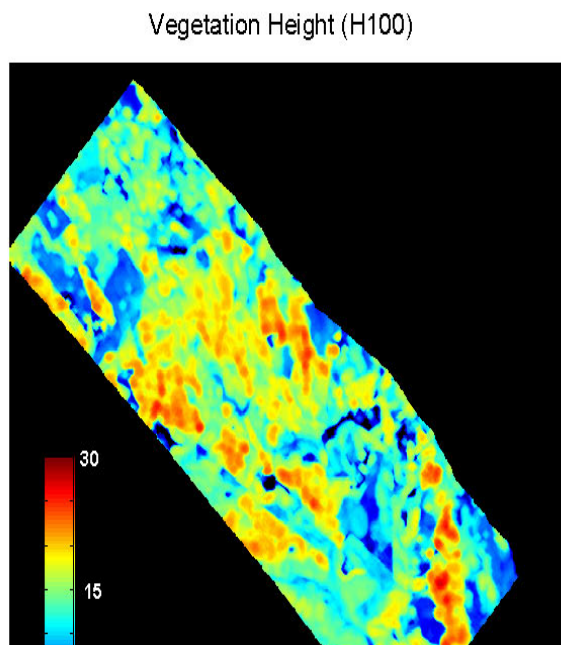


Figure 45: H100 vegetation height [m] obtained from LIDAR measurements.

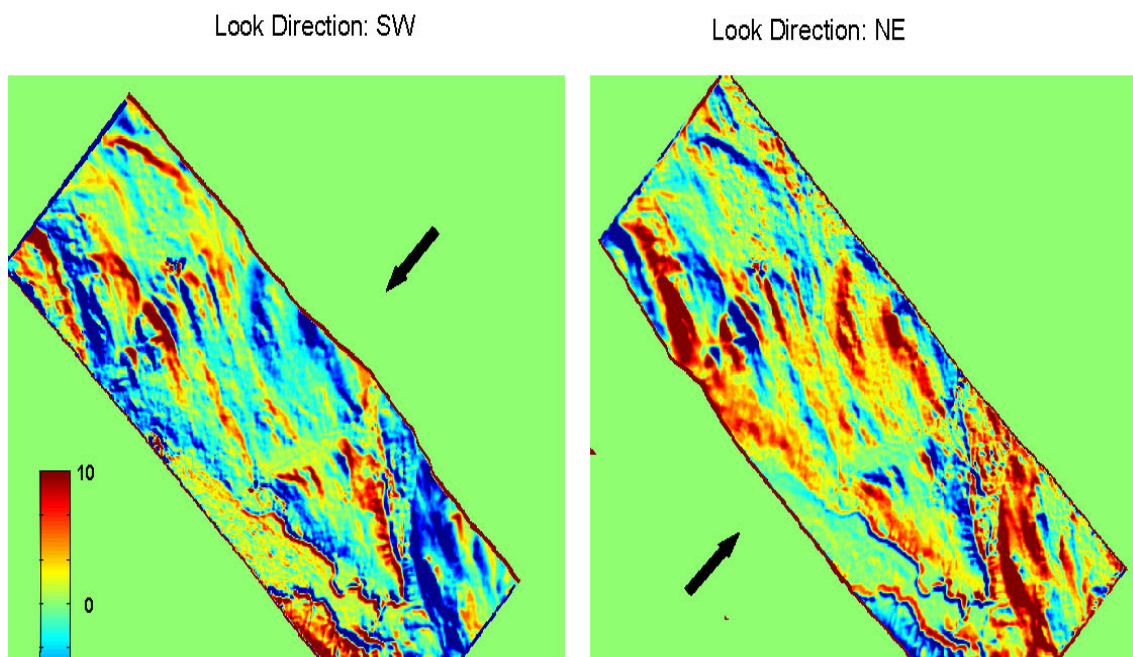


Figure 46: Ground range slope angle [deg] with respect to look direction SW and NE.

9.4.8.1 Tomographic Sections

Whereas in section 9.4.7 the outcomes of the Tomographic analysis have been discussed for a single azimuth cut, in this section the whole imaged scene is considered. In order to provide a meaningful visualization of the results, tomographic sections have been generated for each of the data-sets under analysis. Such sections have been obtained sampling the vertical distribution of the backscattered power at each slant range, azimuth location, in such a way as to retrieve the information about the vertical location of the phase center and the points corresponding to a power loss equal to -3 dB, -4 dB, -5 dB, -7 dB, -10 dB.

All tomographic sections are presented in Radar geometry. To facilitate the interpretation of the results, figures showing tomographic sections also report LIDAR measurements converted in Radar geometry.

Results relative to the backscattered power distributions associated with the HV channel and the Largest Volume Solutions are shown from Figure 47 through Figure 52. In all cases, the conclusions drawn in section 9.4.7 relatively to a single azimuth cut may be generalized to the whole scene.

In all cases, a rising trend can be observed between the retrieved height and the slant range coordinate. This result indicates that the power loss associated with a certain height with respect to the phase center location tends to decrease as the look angle increases, therefore witnessing a vertical resolution loss. As noted in section 9.4.7, this phenomenon is due to large variation of the baseline aperture from near to far range. In support of this conclusion it may be noted that resolution loss affects P-Band data to a larger extent with respect to L-Band data. This is consistent with the fact that Fourier resolution is much better at L-Band, see Figure 28. In fact, the retrieval of the

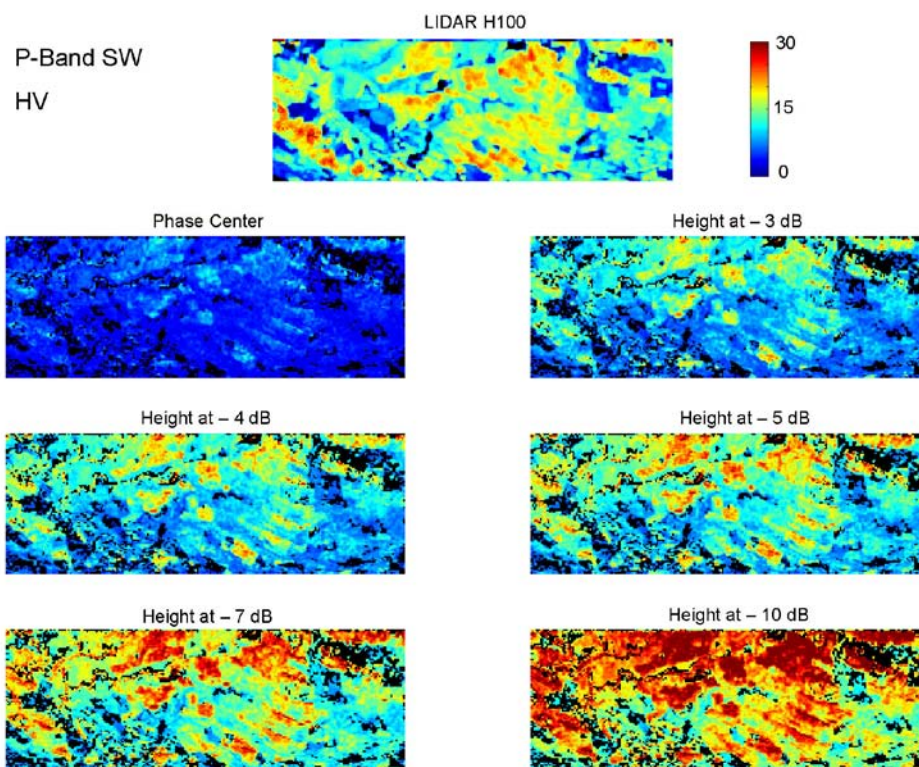


Figure 47: Tomographic sections for the HV channel. Data-set: P-Band SW. Black areas have been identified as being non vegetated.

Backscattered power distribution is intrinsically better conditioned at L-Band, since the shorter wavelength results in an enhanced diversity of the contributions associated with different heights with respect to P-Band, which makes it easier to proceed to their separation along the vertical direction.

As for the P-Band SW data-set, it may be appreciated that the effective phase center in the HV polarization is located in proximity of the ground level throughout the whole scene, whereas the backscattered power that is found in correspondence with LIDAR forest height measurements undergoes a loss of 8 dB to 4.5 dB from near to far range with respect to the phase center location. Accordingly, most of the backscattered power in HV is found in proximity of the ground level. As expected, the backscattered power distribution yielded by the Largest Volume Solution is associated with higher locations with respect to HV, see Figure 48. In this case, agreement with LIDAR measurements is observed in correspondence with a power loss of 5.5 dB to 3 dB from near to far range with respect to the phase center location.

Consistently with section 9.4.7, the phase center location in the HV channel has turned out to be close to the ground level at L-Band as well, see Figure 49. Agreement with LIDAR measurements is observed at a power loss of 6 dB to 5dB from near to far range with respect to the phase center location. Similar results are found in the case of the Largest Volume Solution, where agreement with LIDAR measurements is observed at about 5 dB with respect to the phase center location. Such a result remarks that HV scattering at L-Band is much more sensitive to volume contributions than at P-Band. Hence, the backscattered power distribution associated with the Largest Volume Solution is much closer to the one associated with the HV polarization at L-Band than at P-Band.

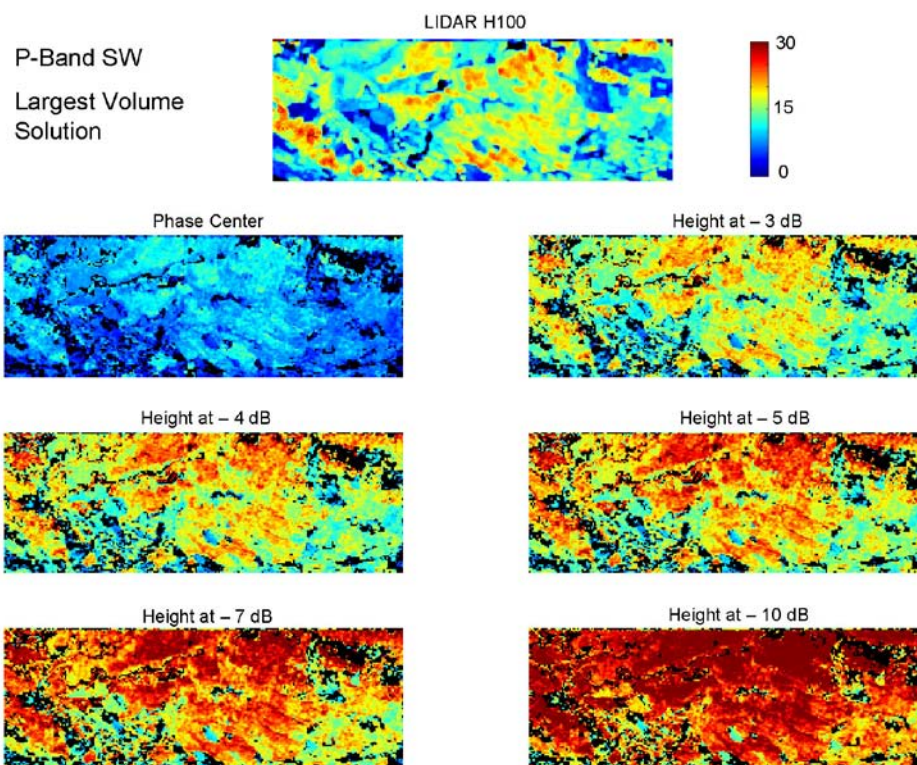


Figure 48: Tomographic sections for the Largest Volume Solution. Data-set: P-Band SW. Black areas have been identified as being non vegetated.

The tomographic sections relative to the BioMass case are shown in Figure 51 and Figure 52. Agreement with LIDAR measurements is observed in correspondence with a power loss of 8 dB to 4 dB from near to far range with respect to the phase center location in the case of the HV channel, and in correspondence with a power loss of 7 dB to 3 dB in the case of the Largest Volume Solution.

Finally, non vegetated areas have been identified basing on: presence of significant backscattered power from beneath the ground, ground coherence, and backscattered intensity. Such an approach has resulted in some differences when applied to P-Band or L-Band data, see for example Figure 47 and Figure 49. A direct comparison between P-Band and L-Band is found in Figure 53, which reports the histograms of the H100 forest height in areas marked as non vegetated. It may be observed that at L-Band the areas marked as non vegetated mostly correspond to forest heights lower than 5 m. At P-Band, instead, a relevant number of cases is found where forest height is in the order of 7-8 m. Two arguments may be invoked to explain such a behavior. On the one hand, it is due to the intrinsic lower sensitivity to volume scattering of P-Band with respect to L-Band, resulting in the objective difficulty in the identification of low vegetated areas. On the other hand, such a behavior is also to be imputed to the lower sensitivity to volume decorrelation of the P-Band data-sets with respect to the L-Band data-sets, which hinders the tomographic imaging of small volumes. In any case, however, a satisfactory agreement is observed between the spatial distributions of low vegetated areas and of areas marked by the tomographic algorithm as non vegetated.

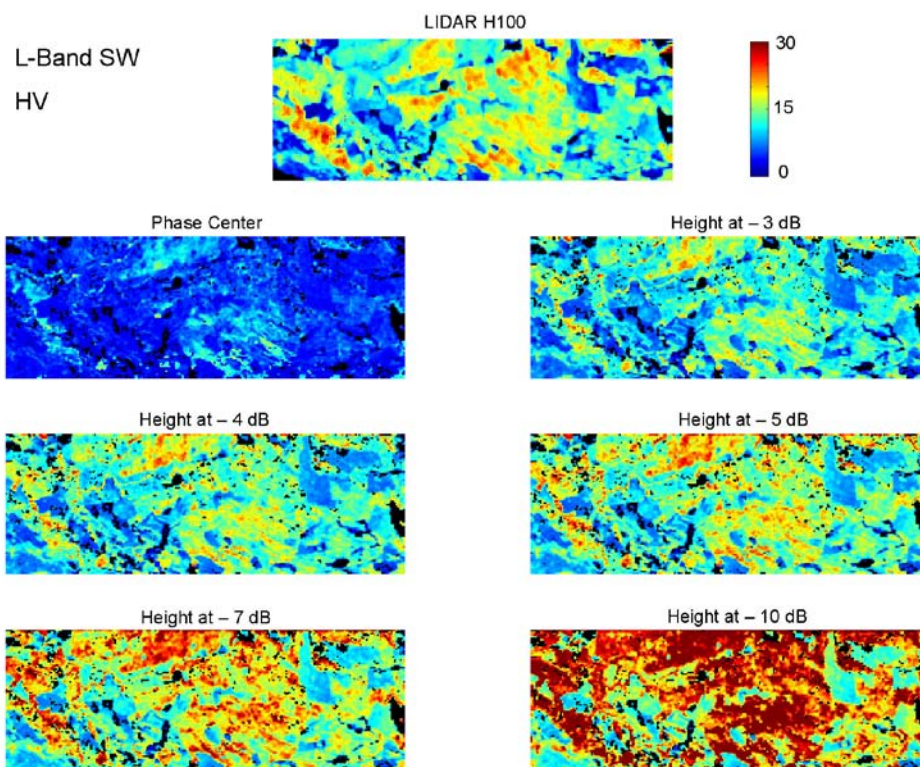


Figure 49: Tomographic sections for the HV channel. Data-set: L-Band SW. Black areas have been Identified as being non vegetated.

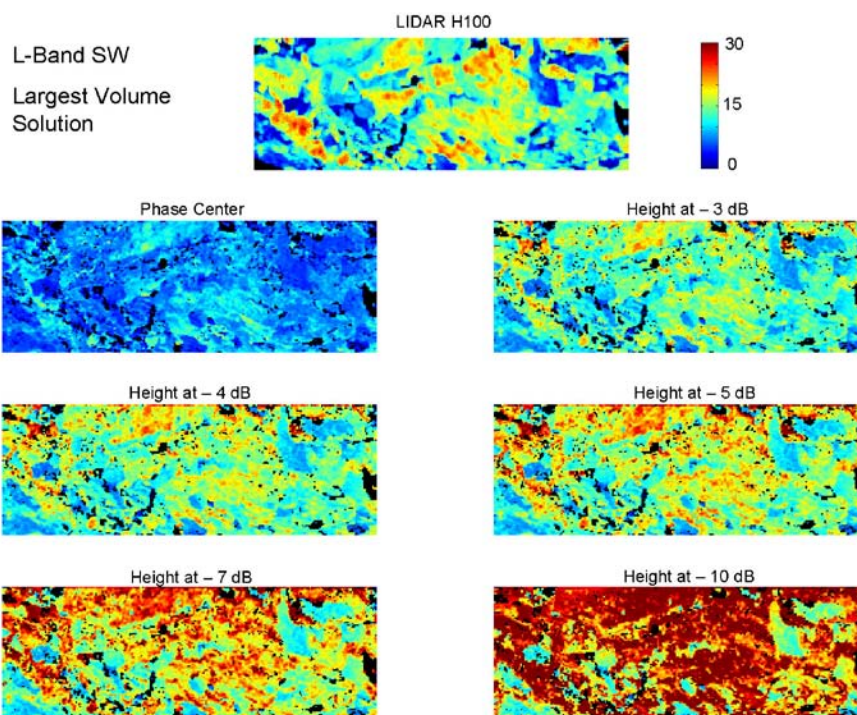


Figure 50 Tomographic sections for the Largest Volume Solution. Data-set: L-Band SW. Black areas have been identified as being non vegetated.

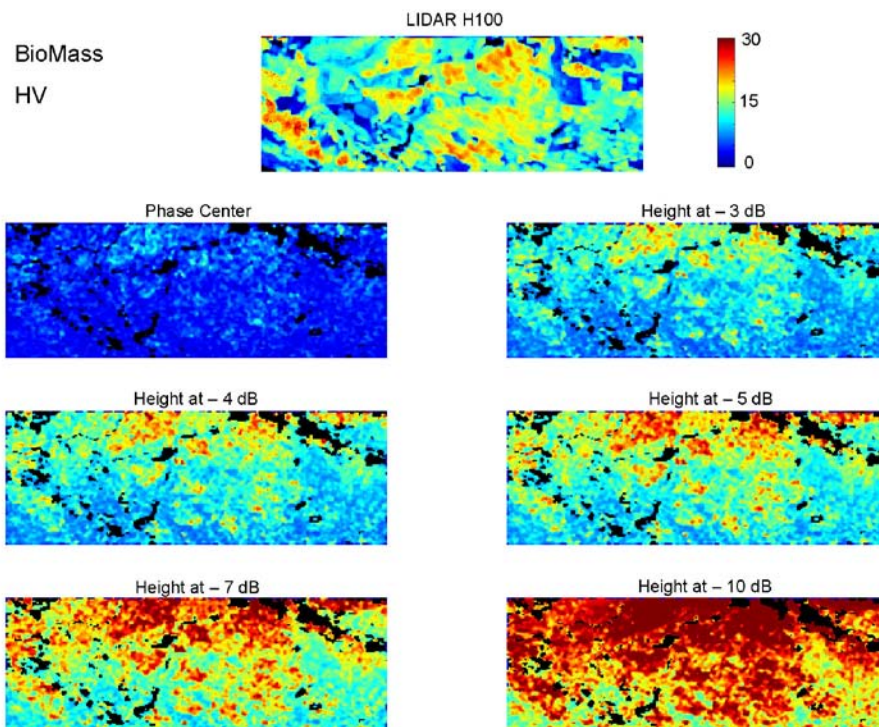


Figure 51: Tomographic sections for the HV channel . Data-set: BioMass. Black areas have been identified as being non vegetated.

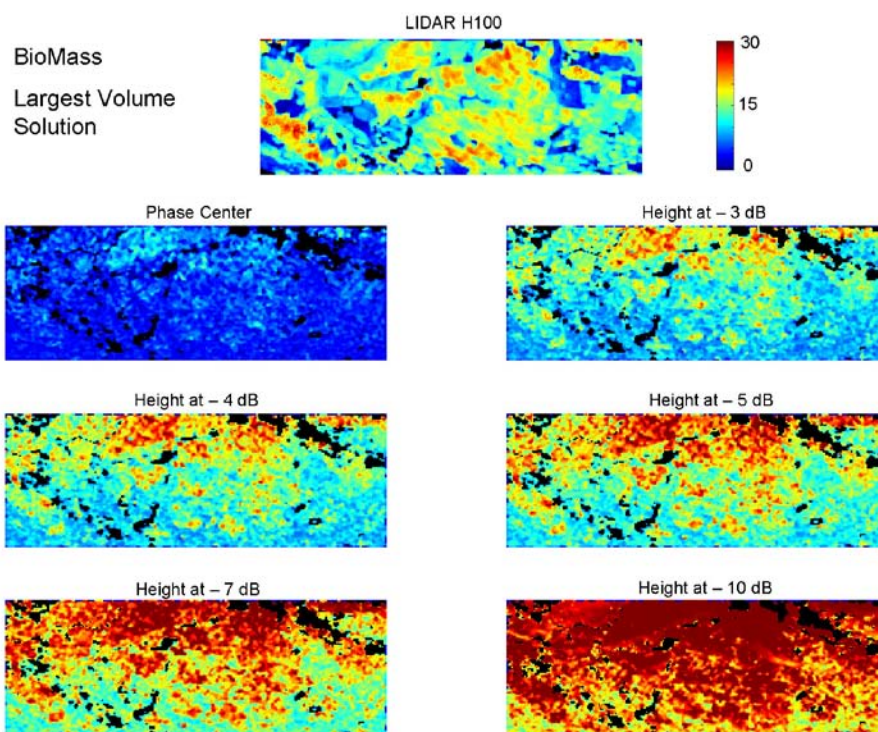


Figure 52: Tomographic sections for the Largest Volume Solution . Data-set: BioMass. Black areas have been identified as being non vegetated.

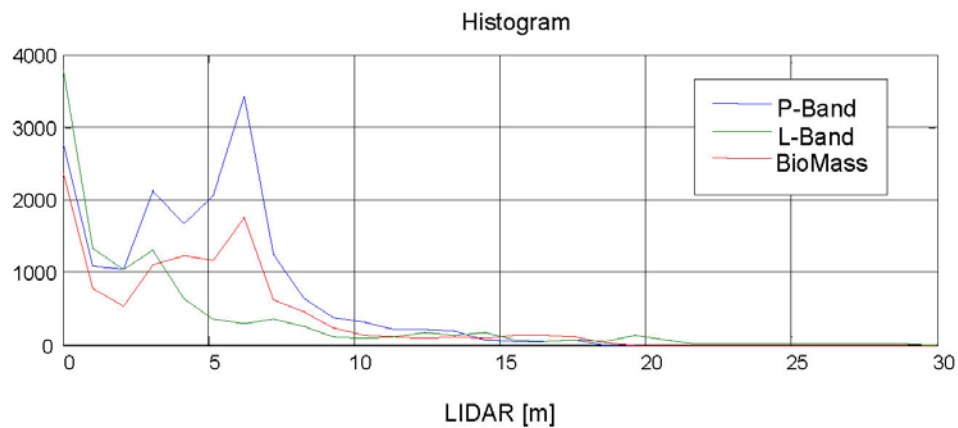


Figure 53: Histograms of LIDAR forest height in areas marked as non vegetated.

9.4.8.2 Volume Height

Volume height has been retrieved directly from the tomographic sections shown in the previous sections, by establishing a threshold for the backscattered power loss with respect to the phase center location. Clearly, the critical point in retaining such an approach is represented by the choice of the proper threshold that corresponds to the true forest height. In fact, backscattered power contributions are found the more the less at every location along the vertical direction, due to the presence of noise or, more important, to the spatial heterogeneity of vegetation within the estimation window. Another issue to deal with is the presence of a rising trend with respect to the slant range coordinate that characterizes the tomographic sections especially at P-Band, as discussed in the previous section. Accordingly, the proper choice of the threshold has to depend on the look angle.

Both these issues could be solved, in principle, by resorting to some physical model for forest scattering, similarly to PolInSAR. Within this work, however, our aim is the development of retrieval techniques which base as less as possible on the a-priori information provided by physical models. For this reason, the value of the threshold corresponding to the top forest height has been assessed by investigating the shape of the backscattered power distribution at each slant range, azimuth location. The criterion adopted for assessing forest top height follows after the basic assumption that the shape of the backscattered power distribution can be roughly divided into three zones, see Figure 54. One is found in correspondence of the phase center location, where most of backscattered power is concentrated. Then, the backscattered power undergoes a loss, due to both the point spread function of the tomographic processors and the (eventual) tapering of the forest density. Further away along the vertical direction backscattered power is mostly contributed by noise and random oscillations of the scatterers within the resolution cell, resulting in this zone not to be likely associated with physically relevant components. According the flex point within the loss zone represents a good guess as for the retrieval of forest top height.

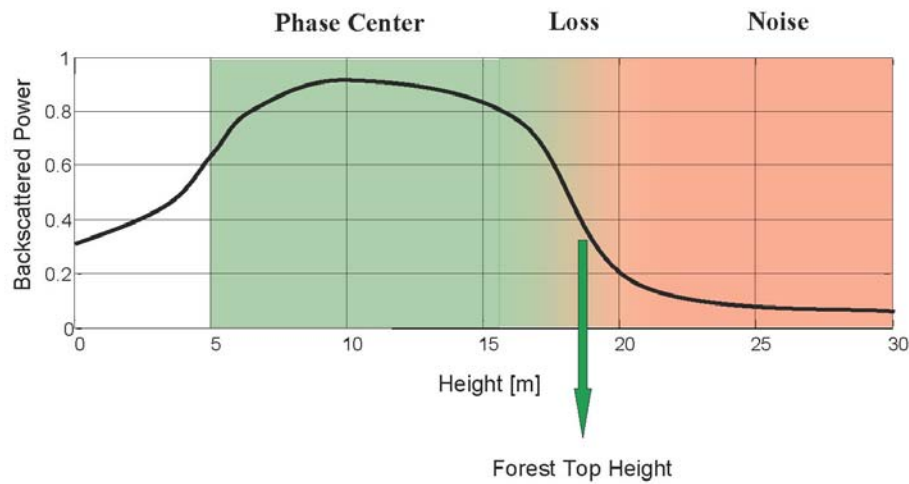


Figure 54: Criterion adopted for the retrieval of forest top height.

Notwithstanding its rather simplistic character, such a criterion has turned out to result in a satisfactory agreement with the H100 forest height derived by LIDAR measurements. Results are shown in Figure 55 through Figure 64. In all cases, forest height has been estimated basing on the backscattered power distribution associated with the Largest Volume Solution. The relative error has been evaluated as:

$$err = \frac{|H_{SAR} - H100|}{H100} \quad \text{Eq 35}$$

Notwithstanding a slight bias (± 1.5 m), the relative error has turned out to be below 10% in most forested areas in all cases, including BioMass, therefore proving the effectiveness of the proposed approach for forest height retrieval. The behavior of the bias curve with respect to the H100 forest height has two distinct characteristics. In first place, it exhibits a linear trend with respect to forest height. This kind of error is likely to be due to the particular approach exploited for forest height retrieval, and may therefore be recovered by resorting to a more sophisticated approach. However, it can also be observed that NE acquisitions are affected by a higher bias in magnitude with respect to SW acquisitions, independently of the carrier wavelengths. At first glance this phenomenon seems to indicate a non perfect compensation of terrain slopes. However, practically the same results have been obtained by using either the LIDAR DEM or the SAR DEM, see section 9.4.8.5. Accordingly, this discrepancy between NE and SW data seems likely to be due to minor errors of the height to phase conversion factors rather than to DEM errors.

It may be observed that the estimate dispersion is noticeably reduced by discarding those pixel exhibiting very large errors. This phenomenon is due to the fact that largest errors are found in correspondence of the borders of forested areas, where the estimate is uncertain due to the heterogeneity of the targets within the resolution cell. This statement is easily confirmed by a simple visual inspection of the panels relative to the residual error between SAR and LIDAR.

It is interesting to note that the estimate dispersion appears to be larger at L-Band than at P-Band in areas where vegetation is higher than 20 m. This phenomenon might indicate that structure estimation in presence of dense vegetation is hindered at L-Band due to a reduced ground visibility. However, there are too few areas where vegetation is significantly higher than 20 m, and thus conclusions can not be drawn about this phenomenon without further analyses in dense forest scenarios. As a further remark, it is worth noting that estimate dispersion beyond 20 m is sensibly lower in the NE data-set than in the SW data-set. In both flight directions, instead, better results are obtained at L-Band as for low vegetated areas. This result is perfectly consistent with the fact that many more areas have been marked as non vegetated at P-Band with respect to L-Band, discussed in the last section.

The NE and SW data have shown an overall good agreement, as shown in Figure 65.

As expected BioMass estimates have turned out to be associated with a larger dispersion with respect to the full bandwidth case. Accordingly, it has been decided to smooth the result by using a median filter as large as 100 x 100 m (ground range, azimuth). This operation has resulted in an improvement of the standard deviation of up to 1 m. However, the most significant discrepancy with respect to the full bandwidth case is relative to the large bias occurring whenever forest height is below 10 m. Beside the arguments exposed in the previous section about the poor sensitivity to low volumes at P-Band, this phenomenon is mostly due to the small pulse bandwidth of the BioMass system. As shown in section 9.4.4.3, the vertical resolution limit due to pulse bandwidth is in the order of 20 m. Such a limit is halved by Common Band filtering each interferometric pair, resulting in a vertical resolution of about 10 m. Accordingly, vegetated structure less high than 10 m are hardly distinguishable in the BioMass case.

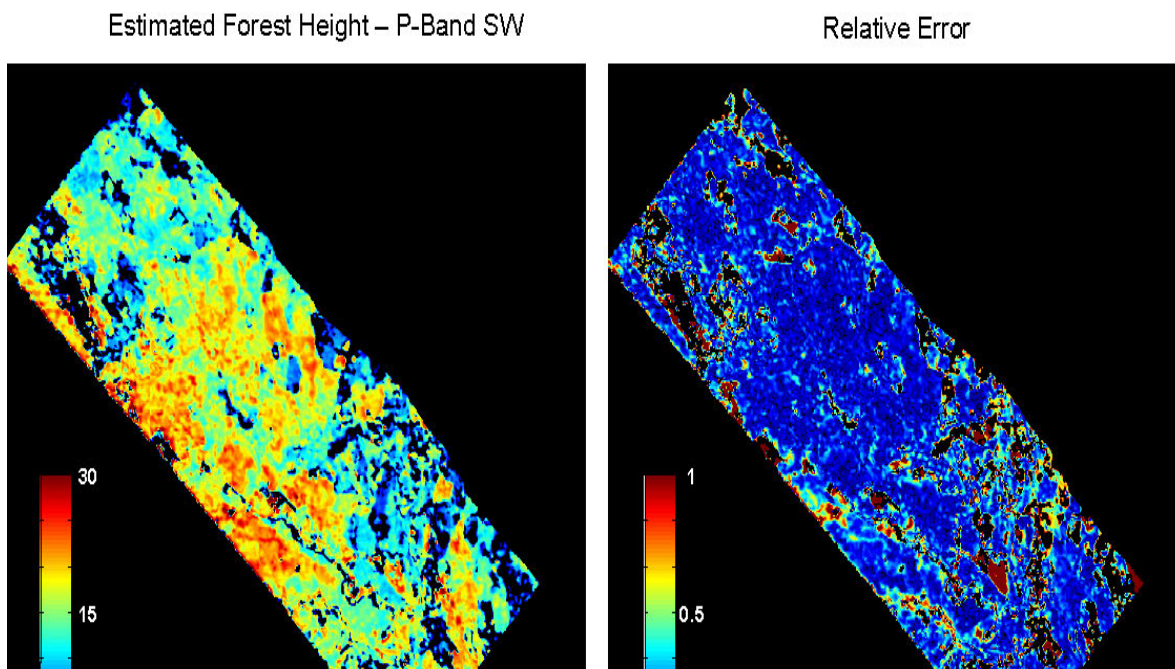


Figure 55: Left panel: estimated forest height. Right panel: relative error with respect to LIDAR measurements. Data set: P-Band SW.

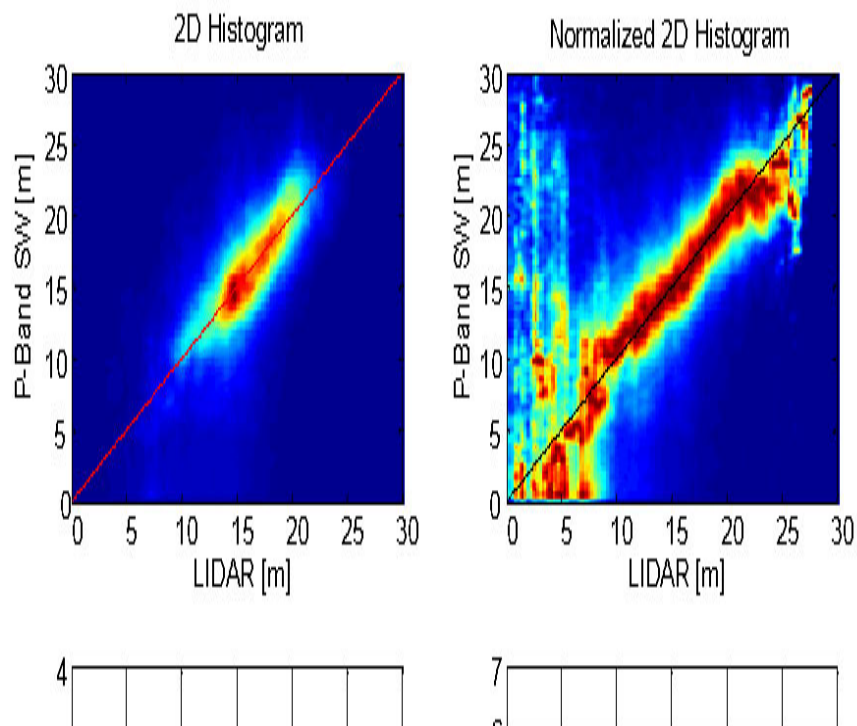


Figure 56: Top row: Joint distribution of forest heights estimated by SAR and LIDAR; bottom row: bias and standard deviation of SAR estimated with respect to LIDAR measurements. The red line has been obtained by discarding pixel associated with a relative error larger than 0.5.

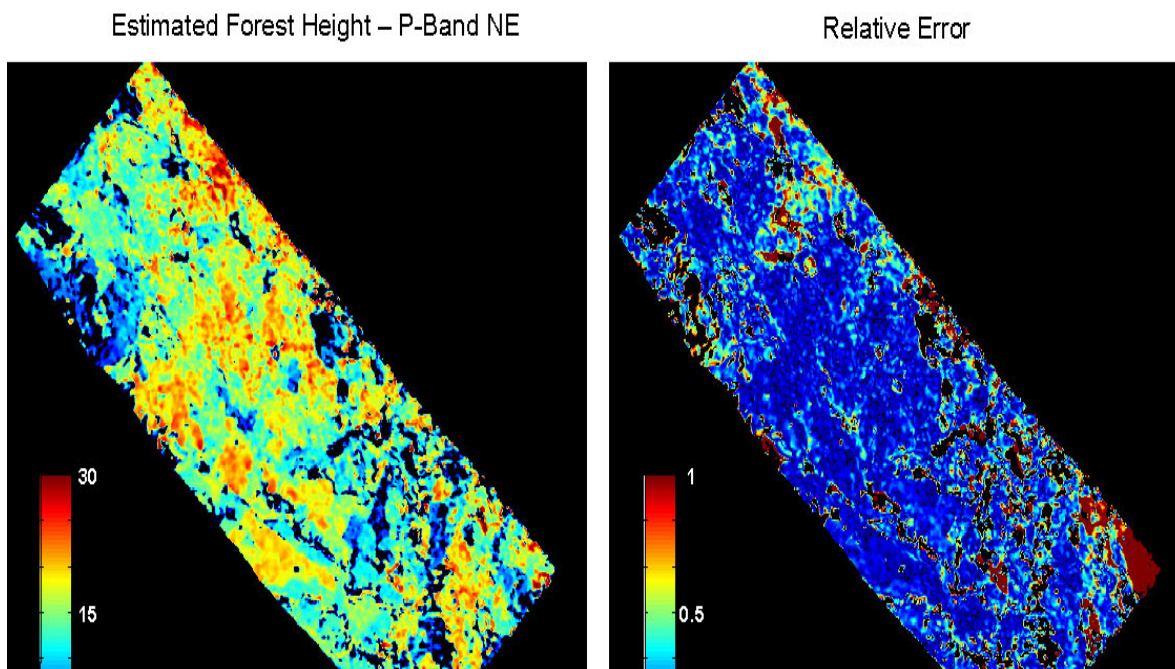


Figure 57: Left panel: estimated forest height. Right panel: relative error with respect to LIDAR measurements. Data set: P-Band NE.

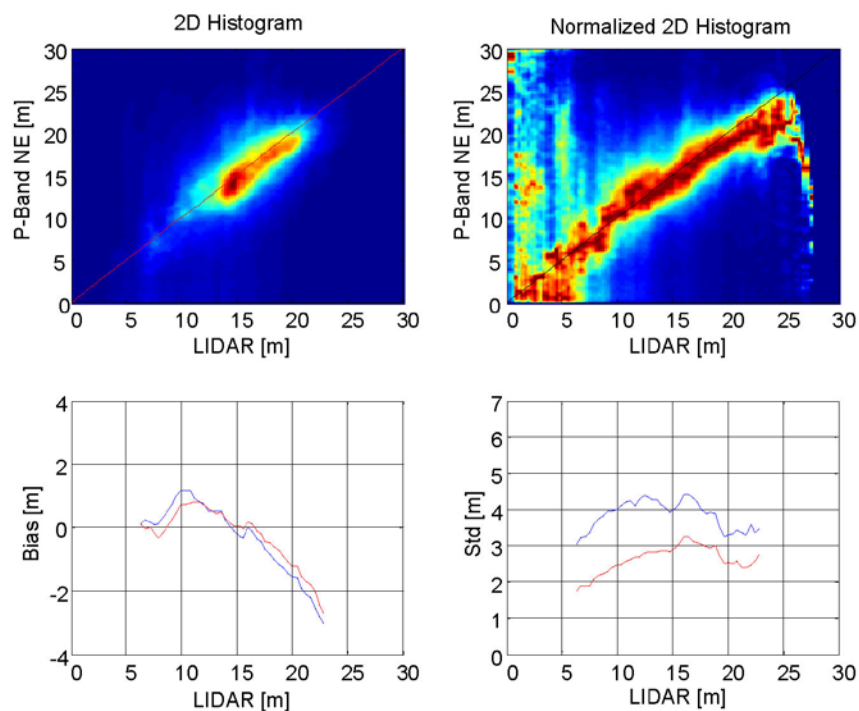


Figure 58: Top row: Joint distribution of forest heights estimated by SAR and LIDAR; bottom row: bias and standard deviation of SAR estimated with respect to LIDAR measurements. The red line has been obtained by discarding pixel associated with a relative error larger than 0.5

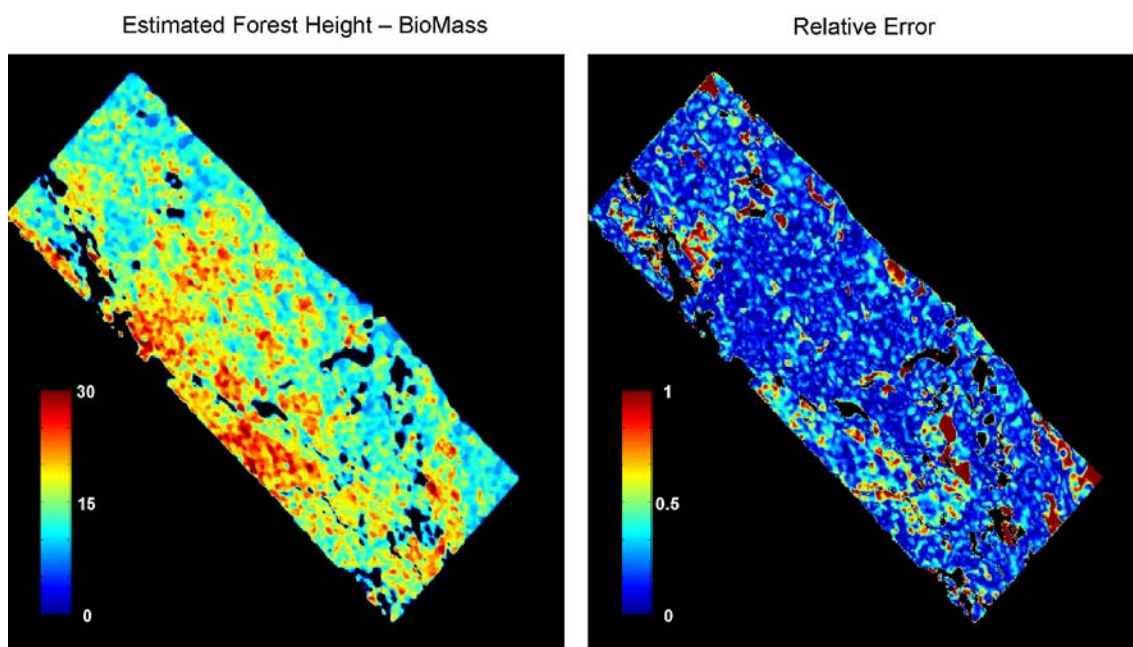


Figure 59: Left panel: estimated forest height. Right panel: relative error with respect to LIDAR measurements. Data set: BioMass. BioMass estimates have been smoothed by using a 100 x 100 m median filter.

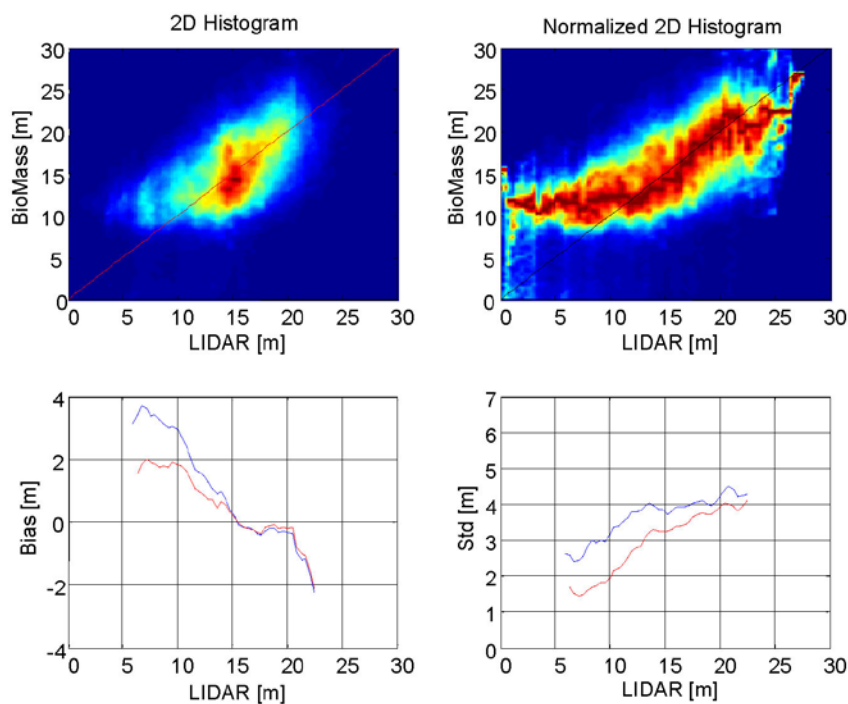


Figure 60: Top row: Joint distribution of forest heights estimated by SAR and LIDAR; bottom row: bias and standard deviation of SAR estimated with respect to LIDAR measurements. The red line has been obtained by discarding pixel associated with a relative error larger than 0.5. BioMass estimates have been smoothed by using a 100 x 100 m median filter.

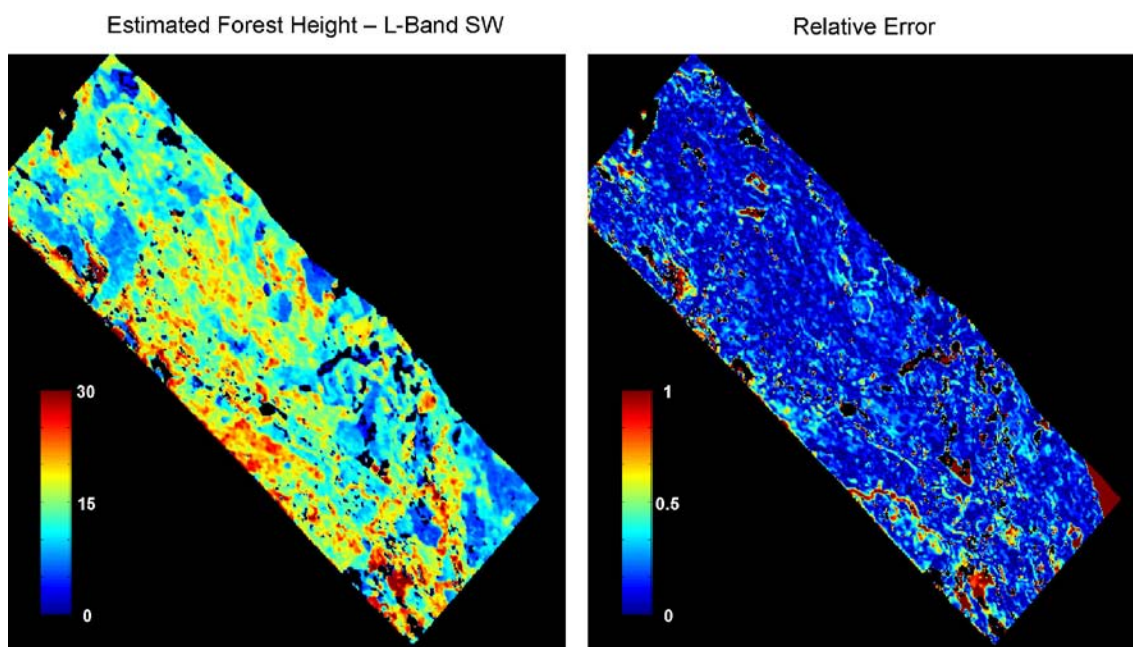


Figure 61: Left panel: estimated forest height. Right panel: relative error with respect to LIDAR measurements. Data set: L-Band SW.

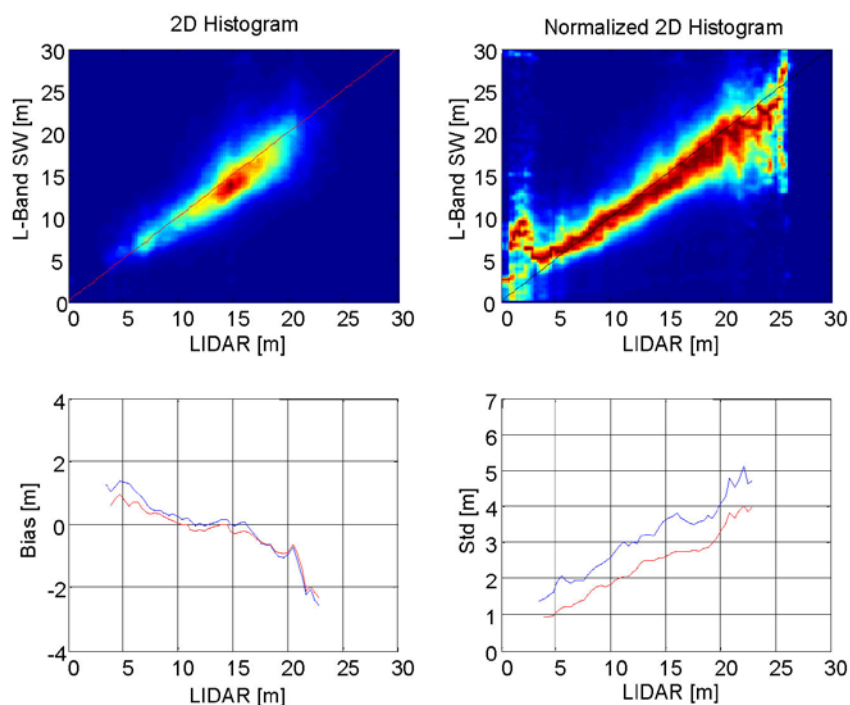


Figure 62: Top row: Joint distribution of forest heights estimated by SAR and LIDAR; bottom row: bias and standard deviation of SAR estimated with respect to LIDAR measurements. The red line has been obtained by discarding pixel associated with a relative error larger than 0.5

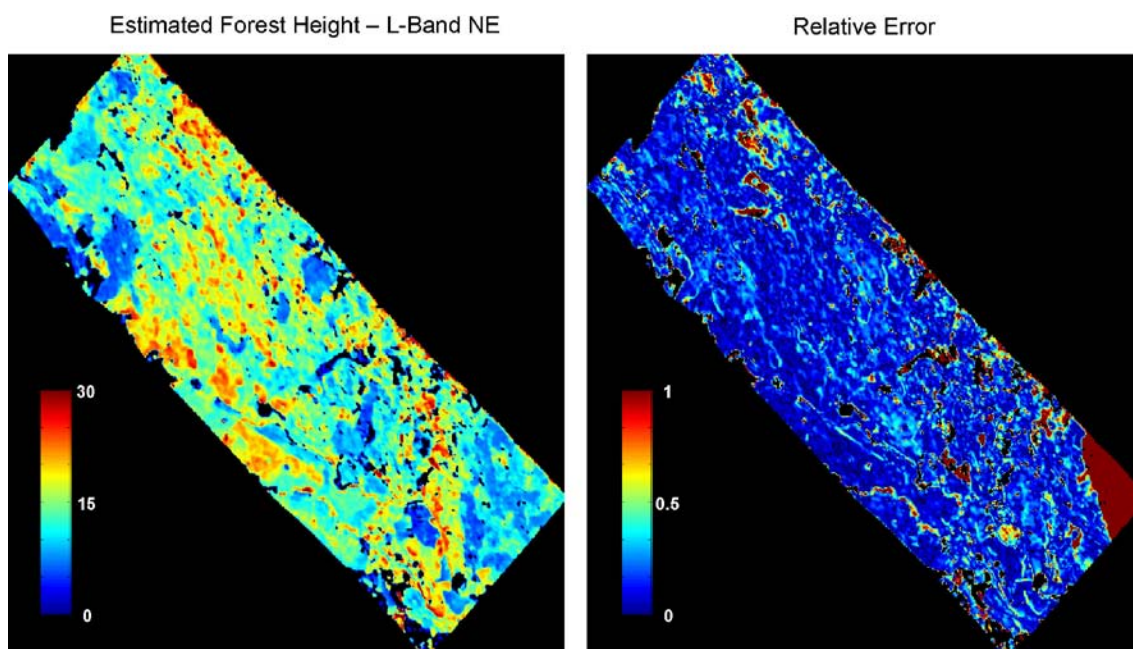


Figure 63: Left panel: estimated forest height. Right panel: relative error with respect to LIDAR measurements. Data set: L-Band NE.

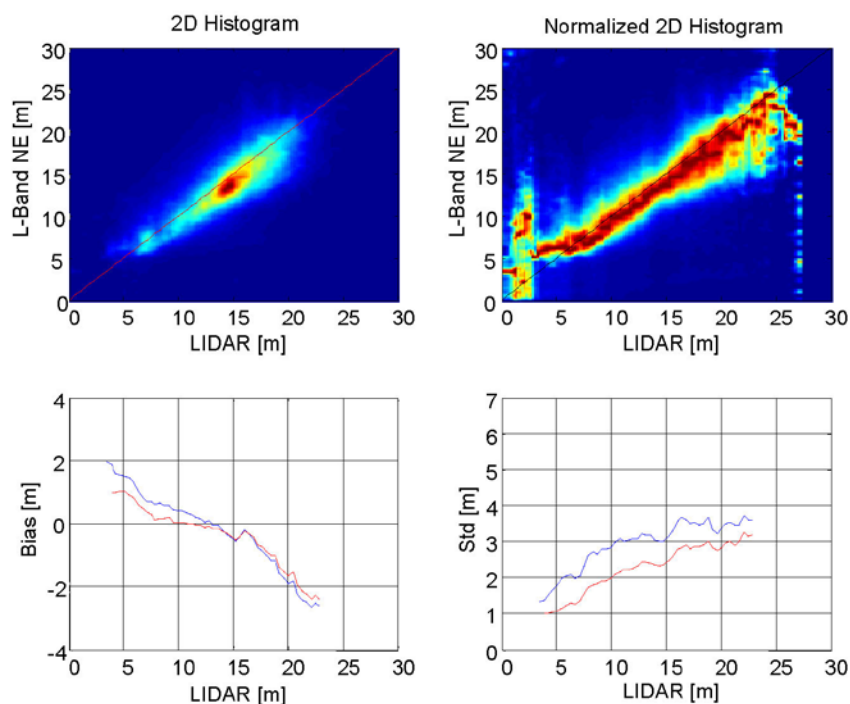


Figure 64: Top row: Joint distribution of forest heights estimated by SAR and LIDAR; bottom row: bias and standard deviation of SAR estimated with respect to LIDAR measurements. The red line has been obtained by discarding pixel associated with a relative error larger than 0.5

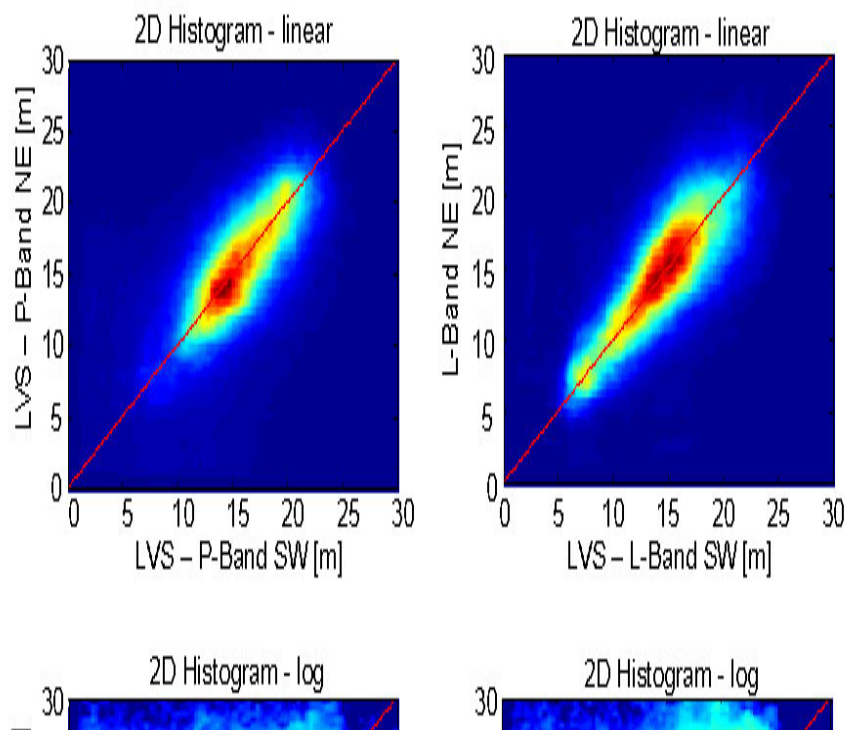


Figure 65: Joint distributions of forest heights estimated by the SW and NE data-sets at P-Band (left column) and L-Band (right column).

9.4.8.3 Ground to Volume Backscattered Power Ratio

The ground to volume backscattered power ratio (GVR) in each polarization has been obtained directly after Eq 32, in correspondence with the two SMs identified as the most coherent ground and the largest volume, see section 9.4.7.2 for details.

It is important to remark that in order for the GVR to carry significant information about the forest structure, ground and volume scattering contributions have to be identified correctly. In other words, the GVR is strictly related to SM separation, and hence depends on the choice of the solution. As shown in section 9.4.7.2, the Inner Boundary solution for volume scattering yields results very close to those found in the HV polarization. As a consequence, the resulting GVR in HV would be close to 0. The Outer Boundary solution, instead, yields thin volumes at a high elevation. Accordingly, this solution would result in very high values of the GVRs in all channels, since more backscattered power has to be assigned to ground scattering in order to explain the backscattered power distribution in each channel, which is fixed. It is worth noting that the the Outer Boundary would provide consistency with the results obtained in the BioSAR 2007 campaign by exploiting the COMET, as discussed at the end of 9.4.5.3.

The Largest Volume solution represents an effort to describe the structure of volume scattering above the ground while avoiding the high-pass effect of the outer boundary solution. As discussed, there are no rigorous arguments in support of its validity. Yet, it appears to be a good choice for describing the structure of volume scattering above the ground, especially in light of the resulting good agreement with LIDAR height measurement reported in the previous section.

Results relative to the SW and NE data-sets are shown in Figure 66 to Figure 69. A remarkable consistency between NE and SW acquisitions has been observed at both P-Band and L-Band, see Figure 70. As expected, P-Band data have turned out to be much more affected by contributions from the ground level, the difference as for the HV GVR being assessed in about 5 dB. The behavior of the HV GVR with respect to forest height and terrain slope is investigated in Figure 71, Figure 72. At both wavelengths it is observed that the HV GVR decreases with forest height, consistently with the enlargement of volumetric structures. Instead, a different behavior is found with reference to terrain slope, as the HV GVR exhibits a dependence on terrain slope at P-Band but not at L-Band. This result seems to further indicate that HV ground contributions are due to specular reflections at P-Band, but not at L-Band. It is worth noting that the HV GVR is higher than 1 at P-Band in flat areas. This seems to indicate that specular reflections are not only due to volume-ground, but also to trunk-ground interactions.

The results relative to the BioMass data-set have turned out to be considerably more dispersed, see Figure 73 and Figure 74. However, the most significant discrepancy with respect to the full bandwidth case is that the HV GVR undergoes a loss of about 7 dB. This result is consistent with what has been observed as the tomographic profiles. The vertical resolution loss that arises from pulse bandwidth reduction results in the spatial structures associated to the different polarization to be closer to each other. As a result, the volume structure associated with the Largest Volume Solution tends to resemble the one found in HV, therefore giving rise to lower values of GVR.

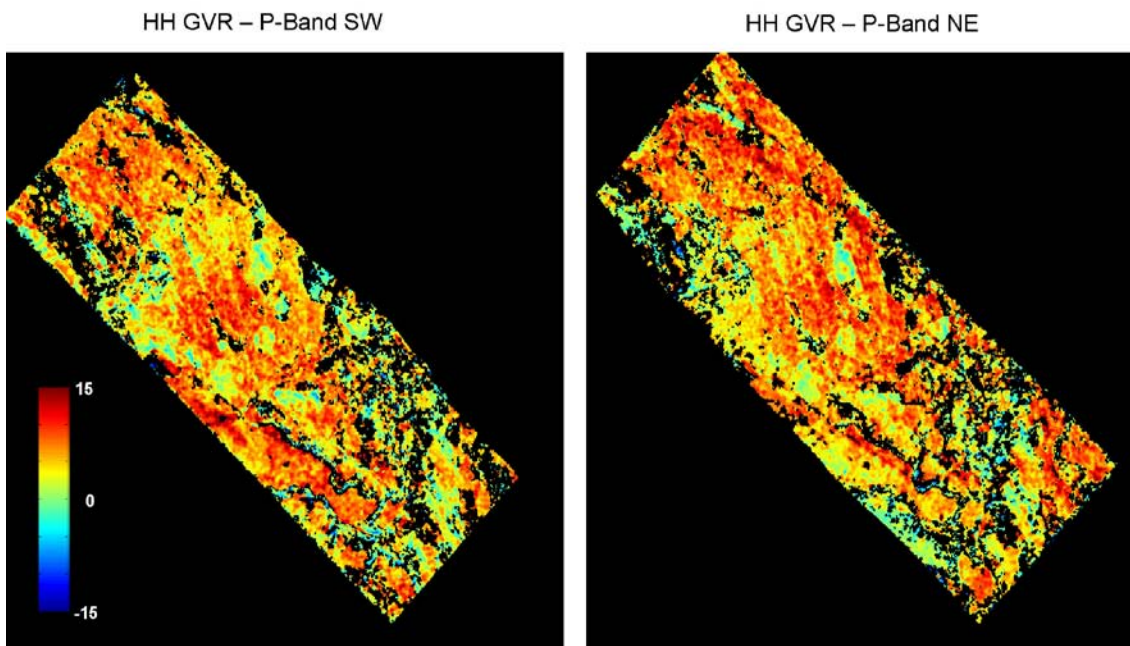


Figure 66: Ground to volume backscattered power ratio in the HH channel for the P-Band SW and NE data-sets.

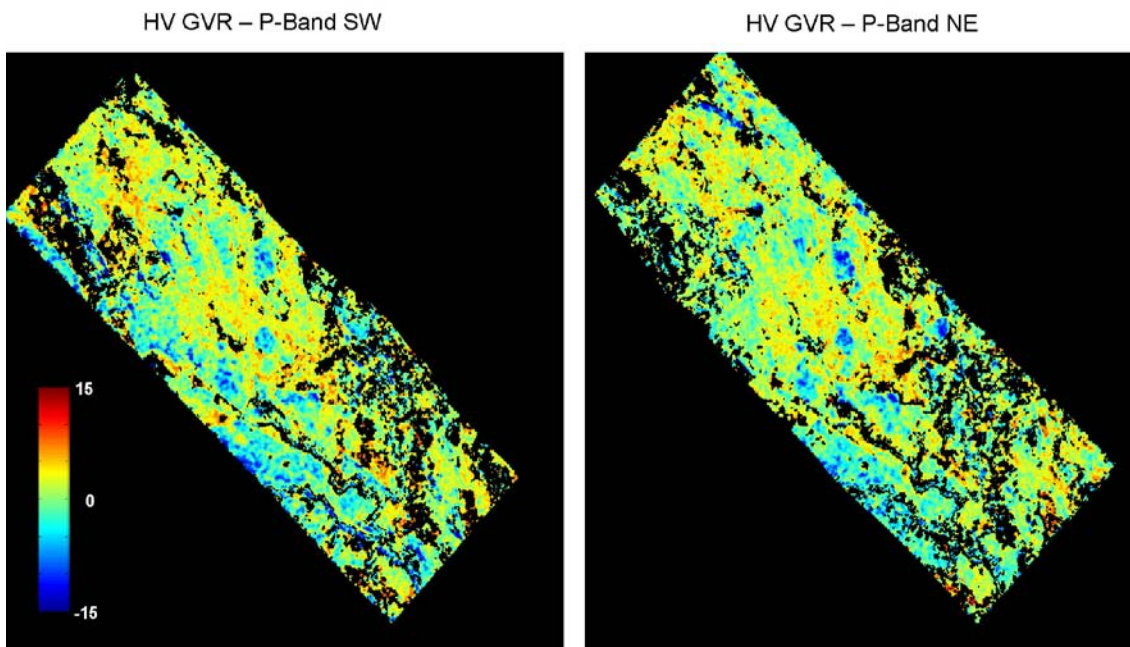
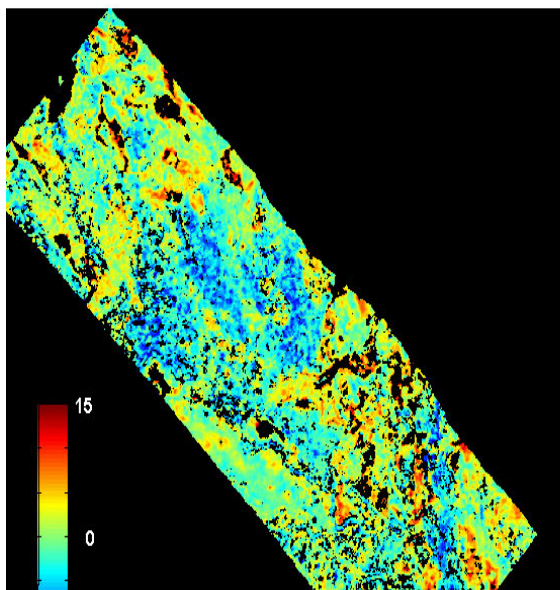


Figure 67: Ground to volume backscattered power ratio in the HV channel for the P-Band SW and NE data-sets

HH GVR – L-Band SW



HH GVR – L-Band NE

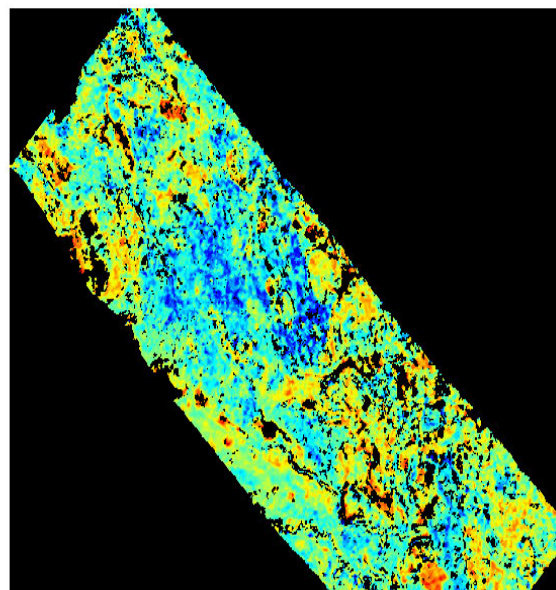
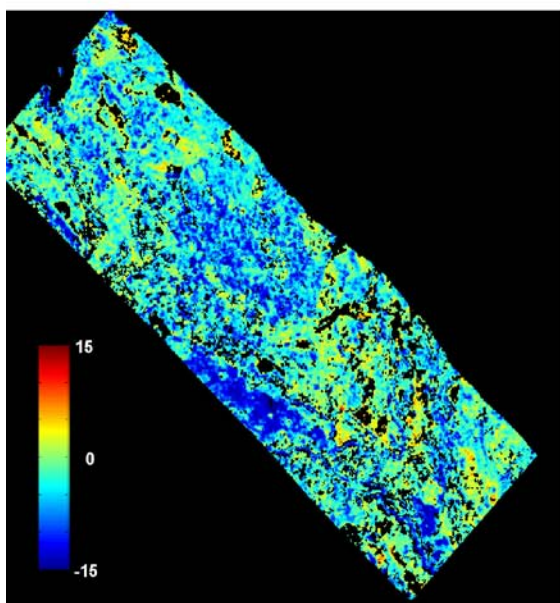


Figure 68: Ground to volume backscattered power ratio in the HH channel for the L-Band SW and NE data-sets

HV GVR – L-Band SW



HV GVR – L-Band NE

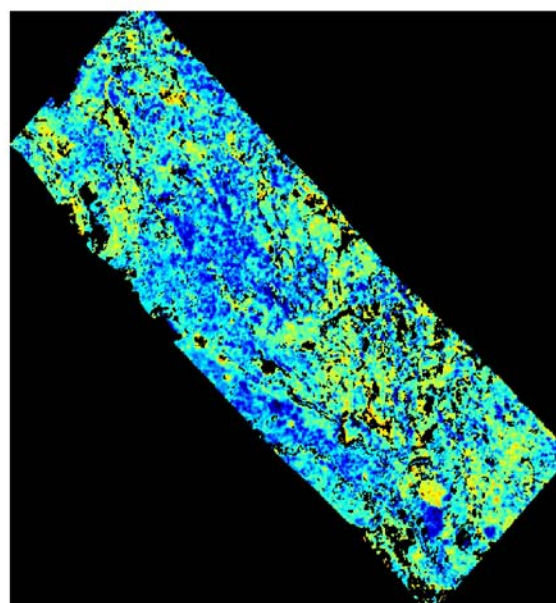


Figure 69: Ground to volume backscattered power ratio in the HV channel for the L-Band SW and NE data-sets.

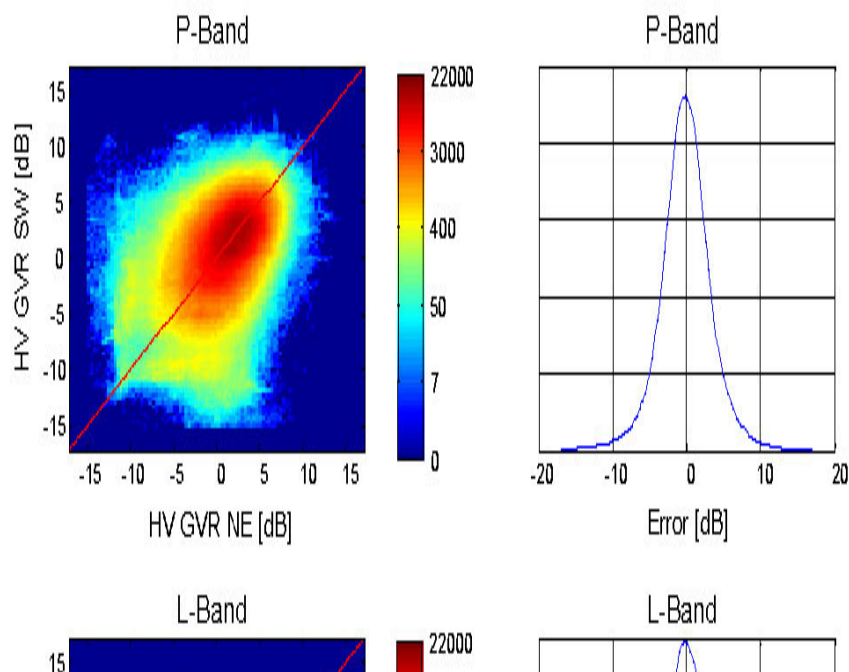


Figure 70: Left column: Joint distribution of the HV GVR measured from the SW and NE data-sets at P-Band (top) and L-Band (bottom). The color scale in each panel is proportional to the logarithm of the number of counts within each bin. Right column: Histograms of the error at P-Band (top) and L-Band (bottom).

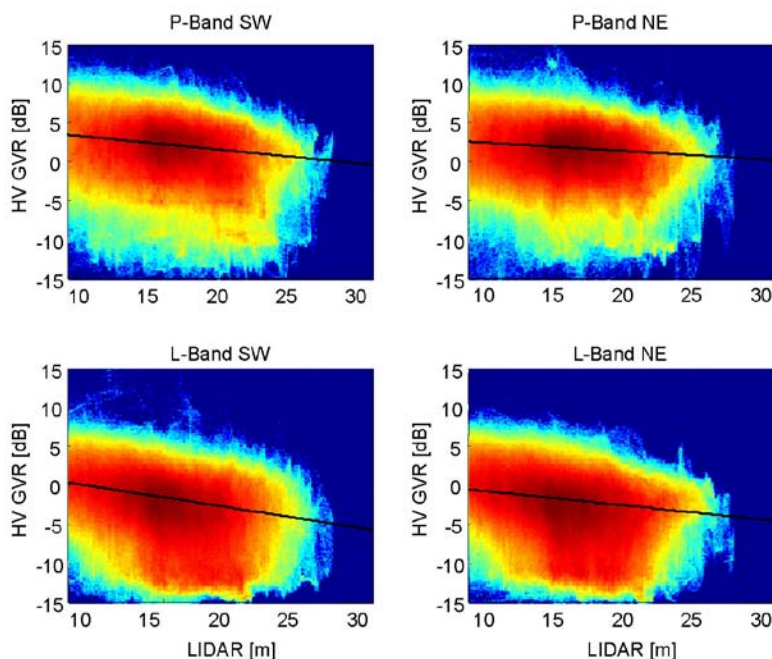


Figure 71: Joint distribution of HV GVR and forest height. Top left: P-Band SW. Top right: P-Band NE. Bottom left: L-Band SW. Bottom right: L-Band NE. The color scale in each panel is proportional to the logarithm of the number of counts within each bin. All panels have been obtained by excluding areas where vegetation is lower than 8 m. The black lines have been obtained through a linear fit of the histogram maxima at each location along the horizontal axis.

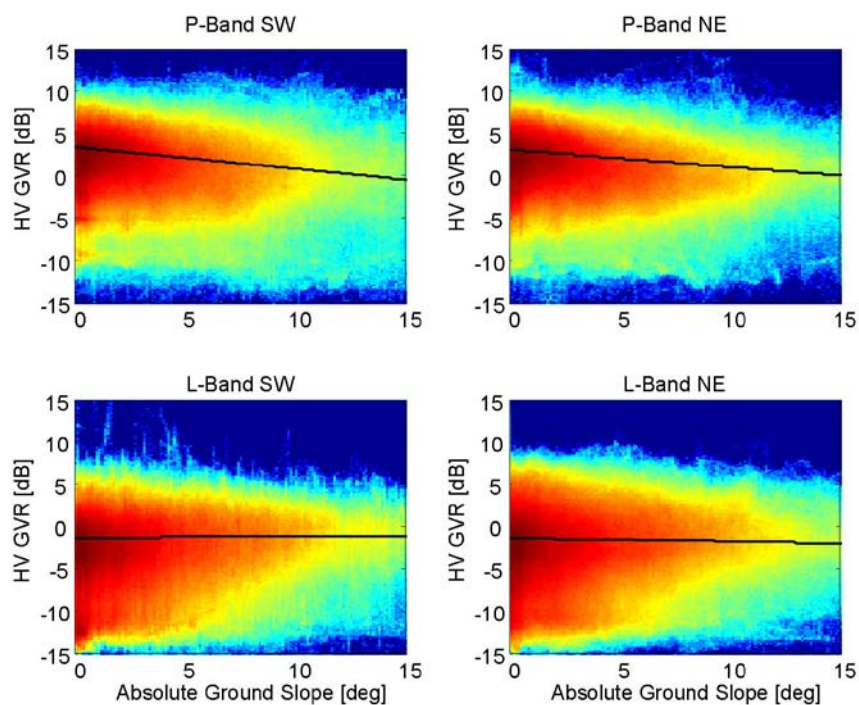


Figure 72: Joint distribution of HV GVR and absolute ground slope. Top left: P-Band SW. Top right: P-Band NE. Bottom left: L-Band SW. Bottom right: L-Band NE. The color scale in each panel is proportional to the logarithm of the number of counts within each bin. All panels have been obtained by excluding areas where vegetation is lower than 8 m. The black lines have been obtained through a linear fit of the histogram maxima at each location along the horizontal axis.

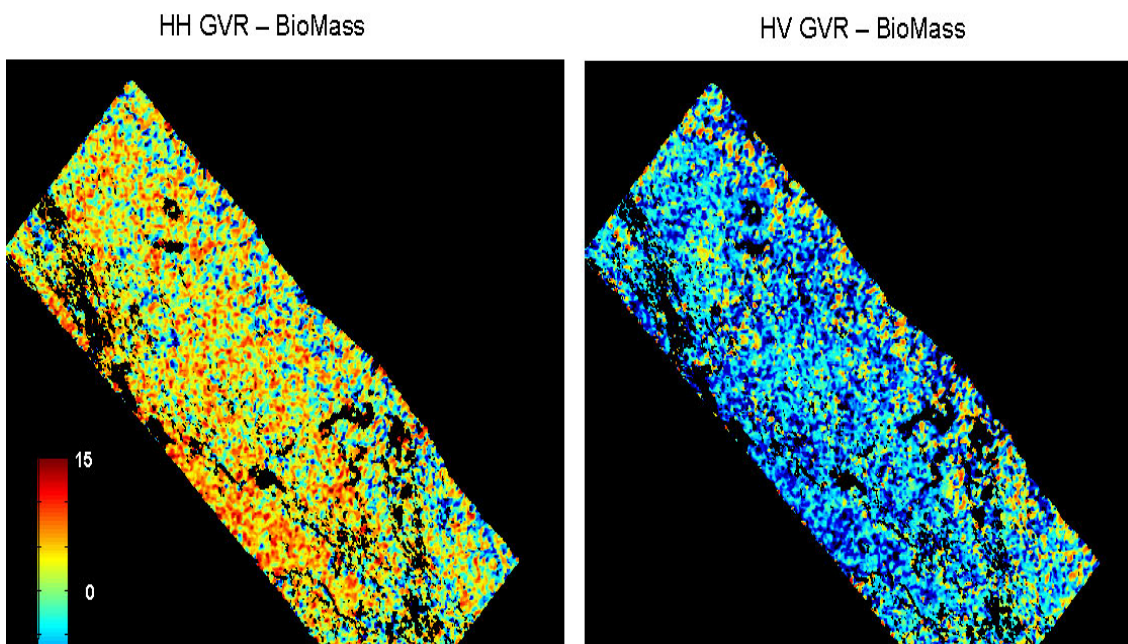


Figure 73: Ground to volume backscattered power ratio in the HH and HV channel for the BioMass data-set.

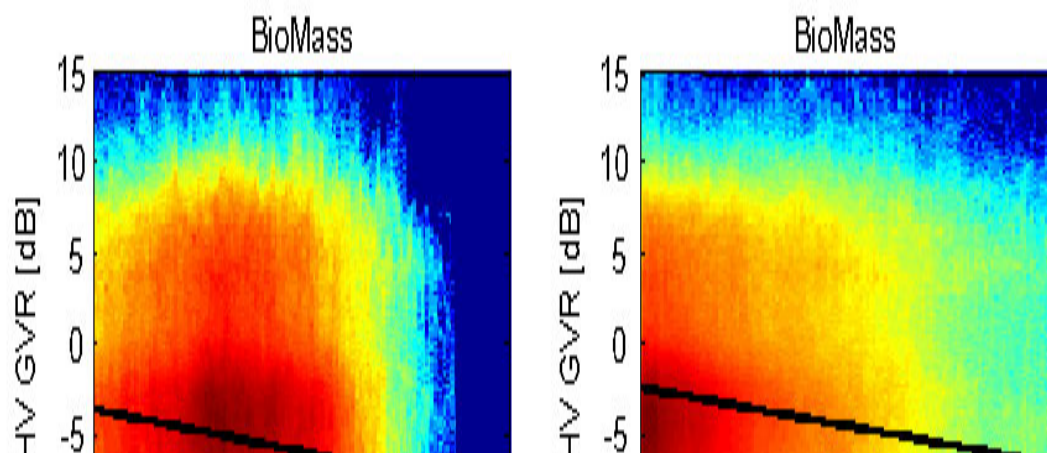


Figure 74: Joint distribution of HV GVR and: forest height (right); absolute ground slope (slope). The color scale in each panel is proportional to the logarithm of the number of counts within each bin. All panels have been obtained by excluding areas where vegetation is lower than 8 m. The black lines have been obtained through a linear fit of the histogram maxima at each location along the horizontal axis.

9.4.8.4 Average Ground Interferometric Coherence

Figure 75, Figure 76, Figure 77 report the average interferometric coherence associated with ground scattering, obtained by averaging the coherence amplitudes over all the interferometric pairs. Ground scattering has been obtained as the most coherent SM under the constraint of positive definitiveness, as discussed in section 9.4.5.

As for the P-Band data-sets, a slight rising trend with respect to the look angle may be appreciated in both look directions, due to the Spectral Shift decorrelation. Besides that, it is observed that ground coherence is extremely high, and substantially uncorrelated with vegetation height. Instead, the spatial variation of ground coherence is clearly correlated with terrain slope. In particular, coherence losses occur at the same locations, independently of flight direction.

Ground coherence has turned out to be lower in the BioMass case. This is due to the much larger resolution cell, resulting in a less homogeneous set of targets to contribute to the received signal.

The spatial variation of ground coherence is correlated with terrain slope, even though to a less extent with respect to the full bandwidth case. This is due to the fact that the interferograms have been evaluated after Common Band Filtering in the Biomass case. For the same reason, near range areas appear as low coherence areas, due to rejection of many interferograms beyond the critical baseline.

L-Band data, see Figure 77, exhibit a quite different behavior, in that ground coherence is largely correlated with vegetation height. This is likely to be due to the leakage phenomena pointed out in section 9.4.7.2. Accordingly, the presence of dense vegetation reduces ground visibility, and thus hinders the retrieval of ground contributions.

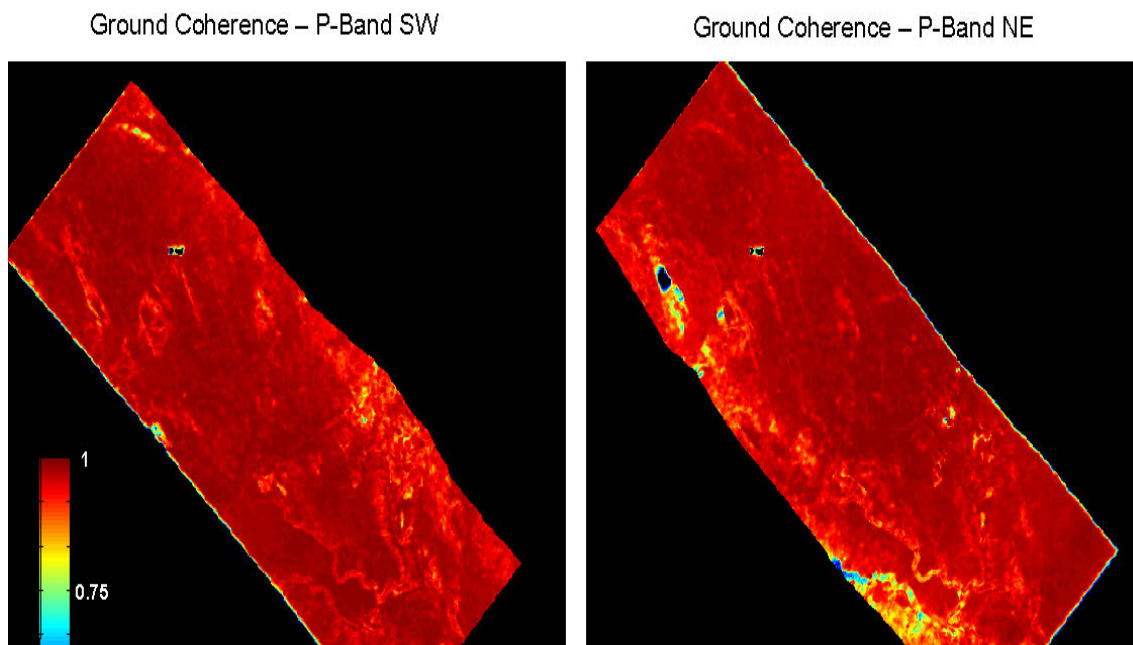


Figure 75: Average ground interferometric coherence for the P-Band SW and P-Band NE data-sets.

Ground Coherence – BioMass

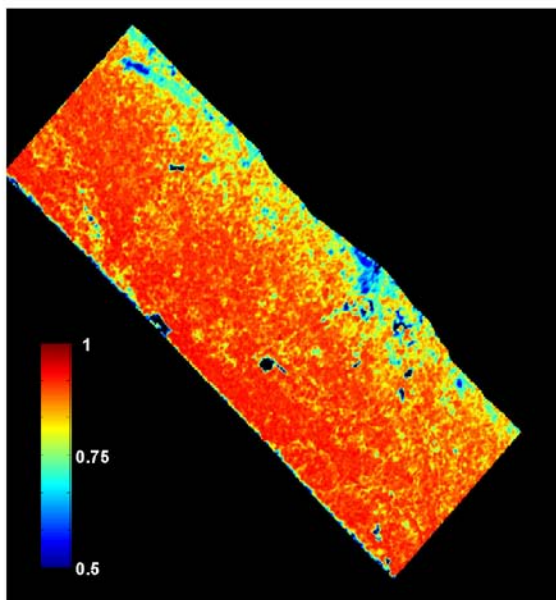
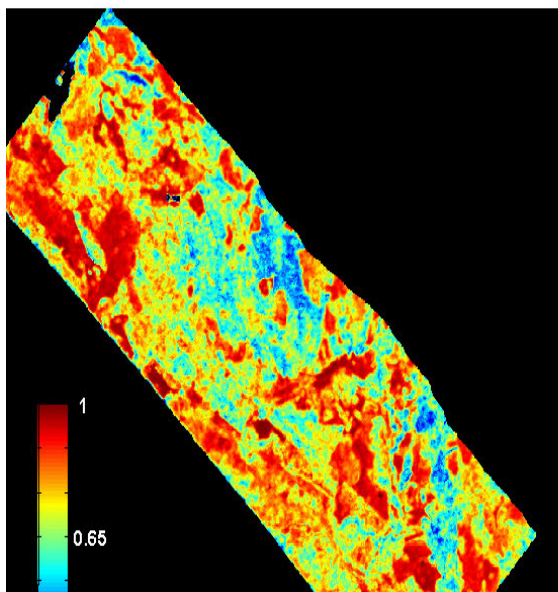


Figure 76: Average ground interferometric coherence for the BioMass data-set.

Ground Coherence – L-Band SW



Ground Coherence – L-Band NE

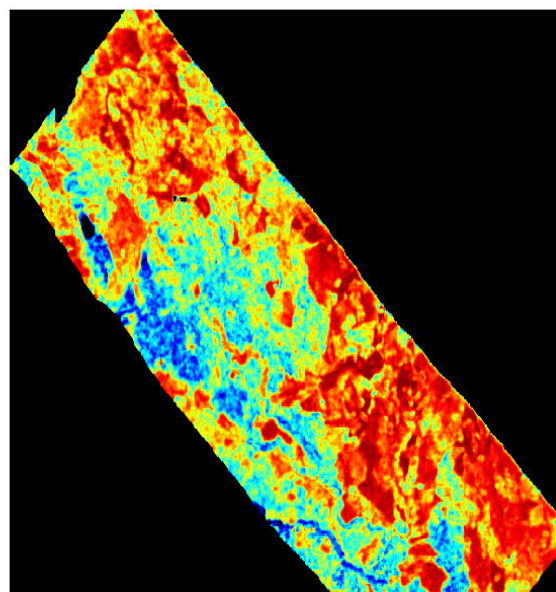


Figure 77 Average ground interferometric coherence for the L-Band SW and L-Band NE data-sets.

9.4.8.5 Terrain Topography Estimation

The estimation of terrain topography has been based directly on the ground phases, retrieved through the AS technique and the Phase Linking algorithm.

Terrain topography is retrieved by solving the problem:

$$\varphi_n(P) = kz_n(P) \cdot q(P) + \Phi_n \quad \text{Eq 36}$$

Where: n is the index of the interferograms, formed with respect to a common master; P denotes the position of a pixel in the slant range, azimuth plane; $\varphi_n(P)$ is the ground phase at location P in the n -th interferogram; $kz_n(P)$ is the phase to height conversion factor at location P in the n -th interferogram; $q(P)$ is terrain elevation at location P ; the terms Φ_n account for the presence of constant phase offsets in each interferogram.

The problem in Eq 36 is well posed only upon the condition that each phase to height conversion factor is characterized by a different spatial variation along the slant range, azimuth coordinates. Otherwise, a 1 dimensional null space arises. If the height to phase conversion factors undergo no (relevant) spatial variation, as it may be the case of spaceborne acquisitions, the null space is simply given by a constant elevation offset. Accordingly, terrain topography is retrieved up to a constant, which may be fixed by phase locking to a reference point.

The problem is well posed in case of airborne acquisitions, due to differential platform motion in different tracks. As a matter of fact, however, it is bad conditioned, hindering the retrieval of absolute terrain elevation. For this reason, terrain topography has been retrieved by allowing a 1 dimensional null space, in order to ensure the robustness of the solution. The effect of the null space, however, can not be described as a simple height offset as in the spaceborne case, but rather as a slowly varying deformation, which represents the intrinsic problem ambiguity.

This is the best solution that can be retrieved in absence of any kind of a-priori information. Therefore, we retained this approach.

Indeed, better results can be obtained by considering ground reference points, or models that account for the physics of Propagation Disturbances. For example, in the airborne case Propagation Disturbances are mainly caused by platform motion, whereas in the spaceborne case ionosphere is expected to play a significant role.

Results are shown in Figure 78 through Figure 80. All panels report the estimation error with respect to the LIDAR DEM. Results relative to data-sets P-Band SW, P-Band NE, and BioMass have been obtained by correcting the data with the calibrating phases provided by DLR. At both P-Band and L-Band, the null space has turned out to be essentially described by a rising a trend along the slant range coordinate. Accordingly, the results have been de-trended in order to give the best match with the LIDAR DEM.

In all cases errors are visible, whose dynamic may be assessed in about ± 15 m at P-Band and ± 30 m at L-Band. Such errors are characterized by a large spatial decorrelation length, and are correlated with the flight direction. These features clearly indicate that terrain elevation errors are the result of uncompensated phase terms, due to the residual platform motion. It has to be remarked that nearly the same result have been obtained by processing the HH channel solely through standard interferometric techniques, see Figure 79, left panel. Therefore, we exclude the presence of artifacts due to the tomographic processing.

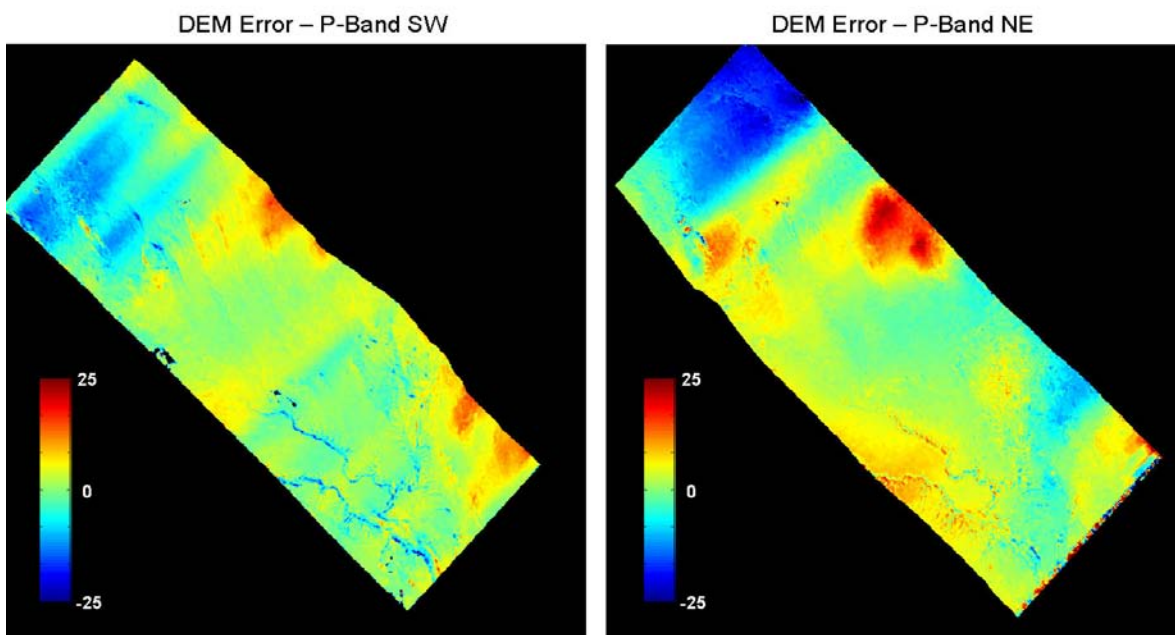


Figure 78: Terrain elevation error [m] with respect to the LIDAR DEM. Left panel: P-Band SW data-set. Right panel: P-Band NE data-set.

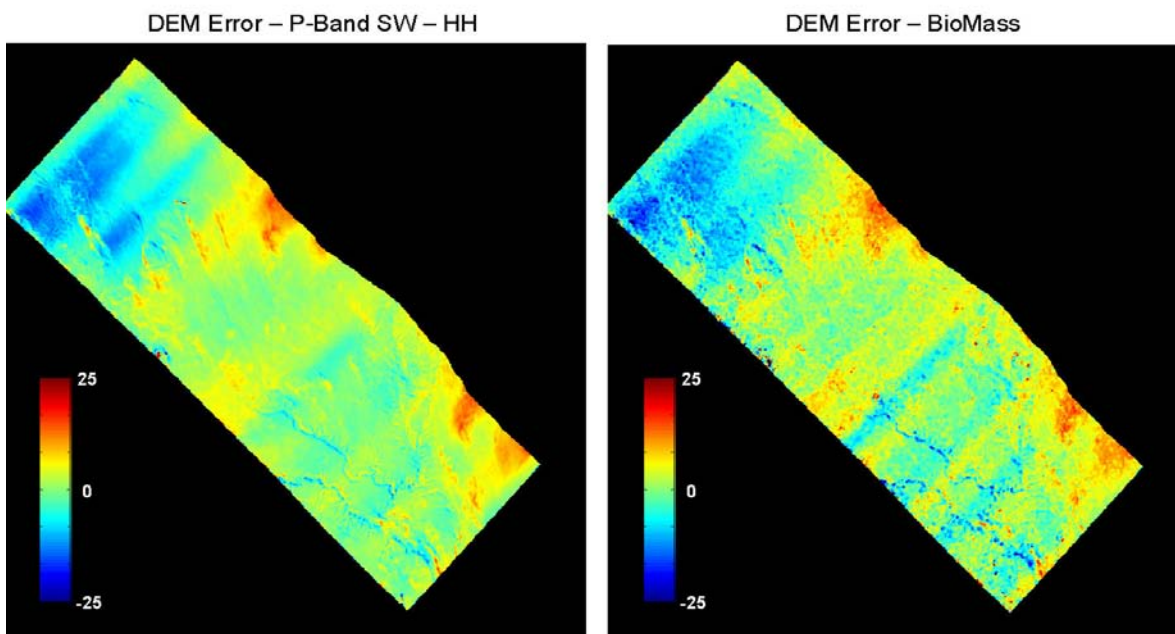


Figure 79: Terrain elevation error [m] with respect to the LIDAR DEM: Left panel: P-Band SW data-set. This DEM has been obtained by processing the HH interferometric phases through standard interferometric techniques. Right panel: BioMass data-set.

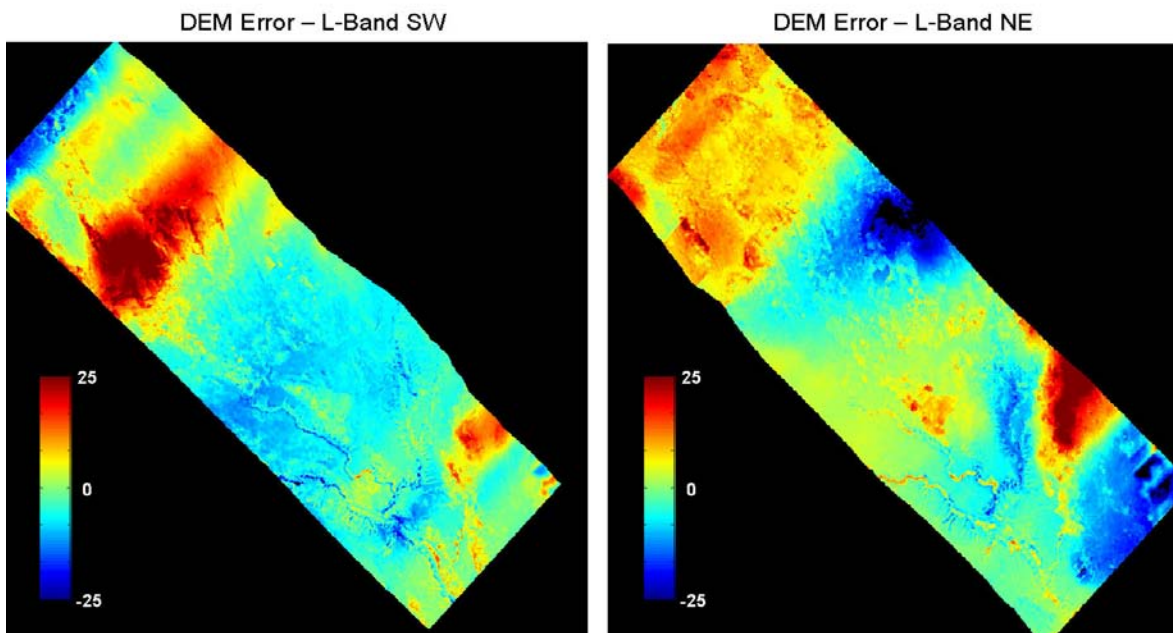


Figure 80: Terrain elevation error [m] with respect to the LIDAR DEM. Left panel: L-Band SW data-set. Right panel: L-Band NE data-set.

Despite the aforementioned elevation errors, however, topography retrieval has turned out to be robust enough as for the estimation of ground slopes, whose accuracy has been assessed in 2.25° . Such an accuracy is converted in a forest height error smaller than 4%, see section 9.4.4.2. Accordingly, the availability of an external DEM is not critical as for the assessment of forest height, even in of topographic areas.

Finally, an excellent agreement is observed between the results achieved by processing the P-Band SW and BioMass data-sets, the estimate accuracy being assessed in about 2 m.

9.4.8.6 Summary

Tomographic analyses clearly show that most scattering contributions at P-Band are associated with the ground level, not only in the HH channel but also in the HV channel. Very similar results were observed relatively to the Remningstorp test site investigated in the framework of the BioSAR 2007 campaign. Therefore, the presence of HV scattering from the ground level appears as a distinctive trait of boreal or boreal like forests as imaged at P-Band.

As expected, L-Band data have shown a remarkable difference, resulting in a more uniform distribution of the backscattered power along the vertical direction. Still, non negligible contributions from the ground level have been observed at L-Band as well.

Open areas are better identified at L-Band, whereas P-Band data have shown poor sensitivity as for the identification of vegetated areas lower than about 8 m.

At both wavelengths, more than 90% of the information carried by the data can be represented by retaining only two scattering mechanisms.

Given the limited number of baselines, the Largest Volume solution has been proposed as a criterion for the retrieval of volume contributions. Such a solution appears to be attractive especially at P-Band, as it manages to reject most contributions from the ground level while resulting in a physically sound volume structure. At L-Band, instead, only minor differences have been observed with respect to HV, consistently with the presence of stronger canopy backscattering contributions.

In both cases, the Largest Volume solution has resulted in a remarkable agreement with LIDAR measurements as for forest top height.

Terrain topography does not seem to hinder the correct estimation of forest height, provided that it has been properly compensated for basing on a-priori knowledge. Besides phase calibration issues, however, terrain topography can be well retrieved directly from SAR, given the good visibility of the ground at P-Band.

The Ground to Volume backscattered power Ratios (GVRs) have turned out to be well consistent with the physics of Radar scattering at P-Band and L-Band. As expected, P-Band data are more affected by contributions from the ground level with respect to L-Band data, the difference as for the HV GVR being assessed in about 5 dB. At both wavelengths it is observed that the HV GVR decreases with forest height, consistently with the enlargement of volumetric structures. A different behavior is found with reference to terrain slope, as the HV GVR exhibits a dependence on terrain slope at P-Band but not at L-Band, consistently with the presence of specular reflections at P-Band, but not at L-Band. Therefore, we conclude that useful information about the forest structure is carried by the GVR.

Terrain topography has been derived also from the ground phases retrieved through the Algebraic Synthesis technique. At P-Band, it has been shown that no significant differences are found in the case where terrain topography is derived through standard interferometric processing basing on the HH polarization, due to the fact that the HH phase center is found very close to the ground level. The residual error with respect to the LIDAR DEM is to be imputed to large scale phase errors, due to residual platform motion, as witnessed by the fact that better results have been obtained by exploiting the calibrating phases provided by DLR.

BioMass represents a challenging problem in the framework of super-resolution imaging, due to the dramatic reduction of the number of independent looks within the estimation window and the stringent limit to vertical resolution arising from pulse bandwidth, which may be assessed in about 20 m with a look angle of 25°. Specific procedures have been adopted in order to deal with such a limit, resulting in a vertical resolution enhancement by a factor of 2.

Forest height has been retrieved to within an accuracy of 20% with respect to LIDAR measurements by exploiting a 1 ha estimation window. No significant bias has been observed for forest heights higher than 10 m, whereas a large bias is found for forest heights below 10 m, consistently with the theoretical vertical resolution limit.

Terrain topography has been retrieved within an accuracy of 2 m with respect to the full bandwidth case.

The GVR is the most sensitive parameter with respect to resolution loss. The volume structure associated with the Largest Volume Solution resembles the one found in HV, therefore yielding lower GVR values.

9.4.9 Phase Stability and Phase Calibration

The aim of this last section is to discuss the effectiveness of different approaches to Phase Calibration at P-Band. Four approaches are considered:

- External Phase Calibration: no further correction is applied to the data, under the assumption that platform motion has been completely corrected basing on navigation data.
- Absolute Phase Offset Estimation Procedure (APO): the data is corrected according to the calibrating phases provided by DLR.
- Permanent Scatterers (PS) based Phase Calibration: the data is corrected basing on the phases of amplitude stable points, identified according to section 9.4.3.3.
- Algebraic Synthesis (AS) based Phase Calibration: the data is corrected basing on the retrieved ground phases, according to section 9.4.4.6.

Phase accuracy will be assessed on the whole scene, considering the cases of the External and APO calibration techniques.

The impact of the residual phase errors produced by the four techniques above will be then discussed in light of the resulting tomographic profiles.

9.4.9.1 Phase Accuracy

Figure 81 shows the maps of the phase accuracy for the P-Band SW data-set. The right panel corresponds to the case of the External Phase Calibration technique, where no further corrections have been applied, whereas the left panel has been obtained by applying the calibrating phases provided by DLR.

In both cases terrain topography is retrieved along with a set of 5 phase offsets, according to section 9.4.8.5. A further phase correction is then applied in order to remove the retrieved phase offsets and the contribution to phase of terrain topography.

It is very important to note that different estimates are produced with different calibration technique as for terrain topography. This phenomenon, however, does not necessarily have an impact of the capability to image the vertical structure of the scene. For example, the presence of phase disturbances correlated with the normal baselines might easily result in large errors as for terrain topography. Yet, nothing changes as for the focusing of targets above the ground, provided that the contributions to phase of the estimated topography are removed. In other words, the decision to estimate and remove topographic contributions in all cases has been taken in order to provide a comparison of different calibration techniques by considering only their impact on the tomographic reconstructions of the targets above the ground.

Phase stability has been evaluated for each pixel by taking the average of the phase residuals along the six tracks. In formula:

$$\hat{\gamma}_\alpha = \text{Re} \left(\sum_n \exp(j\Delta\varphi_n) \right) \quad \text{Eq 37}$$

Where $\Delta\varphi_n$ is the phase residual for the n-th track after removal of terrain topography and phase offsets. Phase stability has then been converted in degrees assuming that phase residuals are normally distributed, see Eq 27.

As visible in Figure 81, no dramatic improvement has been observed to be brought by the APO technique as for the vertical focusing. This is due to the fact that terrain elevation and phase offsets are removed in

all cases. Accordingly, the phase corrections yielded by the APO technique appear to be mostly related to topography and phase offsets, whose effect has been voluntarily excluded from this analysis. Though, applying DLR calibrating phases has resulted in visible improvements of the phase accuracy throughout the whole scene. In particular, it may be appreciated that artifacts due to platform motion have been reduced. Notwithstanding the presence of areas with large errors, phase accuracy is observed to be in the order of $5^\circ - 10^\circ$ in most areas, witnessing the excellent quality of the data delivered by DLR.

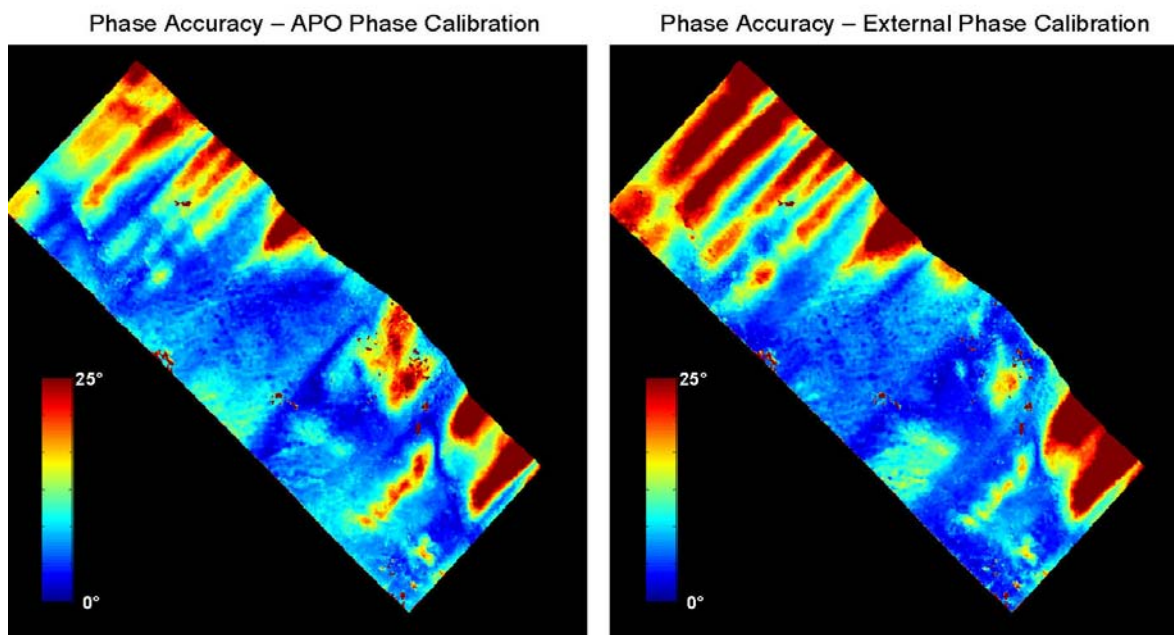


Figure 81: Phase accuracy for the P-Band SW data-set. Left panel: APO Phase Calibration. Right Panel: External Phase Calibration.

9.4.9.2 Tomographic profiles

This section reports the retrieved backscattered power distributions in the HV channel for the same azimuth cut analyzed in 9.4.7. Results are shown in Figure 82 and Figure 83. As in section 9.4.7, all panels are presented in ground geometry.

It may be appreciated that the best focusing quality is obtained by the AS technique. This is not surprising, as such a technique performs an adaptive and continuous phase calibration basing on the retrieved ground phases. The PS-based technique has produced nice results. Though, better performances had been observed in the case of the BioSAR 2007 data-set, as reported in [41]. This result is to be imputed to a less reliable point selection with respect to the BioSAR 2007 case. On the one hand, this phenomenon is due to the fact that baseline aperture is halved with respect to the BioSAR 2007 case, resulting in difficulties as for the identification of point-targets, as discussed in section 9.4.3.3. On the other hand, though, this phenomenon is also the result of the presence of large topographic variations, which weakens dihedral scattering contributions.

Although resulting in a phase accuracy within $5^\circ - 10^\circ$, focusing degradation has been observed in the cases of the External and the APO calibration techniques, witnessing the strict requirements of Tomography.

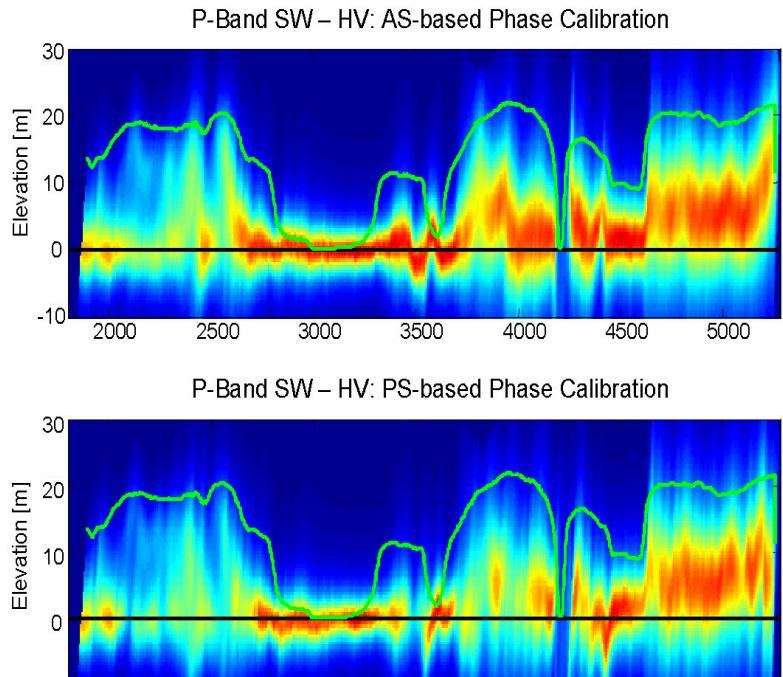


Figure 82: Tomographic Profiles for the selected azimuth cut. Top row: AS-based Phase Calibration. Bottom row: PS-based Phase Calibration. Data-set: P-Band SW. Polarization: HV.

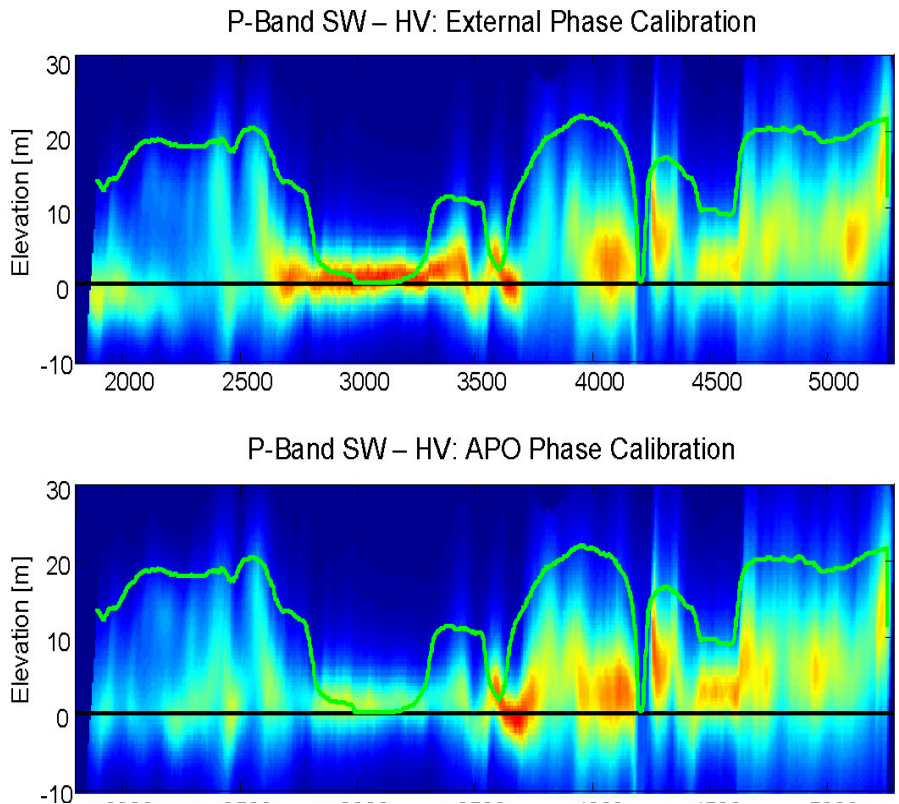


Figure 83: Tomographic Profiles for the selected azimuth cut. Top row: External Phase Calibration. Bottom row: APO Phase Calibration. Data-set: P-Band SW. Polarization: HV.

9.4.10 Conclusions

3D structures of forests have been analyzed through multi-baseline and multi-polarimetric SAR surveys at P-Band and L-Band.

At P-Band the most relevant scattering contributions are observed at the ground level, both in co polar and cross polar channels, implying the presence of ground reflected volume scattering. The observed value of 50° as for the co-polar phase in forested area strongly indicates the presence of specular reflections. Accordingly, the presence of HV scattering contributions from the ground level seems to be better explained as being due to the ensemble of trunk-ground and canopy-ground interactions, eventually perturbed by the presence of understory and trunk-ground dielectric losses. The presence of HV scattering from the ground level appears as a distinctive trait of boreal or boreal like forests at P-Band, as similar results were observed for the Remningstorp data-set investigated in the framework of the BioSAR 2007 campaign.

L-Band data have shown a remarkable difference, resulting in a more uniform distribution of the backscattered power along the vertical direction. Still, non negligible contributions from the ground level have been observed at L-Band as well.

Open areas are better identified at L-Band, whereas P-Band data have shown poor sensitivity as for the identification of vegetated areas lower than about 8 m.

Terrain topography plays two distinct roles in the analysis of forested areas. The first is geometric. The 3D reconstruction produced by a multi-baseline SAR system is naturally described in a slanted coordinated system, according to the Radar Line of Sight. Therefore, a geocoding operation is required in order to represent the scene in ground geometry. It then follows that knowledge of terrain topography is strictly required for the correct evaluation of target elevation above the ground. In particular, an imprecise compensation of terrain slope directly results in errors about the retrieved forest height, the amount of the error depending on the actual terrain slope and the look angle. Excluding phase calibration issues, however, the retrieval of terrain topography directly from SAR data does not seem to give rise to critical problems, by virtue of the good visibility of the ground at P-Band. The other role played by terrain topography is related to the physics of the received signal. As discussed, relevant double-bounce contributions are found at P-Band. Accordingly, terrain topography has a great impact on the nature of the received signal, since topographic slope tends to zero double bounce contributions. This phenomenon has been clearly observed by comparing the Ground to Volume Ratio (GVR) at P-Band and L-Band retrieved by the Tomographic analysis. In fact, the GVR has been observed to decrease with terrain slope at P-Band, whereas such a dependency has not been observed at L-Band.

Most of the analyses have been carried out through the Algebraic Synthesis (AS) technique, recently introduced in literature. Such a technique allows the generalization of the PolInSAR concepts to the case of multiple baselines and multiple Scattering Mechanisms (SMs), while yielding the best Least Square fit with respect to the received signal. Accordingly, a first important result within this campaign is the experimental demonstration that two SMs account for more than 90% of the information carried by the data at both P-Band and L-Band. This result underlines the validity of modeling a forest scenario as being constituted by ground and volume scattering. As discussed, though, the separation of ground and volume scattering contributions is subject to an ambiguity, mostly associated with the possibility that volume scattering may be found at the ground level as well.

In this framework, Tomography represents a powerful tool for investigating the potential solutions. Clearly, the true potentialities of SAR Tomography are revealed only in presence of a suitably large baseline aperture. As discussed, especially at P-Band the accurate reconstruction of the spatial distribution of the backscattered power is hindered by the poor baseline aperture. For this reason the Tomographic imaging

has been performed basing on super-resolution methods. This choice has to be considered as a compromise. Indeed it entails a loss of radiometric accuracy. Still, it permits to appreciate details that would not be accessible otherwise.

The Largest Volume solution has been proposed as a criterion to solve the ambiguity that affects the problem of SM separation with a limited number of baselines. Such a solution appears to be an attractive tool especially at P-Band, as it manages to reject most contributions from the ground level while resulting in a physically sound volume structure. At L-Band, instead, only minor differences have been observed with respect to HV, consistently with the presence of stronger canopy backscattering contributions with respect to P-Band.

The Largest Volume solution has resulted in a remarkable agreement with LIDAR measurements as for forest top height, along with physically consistent GVRs at both P-Band and L-Band. Clearly, these results alone are not sufficient to claim that the Largest Volume solution actually captures the true volume structure. Yet, it represents a first step towards the solution of the SM separation problem, and highlights the importance of structure as for the understanding of the physics of Radar scattering from forested areas. It is also worth noting that the Largest Volume structure represents an example of how Tomography could interface with PolInSAR in the framework of the BioMass mission. The availability of multiple-baselines offers the possibility to examine the structure of scattering contributions identified as being associated with volume-only scattering, and thus to improve both the physical modeling and the retrieval procedures.

Terrain topography has been derived directly from the ground phases retrieved through the Algebraic Synthesis technique. At P-Band, it has been shown that no significant differences are found in the case where terrain topography is derived through standard interferometric processing basing on the HH polarization, due to the fact that the HH phase center is found very close to the ground level. The residual error with respect to the LIDAR DEM is to be imputed to large scale phase errors, due to residual platform motion, as witnessed by the fact that better results have been obtained by exploiting the calibrating phases provided by DLR.

Phase Calibration has to be discussed with reference to two issues. The first, and most important, is relative to the accuracy of the vertical structure reconstruction once that topography and phase offsets contribution have been removed. In this case it has been shown that the AS-based calibration technique is capable of recovering phase miscalibration in absence of external information, therefore proving the feasibility of SAR tomography in the framework of a spaceborne mission. PS-based calibration has produced acceptable results, even though better results had been observed in the case of the BioSAR 2007 data-set. Although resulting in a phase accuracy within 5° - 10° , focusing degradation has been observed in the cases of the External and the APO calibration techniques, witnessing the strict requirements of Tomography. Accordingly, the inclusion of a data-based Phase Calibration step in the processing chain has to be considered as a mandatory requirement. On the other hand, though, blind Phase Calibration techniques can not fully recover the topographic information, especially in presence of a low number of tracks. Phase disturbances due to platform motion do not seem to be critical in the framework of the BioMass mission, due to high orbit accuracy of spaceborne platforms. The impact of ionospheric disturbances, instead, is still to be fully investigated.

BioMass represents a challenging problem in the framework of super-resolution imaging.

Considering both pulse bandwidth and the antenna length along the flight direction, the spatial resolutions of the BioMass and E-SAR systems are separated by a factor of about 100. This entails a dramatic reduction of the number of independent looks within the estimation window, which jeopardizes the retrieval of robust statistics. The only viable strategy to mitigate this phenomenon is the employment of a suitably large estimation window. In this work, a 60 x 60 m estimation window has been assumed, after the need to get robust statistics while ensuring a relatively fine spatial resolution. Furthermore, the pulse bandwidth of

the BioMass system poses a stringent limit to vertical resolution, which may be assessed in about 20 m with a look angle of 25°. Specific procedures have been adopted in order to deal with this phenomenon, resulting in a vertical resolution enhancement by a factor of 2.

Despite these difficulties, however, results have turned out to be consistent with those obtained in the full bandwidth case. The best result has been obtained as for the estimate of terrain topography, whose accuracy with respect to the full bandwidth case has been assessed in about 2 m.

Forest height has been retrieved to within an accuracy of 20% with respect to LIDAR measurements by exploiting a 1 ha estimation window. Furthermore, no significant bias has been observed for forest heights above 10 m. These results confirm the feasibility of inferring structural information from BioMass data.

In particular, the absence of relevant estimate bias indicates that products within a given accuracy may be delivered by enlarging the size of the estimation window. For example, accuracy can be improved to 5% by exploiting a 1 square kilometer estimation window.

Further researches should be devoted to improving ground-volume separation in the BioMass case. In particular, two kinds of a-priori information will be considered. One is relative to the expected polarimetric behavior of ground and volume scattering, to be exploited to solve the ambiguity of the SM separation problem. The other is relative to the expected texture of forested areas, which may be exploited in order to simultaneously achieve super-resolution capabilities along the three geometrical axes.

9.4.11 References

1. Heliere, F.; Lin, C.C.; Fois, F.; Davidson, M.; Thompson, A.; Bensi, P., "BIOMASS: A P-band SAR earth explorer core mission candidate," Radar Conference, 2009 IEEE , vol., no., pp.1-6, 4-8 May 2009
2. Krieger, G.; Hajnsek, I.; Papathanassiou, K.; Eineder, M.; Younis, M.; De Zan, F.; Prats, P.; Huber, S.; Werner, M.; Fiedler, H.; Freeman, A.; Rosen, P.; Hensley, S.; Johnson, W.; Veilleux, L.; Grafmueller, B.; Werninghaus, R.; Bamler, R.; Moreira, A., "The tandem-L mission proposal: Monitoring earth's dynamics with high resolution SAR interferometry," Radar Conference, 2009 IEEE , vol., no., pp.1-6, 4-8 May 2009
3. D'Aria, D.; Giudici, D.; Guarnieri, A.M.; Rizzoli, P.; Medina, J., "A wide swath, full polarimetric, L band spaceborne SAR," Radar Conference, 2008. RADAR '08. IEEE , vol., no., pp.1-4, 26-30 May 2008
4. T. Aulinger, T. Mette, K.P. Papathanassiou, I. Hajnsek, M. Heurich, P. Krzystek "Validation of heights from interferometric sar and lidar over the temperate forest site nationalpark bayerischer wald", PolInSAR 2005, Rome, 2005
5. F. Gatelli, A. Monti Guarnieri, F. Parizzi, P. Pasquali, C. Prati, and F. Rocca, "The wavenumber shift in SAR interferometry," IEEE Transactions on Geoscience and Remote Sensing, vol. 32, no. 4, pp. 855–865, July 1994.
6. M. S. Seymour and I. G. Cumming, "Maximum likelihood estimation for SAR interferometry," in International Geoscience and Remote Sensing Symposium, Pasadena, CA, USA, 8–12 August 1994, 1994, pp. 2272–2275.
7. R. Bamler and P. Hartl, "Synthetic aperture radar interferometry," Inverse Problems, vol. 14, pp. R1–R54, 1998.
8. Monti Guarnieri., S. Tebaldini. "Hybrid Cramér-Rao Bounds for Crustal Displacement Field Estimators in SAR Interferometry" IEEE Letters on Signal Processing, Dec. 2007
9. L. Tsang, J. A. Kong, and R. T. Shin, Theory of Microwave Remote Sensing, New York, Wiley, Interscience, 1985
10. Freeman, "Fitting a two-component scattering model to polarimetric sar data from forests," Geoscience and Remote Sensing, IEEE Transactions on, vol. 45, no. 8, pp. 2583–2592, Aug. 2007.
11. Alessandro Ferretti, Claudio Prati, and Fabio Rocca, "Permanent scatterers in SAR interferometry," IEEE Transactions on Geoscience and Remote Sensing, vol. 39, no. 1, pp. 8–20, Jan. 2001
12. H. A. Zebker and J. Villasenor, "Decorrelation in interferometric radar echoes," IEEE Transactions on Geoscience and Remote Sensing, vol. 30, no. 5, pp. 950–959, sept 1992.
13. K. Papathanassiou and S. Cloude, "Single-baseline polarimetric sar interferometry," Geoscience and Remote Sensing, IEEE Transactions on, vol. 39, no. 11, pp. 2352–2363, Nov 2001.
14. S. Cloude and E. Pottier, "A review of target decomposition theorems in radar polarimetry," Geoscience and Remote Sensing, IEEE Transactions on, vol. 34, no. 2, pp. 498–518, Mar 1996.
15. G. Smith-Jonforsen, L. Ulander, and X. Luo, "Low vhf-band backscatter from coniferous forests on sloping terrain," Geoscience and Remote Sensing, IEEE Transactions on, vol. 43, no. 10, pp. 2246–2260, Oct. 2005.

16. D. R. Sheen, N. L. VandenBerg, S. J. Shackman, D. L. Wiseman, L. P. Elenbogen, and R. F. Rawson, "P-3 ultra-wideband SAR: Description and examples," IEEE AES Systems Magazine, pp. 25–29, Nov. 1996.
17. G. Fornaro and A. M. Guarnieri, "Minimum mean square error space-varying filtering of interferometric SAR data," IEEE Transactions on Geoscience and Remote Sensing, vol. 40, no. 1, pp. 11–21, July 2002.
18. R.-S. Wu and M.-N. Toksz, "Diffraction tomography and multisource holography applied to seismic imaging," Geophysics, vol. 52, pp. 11–+, Jan. 1987.
19. Reigber and A. Moreira, "First demonstration of airborne sar tomography using multibaseline l-band data," IEEE Trans. on Geoscience and Remote Sensing, pp. 2142–2152, Sept. 2000.
20. S. Tebaldini, "Multibaseline SAR Imaging: Models and Algorithms", Ph.D. Thesis, Politecnico di Milano, 2009.
21. P. Stoica and R. L. Moses, Introduction to Spectral Analysis. New Jersey: Prentice-Hall, 1997.
22. Ziskind and M. Wax, "Maximum likelihood localization of multiple sources by alternating projection," IEEE Trans. Acoustics, Speech and Signal Processing, vol. ASSP-36, no. 10, pp. 1553, 1988.
23. Richard Roy and Thomas Kailath, "ESPRIT-estimation of signal parameters via rotational invariance techniques," Acoustics, Speech, and Signal Processing, IEEE Transactions on, vol. 37, 1989.
24. P. Stoica, H. Li, and J. Li, "A new derivation of the apes filter," Signal Processing Letters, , no. 6, pp. 205–206, 1999.
25. M. Montanari F. Gini, F. Lombardini, "Layover solution in multibaseline sar interferometry," IEEE Trans. on Aerospace and Electronic Systems, Apr. 2002.
26. G. Fornaro and F. Serafino, "Imaging of single and double scatterers in urban areas via sar tomography," Geoscience and Remote Sensing, IEEE Transactions on, vol. 44, no. 12, pp. 3497–3505, Dec. 2006.
27. G. Fornaro, F. Lombardini, and F. Serafino, "Three-dimensional multipass sar focusing: experiments with long-term spaceborne data," Geoscience and Remote Sensing, IEEE Transactions on, vol. 43, no. 4, pp. 702–714, April 2005.
28. S. R. Cloude, "Dual-baseline coherence tomography," Geoscience and Remote Sensing Letters, IEEE, vol. 4, no. 1, pp. 127–131, Jan. 2007.
29. S. R. Cloude "Multifrequency 3d imaging of tropical forest using polarization coherence tomography," in Eusar 2008, 2008.
30. F. Rocca, S. Tebaldini "BioSAR – WP43" ESTEC Contract No. 20755/07/NL/CB , 2007
31. S. Tebaldini "P-Band SAR Tomography of the Remningstorp Forest Site" PolInSAR 2009, Rome , 2009
32. S. Tebaldini. "Forest SAR tomography: a Covariance Matching Approach" RADARCON 2008, Rome , 2008
33. S. Tebaldini "Minimal Slant Range Resolution for SAR Tomography of Forested Areas" PolInSAR 2009, Roma , 2009
34. P. Stoica, J. Li, X. Tan, "On Spatial Power Spectrum and Signal Estimation Using the Pisarenko Framework", Signal Processing, IEEE Transactions on, vol 56, no 10, pp. 5109-5119, October 2008.
35. Oppenheim, R. Schafer, Digital Signal Processing, Prentice-Hall, Englewood Cliffs, NJ, 1975

36. G. Fornaro, G. Franceschetti, and S. Perna, "Motion compensation errors: effects on the accuracy of airborne sar images," *Aerospace and Electronic Systems, IEEE Transactions on*, vol. 41, no. 4, pp. 1338–1352, Oct. 2005.
37. Ramon F Hanssen, *Radar Interferometry: Data Interpretation and Error Analysis*, Springer Verlag, Heidelberg, 2 edition, 2005
38. Ferretti, C. Prati, F.Rocca, "Nonlinear subsidence rate estimation using permanent scatterers in differentialSAR interferometry," *IEEE Transactions on Geoscience and Remote Sensing*, vol. 38, no. 5, pp. 2202–2212, Sept. 2000.
39. S. Tebaldini and A. Monti Guarnieri "Phase Stability Requirements for SAR Tomography" *CEOS 2008, Oberpfaffenhoffen* , 2008
40. S. Tebaldini: "On the impact of propagation disturbances on SAR multibaseline applications", *Geoscience and Remote Sensing*, IEEE Transaction on, submitted
41. S. Tebaldini and F. Rocca "On the impact of propagation disturbances on SAR Tomography: Analysis and compensation" *RadarCon 2009, Pasadena* , 2009
42. S. Tebaldini and F. Rocca "Polarimetric Options for P-Band SAR Tomography of Forested Areas" *PolInSAR 2009, Roma* , 2009
43. S. Tebaldini. "Algebraic Synthesis of Forest Scenarios from Multi-Baseline PolInSAR Data" *IEEE Transactions on Geoscience and Remote Sensing* , Accepted for publication
44. Monti Guarnieri., S. Tebaldini. "On the exploitation of target statistics for SAR Interferometry applications" *IEEE Transactions on Geoscience and Remote Sensing* ,Vol. 46, November 2008
45. K. P. Papathanassiou and S. R. Cloude, "Three-stage inversion process for polarimetric sar interferometry," *Proc. Inst. Electr. Eng.Radar Sonar Navig.*, vol. 150, p. 125134, June 2003.
46. C. V. Loan and N. Pitsianis, "Approximation with Kronecker products," *Linear Algebra for Large Scale and Real Time Applications*, M. S. Moonen, G. H. Golub, and B. L. R. De Moor, Ed. Norwell, MA: Kluwer, pp. 293–314, 1993.
47. F. Lombardini and A. Reigber, "Adaptive spectral estimation for multibaseline sar tomography with airborne l-band data," *Geoscience and Remote Sensing Symposium, 2003. IGARSS '03. Proceedings. 2003 IEEE International*, vol. 3, pp. 2014–2016, July 2003.

10 SUMMARY

Will be delivered in the next version!

11 RECOMMENDATION

Will be delivered in the next version!

12 APPENDIX: DATA TABLE

This appendix contains tables with stand-wise averages of e.g. SAR backscatter, incidence angles and aspect angles for the different SAR images acquired within the BIOSAR 2008 experiment. The appendix also contains a description of how each of the quantities in the tables was calculated.

12.1 Data Processing

The main part of the tables is SAR backscatter values for each image scene and stand. The stands are the 31 forest stands for which *in-situ* measurements were made within the framework of BIOSAR 2008. Three backscatter measurements are presented in the table: β° , σ° and $\gamma^\circ = \sigma^\circ / \cos\theta_i$, where β° is the averaged radar-cross section per unit image area (azimuth x slant range), σ° is the averaged radar-cross section per unit ground-projected area, γ° is σ° normalized with the projection factor $\cos\theta_i$, and θ_i is the local incidence angle as defined in Figure 12.1. The projection from β° to σ° was done using the ground-projection factor $\cos\psi$ according to [1]:

$$\sigma^\circ = \beta^\circ \cos\psi \tag{12.1}$$

where ψ is the angle between the surface normal and the image plane normal (see Figure 12.2). As shown in [1] this projection formula can be approximated by the commonly used projection formula $\sigma^\circ = \beta^\circ \sin\theta_i$ for areas which are fairly flat and/or has small azimuth surface tilt. However, the area studied in the BIOSAR 2008 campaign (Krycklan) has strong topographic variations and therefore Eq. 12.1 was used.

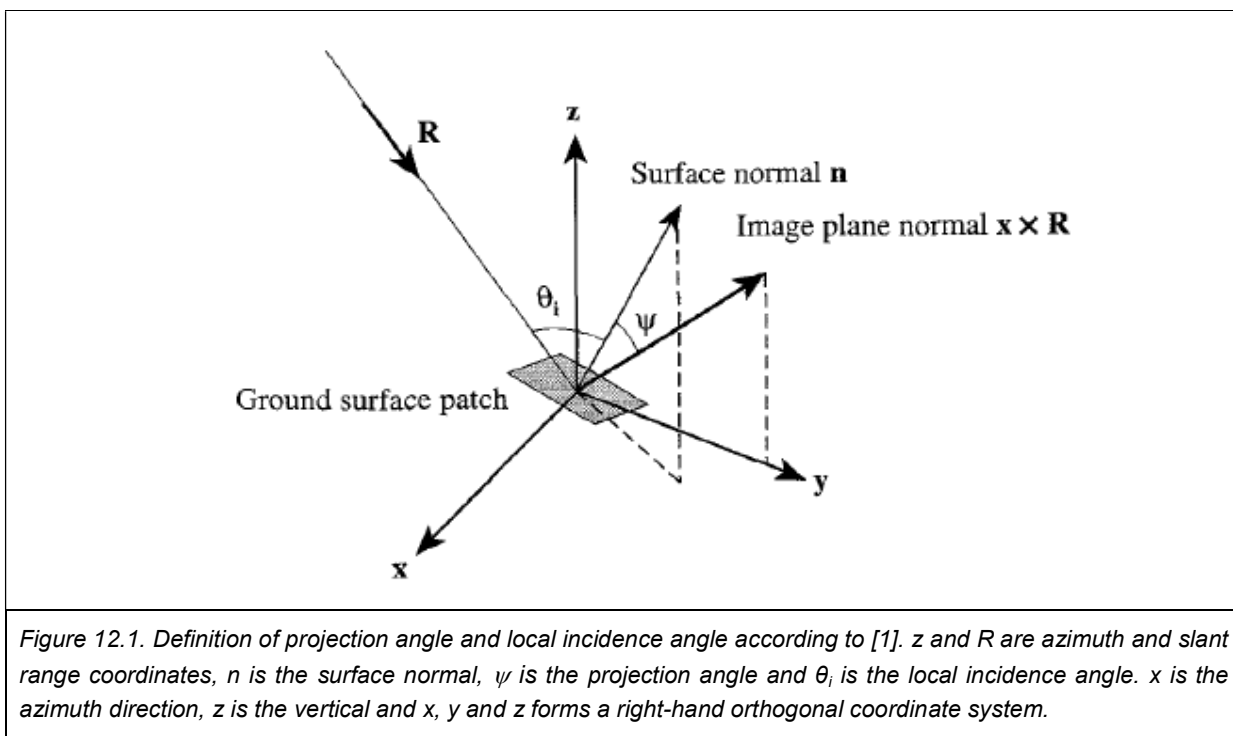
The angles in Figure 12.1 and Figure 12.2 were calculated based on the DEM used for geocoding of SAR images and recorded (reference) flight track positions for ESAR (files named "track_wgs8408biosarXXXx1_ch1_t0X", delivered with radar geometry images). A linear flight path was fitted to the flight track positions. The flight altitude was assumed to be constant. The deviations between the approximate linear path and the true flight path were typically less than a few meters. The used DEM had the same geometry as the geocoded SAR images, i.e. each SAR pixel was associated with a ground height. In order to calculate local surface normals, a plane was fitted, using least squares, to a 50 m by 50 m area centered on each pixel position. The coefficients for the planes were calculated using linear filtering operations, which were implemented as multiplications in the frequency domain. Since the DEM was large it was processed in blocks. Care was taken to avoid wrap-around effects due to the periodicity of the FFT. The shortest vector (R) from the linear track to each pixel position was calculated. After these calculations the vector R and the surface normal were available, and with the added knowledge of the flight direction the angles θ , u and ν were readily calculated. From this the projection factor $\cos\psi$ was calculated using Eq. 4 in [1]. Measured values for β° were then extracted for each pixel and polarization, and estimates of σ° were calculated. These (pixel level) estimates of σ° (four polarizations) and the angles θ , u and ν were stored in an image with seven bands. The image scenes which were divided into three sub-scenes by DLR were combined into a single large image. Only geocoded image scenes were processed.

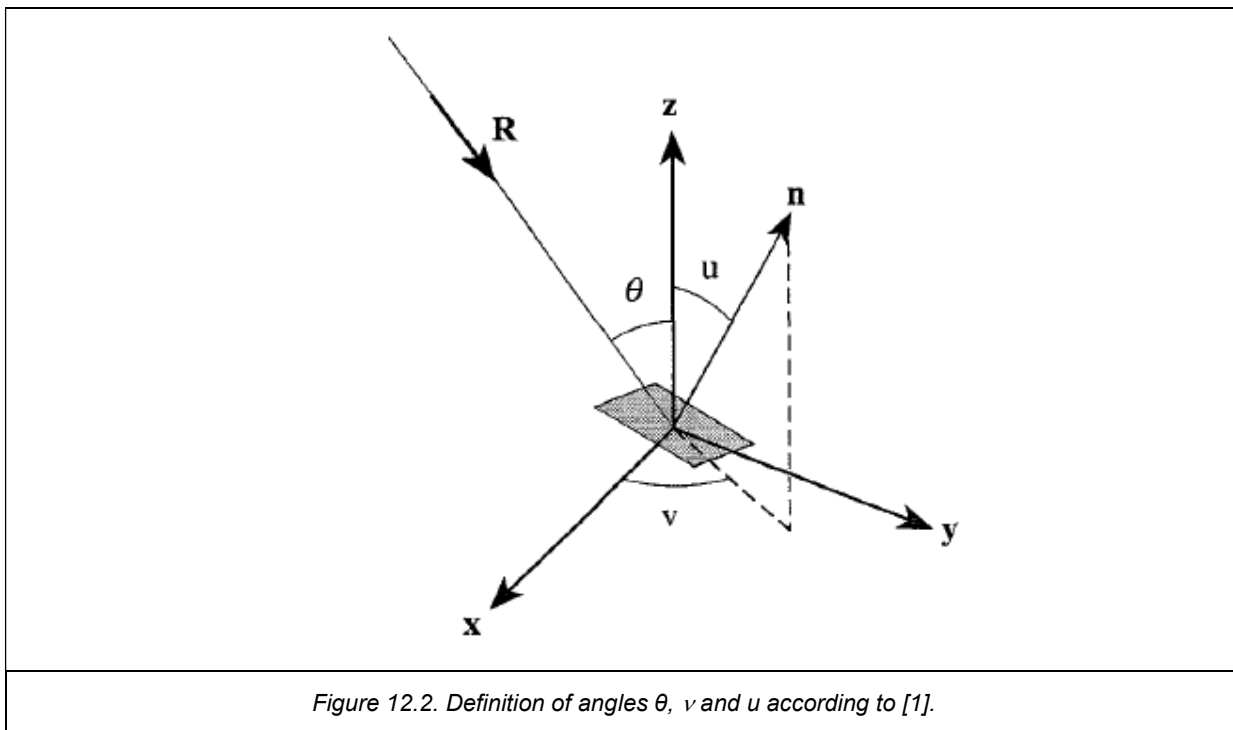
In order to reduce border effects and geographical positioning errors, a 10 m buffer zone was removed for each stand. A file containing stand delineations after the buffer removal is part of the BIOSAR 2008 data

set. For all pixels whose centers were located within a stand (after buffer removal), the estimated value for each of the seven bands described above was extracted. For each pixel, estimates of β° , γ° , θ_i and ψ were then calculated. Stand averages for each of these quantities were then made by averaging all pixel values within each stand. For the backscatter measurements, the averaging was done in linear units and the average value was then transformed to decibel. Average values for u and v were not calculated by simple averaging. Instead, an average surface normal was calculated by first adding together the surface normals for each pixel, then dividing by the number of pixels, and finally normalizing the mean surface normal so that its length was equal to unity. The surface normals for each pixel were calculated from the angles u and v . Stand values for u and v were then calculated from the mean surface normal. For the backscatter measurements a measure of within-stand variation was calculated as the coefficient of variation, defined as $CV(x) = \text{mean}(x) / \text{std}(x)$, where std is the standard deviation and x is the set of pixel level estimates (in linear units) for each stand. As a measure of local topographic variations the standard deviation of the local incidence angle (θ_i) was calculated.

The stand averages described above were stored as tables in an Excel-document. Each sheet in the document corresponds to an image scene and each row corresponds to a stand. In addition to the stand averages described above, the stand identification number, the stand area, an estimate of the stand biomass (based on *in-situ* measurements) and the estimated standard error of the biomass estimates were included in the tables. Moreover, stand-wise averages of the local incidence angles calculated by DLR, which are delivered together with the geocoded SAR data, were included in the tables. The values for these incidence angles differ slightly from the incidence angles described above, since they only take slopes in the range direction into account.

Further the stand average values derived from the available Lidar data for the 100 highest trees were added as well as the inverted forest height values derived from L- and P-band using the Random-Volume-over-Ground model for the ascending and the descending as well as a combined value.





12.2 Description of Table

Table 12.1 gives a description of the data found in each column in the data tables in Section 12.3. In most column headers, the unit of the quantity in the corresponding column is given in square brackets. The angles found in Table 12.1 are defined in Figure 12.1 and Figure 12.2. Furthermore, the notation XY in the description table indicates the polarization combination of the backscatter, i.e. XY is replaced by HH, HV, VV or VH in all data tables.

Table 12-1. Description of column headers and data.

Column header	Description of data in column
Stand ID	Stand identification number
Stand area [ha]	Stand area
Biomass [tons/ha]	Estimated stand biomass
SE(Biomass) [%]	Standard error for biomass estimate
beta0XY [dB]	Stand average for β_{xy}^0
CV(beta0XY)	Coefficient of variation for β_{xy}^0 (has no units)
sigma0XY [dB]	Stand average for σ_{xy}^0
CV(sigma0XY)	Coefficient of variation for σ_{xy}^0 (has no units)
gamma0XY [dB]	Stand average for γ_{xy}^0
CV(gamma0XY)	Coefficient of variation for γ_{xy}^0 (has no units)
theta_i (Chalmers) [degrees]	Stand average of local incidence angle (θ_i)

std(theta_i) (Chalmers) [degrees]	Standard deviation of local incidence angle (θ_i)
theta_i (DLR) [degrees]	Stand average of local incidence angle provided by DLR
psi [degrees]	Stand average of projection angle (ψ)
u [degrees]	Stand average of ground slope angle (u)
v [degrees]	Stand average of aspect angle (v)
Lidar H100	Lidar forest height of the 100 highest trees (stand average)
L-band inversion heights [m]	L-band Pol-InSAR inverted forest height (stand average)
P-band inversion heights [m]	P-band Pol-InSAR inverted forest height (stand average)

12.3 Data Tables

(Further tables are available and will be delivered in the next version of the final report!)

12.4 References

[1] L.M.H. Ulander, "Radiometric slope correction of synthetic-aperture radar images," *IEEE Transactions on Geoscience and Remote Sensing*, vol. 34, no. 5, pp. 1115-1122, 1996.

13 APPENDIX: GROUND PHOTOS

Image Name	GPS Name	Position E	Position N	View to	Date	Description
IMG_XXXX.JPG		UTM z.34	UTM z.34			
1330	CR6A	444061	7123443	SE	09.Oct.08	CR6A
1331	CR6A	444061	7123443	SW	09.Oct.08	CR6A
1332	CR6A	444061	7123443	NW	09.Oct.08	CR6A
1333	CR6A	444061	7123443	NE	09.Oct.08	CR6A, CR6B
1334	CR6A	444061	7123443		09.Oct.08	CR6A peg
1335	CR6B	444067	7123452	SE	09.Oct.08	CR6B
1336	CR6B	444067	7123452	SW	09.Oct.08	CR6A, CR6B
1337	CR6B	444067	7123452	NW	09.Oct.08	CR6B
1338	CR6B	444067	7123452		09.Oct.08	CR6B detail
1339	CR6B	444067	7123452	NE	09.Oct.08	CR6B
1340	CR6B	444067	7123452		09.Oct.08	CR6B peg
1341				E	09.Oct.08	CR6A, CR6B from road
1342	CR5A	442760	7122287	SE	10.Oct.08	CR5A
1343	CR5A	442760	7122287	N	10.Oct.08	CR5A, CR5B
1344	CR5A	442760	7122287	NE	10.Oct.08	CR5A, CR5B
1345	CR5A	442760	7122287	SE	10.Oct.08	CR5A
1346	CR5A	442760	7122287		10.Oct.08	CR5A peg
1347	CR5B	442762	7122291	NE	10.Oct.08	CR5B
1348	CR5B	442762	7122291	SE	10.Oct.08	CR5B
1349	CR5B	442762	7122291	SW	10.Oct.08	CR5B
1350	CR5B	442762	7122291	W	10.Oct.08	CR5B
1351	CR5B	442762	7122291		10.Oct.08	CR5B peg
1352	CR7A	438678	7127703	SE	10.Oct.08	CR7A from road
1353	CR7A	438678	7127703	SW	10.Oct.08	CR7A, CR7B
1354	CR7A	438678	7127703	NW	10.Oct.08	CR7A
1355	CR7A	438678	7127703	NE	10.Oct.08	CR7A
1356	CR7A	438678	7127703		10.Oct.08	CR7A peg
1357	CR7B	438671	7127694	NW	10.Oct.08	CR7B
1358	CR7B	438671	7127694	NE	10.Oct.08	CR7A, CR7B
1359	CR7B	438671	7127694	SE	10.Oct.08	CR7B
1360	CR7B	438671	7127694	SW	10.Oct.08	CR7B
1361	CR7B	438671	7127694		10.Oct.08	CR7B peg
1363	SA01	440125	7124713	N	11.Oct.08	Vindelns Försöksparker
1364	SA01	440125	7124713	S	11.Oct.08	Vindelns Försöksparker
1365	SA03	439533	7124404	NE	11.Oct.08	Forest Border at testsite boundary
1366	SA04	439718	7124437	SE	11.Oct.08	Forest Border at testsite boundary
1367	SA05	440301	7123973	SE	11.Oct.08	Road to Åheden
1368	SA06	441119	7123441	NE	11.Oct.08	Crossroads near Åheden
1369	SA07	441998	7124065	NE	11.Oct.08	Grassland near Åheden
1370	SA08	442583	7124305	NE	11.Oct.08	Grassland near Kryckeltjärn

Image Name	GPS Name	Position E	Position N	View to	Date	Description
IMG_XXXX.JPG		UTM z.34	UTM z.34			
1371	SA08	442583	7124305	E	11.Oct.08	Grassland near Kryckeltjärn
1372	SA10	443199	7124570	SE	11.Oct.08	Kryckeltjärn
1373					11.Oct.08	Waiting for Elks
1374	SA12	444172	7124459	N	11.Oct.08	Kryckeltjärn
1375	SA12	444172	7124459	NE	11.Oct.08	Kryckeltjärn
1376	SA12	444172	7124459	S	11.Oct.08	Kryckeltjärn
1377	SA15	443754	7124697	W	11.Oct.08	Road near Kryckeltjärn
1378	SA15	443754	7124697	E	11.Oct.08	Road near Kryckeltjärn
1379	SA17	438332	7125738	SE	11.Oct.08	Panorama Stor-Koverberget
1380	SA17	438332	7125738	E	11.Oct.08	Panorama Stor-Koverberget
1381	SA17	438332	7125738	NE	11.Oct.08	Panorama Stor-Koverberget
1382	SA17	438332	7125738	N	11.Oct.08	Panorama Stor-Koverberget
1383	SA17	438332	7125738	NW	11.Oct.08	Panorama Stor-Koverberget
1384	SA17	438332	7125738	W	11.Oct.08	Panorama Stor-Koverberget
1385	SA22	438153	7126320	N	11.Oct.08	Turning option Stor-Koverberget
1386	SA23	438157	7126593	NW	11.Oct.08	Gravel pile Stor-Koverberget
1387	SA24	438883	7126507	NW	11.Oct.08	End of road Fäbodliden
1388	SA25	438186	7126805	W	11.Oct.08	Fäbodliden
1389	SA26	438368	7128675	SE	11.Oct.08	Near Yttersjön lake
1390	SA27	438275	7128364	S	11.Oct.08	Yttersjön lake
1391	SA27	438275	7128364	N	11.Oct.08	Yttersjön lake
1392	SA27	438275	7128364	N	11.Oct.08	Yttersjön lake, fireplace
1394				SW	11.Oct.08	Toilet hut, about 50m S fireplace
1395	SA31	438802	7128187	N	11.Oct.08	Crossroads Stormyrberget
1396	SA31	438802	7128187	S	11.Oct.08	Crossroads Stormyrberget
1397	SA33	438993	7128206	E	11.Oct.08	Stormyrberget
1398	SA34	439226	7128053	N	11.Oct.08	Stormyrberget
1399	SA34	439226	7128053	S	11.Oct.08	Stormyrberget
1401	SA36	439687	7128035	NE	11.Oct.08	Stormyrberget, end of road
1402	SA36	439687	7128035	SE	11.Oct.08	Stormyrberget, end of road
1403	SA36	439687	7128035	SW	11.Oct.08	Stormyrberget, end of road
1404	SA39	438841	7127838	E	11.Oct.08	Stormyrberget, crossroad
1405	SA39	438841	7127838	S	11.Oct.08	Stormyrberget, crossroad
1406	SA39	438841	7127838	W	11.Oct.08	Stormyrberget, crossroad
1407	SA42	438991	7127570	N	11.Oct.08	Stormyrberget, Fäboliden, near end of road
1408	SA42	438991	7127570	NE	11.Oct.08	Stormyrberget, Fäboliden, near end of road
1409	SA42	438991	7127570	E	11.Oct.08	Stormyrberget, Fäboliden, near end of road
1410	SA42	438991	7127570	S	11.Oct.08	Stormyrberget, Fäboliden, near end of road
1411	SA42	438991	7127570	W	11.Oct.08	Stormyrberget, Fäboliden, near end of road
1412	SA47	437691	7127713	E	11.Oct.08	Between Långslånbacken and Yttersjön

Image Name	GPS Name	Position E	Position N	View to	Date	Description
IMG_XXXX.JPG		UTM z.34	UTM z.34			
1413	SA47	437691	7127713	S	11.Oct.08	Between Långslånbacken and Yttersjön
1414	SA49	437804	7127567	N	11.Oct.08	Between Långslånbacken and Yttersjön
1415	SA49	437804	7127567	NE	11.Oct.08	Between Långslånbacken and Yttersjön
1416	SA49	437804	7127567	E	11.Oct.08	Between Långslånbacken and Yttersjön
1417	SA49	437804	7127567	SE	11.Oct.08	Between Långslånbacken and Yttersjön
1418	SA49	437804	7127567	S	11.Oct.08	Between Långslånbacken and Yttersjön
1419	SA49	437804	7127567	W	11.Oct.08	Between Långslånbacken and Yttersjön
1421	SA55	440113	7128400	SE	11.Oct.08	
1422	SA55	440113	7128400	SW	11.Oct.08	
1423	SU01	440703	7123459	NW	12.Oct.08	
1424	SU01	440703	7123459	NE	12.Oct.08	
1425	SU03	440832	7123470	N	12.Oct.08	
1426	SU03	440832	7123470	E	12.Oct.08	
1427	SU05	440884	7123439	NW	12.Oct.08	
1428	SU05	440884	7123439	E	12.Oct.08	
1429	SU05	440884	7123439	S	12.Oct.08	
1430	SU08	440937	7123429	NE	12.Oct.08	
1431	SU09	441062	7123334	SE	12.Oct.08	
1432	SU10	441773	7123110	SW	12.Oct.08	
1433	SU10	441773	7123110	SSW	12.Oct.08	
1434	SU10	441773	7123110	S	12.Oct.08	
1435	SU10	441773	7123110	SSE	12.Oct.08	
1436	SU10	441773	7123110	SE	12.Oct.08	
1437	SU15	441988	7123115	NW	12.Oct.08	scarp of Långbäcken
1438	SU15	441988	7123115	NNW	12.Oct.08	scarp of Långbäcken
1439	SU15	441988	7123115	N	12.Oct.08	scarp of Långbäcken
1440	SU15	441988	7123115	NE	12.Oct.08	scarp of Långbäcken
1441	SU19	442022	7122962	E	12.Oct.08	
1442	SU19	442022	7122962	W	12.Oct.08	
1443	SU21	441332	7123157	E	12.Oct.08	
1444	SU22	441622	7122903	N	12.Oct.08	Fenced forest test field
1445	SU22	441622	7122903	E	12.Oct.08	
1446	SU24	441681	7122823	N	12.Oct.08	dirt pile
1447	SU24	441681	7122823	NE	12.Oct.08	
1448	SU24	441681	7122823	SE	12.Oct.08	
1449	SU27	441763	7122458		12.Oct.08	old wreck of bus
1450	SU27	441763	7122458		12.Oct.08	old wreck of bus
1451	SU27	441763	7122458		12.Oct.08	old wreck of bus
1452	SU30	441727	7122392	W	12.Oct.08	scarp of Åhedbäcken
1453	SU30	441727	7122392	SW	12.Oct.08	scarp of Åhedbäcken

Image Name	GPS Name	Position E	Position N	View to	Date	Description
IMG_XXXX.JPG		UTM z.34	UTM z.34			
1454	SU30	441727	7122392	S	12.Oct.08	scarp of Åhedbäcken
1455	SU30	441727	7122392	SE	12.Oct.08	scarp of Åhedbäcken
1456	SU30	441727	7122392	E	12.Oct.08	scarp of Åhedbäcken
1457	SU35	441845	7122752	W	12.Oct.08	Fenced forest test field
1458	SU35	441845	7122752	N	12.Oct.08	Fenced forest test field
1459	SU35	441845	7122752	E	12.Oct.08	Fenced forest test field
1460	SU38	441987	7122678	E	12.Oct.08	
1461	SU39	442519	7122534	N	12.Oct.08	
1463	SU40	442874	7122054	SW	12.Oct.08	
1464	SU40	442874	7122054	NW	12.Oct.08	
1465	SU42	443324	7121712	SE	12.Oct.08	
1466	SU42	443324	7121712	NE	12.Oct.08	
1467	SU44	443456	7121655	SE	12.Oct.08	ridge
1468	SU44	443456	7121655	NW	12.Oct.08	ridge
1469	SU46	443734	7121569	N	12.Oct.08	bridge
1470	SU46	443734	7121569	W	12.Oct.08	bridge
1471	SU46	443734	7121569	E	12.Oct.08	bridge, corner reflector 2
1472	CR02	443772	7121604		12.Oct.08	
1473	SU49	443797	7121692	E	12.Oct.08	path crossing
1474	SU49	443797	7121692	N	12.Oct.08	path crossing
1475	SU49	443797	7121692	W	12.Oct.08	path crossing
1476					12.Oct.08	elk was there...
1477	SU52	443829	7121612	SE	12.Oct.08	land slide area
1478	SU52	443829	7121612	S	12.Oct.08	land slide area
1479	SU52	443829	7121612	SW	12.Oct.08	land slide area
1480	SU52	443829	7121612	W	12.Oct.08	land slide area
1481	SU52	443829	7121612	NW	12.Oct.08	land slide area
1482	SU52	443829	7121612	NE	12.Oct.08	land slide area
1483	SU58	443905	7121471	W	12.Oct.08	land slide area
1484	SU58	443905	7121471	NW	12.Oct.08	land slide area
1485	SU58	443905	7121471	N	12.Oct.08	land slide area
1486	SU61	443785	7121526	E	12.Oct.08	land slide area
1487	CR02	443772	7121604		12.Oct.08	corner reflector details CR02
1488	CR02	443772	7121604		12.Oct.08	corner reflector details CR02
1489	CR02	443772	7121604		12.Oct.08	corner reflector details CR02
1490	CR02	443772	7121604		12.Oct.08	corner reflector details CR02
1491	CR02	443772	7121604		12.Oct.08	corner reflector details CR02
1492	CR02	443772	7121604		12.Oct.08	corner reflector details CR02
1493	SU62	441468	7122179	NE	12.Oct.08	View from Mulkälen to Åhedbäcken
1494	SU62	441468	7122179	E	12.Oct.08	View from Mulkälen to Åhedbäcken

Image Name	GPS Name	Position E	Position N	View to	Date	Description
IMG_XXXX.JPG		UTM z.34	UTM z.34			
1495	SU64	443621	7120473	NW	12. Oct.08	Near Hägglund
1496	SU64	443621	7120473	N	12. Oct.08	Near Hägglund
1497	SU64	443621	7120473	NE	12. Oct.08	Near Hägglund
1498	SU64	443621	7120473	E	12. Oct.08	Near Hägglund
1499	SU64	443621	7120473	SE	12. Oct.08	Near Hägglund
1500	SU69	444641	7119996	NW	12. Oct.08	View from Lillkludden
1501	SU69	444641	7119996	N	12. Oct.08	View from Lillkludden
1502	SU69	444641	7119996	NE	12. Oct.08	View from Lillkludden
1503	SU72	443975	7120675	S	12. Oct.08	end of road near Hägglund
1504	SU72	443975	7120675	E	12. Oct.08	end of road near Hägglund
1505	SU74	445254	7120467	SW	12. Oct.08	road crossing south of Storkludden
1506	SU74	445254	7120467	N	12. Oct.08	road crossing south of Storkludden
1507	SU74	445254	7120467	S	12. Oct.08	road crossing south of Storkludden
1508	SU77	445451	7121563	N	12. Oct.08	end of road at Kluddtjärnen
1509	SU77	445451	7121563	NE	12. Oct.08	end of road at Kluddtjärnen
1510	SU79	445605	7121413	NE	12. Oct.08	Kluddtjärnen
1511	SU80	445837	7121346	NE	12. Oct.08	Birches near Kluddtjärnen
1512	SU81	445907	7121286	NE	12. Oct.08	Pines near Kluddtjärnen
1513	SU82	445415	7120568	NW	12. Oct.08	Storkludden, jung trees
1514	SU82	445415	7120568	N	12. Oct.08	Storkludden, jung trees + 3 old trees
1515	SU84	445061	7120632	SE	12. Oct.08	Storkludden hillside
1516	SU84	445061	7120632	E	12. Oct.08	Storkludden hillside
1517	SU84	445061	7120632	NE	12. Oct.08	Storkludden hillside
1518	SU84	445061	7120632	N	12. Oct.08	Storkludden hillside
1519	SU84	445061	7120632	NW	12. Oct.08	Storkludden hillside
1520	SU84	445061	7120632	W	12. Oct.08	Storkludden hillside
1521	SU90	444726	7120796	S	12. Oct.08	Wood storage place
1522				NE	12. Oct.08	Large pine forest
1523	SU92	444676	7120943	NE	12. Oct.08	different forest types
1524	SU93	444761	7121282	W	12. Oct.08	land slide
1525	SU93	444761	7121282	W	12. Oct.08	land slide
1526				N	12. Oct.08	birch forest
1527	SU96	444723	7121619	W	12. Oct.08	crossroad near CR01
1528	SU96	444723	7121619	N	12. Oct.08	crossroad near CR01
1529	SU96	444723	7121619	SE	12. Oct.08	crossroad near CR01
1530	SU99	444506	7122337	SE	12. Oct.08	end of road
1531	SU100	444529	7121499	N	12. Oct.08	young coniferous forest
1532	CR01	444417	7121818	NE	12. Oct.08	corner reflector CR01
1533	CR01	444417	7121818	E	12. Oct.08	corner reflector CR01
1534	CR01	444417	7121818	S	12. Oct.08	corner reflector CR01

Image Name	GPS Name	Position E	Position N	View to	Date	Description
IMG_XXXX.JPG		UTM z.34	UTM z.34			
1535	CR07	438671	7127694	W	13.Oct.08	CR7B with cut young trees
1536	CR07	438678	7127703	NW	13.Oct.08	CR7A with cut young trees
1537	Bus13Oct	443973	7123367	SW	13.Oct.08	Transporter in forest, no SAR data recorded!!!
1538	Bus13Oct	443973	7123367	N	13.Oct.08	Transporter in forest, no SAR data recorded!!!
1539	Bus13Oct	443973	7123367	NE	13.Oct.08	Transporter in forest, no SAR data recorded!!!
1540	Mo01	443953	7123127	W	13.Oct.08	grassland
1541	Mo01	443953	7123127	N	13.Oct.08	birch alley
1542	Mo01	443953	7123127	E	13.Oct.08	grassland, Brandbärliden
1543	Mo01	443953	7123127	SE	13.Oct.08	grassland, Brandbärliden
1544	Mo05	443898	7123015	NE	13.Oct.08	road down to Krycklan river
1545	Mo05	443898	7123015	S	13.Oct.08	road down to Krycklan river
1546	Mo07	443872	7122938	NW	13.Oct.08	Krycklan river
1547	Mo08	443992	7122777	NW	13.Oct.08	
1548	Mo08	443992	7122777	SE	13.Oct.08	
1549	Mo10	444010	7122755	S	13.Oct.08	dirt pile, beton tubes
1550	Mo10	444010	7122755	NW	13.Oct.08	bridge
1551	Mo12	444033	7122722		13.Oct.08	Krycklan river
1552	Mo12	444033	7122722		13.Oct.08	Krycklan river
1553	Mo12	444033	7122722		13.Oct.08	dense birches
1554	Mo15	444047	7122661	SE	13.Oct.08	
1555	Mo16	443895	7122748	NE	13.Oct.08	
1556	Mo17	443805	7122709	SE	13.Oct.08	Free area with CR03 and seed trees
1557	Mo17	443805	7122709	E	13.Oct.08	Free area with CR03 and seed trees
1558	Mo17	443805	7122709	NE	13.Oct.08	Free area with CR03 and seed trees
1559	Mo17	443805	7122709	N	13.Oct.08	Free area with CR03 and seed trees
1560	Mo17	443805	7122709	NW	13.Oct.08	Free area with CR03 and seed trees
1561	Mo17	443805	7122709	W	13.Oct.08	Free area with CR03 and seed trees
1564	CR03	443682	7122736		13.Oct.08	CR03 to near at seed trees
1565	CR03	443682	7122736		13.Oct.08	CR03 to near at seed trees
1566	Mo23	443577	7122804	W	13.Oct.08	end of road
1567	Mo24	443412	7123054	SW	13.Oct.08	
1568	Mo24	443412	7123054	NW	13.Oct.08	
1569	Mo24	443412	7123054	NE	13.Oct.08	
1570	Mo24	443412	7123054	SE	13.Oct.08	
1571	Mo28	443794	7123702	W	13.Oct.08	slope to Krycklan river
1572	Mo28	443794	7123702	NW	13.Oct.08	grassland, slope to Krycklan river
1573	Tu01	441525	7123768	W	14.Oct.08	Åhedan
1574	Tu01	441525	7123768	SW	14.Oct.08	Åhedan
1575	Tu01	441525	7123768	S	14.Oct.08	Åhedan
1576	Tu04	441580	7123772	S	14.Oct.08	drainage

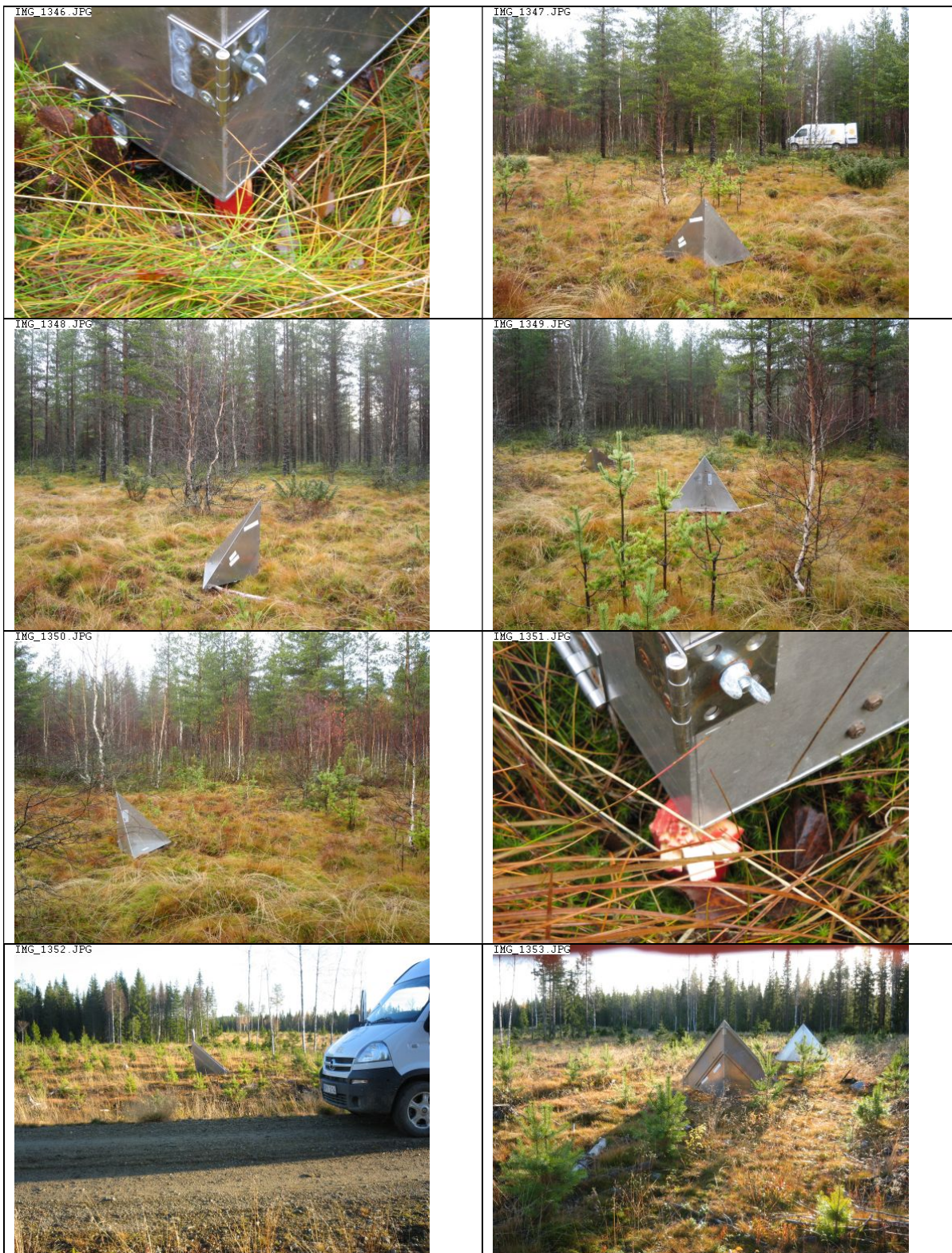
Image Name	GPS Name	Position E	Position N	View to	Date	Description
IMG_XXXX.JPG		UTM z.34	UTM z.34			
1577	Tu05	441625	7123782	E	14. Oct.08	power line
1578	Tu06	441729	7123762	S	14. Oct.08	liquid manure at grassland
1579	Tu06	441729	7123762	W	14. Oct.08	grassland, Åhedan
1580	Tu08	441867	7123639	SW	14. Oct.08	shelter in forest
1581	Tu09	442067	7123481	S	14. Oct.08	
1582	Tu10	442205	7123319	NW	14. Oct.08	
1583	Tu11	442347	7123198	N	14. Oct.08	
1584	Tu12	442822	7123091	W	14. Oct.08	power line in forest
1585	Tu13	442950	7122991	N	14. Oct.08	drainage in forest
1586	Tu13	442950	7122991	S	14. Oct.08	
1587	Tu15	443043	7122915	W	14. Oct.08	
1588	Tu16	443135	7122889	E	14. Oct.08	end of road near CR04
1589	Bus14Oct	441441	7123129	SE	14. Oct.08	Transporter in forest, direction 130°
1590	Bus14Oct	441441	7123129	N	14. Oct.08	Transporter in forest, direction 130°
1591	CR03	443682	7122736		14. Oct.08	Cutting trees at CR03
1592	CR03	443682	7122736		14. Oct.08	Cutting trees at CR03
1593	CR03	443682	7122736		14. Oct.08	Cutting trees at CR03
1594	Tu17	440198	7124836	S	14. Oct.08	Svartberget Försöksparker
1595	Tu18	440289	7125139	W	14. Oct.08	beton tubes
1596	Tu19	440402	7125231	W	14. Oct.08	metal shelter
1597	Tu19	440402	7125231	S	14. Oct.08	metal site caravan
1598	Tu21	440563	7125036	SE	14. Oct.08	
1599	Tu22	440710	7124771	NE	14. Oct.08	drainage in forest
1600	Tu23	440997	7124386	SW	14. Oct.08	artificial trees?
1601	Tu24	441081	7124435		14. Oct.08	big rock
1602	Tu24	441081	7124435		14. Oct.08	big rock
1603	Tu26	441403	7124035		14. Oct.08	water level measurement
1604	Tu27	441482	7123950	S	14. Oct.08	metal tubes
1605	Tu27	441482	7123950	E	14. Oct.08	sand/gravel piles
1606	Tu27	441482	7123950	NE	14. Oct.08	sand/gravel piles
1607	Tu30	441517	7123884	SE	14. Oct.08	boom gate
1608	Tu31	442883	7122310	NW	14. Oct.08	scarp of Långbäcken
1609	Tu32	442895	7122326		14. Oct.08	river Långbäcken
1610	Tu32	442895	7122326		14. Oct.08	river Långbäcken
1611	Tu32	442895	7122326		14. Oct.08	river Långbäcken
1612	Tu35	442928	7122366	SE	14. Oct.08	scarp of Långbäcken
1613	Tu35	442928	7122366	E	14. Oct.08	scarp of Långbäcken
1614	Tu35	442928	7122366	NE	14. Oct.08	scarp of Långbäcken
1615	Tu35	442928	7122366	N	14. Oct.08	scarp of Långbäcken
1616	Tu35	442928	7122366	NW	14. Oct.08	scarp of Långbäcken

Image Name	GPS Name	Position E	Position N	View to	Date	Description
IMG_XXXX.JPG		UTM z.34	UTM z.34			
1617	Tu40	442930	7122415		14.Oct.08	tree stumps
1618	Tu40	442930	7122415		14.Oct.08	tree stumps
1619					14.Oct.08	anthill
1622					15.Oct.08	tree stump
1623					15.Oct.08	grassland between Kryckeltjäm and CR6
1624	We01	441563	7124202	W	15.Oct.08	uncongested forest
1625	We01	441563	7124202	NW	15.Oct.08	uncongested forest
1626	We01	441563	7124202	NE	15.Oct.08	dense forest
1627	We01	441563	7124202	E	15.Oct.08	dense forest
1628	We05	441669	7124586	SE	15.Oct.08	Tall trees, few underwood
1629	We05	441669	7124586	NW	15.Oct.08	Tall trees, few underwood
1630	We07	441589	7124922	S	15.Oct.08	Tall trees, few underwood
1631	We07	441589	7124922	W	15.Oct.08	dense young forest
1632	We07	441589	7124922	N	15.Oct.08	dense young forest
1633	We07	441589	7124922	E	15.Oct.08	tall trees
1634	We11	441820	7125138	E	15.Oct.08	red rocks
1635	We11	441820	7125138	N	15.Oct.08	fenced young forest
1636	We13	441970	7125129	W	15.Oct.08	fenced young forest
1637	We13	441970	7125129	NW	15.Oct.08	fenced young forest
1638	We15	442066	7125197	W	15.Oct.08	end of fenced area
1639	We15	442066	7125197	NE	15.Oct.08	dense old forest
1641	We17	442234	7125260	N	15.Oct.08	measurements, aluminium
1642	We18	442415	7125378	W	15.Oct.08	old forest
1643	We18	442415	7125378	N	15.Oct.08	fenced young forest
1644	We18	442415	7125378	E	15.Oct.08	old forest
1645	We21	441712	7125499	W	15.Oct.08	young coniferous forest
1646	We21	441712	7125499	N	15.Oct.08	old forest
1647	We21	441712	7125499	S	15.Oct.08	dense old forest
1648	We24	441626	7125734	N	15.Oct.08	several fenced forest areas
1649	We25	441394	7126219	SE	15.Oct.08	road, wide ditch
1650	We26	441389	7126404	SE	15.Oct.08	
1651	We26	441389	7126404	E	15.Oct.08	
1652	We26	441389	7126404	NE	15.Oct.08	fence
1653	We26	441389	7126404	N	15.Oct.08	road, ditch, fence
1654	We26	441389	7126404	W	15.Oct.08	
1655	We31	441426	7126522	N	15.Oct.08	end of road, fence
1656	We32	441219	7126158	SE	15.Oct.08	fenced open area
1657	We33	441135	7126307	W	15.Oct.08	drainage
1658	We33	441135	7126307	N	15.Oct.08	road
1659	We35	441017	7126736	S	15.Oct.08	old forest, road

Image Name	GPS Name	Position E	Position N	View to	Date	Description
IMG_xxxx.JPG		UTM z.34	UTM z.34			
1660	We35	441017	7126736	SE	15.Oct.08	old forest
1661	We37	440930	7125939	E	15.Oct.08	Toilet hut with metal roof
1662	We37	440930	7125939	S	15.Oct.08	measurements, aluminium
1663	We37	440930	7125939	W	15.Oct.08	road
1664	We37	440930	7125939		15.Oct.08	measurements, aluminium
1665	Truck	440660	7125710		15.Oct.08	Truck in forest
1666	Truck	440660	7125710		15.Oct.08	Truck in forest
1667	We40	440210	7124775	S	15.Oct.08	Svartberget Försöksparker
1668	We40	440210	7124775	E	15.Oct.08	Svartberget Försöksparker
1669	We40	440210	7124775	N	15.Oct.08	Svartberget Försöksparker
1670	We40	440210	7124775	W	15.Oct.08	Svartberget Försöksparker
1671	We44	440097	7124108	S	15.Oct.08	Hut, metal roof
1672	Bus15Oct	441441	7123129		15.Oct.08	Transporter in forest
1673	Bus15Oct	441441	7123129		15.Oct.08	Transporter in forest
1674	Bus15Oct	441441	7123129		15.Oct.08	Transporter in forest
1675	CR04	443275	7122891		16.Oct.08	dismounting CR04
1676	CR04	443275	7122891		16.Oct.08	dismounting CR04
1677	CR04	443275	7122891		16.Oct.08	dismounting CR04
1678	CR04	443275	7122891		16.Oct.08	dismounting CR04
1679					17.Oct.08	bear track near crossroad at CR04
1680					17.Oct.08	bear track near crossroad at CR04
1681	CR01	444417	7121818		17.Oct.08	dismounting CR01
1682		443577	7122804		17.Oct.08	dismounting CR03, truck at end of road
1683		443577	7122804		17.Oct.08	dismounting CR03, truck at end of road
1684		443577	7122804		17.Oct.08	dismounting CR03, truck at end of road
1685	CR03	443682	7122736		17.Oct.08	dismounting CR03
1686	Fr01	443251	7123404		17.Oct.08	digger, about 200m SE of viewpoint
1687	Fr01	443251	7123404		17.Oct.08	junkyard near Nymyrkälen
1688	Fr01	443251	7123404		17.Oct.08	junkyard near Nymyrkälen
1689	Fr01	443251	7123404		17.Oct.08	junkyard near Nymyrkälen
1690	Fr01	443251	7123404		17.Oct.08	junkyard near Nymyrkälen
1691	Fr02	443120	7123595		17.Oct.08	farmer houses at Nymyrkälen
1692		443734	7121569		17.Oct.08	dismounting CR02
1693		443734	7121569		17.Oct.08	dismounting CR02
1694		443734	7121569		17.Oct.08	dismounting CR02
1695		443734	7121569		17.Oct.08	dismounting CR02
1696		443734	7121569		17.Oct.08	dismounting CR02
1697		443734	7121569		17.Oct.08	dismounting CR02
1698		443734	7121569		17.Oct.08	dismounting CR02
1699					17.Oct.08	last sunlight at end of flight campaign...













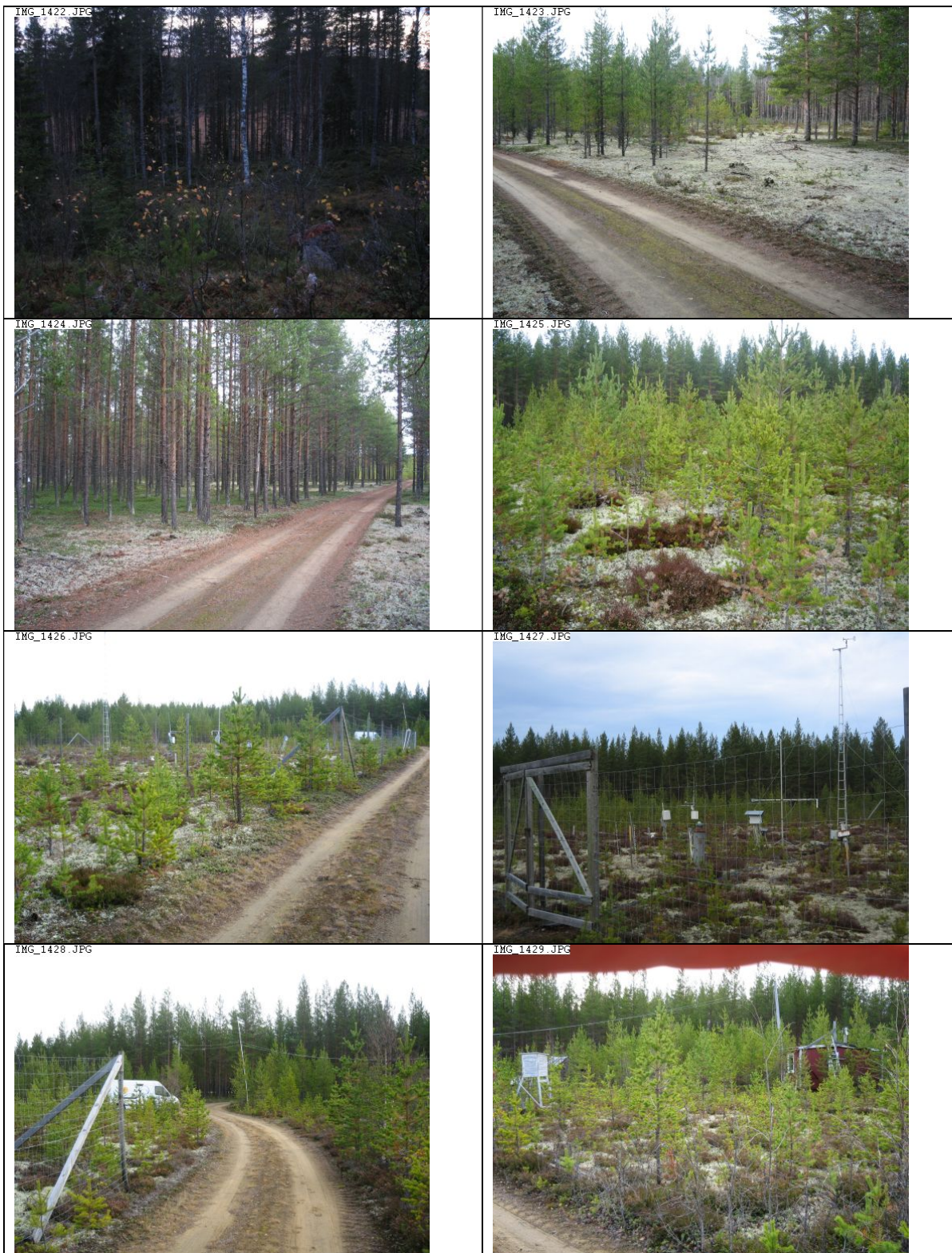














IMG_1438.JPG



Img_1439.jpg



IMG_1440.JPG



Img_1441.jpg



Img_1442.jpg



IMG_1443.JPG





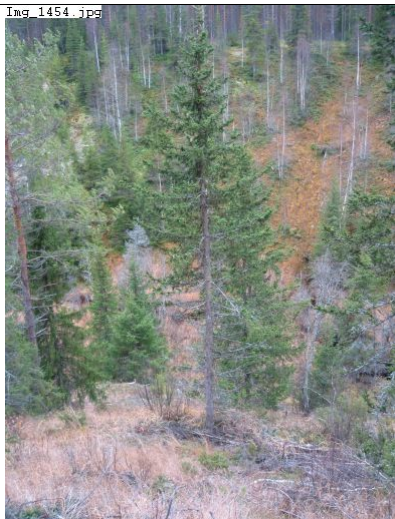
IMG_1452.JPG



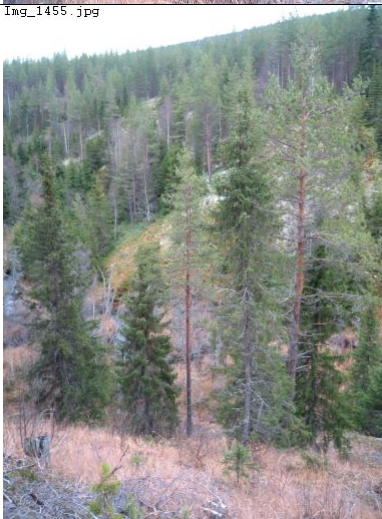
Img_1453.jpg



Img_1454.jpg



Img_1455.jpg



IMG_1456.JPG

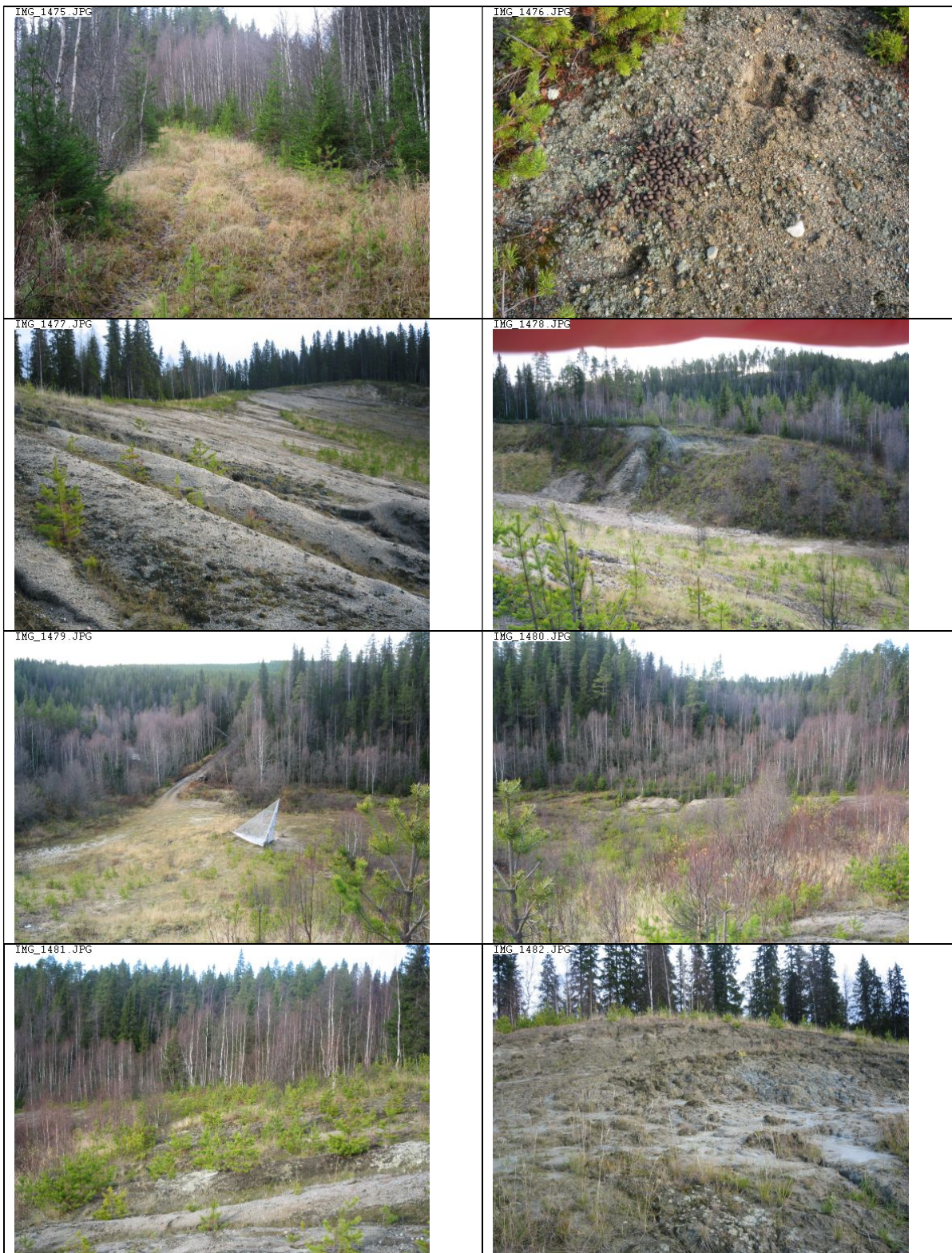


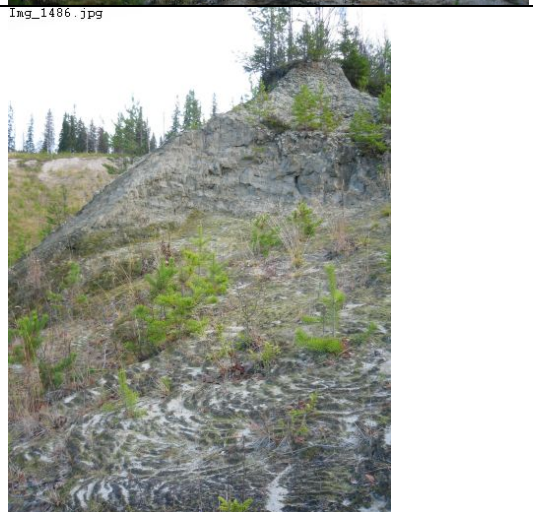
IMG_1457.JPG

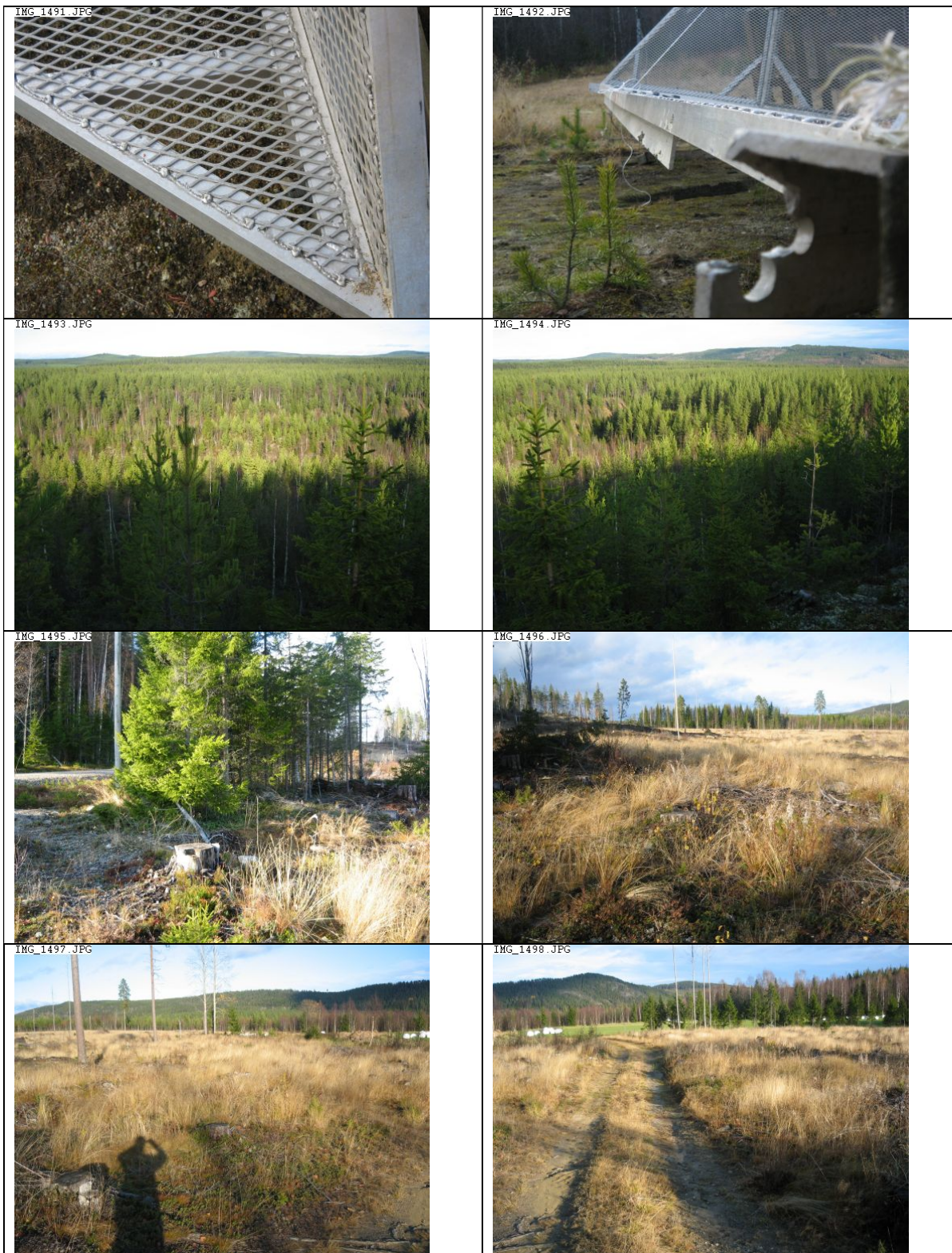


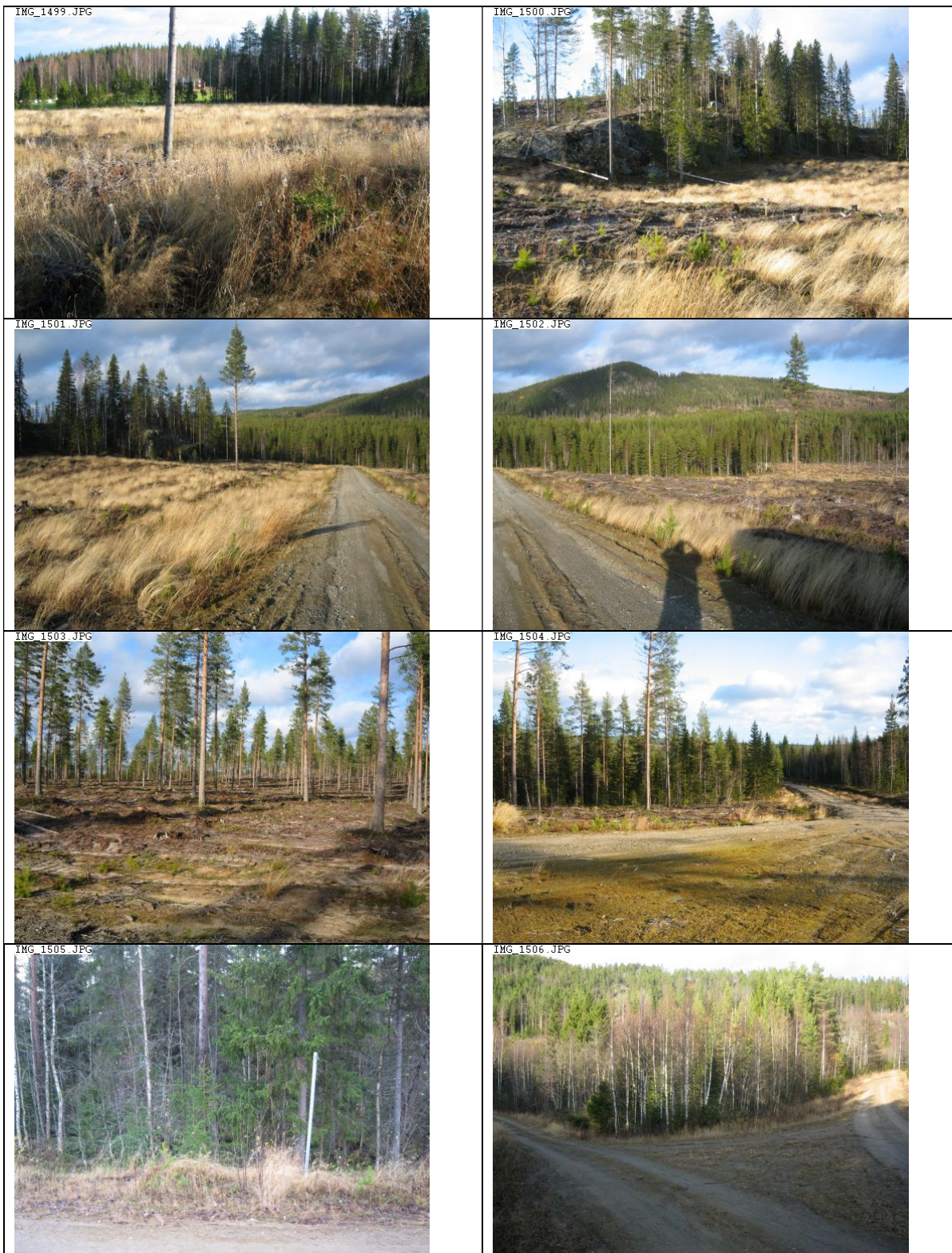


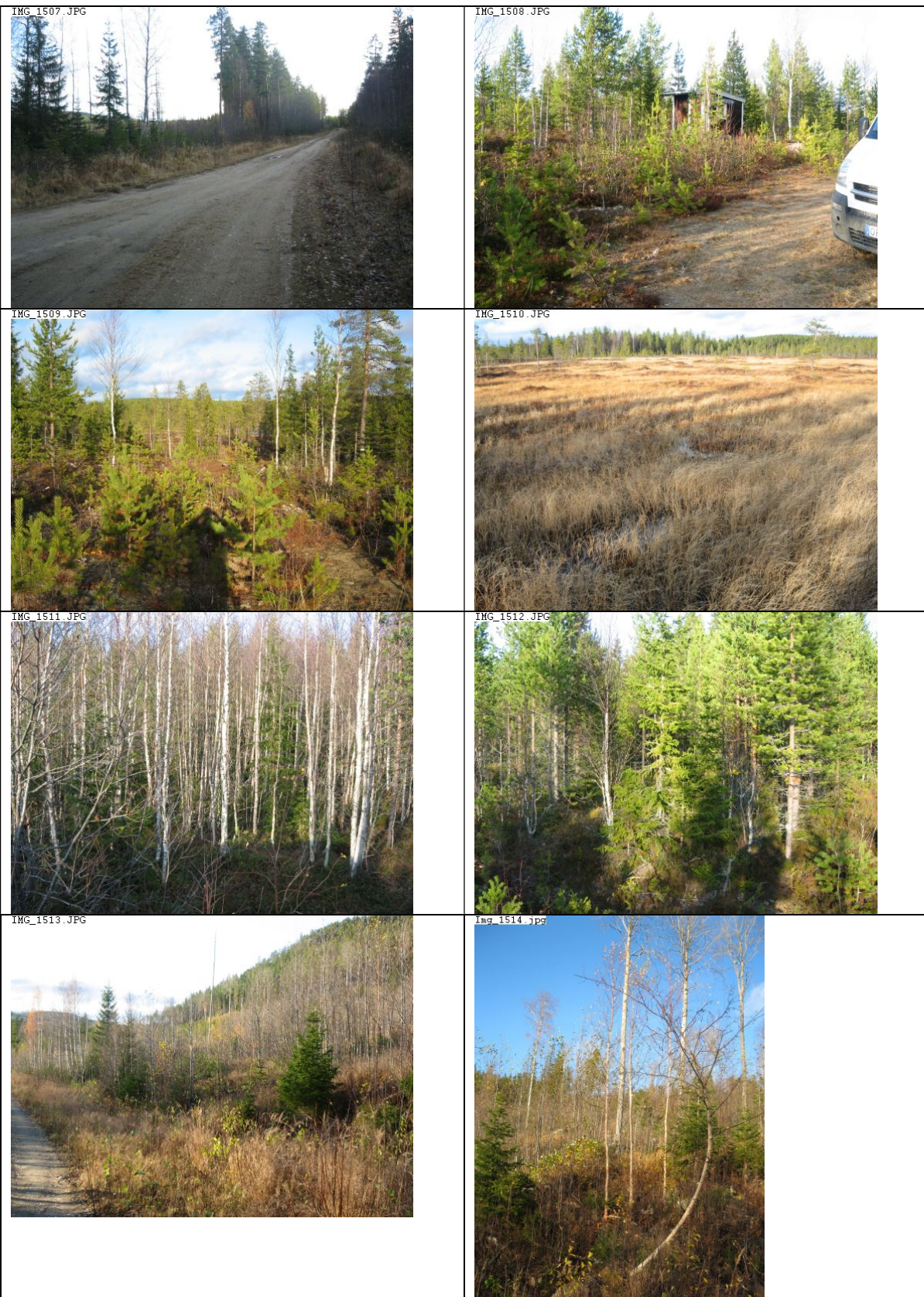




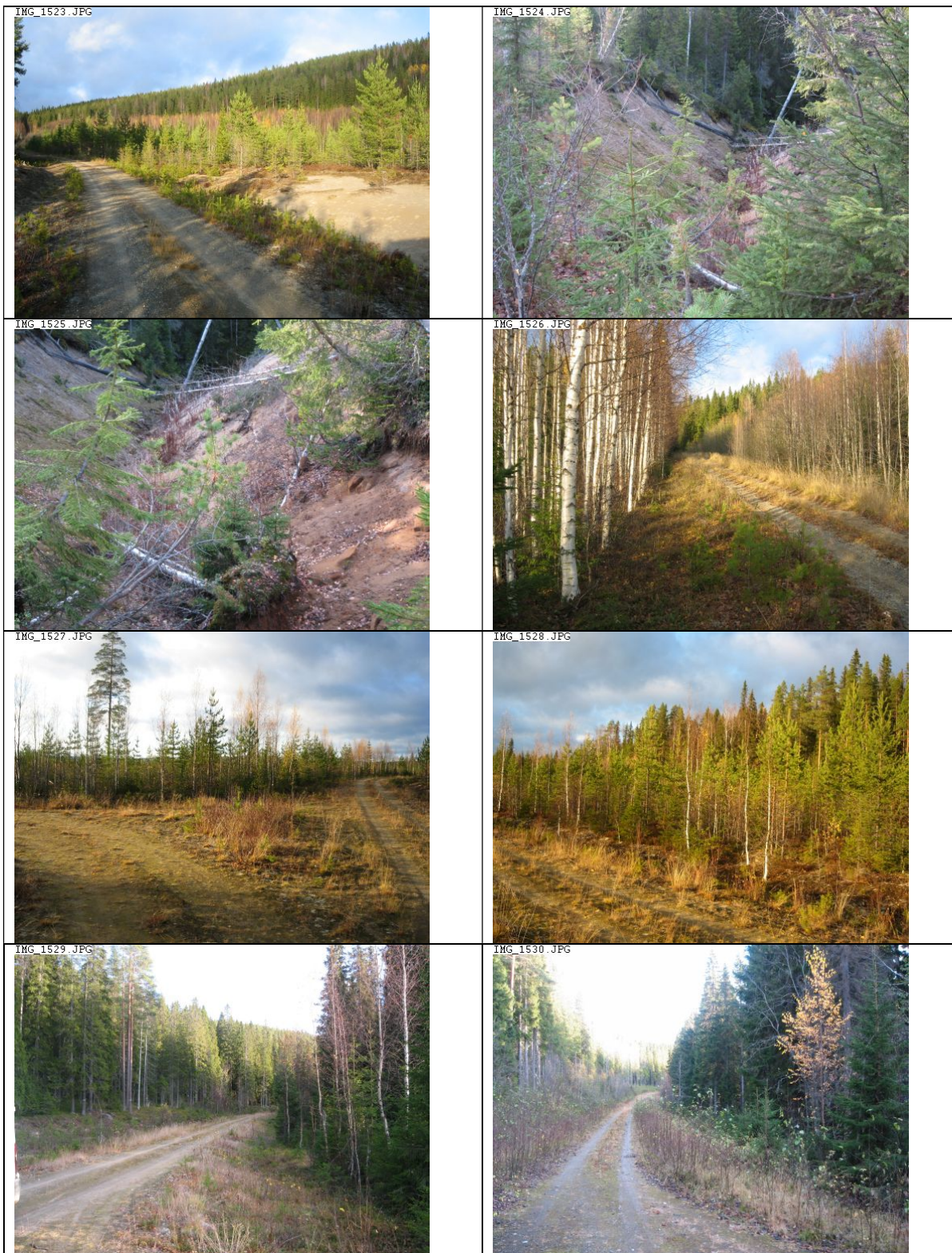


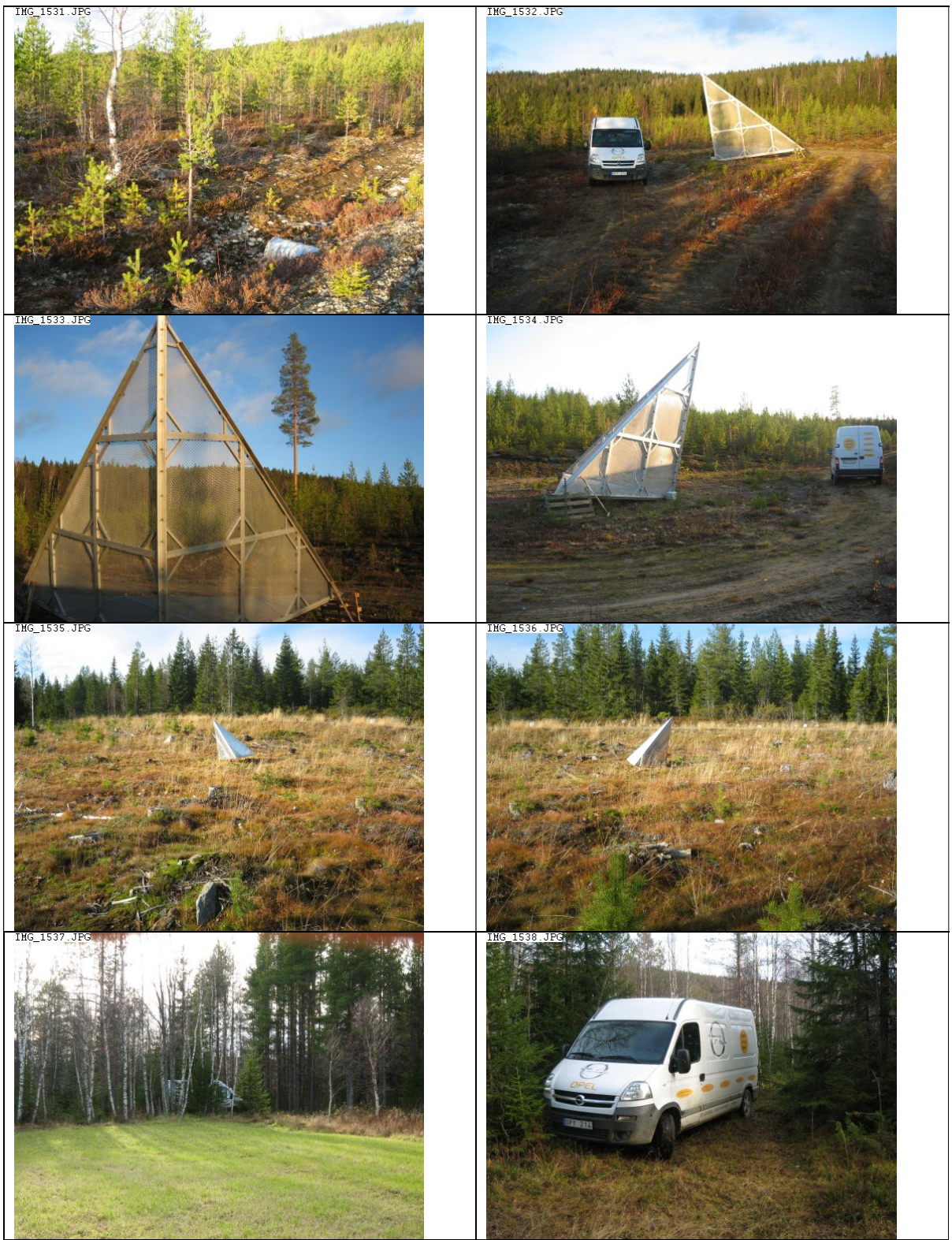


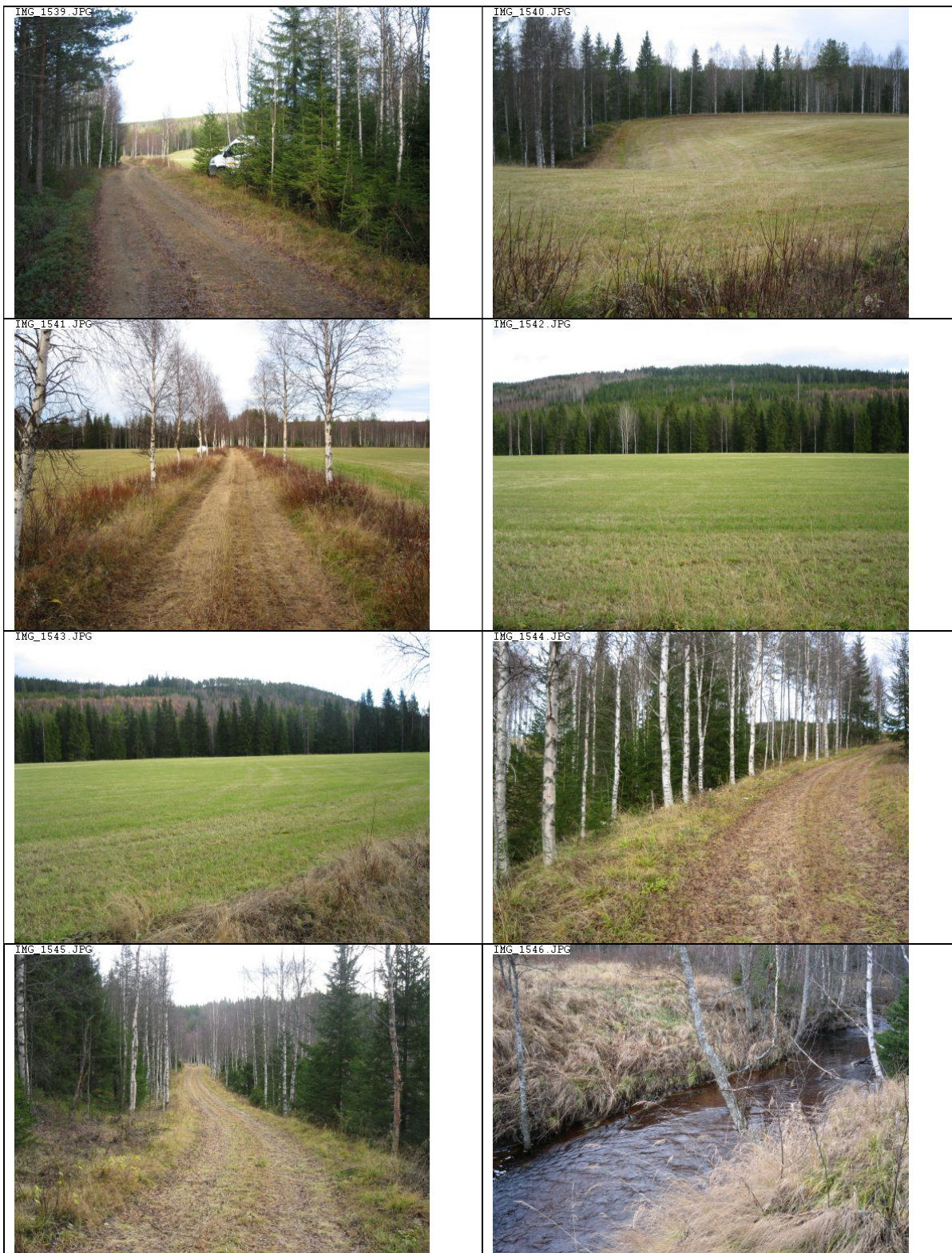




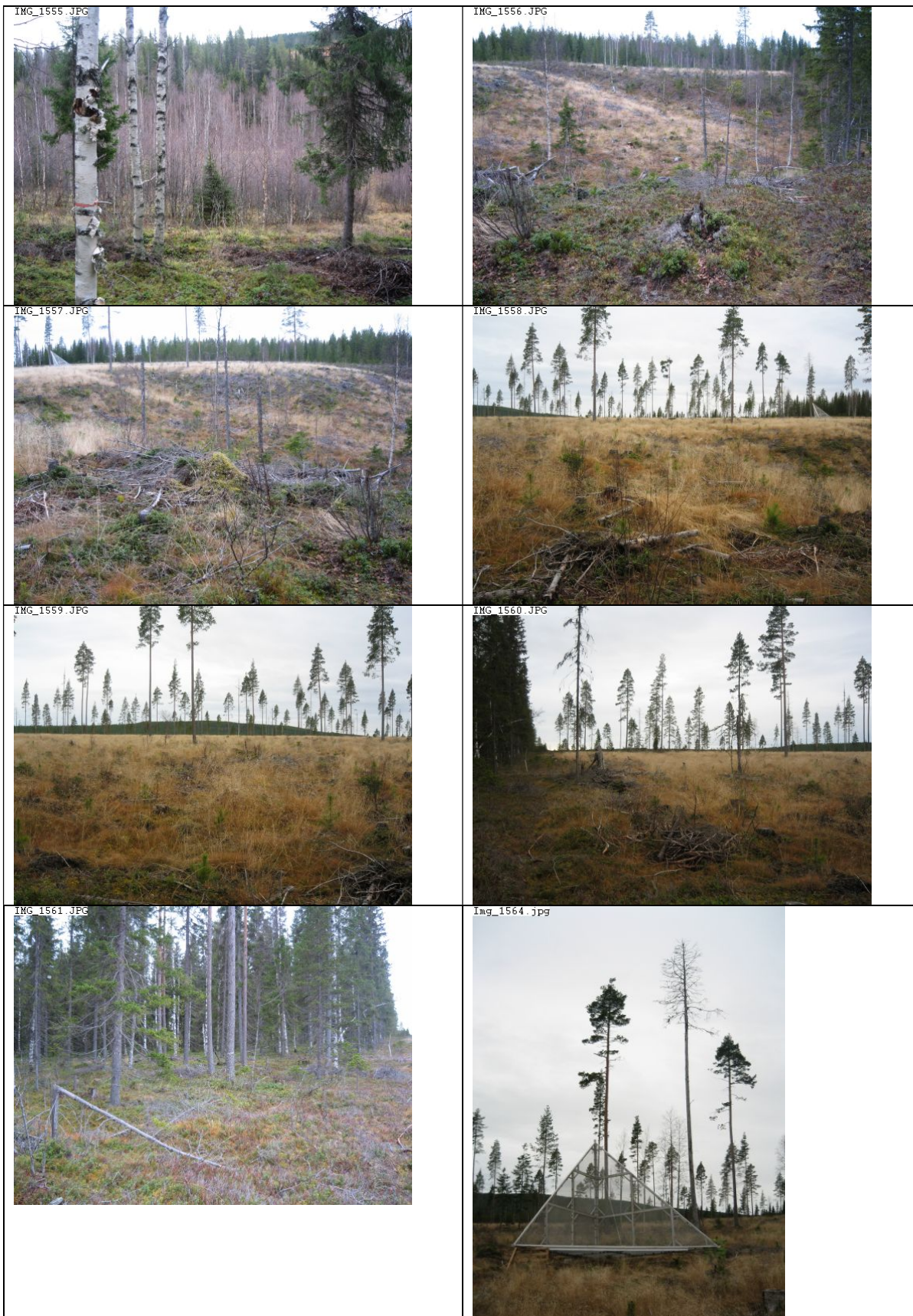














IMG_1573.JPG



IMG_1574.JPG



IMG_1575.JPG



img_1576.jpg



img_1577.jpg



IMG_1578.JPG





IMG_1587.JPG



IMG_1588.JPG



IMG_1589.JPG



IMG_1590.JPG



IMG_1591.JPG



IMG_1592.JPG



IMG_1593.JPG



IMG_1594.JPG



IMG_1595.JPG



IMG_1596.JPG



IMG_1597.JPG



IMG_1598.JPG



img_1599.jpg



IMG_1600.JPG





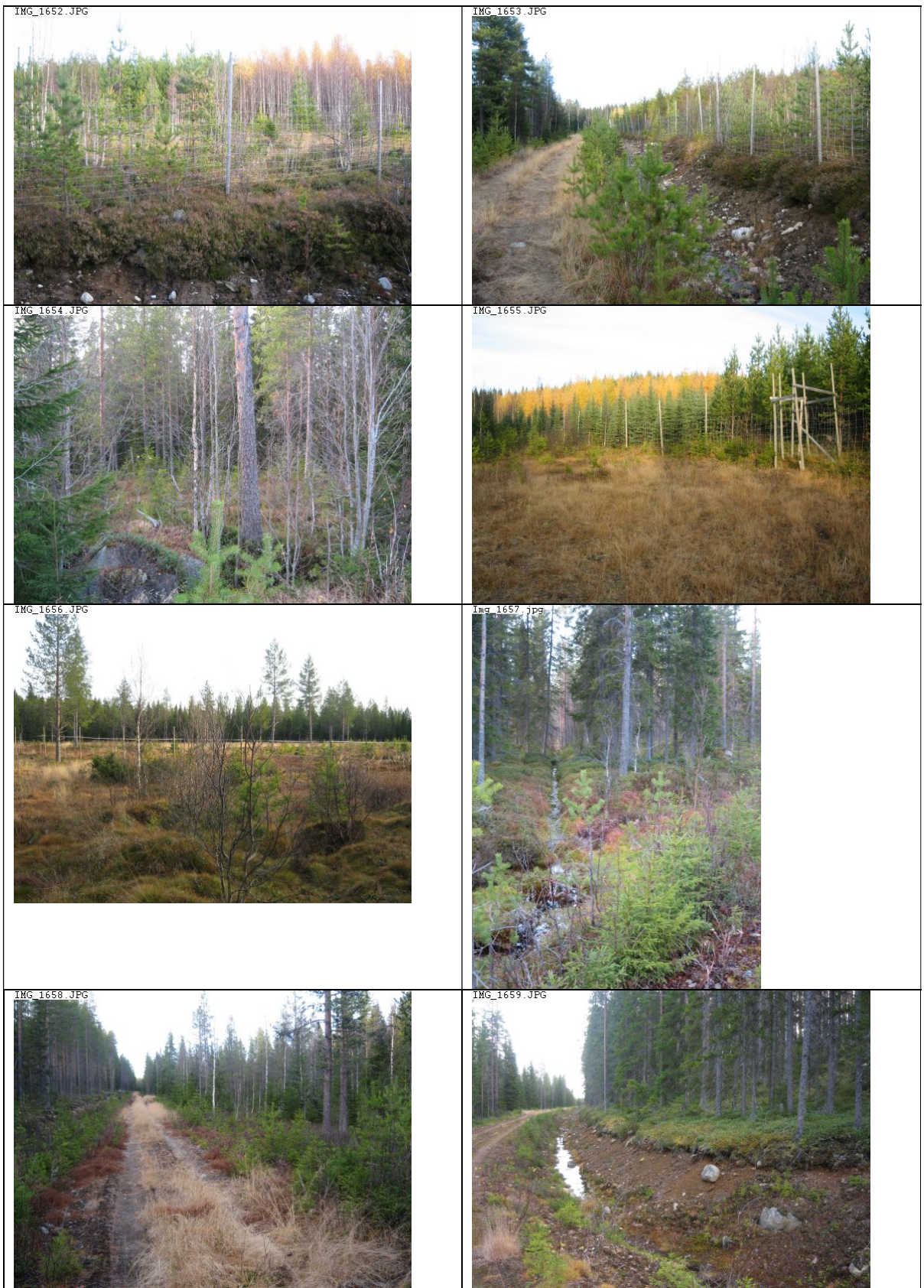




















IMG_1690.JPG



IMG_1691.JPG



IMG_1692.JPG



IMG_1693.JPG



IMG_1694.JPG



IMG_1695.JPG



IMG_1696.JPG



IMG_1697.JPG



IMG_1698.JPG



IMG_1699.JPG

